THE EFFECT OF RESPIRATION, EXERCISE, AND PULSATILITY ON *IN VITRO* FONTAN HEMODYNAMICS

A Dissertation

Presented to

The Academic Faculty

by

Michael Vaughn Tree

In Partial Fulfillment

of the Requirements for the Degree

Doctor of Philosophy in the

School of Mechanical Engineering

Georgia Institute of Technology

May 2017

THE EFFECT OF RESPIRATION, EXERCISE, AND PULSATILITY ON *IN VITRO* FONTAN HEMODYNAMICS

Approved by:

Dr. Ajit Yoganathan, PhD, Advisor
School of Mechanical Engineering
Georgia Institute of Technology

Dr. Rudolph Gleason, PhD
School of Biomedical Engineering
Georgia Institute of Technology

Dr. Cyrus Aidun, PhD
School of Mechanical Engineering
Georgia Institute of Technology

Dr. Kevin Maher, MD
Department of Pediatrics
Emory University

Dr. Brandon Dixon, PhD
School of Mechanical Engineering
Georgia Institute of Technology

Date Approved: March 16, 2017

To my wife, Rachel, and my children, Clara and Anna

ACKNOWLEDGEMENTS

First, and foremost, I thank my wife. Her endless support and sacrifice for my personal pursuit of knowledge and happiness was the single most sustaining ground on which I stood in this effort. These written words can never repay the debt I owe her for her kindness, compassion, and interest regarding my day-to-day challenges. My convincing her of marriage was truly the greatest con anyone has ever pulled.

I also thank my family, both near and far. More than once the highlight of my day was the excited hug I received from Clara as I walked in the door. Just as rewarding, was holding a sleeping Anna, whose peaceful demeanor brought relaxation to an otherwise stressful atmosphere. Many thanks go to my father, who talked me through a thesis advisor change and helped me see a faculty perspective. His passion for thermodynamics, internal combustion engines, and engineering in general paved the way for me to explore how everything works. I will never forget him telling me, “Sometimes you have to do things you don’t want to do; suck it up.” Of course, I also thank my mother. Though she claims to be the least intellectual in the family, her astute understanding of my social and emotional needs throughout my life betray this claim. The countless hours she spent encouraging me to complete my schoolwork are manifest in this accomplishment.

Naturally, I must thank Dr. Yoganathan. I appreciate the chance he took on me when we met through Dr. Aidun. I appreciate his allowing me to focus on the skills I found important. I appreciate the experience I gained in his lab beyond those of many PhD students – instructing in his class, advising numerous undergraduate students, and composing grants. I give a rather unique thank you to Dr. Caroline Genzale, my first PhD advisor at Georgia Tech, who runs the Spray Physics and Engine Research Lab. Though

funding issues ended our continued efforts, I am forever grateful for her getting me in the door.

I also thank my fellow students – from my previous lab and this lab, both alumni and those yet to graduate. I doubt I can name all who have influenced and aided me, but here is my attempt: Ben Knox, Gina Magnotti, Tom Furlong, JP Rabbah, Andrew Siefert, Min Yun, Arvind Santhanakrishnan, Maria Restrepo, Elaine Tang, Zhenglun (Alan) Wei, Vrishank Raghav, Shelly Singh, Prem Midha, Ikay Okafor, and Phillip Trusty.

And finally, I thank my family again. I especially thank my paternal grandfather, David Tree. Before his passing in September 2016, he stood as the great patriarch of our family and served for 40 years as a mechanical engineering professor at Purdue University. I often admired him from afar, and will never forget a particular summer spent building a shed and attending a Cubs game. Our entire family owes our work ethic, among other things, to his example. I appreciate the story he tells of how his blue-eyed thesis advisor's eyes became brown, and what he did about it. And we are all indebted to his adaptation of a well-known poem, "I think that I shall never see [anything] as beautiful as a Tree."

TABLE OF CONTENTS

LIST OF TABLES

LIST OF FIGURES

NOMENCLATURE

TCPC	Total Cavopulmonary Connection
EC	Extra-Cardiac Total Cavopulmonary Connection
IA	Intra-atria Total Cavopulmonary Connection
BH	Breath-held
FB	Free-breathing
EX	Exercise

SUMMARY

The Fontan procedure is the current intervention for single ventricle congenital heart defect patients. Eventually, all Fontan patients suffer long-term complications. These comorbidities are associated with blood fluid dynamics (hemodynamics) within the Fontan surgical connection. Numerous *in vitro* studies explore the effects of different patient conditions (breath-held, free-breathing, exercise, etc.) on Fontan hemodynamics. However, none of these studies are conducted with a flexible wall Fontan connection model. The purpose of this study was to develop a flexible Fontan connection model and examine the effect of patient condition on Fontan connection hemodynamics.

The study employed model verification, bulk hemodynamic measurement, particle image velocimetry, and computational methods to explore the effects of respiration, exercise, and pulsatility on Fontan hemodynamics. Development resulted in a patient-specific compliance-verified *in vitro* Fontan circulation model. The model was then used to find the apparent power loss, viscous dissipation, and hepatic flow distribution of the Fontan connection under both physiological and derived experimental conditions.

The study found respiration consistently increased apparent power loss. Increasing exercise intensity also increased apparent power loss; the indexed viscous dissipation term also increased with increasing exercise intensity. Increasing pulsatility increased apparent power loss monotonically, but viscous dissipation showed a consistent non-monotonic relationship. This relationship is explained using the Womersley parameter. Power loss and viscous dissipation are further compared, concluding that viscous dissipation is a superior hemodynamic metric. Hepatic flow distribution showed no consistent trends due to respiration, exercise, or pulsatility effects. The time-resolved three-dimensional velocity

fields acquired to compute the metrics are useful for computational fluid dynamics simulation verification.

1 INTRODUCTION

Single ventricle congenital heart defects are a complex and costly form of congenital heart disease in which there is only one functional pump to move blood throughout the body. At diagnosis the single ventricle circulation contains a mixture of oxygenated and deoxygenated blood which reduces the blood-oxygen saturation throughout the circulation. This scenario requires intervention to prevent systemic organ oxygen starvation and eventual organ failure. The current intervention standard is a set of staged palliative surgeries first completed by Dr. Francois Fontan in 1971 [1]. The Fontan procedure results in the isolation of pure, oxygenated blood in the single ventricle. This restoration of pure oxygenated blood pumping to the systemic organs is finalized through the creation of a total cavopulmonary connection (TCPC), an anastomosis of the inferior vena cava (IVC), superior vena cava (SVC), and the left and right pulmonary arteries (LPA and RPA, respectively). The resulting circulatory system is fundamentally different from a biventricular circulation, and is commonly known as the Fontan circulation.

The Fontan palliation provides low operative mortality and satisfactory early to mid-term patient outcomes, but many patients suffer long-term complications. Over the approximate 40 year history of Fontan procedures the single ventricle patient's short-term survival outcome has risen from 10% during the pre-Fontan era [2] to 90% during the first decade of life [3]. By 25 years of life, though, the survival rate drops to 70% [4]. The factors relating to this survival drop are a complex composition of circulatory complications. These complications include heart arrhythmia, liver fibrosis/cirrhosis, protein losing enteropathy, thromboembolism, renal dysfunction, ascites, plastic bronchitis, pulmonary arteriovenous malformations, and decreased exercise capacity [5,6].

These complications are ubiquitous, eventually appearing in almost every Fontan patient. In fact, studies following Fontan patient outcomes over the last several decades have led some experts to state, "…it is reasonable to conclude that freedom from morbidity [for Fontan patients] is likely close to zero." [7] Yet another study finds that Fontan patients are, "doomed to a circulatory failure." [8] To avoid this doom one must address the cause or causes of these complications – one of which is Fontan circulation fluid dynamics.

Numerous studies show association between Fontan circulation hemodynamics and long-term complications [9–14]. This knowledge fueled and continues to fuel hemodynamic studies of the Fontan circulation using computational simulations [15–21] , *in vitro* methods [9,22–28], and animal or *in vivo* methods [29,30]. Each study approach has different merits. *In vivo* methods provide an incomplete view of the real Fontan system: a full truth partially revealed, while computational methods provide a complete view of a modeled Fontan system: a partial truth fully revealed. *In vitro* methods attempt to bridge this difference by providing a fuller truth of key Fontan subsystems (i.e. the Fontan connection) while modeling the remaining circulation. Current *in vitro* models of the Fontan circulation employ rigid TCPC sections [22,23,27,28,31–35]. These models have provided excellent scientific insight; however, the rigid chambers of these models have been criticized for their physiologic approximation to the comparatively more compliant TCPC connections observed in-vivo. *In vitro* studies that have employed a compliant TCPC have not verified their model compliance with *in vivo* data [24]. By neglecting *in vivo* verification the TCPC will not deform accurately, which affects both small scale hemodynamics within the TCPC and global pressure waves through the Fontan circulation due to cardiac or respiratory sources.

Therefore, the following work develops and verifies compliant TCPC models for inclusion in a physiologically accurate *in vitro* Fontan circulation model. This model is then employed to study the effects of respiration, exercise, and general waveform pulsatility on Fontan hemodynamics. The work includes both hemodynamic and flow field analysis with the intent of providing relationships between respiration, exercise, and waveform pulsatility and key hemodynamic metrics related to patient complications and outcomes. In addition, the flow field data collected will provide validation for detailed fluid structure interaction computational analysis. The hypothesis of the work is that respiration, exercise, and waveform pulsatility affect TCPC flow field and hemodynamic metrics important to Fontan patient outcomes.

2 HYPOTHESIS AND SPECIFIC AIMS

The proposed work intends to employ a physiologically relevant *in vitro* Fontan circulation model to explore the effects of respiration, exercise, and pulsatility on Fontan hemodynamics. The hypothesis of the work is that respiration, exercise, and waveform pulsatility affect TCPC flow field and hemodynamic metrics important to Fontan patient outcomes. This hypothesis will be examined through three specific aims: (1) Development and Verification of a Comprehensive Fontan *In vitro* Model, (2) Understanding the Effects of Respiration on Fontan Hemodynamics, and (3) Understanding the Effects of Exercise and Pulsatility on Fontan Hemodynamics.

2.1 Specific Aim 1: Development and Validation of a Comprehensive Fontan *In Vitro* Model

In vitro models of the Fontan circulation are employed in numerous studies to understand Fontan hemodynamics. Early models employed rigid walls and steady flow. Subsequent studies utilized pulsatile, and even patient-specific waveforms. Compliant test sections, such as the TCPC, are the latest subject of accuracy improvement, but thus far only arbitrary compliance values exist in these models. Proper TCPC compliance verification will provide transient anatomical changes observed *in vivo*, improving the *in vitro* model's reflection of *in vivo* physiology. The increased data collectable during an *in vitro* study (versus an *in vivo* study) will be incrementally more trustworthy. In addition, a verified Fontan *in vitro* model can provide data for computational simulation model validation en route to a complete view of the Fontan system.

In order to verify against *in vivo* data, consistent TCPC compliance measurement methods will be developed for both *in vivo* datasets and the physical *in vitro* models. The

in vivo datasets provided include phase contrast magnetic resonance images (PCMRI) which provide the unstressed TCPC anatomy as well as the TCPC inlet and outlet flows. Age-matched pulse pressure data is available from the same center to provide the rest of the compliance calculation's necessary requirements. With the *in vivo* compliance established from this data, a silicone *in vitro* test model will be constructed via spin molding. The test model compliance will be measured via pressure transducers during a fluid injection event. Any compliance value discrepancies between the *in vivo* data and the *in vitro* test model will be remedied through silicone composition or model wall thickness alterations of subsequent test models. Each test model alteration will incur subsequent compliance testing until the *in vitro* model compliance matches the patient-specific *in vivo* compliance value. The *in vitro* Fontan model is then considered verified.

The product of this aim will be an *in vivo* verified Fontan circulation model as evidenced by matching flow waveforms and TCPC compliance to the provided PCMRI data.

2.2 Specific Aim 2: Understanding the Effects of Respiration on Fontan Hemodynamics

One key difference between the Fontan and healthy circulations is the presence of a sub-pulmonary pump [36]. The Fontan circulation lacks this pump and, thus, relies on passive pressure gradients for its blood to reach the lungs. Under these conditions, numerous studies have verified that intrathoracic pressure variations due to respiration affect Fontan patients more drastically than those with a biventricular circulation. These studies include *in vitro* [27,37,38] , *in vivo* [39–43], and computational approaches [15,44,45]. However, none of these approaches utilize an *in vivo* compliance verified TCPC model. Thus, this

aim will utilize the Fontan circulation from Aim 1 to understand the effects of respiration on Fontan hemodynamics, and compare to previous results.

Respiration effects will be isolated from cardiac effects through patient-specific real-time phase contrast magnetic resonance images. The effect of respiration will be measured by changes in global pressure, flow, TCPC pressure loss, and TCPC flow structures both instantaneously, and on a cycle-averaged basis.

2.3 Specific Aim 3: Understanding the Effects of Exercise and Pulsatility on Fontan Hemodynamics

Several studies show a relationship between patient exercise level and flow pulsatility and Fontan circulation hemodynamics (global pressure and flow) [44,46–48]. To date, this relationship is the strongest tie between Fontan hemodynamics and patient quality of life. However, none of the studies used in discovering this relationship utilized an *in vivo* verified TCPC model. Additionally, no computational models exploring this issue with fluid structure interaction models have done so with proper experimental validation [45,49–51]. Hence, the *in vivo* verified Fontan circulation from Aim 1 will be employed to explore the effects of exercise and pulsatility on Fontan hemodynamics.

Exercise will be represented using patient-specific exercise flows and literature-based decreases in pulmonary vascular resistance (PVR). Defining the loop conditions as such will automatically set the modeled pressure waveform, which will be checked against literature-based Fontan exercise values for verification. Heart rate and respiratory rate during exercise are also available from the patient-specific data set and will be assigned their corresponding value.

3 BACKGROUND AND SIGNIFICANCE

3.1 The Healthy Cardiovascular System

The human cardiovascular system serves to supply the body with nutrient-containing blood essential to all organ functions. The healthy cardiovascular system performs this service by means of two parallel pumps within the heart, the left and right ventricle. The left, and more dominant, ventricle circulates oxygenated, nutrient-rich blood to the systemic organs. The systemic organs process the oxygen and nutrients in their various tasks and passively return the blood to the right ventricle. The right ventricle then pumps the oxygen-poor blood to the lungs for oxygenation. Oxygenated blood from the lungs then flows passively to the heart's left side completing the circulatory path. Figure 3-1 shows a schematic representation of the healthy cardiovascular system.

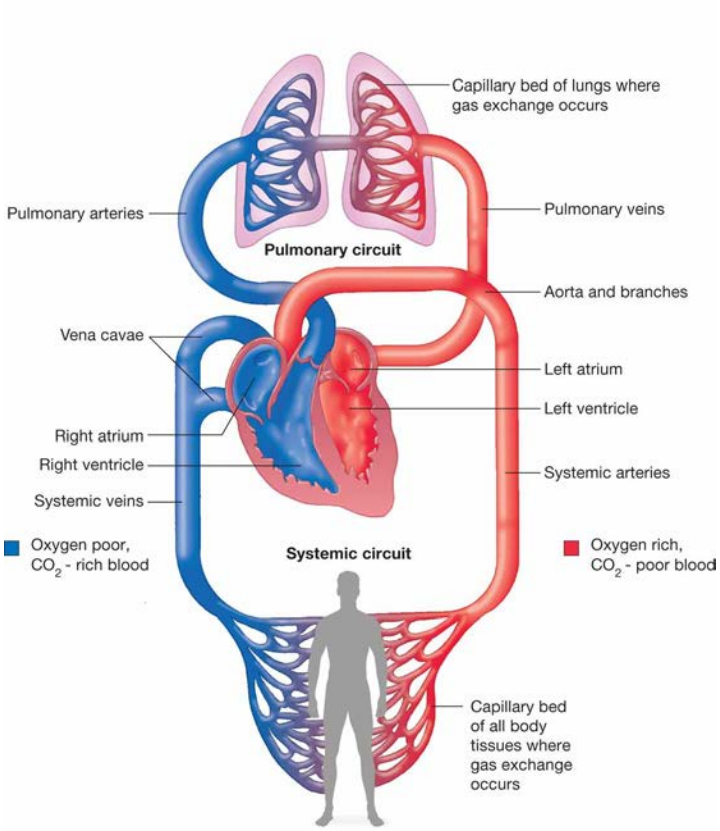

Figure 3-1: Healthy cardiovascular system schematic showing the separation of oxygenated and de-oxygenated blood (courtesy aireurbano.com)

One key aspect of the healthy circulation is the separation of oxygen-rich and oxygen-poor blood. This separation ensures that the systemic organs (liver, kidneys, stomach, etc.) and even the heart itself (via the coronary arteries) receive a full oxygen supply with every stroke of the left ventricle. Without this full oxygen supply these systemic organs can fail.

3.2 Congenital Heart Disease

Congenital heart disease is a general term categorizing heart anatomy anomalies present at birth. The severity of the defects range from small, repairable holes in the wall between the left and right ventricle called the septum, or septal defects, to complex combinations of

defects including both ventricles, heart valves, and displacement of the major blood vessels surrounding the heart. Approximately 0.8-1% of all births in the United States include some form of congenital heart disease [52]. Table 3-1 shows incidence estimates for typical congenital heart diseases.

Table 3-1: Common congenital heart disease incidence with emphasis on cyanotic births [52]**. The cyanotic lesions are denoted with italics.**

Congenital Heart Disease	Incidence (per 1,000 births)
Bicuspid Aortic Valve	13.56
Ventricular Septal Defect	3.57
Atrial Septal Defect	0.94
Patent Ductus Arteriosus	0.80
Pulmonary Stenosis	0.73
Tetralogy of Fallot	0.42
Hypoplastic Left Heart	0.26
Hypoplastic Right Heart	0.22
Double Outlet Right Ventricle	0.16
Pulmonary Atresia	0.13
Single Ventricle	0.11
Tricuspid Atresia	0.08
All Cyanotic	***1.38***

Some of the most time-sensitive and complex congenital heart diseases are those that result in patient cyanosis. Cyanosis is a blue coloring of the skin due to a lack of oxygen saturation in and around the region. Children born with certain congenital heart diseases have hearts that mix their oxygen-rich and oxygen-poor blood and result in cyanosis. These patients are often termed “blue babies” because of their skin hue, and regularly require surgery. In fact, approximately 50% of children born with a congenital heart disease will require at least one surgery in their lifetime. Congenital heart disease patients are living much longer due to recent advances in surgical techniques and patient care, providing hope for further improvements but new challenges in the adult physiology [53].

3.3 Single Ventricle Congenital Heart Disease

The most complex congenital heart diseases that exist are anatomies in which only one functional ventricle remains, and are aptly called single ventricle congenital heart diseases. Although single ventricle defects occur in only 7.7% of congenital heart diseases (0.077% of all patients), their healthcare financial burden is extremely disproportionate [54,55]. Single ventricle congenital heart disease are, by definition, the most cyanotic patients of any congenital heart disease because they include only one functional ventricle to which all blood eventually travels. In contrast to Figure 3-1, the single ventricle physiology mixes oxygen-rich and oxygen-poor blood in the single ventricle, providing less than 100% blood-oxygen saturation to the systemic organs. This mixing is demonstrated in Figure 3-2.

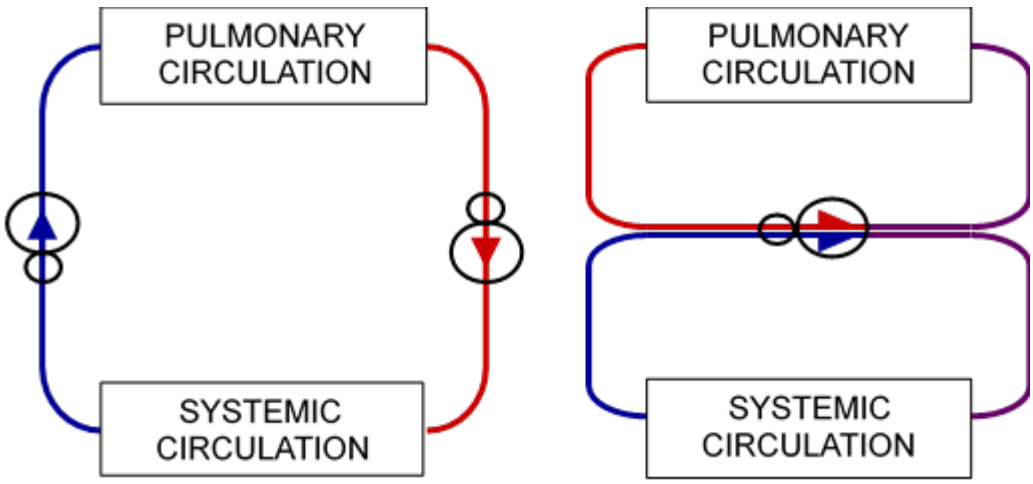

Figure 3-2: Schematic of healthy circulation (left) and single ventricle circulation (right) showing respective separation and mixing of oxygen-rich and oxygen-poor blood.

One objective in treating patients with single ventricle congenital heart diseases is to restore the separation of oxygen-rich and oxygen-poor blood flow. This objective can be handled through a few different procedures depending on the cause of the single ventricle phenomena, but the most common method is the Fontan procedure.

3.3.1 The Staged Fontan Procedure

The Fontan procedure is a palliative set of staged surgical interventions that shunt the oxygen-poor systemic venous return past the single ventricle and connect it directly into the pulmonary circulation (Figure 3-3).

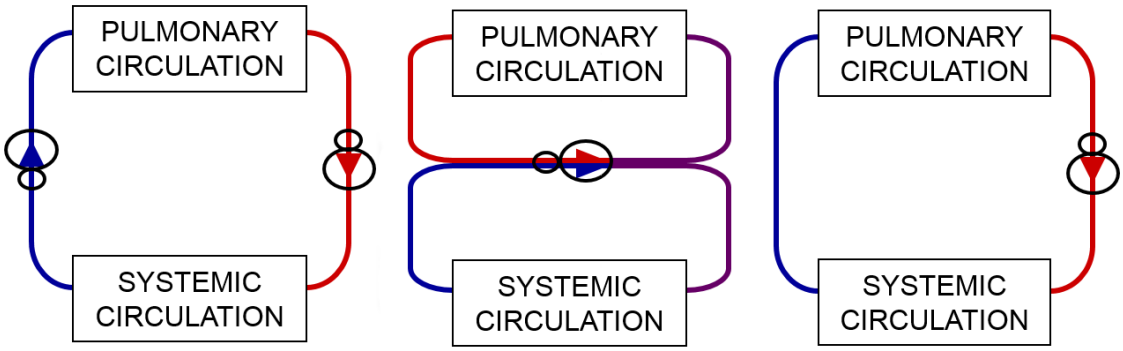

Figure 3-3: Healthy circulation (left), single ventricle congenital heart disease circulation (center), and repaired single ventricle congenital heart disease (right) circulation schematics.

Though simple in concept, the practical application of this solution to single ventricle congenital heart disease is actually quite complicated. Neonatal physiology includes relatively high pulmonary vascular resistance which prevents successful routing of the entire venous return to the pulmonary vasculature. So, the systemic venous return cannot be connected directly to the pulmonary circulation right after birth. With imminent mortality approaching, the patient's best option is a systemic to pulmonary circulation shunt. The first to report this first stage of the Fontan palliation was Dr. William Norwood [56].

3.3.2 The Norwood Procedure

The Norwood procedure is performed within the first days to weeks of life. The implanted shunt re-circulates some partially oxygenated blood exiting the ventricle directly back to

the lungs, attempting to double-dip in the oxygen existing there. In some cases, including Norwood's original case, the patient's aorta is underdeveloped and requires combination with the pulmonary arteries to maintain sufficient diameter to support adequate blood flow. The pulmonary artery, then, no longer exists and the Norwood shunt acts as the only source of pulmonary blood flow. This situation further complicates the already delicate Norwood procedure, which places among the highest mortality rates among congenital heart practices [57]. Variations on the procedure exist through changing the specific endpoints of the shunt. The modified Blalock-Taussig shunt connects the right subclavian artery to the right pulmonary artery [56]. The Sano procedure shunts directly from the right ventricle to the pulmonary artery bifurcation [58] (Figure 3-4).

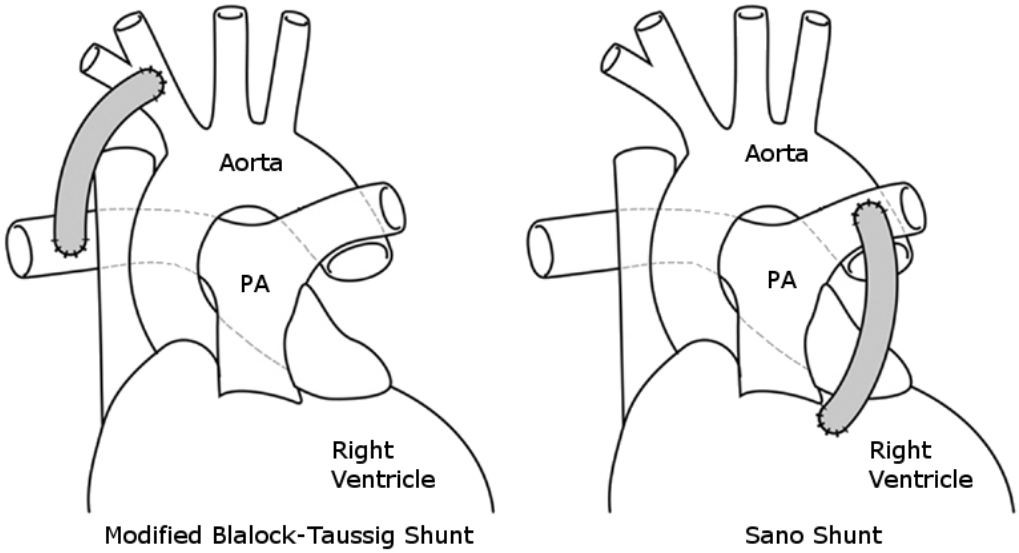

Figure 3-4: Stage 1 Fontan procedure variation schematics: Modified Blalock-Taussig Shunt and Sano Shunt

No matter the variation, the shunting of systemic to pulmonary circulations provides sufficient stabilization until the second stage of the Fontan palliation, the Glenn procedure, can be performed.

3.3.3 The Glenn Procedure

Between 3 to 6 months of age, the relatively high pulmonary vascular resistance to flow in the neonatal circulation has subsided and the patient is prepared for a Glenn procedure. This second stage of the Fontan palliation first removes the Norwood shunt and replaces its effects by rerouting superior vena cava (SVC) flow from the right atrium to the pulmonary arteries. Figure 3-5 illustrates the Glenn procedure.

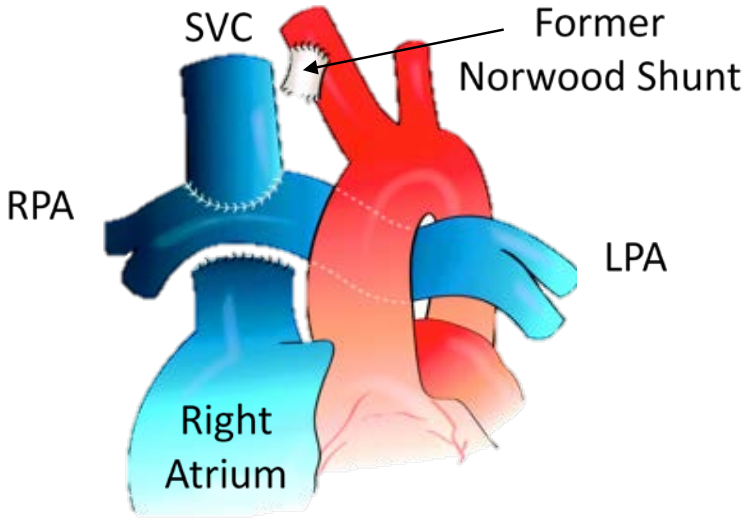

Figure 3-5: Glenn procedure illustration. RPA -- right pulmonary artery, SVC -- superior vena cava, LPA -- left pulmonary artery.

The Glenn procedure successfully separates a larger fraction of oxygen-poor and oxygen-rich blood between the systemic and pulmonary circulation. The procedure focuses on SVC flow because approximately 60% of an infant's total cardiac output is routed to their brain and upper extremities. As the child grows this ratio flips to 60% of total flow routing to the lower extremities. To account for this change in blood flow and finalize the separation of oxygenated and de-oxygenated blood, the Fontan procedure is performed.

3.3.4 The Fontan Procedure

First reported in 1971, the Fontan procedure completes the separation of oxygen-poor and oxygen-rich blood by re-routing the inferior vena cava (IVC) from the right atrium to the pulmonary arteries [1]. The original procedure by Fontan and Baudet called for superior vena cava (SVC) flow to be routed to the right pulmonary artery (RPA), and a separate routing of the IVC to the left pulmonary artery (LPA). The original procedure also included the placement of a valve in the IVC to maintain unidirectional flow. In 1973, Kreutzer et al. proposed utilizing the native right atrium as the conduit through which the systemic venous return connects to the pulmonary arteries [59]. This atrio-pulmonary connection, served as the standard for almost 20 years, but was eventually replaced because it caused arrhythmias and thrombus formation (blood clots) [60,61]. The atrio-pulmonary connection was replaced by the total cavopulmonary connection beginning in 1988 [62]. The total cavopulmonary connection is performed either through the right atrium (an intra-atrial connection) or outside the heart (an extra-cardiac connection). The intra-atrial TCPC differs from the atrio-pulmonary connection because the intra-atrial TCPC employs a graft along the atrial wall that restricts the effective flow diameter. A 1991 study showed the decrease in arrhythmia incidence for Fontan patients with a TCPC versus an atrio-pulmonary connection [63]. Comparison between the extra-cardiac TCPC and the intra-atrial TCPC is more recent, and still an area of active research. The decision whether to employ an extra-cardiac or intra-atrial TCPC for a given patient is dependent on numerous factors including patient size, anatomical geometry, and surgeon preference. One argument for preferring one TCPC type over the other comes from the Society of Thoracic Surgeons which found a higher likelihood of in hospital death during Fontan patient surgical

revisions for extra-cardiac connection types [64]. Figure 3-6 summarizes the differences between the Fontan procedure types.

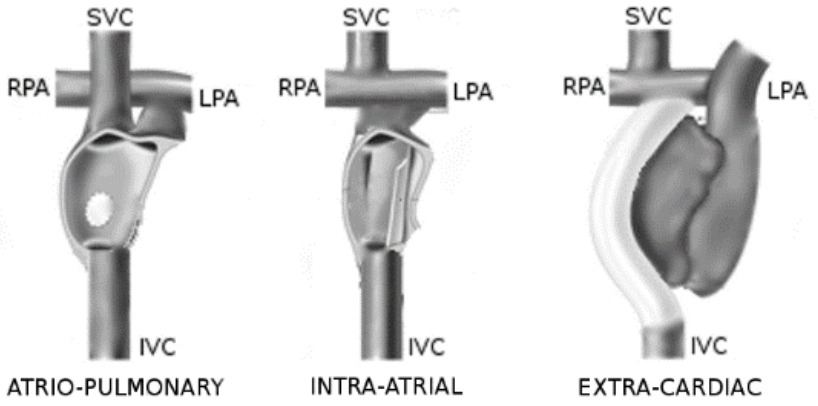

Figure 3-6: Schematic representation of the different Fontan connection types

3.4 Fontan Patient Outcomes

The half-century long development process of Fontan patient care has led to relatively favorable short-term outcomes for Fontan patients. These patients are reaching adulthood at an unprecedented rate and with ever-increasing quality of life [65]. Of approximately 200 intra-atrial Fontan patients from Boston Children's Hospital, estimated survival at 10 years was 91% with freedom from complications at 87% over the same period [66]. The more daunting prospect for Fontan patients are the seemingly unavoidable long-term complications they are doomed to suffer. Unfortunately the Fontan procedure is only considered palliative, instead of curative, because of its long-term complications [12]. Twenty-year survival shows a sudden drop off for these patients, with survival rates varying between 69 and 83% [67]. Another study of 500 extra-cardiac (EC) Fontan patients show a survival rate of 96.2% at 10 years and 92.8% at 15 years, but with 15 year freedom from morbidities at only 82.1% [68]. To further complicate matters, the short-term success

enjoyed by these patients only further emphasizes the impact of long-term Fontan complications on the healthcare industry overall [55]. Numerous researchers recognize this problem and are now focused on mitigating these complications, if not curing all together, the failing Fontan.

3.4.1 The Failing Fontan

The traditional failure mode from Fontan's original surgeries were mostly related to arrhythmias [63]. The atrio-pulmonary connection required surgical manipulation of the right atrium, an essential location in cardiac electrophysiology. Formation of the atrio-pulmonary connection often mistakenly altered the AV node on the right atrium and thus affected the whole cardiac rhythm. The high arrhythmia incidence of atrio-pulmonary Fontan connections is one reason for clinical practice shifting to total cavopulmonary connection (TCPC) connections [63]. Of course, the almost half-century history of iterations on the Fontan connection has drastically reduced the incidence of arrhythmia in Fontan patients. Despite these advances the Fontan circulation still fails in a variety of ways. Fontan failure is most easily understood through categorization into two failure modes: ventricular dysfunction, and chronic Fontan failure.

3.4.1.1 Ventricular Dysfunction

Fontan patients suffer from an underdeveloped heart leaving them with only a single ventricle. Unfortunately, their remaining ventricle also behaves abnormally. Whether this abnormal behavior is due to fetal development issues, Fontan circulation hemodynamics, or both is a complicated problem under active research. Regardless of the cause, the fact that remaining single ventricle misbehaves is important because both systolic and diastolic dysfunction are common among Fontan patients. A cross-sectional analysis of 546 Fontan

patients revealed that 27% had abnormal ventricular ejection fractions and 72% had diastolic dysfunction [69]. Some attribute this ventricular dysfunction to chronic hypoxemia (low blood oxygen concentration) and relatively early volume loading of the ventricle seen by all Fontan patients through the surgical staging process [36].

Beyond poor ejection fractions and abnormal ventricular volumes, in most cases the Fontan patients suffers from low exercise tolerance. The normal heart compensates for increased systemic blood flow needs by increasing heart rate, contractility, and filling volumes in order to eject more blood. In general, Fontan patients possess an ability to eject whatever blood fills their heart through increased contractility, but the Fontan circulation prevents adequate filling and heart rate increase for high intensity exercise [70–72].

3.4.1.2 Chronic Fontan Failure

Even among those who have functioning single ventricles, Fontan circulatory systems eventually fail in time. Indeed, one study bluntly stated that the Fontan patient is "doomed to fail" [8]. This hopelessness comes from the fact that chronic Fontan failure is a function of the nature of the Fontan circulation itself.

The premise of the Fontan circulation is that when only one ventricle is available it should be used to pump to the systemic circulation. This leaves pulmonary circulation as a passive system. No longer supplemented by the right ventricle, the oxygen-poor blood returning from the systemic organs has no additional energy source to overcome the vascular resistance in the lungs. Therefore, in order to reach the lungs, this blood must exist at a higher pressure than the lungs. Figure 3-7 shows a schematic representation of the differences between a healthy biventricular circulation, a Fontan circulation, and a chronically failing Fontan circulation.

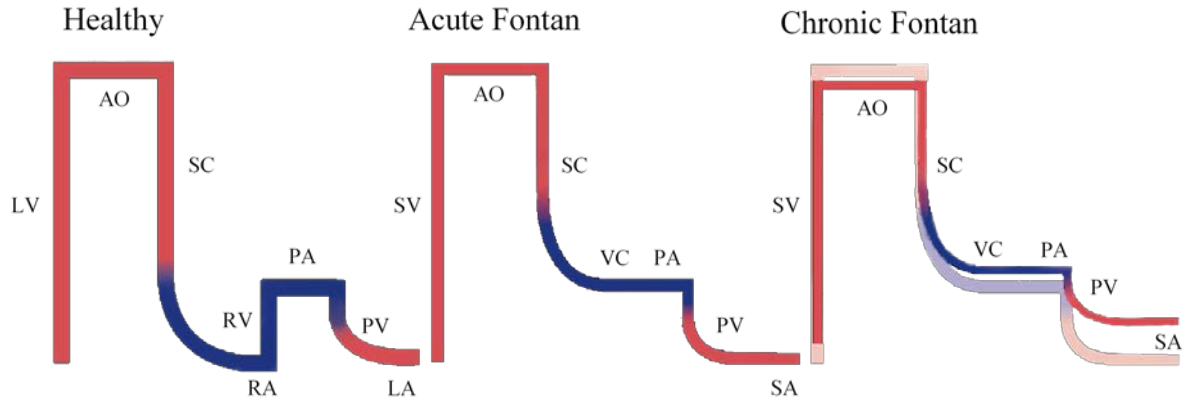

Figure 3-7: Schematic representation of pressure values in different circulatory systems. LV – Left Ventricle, AO – Aorta, SC – Systemic Circulation, RV – Right Ventricle, RA – Right Atrium, PA – Pulmonary Arteries, PV – Pulmonary Veins, LA – Left Atrium, SV – Single Ventricle, VC – Vena Cavae, SA – Single Atrium

The lack of a right ventricle also reduces the oscillatory nature of the pulmonary blood flow. Pulmonary flow in a biventricular circulation is pulsatile, but is slow, steady, and sluggish in the Fontan patient. These effects of the Fontan circulation place the patient in a state equivalent to early heart failure, which almost always deteriorates and eventually fails [73].

This chronic Fontan failure is engrossed with several systemic organ complications. In fact, one reviewer argues that the nature of the Fontan circulation is to blame for all Fontan patient long-term complications [7]. Systemic organ complications include liver fibrosis/cirrhosis, protein losing enteropathy, thromboembolism, renal dysfunction, ascites, plastic bronchitis, and pulmonary arteriovenous malformations [6].

Numerous studies have examined systemic organ complications in Fontan circulations and attempted to discover their cause. Liver cirrhosis is hypothesized to exist

due to the increased central venous pressures just downstream from the hepatic veins seen in the Fontan circulation [74]. Protein losing enteropathy, excessive loss of essential blood proteins through artery and vein side walls, is also associated with abnormally high blood pressures and low cardiac output [75]. Thromboembolism, the formation of blood clots which travel throughout the circulation and block smaller vessels, is associated with the numerous interventions each Fontan patient receives, especially those involving sutures and grafts [76]. Renal dysfunction is abnormal kidney behavior and is associated with low cardiac output [74]. Ascites is accumulation of fluid in the abdominal region and is associated with abnormally high local blood pressures [77]. Plastic bronchitis is the development of casts in the bronchial tree which obstruct the airway. Its cause is unknown. Pulmonary arteriovenous malformations are the shunting of pulmonary arterioles to pulmonary venues, short-circuiting the pulmonary capillary bed. This complication is particularly detrimental for Fontan patients because it further desaturates their already oxygen-poor blood. Pulmonary arteriovenous malformations are associated with an uneven distribution of hepatic factor (liver-based protein) to each lung [78]. In addition to the sheer number complications, a patient's individual care can be further complicated by the interplay between complications.

Several differences between Fontan and biventricular circulations have direct effects on both ventricular dysfunction and systemic organ complications. First, functioning on a single ventricle leaves the remaining ventricle in a compromised situation – maintained flow energy requirements with decreased energy budget. This can lead to ventricular dysfunction and decreased exercise performance. Second, in a biventricular physiology the cardiac atriums possess the lowest pressure environment of anywhere in the

circulatory system. Thus, disconnecting the superior and inferior vena cavae (SVC and IVC) from the atrium increases their pressure environment. This increased pressure must propagate upstream in order to maintain passive downstream flow, so the upstream organs are also exposed to higher-than-normal pressures. This can lead to numerous systemic organ complications: liver cirrhosis, protein-losing enteropathy, renal dysfunction, and ascites. Third, disconnecting the SVC and IVC from the atrium and connecting them directly to the pulmonary arteries also alters the velocity fields within these vessels. This velocity field alteration changes lumen wall shear stress and hepatic vein (just upstream of the IVC) flow distributions, among numerous other factors. Thrombosis and pulmonary arteriovenous malformations are related to lumen wall shear stress and hepatic vein flow distribution, respectively [76,78].

3.4.2 Hemodynamics and Fontan Complications

Hemodynamics encompasses the dynamics associated with blood flow. These dynamics are most readily characterized by blood flow velocity, but also include the kinetic and potential energy (blood pressure) required to move blood. In fact, it is into these three hemodynamic categories that we can group the observed Fontan complications.

The first hemodynamic category altered by the Fontan circulation is blood velocity. A biventricular circulation includes the emptying of IVC and SVC blood streams into the right atrium. This venous return blood velocity almost reaches instantaneous stagnation in the atrium before it is emptied into the right ventricle and quickly ejected to the pulmonary arteries. This drastic velocity change imbues blood constituent mixing. In contrast, the Fontan circulation eschews an atrial reservoir and never experiences the acceleration and deceleration associated with a sub-pulmonary ventricle. This not only discourages blood

constituent mixing, but also alters the geometrically and anatomically relative flow distributions of these constituents. Both the lack of flow pulsatility and relative flow distributions are associated with Fontan complications [78].

The kinetic energy required to move blood through the body is provided by ventricles within the heart. The biventricular circulation provides the blood with kinetic energy twice: once just before the aorta and once just before the pulmonary arteries. This system provides more than enough kinetic energy during rest for blood flow. Of course, the Fontan circulation only has one ventricle and can, therefore, only provide kinetic energy once. Though it only provides the kinetic energy once per cycle, the single ventricle actually provides the same amount of kinetic energy during rest as two ventricles from the biventricular circulation. This is truly remarkable evidence of the human body's ability to adapt, but ultimately results in an overworked ventricle. The single ventricle is already providing kinetic energy at close to maximum capacity, and thus the Fontan patient suffers decreased exercise performance [79]. Eventually the overworked ventricle no longer functions adequately [80,81].

Kinetic energy differences are not only important at the heart. Two recent studies showed an association between kinetic energy losses taking place at the total cavopulmonary connection (TCPC) and Fontan patient exercise performance [48,82]. Ultimately, this association is more readily remedied than energy losses related to a missing ventricle. The TCPC can, conceivably, be optimized to reduce kinetic energy losses at the time of surgery, but the single ventricle cannot be replaced with a biventricular heart without transplant.

The final hemodynamic category is potential energy, or blood pressure. The biventricular circulation establishes a normal, physiological blood pressure mapping throughout the circulatory system. Arteries experience relatively high pressures. Veins experience relatively low pressures. Above all, pressure drives blood flow. So, blood exiting the heart has the highest pressure and blood returning to the heart has the lowest pressure through either the systemic or pulmonary paths. The act of combining these paths in the Fontan circulation replaces the low pressures normally seen by the systemic venous return with higher pressures seen at the pulmonary arteries. This has two major effects. First, the relatively thin-walled veins cannot adequately hold this pressure and they begin to leak. Second, the relative pressure drop between upstream and downstream of the SVC and IVC is decreased and sluggish flow with high upstream pressures follows. These phenomena are associated with a many of the systemic organ complications suffered by Fontan patients [74,83,84].

3.5 Previous Fontan Hemodynamics Studies

The Fontan circulation originated as a clinical palliation for a dysfunctional or non-existing tricuspid valve (tricuspid atresia). A non-working tricuspid valve effectually reduces a bi-ventricular heart to a single ventricle, a fatal condition if not for the ground-breaking effort of Fontan and Baudet [1]. Naturally, clinicians followed the outcome of these patients, reporting low cardiac output, low oxygen saturations, high atrial pressures, and calcified/stenotic conduits [85]. Despite these observations the remaining ventricle appeared to work well under resting conditions [86]. Short-term complications were relatively minor compared to fatality, and the surgical history was not deep enough to

observe any of the looming long-term issues. The Fontan circulation was deemed a success, even if rather miraculously.

3.5.1 Previous Clinical Studies

The first sign of clinical Fontan circulation trouble came in the form of heart arrhythmias [63]. As Fontan patient follow-up continued, more and more long-term complications arose causing a re-evaluation of the Fontan circulation success [4,5,66,87–91]. Altered hemodynamics was hypothesized as playing a role, and has since been investigated with clinical tools (magnetic resonance imaging, echocardiography, catheterization pressure measurements, etc.) for virtually every complication [92–101]. The strongest ties between Fontan circulation hemodynamics and circulatory system complications are between Fontan connection power loss and patient exercise tolerance from Khiabani et al [48], and hepatic flow distribution and pulmonary arteriovenous malformations from [78] Srivistava et al. Though significant strides were made to highlight decreased cardiac output and elevated central venous (and atrial) pressures as macro-level hemodynamic issues related to Fontan complications, clinical analysis technology lacks the spatial and temporal resolution to comprehensively understand velocity fields and other fundamental hemodynamic details related to patient outcomes. Beyond the incomplete view provided by clinical data, these *in vivo* studies are simply difficult. *In vivo* study parameters are widely varying requiring high patient numbers for only correlated results and involve numerous ethical issues.

3.5.2 Previous Computational Studies and Lumped Parameter Modelling

Computational studies provide the most detailed hemodynamic view of the Fontan circulation of the exploration paths mentioned. Computational studies of Fontan

hemodynamics are the most recent path explored, and they began with lumped parameter modelling. Lumped parameter models, or lumped parameter networks, operate on the analog between fluid and electrical systems to group circulatory system regions with similar flow resistance, vessel compliance, and fluid inertia. This zero-dimensional model of the circulatory system can then be solved through a system of non-linear ordinary differential equations to give transient pressure and flow solutions. Optimizing the regional resistances, compliances, and inertias to result in patient-specific flow and pressure curves can then lead to parameterization studies of the system (i.e. the effect of systemic resistance on cardiac output). Sundareswaran et al used lumped parameter modeling in several studies to explore the global Fontan circulation effects of TCPC resistance [102]. Pekkan et al, Haggerty et al, and Di Molfetta et al used lumped parameter modeling to simulate the use of Fontan mechanical assist devices to reverse the failing Fontan circulation [103–105]. Fogel et al and Restrepo et al used lumped parameter modeling as boundary conditions for simulations involving pre-interventional planning [106,107]. By far, the most common use of lumped parameter models is to inform higher dimensional computational model boundary conditions [16,18,20,44,45,108–119].

Higher-order computational fluid dynamics (CFD) studies focus on the detailed flow fields within the TCPC. Early CFD studies focused on steady flow boundary conditions with rigid wall vessel models. Even under these simplified conditions, complex secondary flow features were shown [22]. Energy dissipation and TCPC flow efficiency soon became and emphasis. DeGroff et al showed that even simplified models produced instabilities and secondary flows which significantly affect energy losses [120]. Similar observations were made as computational simulations advanced to include patient-specific

geometries [121]. Though significant contributions, it is now recognized that only fully-coupled 2-way fluid structure interaction models of the TCPC will include all of the physiological cardiac and respiratory pulsatility effects necessary. The current standard for TCPC computational modelling comes from Long et al [45,122]. Though extremely detailed computational studies are still models of true physics and must rely on experimental validation to prove effective.

3.5.3 Previous *In Vitro* Studies

Experimental, or *in vitro,* investigations of Fontan hemodynamics furthered the research field through the ground-breaking effort of de Leval [62]. In this study, de Leval explored the deficiencies of the atrio-pulmonary connection and hypothesized that streamlining the connection would improve TCPC flow efficiencies and overall Fontan circulation performance. This work fueled numerous subsequent simplified TCPC studies. Sharma et al. experimentally demonstrated improved efficiency through the introduction of a caval offset [28]. Gerdes et al. showed similar effects with the introduction of baffle curvature [33], while Ensley et al. advocated for connection flaring [9]. These early experiments paved the way for employing physical lumped parameter models patterned after computational lumped parameter models to more realistically capture the physiological Fontan circulatory system. As this thesis includes *in vitro* model development, specifically, it's detailed study history is now outlined.

3.5.4 *In Vitro* Fontan Circulation Model Development

To model the Fontan circulation in an *in vitro* setting the complex network of flexible vessels in the body is modeled as a simplified fluid network with common elements lumped together. The earliest Fontan circulation physical lumped parameter models employed

rigid, idealized TCPC geometries and steady flow conditions [22,31,33]. De Zelicourt et al and Chopski et al added patient specific geometries from MRI scans, but maintained rigid vessel walls and steady flow conditions [23,35]. Tang et al, Figliola et al, and Vukicevic et al conducted studies with patient-specific geometries, rigid vessel walls, and pulsatile flow conditions [27,32,47]. The most physiologically accurate *in vitro* Fontan circulation model studies is by Vukicevic et al [38]. Vukicevic's mock circulatory system is modeled after a computational model of the circulatory fluid network [44,123]. It includes patient-specific flow conditions, cardiac and respiratory pulsatility, and a flexible total cavopulmonary connection (TCPC). Unfortunately, though the pressure and flow waveforms are verified against patient-specific data, the TCPC compliance is not. Without proper TCPC compliance, proper TCPC deformation cannot be ensured. Without proper TCPC deformation the fluid velocity near the TCPC wall is not the same as in the patient. Thus, questions remain as to the local TCPC velocity field accuracy. The local TCPC velocity accuracy is important in so far as it contributes to fluid power loss occurring within the TCPC – one of the key metrics relating TCPC hemodynamics to patient outcomes.

3.5.5 Respiration and Fontan Hemodynamics

Once pulsatile flow was realized in Fontan circulation *in vitro* models, the possibility of examining the effect of respiration on Fontan connection hemodynamics was realized. Lack of a functional right ventricle leaves Fontan patients with passive blood flow to the lungs. Numerous studies note this phenomena and emphasize the importance of respiration-induced pressure effects on the Fontan circulation as a result [15,27,37,38,40–43,124–127].

In vivo studies unanimously agree that Fontan caval flows are higher during inspiration than during expiration. Hsia et al attributes the increased Fontan baffle flow entirely to increase hepatic vein flow, rather than increased flow through the sub-hepatic IVC [42]. Hjortdal et al used a real-time MRI sequence to examine respiration effects during both rest and exercise [43]. This study also found increased caval flow during inspiration, but added that the inspiration to mean flow ratio found during rest was decreased during exercise, possibly contributing to the Fontan patient's exercise intolerance. Ultimately, respiration increases Fontan patient end diastolic volumes and stroke volumes, and is a key component in analyzing Fontan hemodynamics [41].

Recognizing the importance of respiration effects as outlined by *in vivo* studies, both computational [15,45,124,127] and experimental studies [27,37,38] now include them. However, only Long et al includes fluid-structure interactions to include proper respiration-driven vessel wall motion [45]. No computational studies of respiration effects on Fontan hemodynamics are validated against any physical flow fields. Similarly, only one *in vitro* study employs a patient-specific flexible wall Fontan connection [38], while the others use a rigid wall model and reservoirs in series with the flow to represent vessel compliance. The single study employing a patient-specific flexible wall provides no compliance verification, and does not include any flow field measurements.

3.5.6 Exercise and Fontan Hemodynamics

Though deemed a success during resting conditions, clinical studies highlight the Fontan patient's inability to tolerate exercise conditions [43,70–72,85,128]. Spurred by these findings, and the correlation of Fontan patient quality of life to exercise capacity [129], numerous clinical [79,130,131] and biomedical engineering studies

[11,15,16,41,44,48,102,117,132–135] sought to correlate and increase Fontan patient exercise capacity. These studies found that, unless already failing, the Fontan single ventricle is capable of pumping whatever volume of blood that reaches it during exercise. During exercise, a biventricular heart senses the need for increased oxygen to the body and simultaneously increases heart rate and stroke volume in both ventricles. The left ventricle feeds more oxygen-rich blood to the body and the right ventricle pushes more oxygen-poor blood to the lungs and the left ventricle. The Fontan circulation has no functioning right ventricle. Therefore, it cannot fill the single ventricle with a larger stroke volume. Partial compensation for Fontan patients comes in the form of increased exercise heart rates, but ultimately their exercise capacity is limited. The strongest ties between Fontan circulation hemodynamics and circulatory system complications are between Fontan connection power loss and patient exercise tolerance, highlighted by Khiabani et al [48].

The total cavopulmonary connection (TCPC) replaces the physiological right ventricle for Fontan patients. For this reason, it was the focus of many studies mentioned above. However, none of the *in vitro* studies above account for patient-specific flexible walls, and none of the computationally-based studies were quantitatively validated against patient-specific flexible wall datasets.

3.6 Study Significance

The work presented here is significant to both the clinical and engineering fields. From a clinical perspective, the work explores the relationship between respiration, exercise, and pulsatility flow effects on key hemodynamic metrics related to Fontan patient outcomes. Though these factors have been commented on in this context before, no previous studies employed a compliance verified patient-specific flexible Fontan connection model. Proper

compliance verification and flexibility at the Fontan connection will affect the flow field within the connection, and all hemodynamic metrics derived from the flow field [45]. If the effect of compliance in the Fontan connection is large enough, the relationship between these key hemodynamic metrics and patient outcomes may change.

From an engineering perspective, an *in vitro* model bridges the gap between limited data available from *in vivo* patient specific studies (a partial view of a full truth), and limitless data available from computational hemodynamic models (a full view of a partial truth). The *in vitro* model developed and the conditions tested in this study provide the first compliant model patient-specific stereoscopic flow field with sufficiently high spatial and temporal resolution for computational hemodynamic simulation validation.

4 METHODS

4.1 Instrumentation

The following section provides the technical specifications and relevant information for the instruments used to both control the experiments and acquire data in this study.

4.1.1 MRI Instrumentation

The patient-specific anatomical models and flow conditions used in this study were acquired from MRI scans performed at the Children's Hospital of Philadelphia. An Avanto Whole Body system (Siemens Medical Solutions, Malvern, PA) was used for the anatomic and PCMR imaging. The Avanto system magnet had a field strength of 1.5 T and a gradient strength of 33 mT/m at 125 T/m/s. The system was 160 cm long with a 60 cm bore. The specific procedure used to acquire the anatomy and flows for this study are in section 4.2.1.1.

4.1.2 Fontan Circulation Model Instrumentation

The Fontan circulation model employed in this study was a physical lumped parameter model. Figure 4-1 shows a schematic of the gravity-driven mock circulatory system.

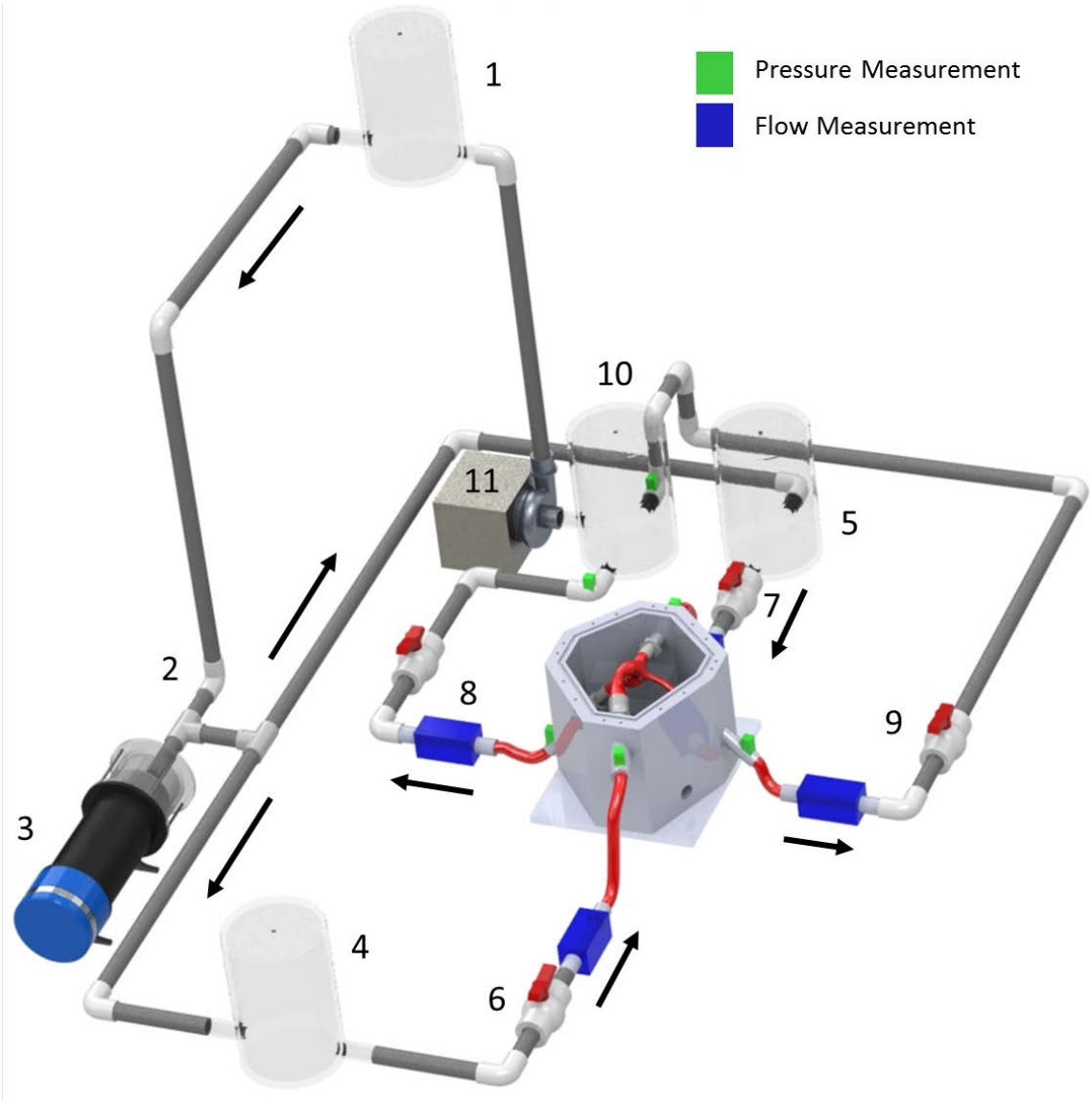

Figure 4-1: Fontan circulation model schematic with labeled components. The large blue rectangular prisms represent volumetric flow rate measurement locations. The small green rectangular prisms represent static pressure measurement locations.

Flow began in an elevated reservoir (1) with a pressure head representing mean ventricular pressures. Flow then proceeded down the piping network through a check valve (2) to a junction with a programmable piston pump (3). This pump was a Vivitro SuperPump (Model SPL 39891; Vivitro Systems Inc, Victoria, British Columbia) controlled by a voltage waveform output from a custom LabVIEW 13.1 virtual instrument

(National Instruments, Austin TX). Pulsatile flow output from the pump was split at a tee junction to both the IVC and SVC inlet lines, and proceeded through pressurized air compliance chambers (4,5) and ball valves (6,7), which modified flow waveform frequency and mean flow, respectively. Flow then entered the flexible TCPC model test section, and proceeded out through the LPA and RPA lines, passing through two more ball valves (8,9) that controlled mean outlet flow rate. The pulmonary artery outflow lines met at a reservoir representing the Fontan single atrium (10) before the flow was then pumped back to the elevated reservoir by a steady centrifugal pump (11, Model 12U596; Dayton Pumps, Lake Forest, IL). The steady centrifugal pump rotational speed was controlled by the DC voltage output from a Powerstat variable autotransformer (type 3PM126; The Superior Electric Co, Bristol CT). The variable transformer accepted 120 V 50/60 Hz AC electricity signal and output a 15 A DC power source signal ranging from 0-140 V. The procedure for the Fontan circulation model patient-specific verification is in section 4.2.1.

4.1.2.1 Pressure and Flow Measurement

Figure 4-1 also outlines the pressure and flow measurement within the schematic. Pressure relative to atmospheric pressure was measured via fluid-filled strain gauge pressure transducers (Model 6199; Utah Medical Products Inc., Midvale, UT). The pressure transducers had a measurement range of -50 to 300 mmHg and a sensitivity of 5 μV/V/mmHg, or ± 2 %. The pressure transducer excitation voltage and signal amplification was provided by a custom-built signal conditioning box constructed by the Georgia Tech Mechanical Engineering Electronics Lab. Signal output from the conditioning box was read by LabVIEW.

Flow rates were measured with 3 in-line and 1 clamp-on ultrasonic flow probes (Transonic Systems, Ithaca, NY). The 3 in-line flow measurements were performed with model 10PXN probes. The clamp-on measurement was with a model 8PXL probe. The flow probes utilized the Doppler effect to measure the flow at a frequency of 1.2 MHz. The flow signal from each probe was sent to a TS410 tubing flow module housed within a T402 multi-channel research console. The research console applied a low pass filter at 100 Hz to each signal before the signal was read by LabVIEW. All flow probes had a resolution of 0.01 L/min.

4.1.2.2 Data Acquisition and Control System

Two software-coupled National Instruments data acquisition (DAQ) systems and a custom LabVIEW program were used to control the pulsatile piston pump, trigger imaging systems, and record pressure and flow measurements. The two DAQ systems were model USB-6251 devices, which included 8 16-bit, 1.25 MS/s BNC analog input channels and 2 16-Bit 2.8 MS/s BNC analog output channels. One of the 4 output channels sent a piston position waveform to the programmable piston pump during pulsatile flow conditions. Another of the analog out channels was used to send trigger signals to the PIV acquisition system. Of the 16 total input channels, 4 recorded flow rates (IVC, SVC, LPA, and RPA), 7 recorded pressures (IVC, SVC, LPA, RPA, atrium, before steady pump, after steady pump), and 2 recorded the analog output channels re-read back to the DAQ.

A custom LabVIEW virtual instrument controlled the system and allowed the investigator to acquire, calibrate, and display all 16 analog input voltage signals. Acquisition sampling frequency was adjustable, and the incoming signals were used in the real-time calculation of several important verification parameters: signal mean, signal

maximum, and signal minimum. The time period over which each of these parameters was calculated was set independent of the sampling frequency. This allowed for cyclic averages during pulsatile experimental conditions. These parameters could be calculated on multiple signals at the same time, which allowed for additional flow pulsatility and resistance verification. The two output signals were controlled from the custom LabVIEW virtual instrument as well. Each output signal was created from a time-normalized (0 to 1) and amplitude-normalized (0 to 1) comma-separated variables file. The custom waveform file was then scaled to a specifiable time period and amplitude within the LabVIEW virtual instrument. More information regarding the functions and utilization of the virtual instrument can be found in appendix 11.1.

4.1.3 Particle Image Velocimetry Instrumentation

A double-cavity Nd:YAG laser with 50 mJ pulse energy and 532 nm wavelength (LaVision GmbH, Goettingen, Germany) provided the particle image velocimetry illumination. The laser beam was delivered to the measurement plane via a covered beam path laser arm. A collimator and sheet optics were used at the end of the laser arm to generate a light sheet of approximately 1 mm thickness. Fluorescent Rhodamine-B (excitation wavelength – 535 nm and emission wavelength – 580 nm) particles with a diameter of 1-20μm were used to seed the flow. Two LaVision PRO-X 2M cameras were used, each with 1600x1200 pixel resolution. The focal length of each lens system was 60 mm, and each lens was fitted with an OD 4, 50 mm diameter, 600 ± 50 nm bandpass filter (Stock No. 84-797 Edmund Optics Inc., Barrington, NJ). LaVision DaVis 8.2 software was used to acquire and process the PIV data.

4.2 Procedures

The instruments found in section 4.1 were used in specific procedures in order to verify patient-specific Fontan circulation model behavior, and assess the effects of respiration, exercise, and pulsatility on Fontan circulation hemodynamics. The following section outlines these procedures.

4.2.1 Patient-Specific Verification

In order to verify patient-specific hemodynamic behavior of the Fontan circulation model, patient-specific data was first acquired. Then, the Fontan circulation model was developed to match key patient-specific hemodynamic metrics. The procedures that follow were those used in this verification process.

4.2.1.1 Magnetic Resonance Imaging Protocols

Magnetic resonance imaging (MRI) was used to acquire anatomy and flow data for 2 Fontan patients from the Children's Hospital of Philadelphia (CHOP). The instruments used for this procedure are detailed in section 4.1.1.

The imaging protocol began with an static steady state free precession anatomic survey. This data was then reformatted to acquire slice orientations and positions perpendicular to flow for both real-time Phase Contrast Magnetic Resonance (rtPCMR) and segmented Phase Contrast Magnetic Resonance (sPCMR) acquisitions. The rtPCMR was an echoplanar sequence that used shared velocity encoding, the details of which have been described previously [136]. It used, in general, the following variables: repetition time of 9.5 milliseconds, echo time of 4.1 milliseconds, flip angle of 30 degrees, field of view of 320 to 400 mm, slice thickness of 8 to 10 mm, and bandwidth of 2,841 Hz/pixel. The acquisition protocol consisted of through-plane PCMR across the superior (SVC) and

inferior (IVC) vena cava, AAo, and DAo aorta for at least 10 seconds (approximately 20 frames/second). The IVC flow was acquired near the diaphragm but above the hepatic entrance to the IVC. The same imaging protocol was performed under the resting free-breathing (FB) and exercise (EX) conditions. Both FB and EX flows include respiration (inspiration and expiration) effects. After the resting free-breathing rtPCMR acquisition, the patients were slid partially out from the MRI bore to perform lower leg exercise with the use of an MRI-compatible supine bicycle ergometer (Lode BV, Groningen, the Netherlands). This ergometer allows revolutions per minute-independent workload, ranging from 10 to 250 watts while the patient maintains his or her position by bracing with hand grips. The goal was to bring the patients from the resting conditions up to a steady work rate at their ventilatory anaerobic threshold (VAT) (as measured in a previous metabolic exercise test), which was a sustainable work rate for the completion of the PCMR data acquisition. HR was monitored continuously. Initially, the workload was set to 20 watts and was increased progressively at a rate of 20 watts per minute to obtain a HR corresponding to that of the HR at VAT on their prior metabolic exercise test. Exercise was then suspended, their feet quickly removed from the ergometer pedals, and they were automatically returned to the MRI bore isocenter for imaging. Exercise imaging took place less than ten seconds after the patient stopped pedaling. Real-time PCMR measurements of the AAo, DAo, IVC, and SVC were acquired with repeated exercise performed in between for the patient to return to the target HR.

Breath-held (BH) data was acquired using a more standard segmented Phase Contrast Magnetic Resonance (sPCMR) procedure.

4.2.1.2 Patient-Specific Anatomy Acquisition

The anatomical shape of the patient-specific verified Fontan connection model was created by segmenting the anatomical MRI data for each patient. Segmentation was performed via ITK-SNAP 3.6.0 [137]. Segmentation resulted in a three-dimensional computational model (.stl file) that was passed to the manufacturer for mold-making. The models were manufactured by BDC Labs (Wheat Ridge, CO).

4.2.1.3 Patient-Specific Flow Waveform Calculations

The MRI protocols described in section 4.2.1.1 resulted in a Digital Imaging and Communications in Medicine (DICOM) standard file data set for each condition: breath-held, free-breathing, and exercise. The flow measurement DICOM files appear as images, but also include fluid velocity information in the direction normal to the image. This velocity information was extracted and converted to a flow rate via the Segment computer program from Medviso (v1.9) [138]. Segment is a well-tested MRI analysis program which our lab has found to provide accurate flow rate estimations when compared to clinical reports within 5% error. Segment was operated by loading both the magnitude and phase DICOM files into the program and tracing the vessel of interest (Figure 4-2). The Segment manual chapter containing directions on flow analysis is included in Appendix 11.2.

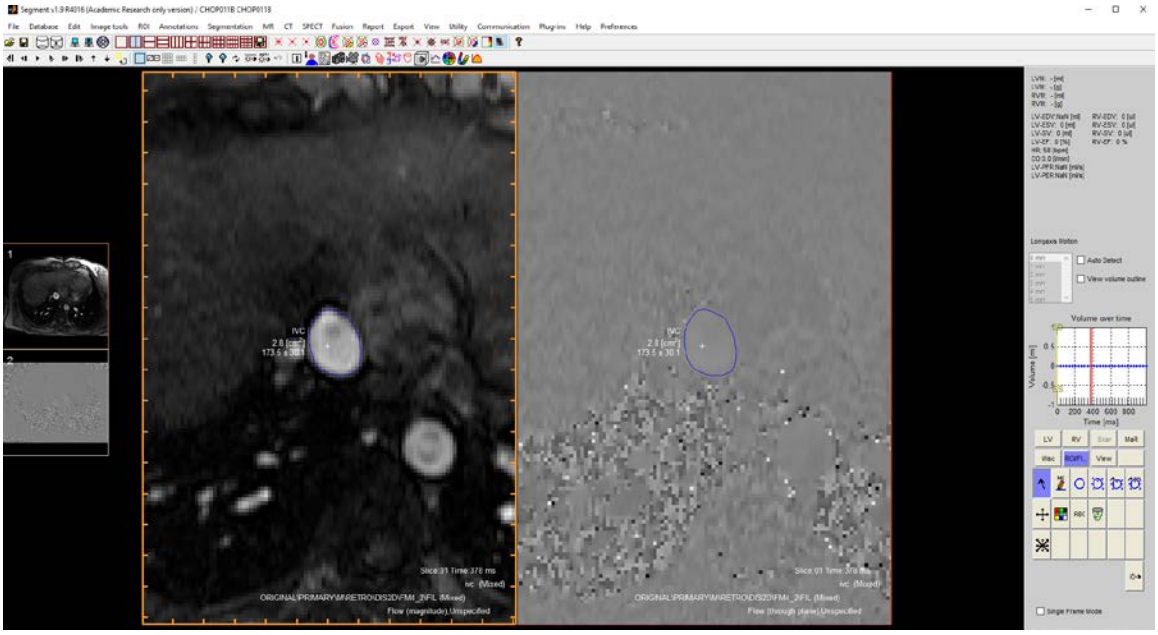

Figure 4-2: Medviso Segment DICOM processing program screenshot showing breath-held PCMRI IVC vessel tracing to extract flow rate data

Segment flow analysis was performed for each vessel of interest (IVC, SVC, LPA, RPA) during each patient condition (BH, FB, EX). Table 4-1 summarizes the patient-specific data acquired from the MRI protocols and processed in Segment. The table lists the mean flow rate of each vessel, which was determined over 1 cardiac cycle worth of data for the breath-held conditions and 3 respiration cycles for the free-breathing and exercise conditions.

Table 4-1: Mean flow rate values (L/min) of each patient and each condition acquired from MRI. The * denotes those vessel values that were calculated instead of directly acquired.

	Patient ID	CHOP11B	CHOP235A
	Fontan Type	Extra-Cardiac	Intra-Atrial
Breath-Held PCMRI Mean Flow Rate (L/min)	**IVC**	2.35	2.36
	SVC	0.86	0.75
	LPA	1.45	0.70
	RPA	1.76	2.41
Free-Breathing RTMRI Mean Flow Rate (L/min)	**IVC**	3.07	2.20
	SVC	0.97	2.85
	LPA	2.24*	1.14*
	RPA	1.80*	3.91*
Exercise RTMRI Mean Flow Rate (L/min)	**IVC**	6.38	3.55
	SVC	1.76	3.67
	LPA	3.71	1.94
	RPA	4.43	5.28

A difference in data lengths for the different patient-specific conditions was caused by the difference in MRI protocols. The breath-held condition was acquired under a standard cardiac gated phase contrast protocol which uses data over multiple cardiac cycles to phase average a single cardiac period length of data. The single cardiac cycle reported was then an average of multiple cardiac cycles acquired over approximately one minute of wall time. In contrast, the free-breathing and exercise data sets were acquired with real-time MRI protocols which resulted in only 20 secs of wall time data acquisition. These data sets are acquired at a higher frequency than the standard phase contrast MRI protocol used for the breath-held data, but are not cardiac- nor respiratory-gated. Without gating, the cardiac and respiratory cycles cannot be phase averaged, and an integer number of cardiac and respiratory cycles is not guaranteed within the 20 seconds of acquisition. Hemodynamic analyses and particle image velocimetry experiments (sections 4.2.2.1 and 4.2.2.2) required periodic experimental model boundary conditions for proper phase averaging and experimental uncertainty reduction, so a Fourier analysis procedure was

implemented to generalize all patient-specific waveforms from all MRI protocols. This procedure is discussed in section 4.2.1.3.2.

4.2.1.3.1 Missing Waveforms

Some vessel waveforms (LPA and RPA during free-breathing conditions) were not collected clinically, as denoted by an asterisk in Table 4-1. These vessel waveforms were calculated by summing the IVC and SVC free-breathing waveforms, and multiplying the resultant waveform by the ratio of the mean outlet flow from the breath-held condition. For example, the free-breathing LPA waveform for CHOP11B was calculated by summing the CHOP11B free-breathing IVC and SVC waveforms and multiplying this waveform by the ratio of the mean CHOP11B breath-held LPA flow (1.45 L/min) to the CHOP11B breath-held total outflow (3.21 L/min; 1.45/3.21 = 45.2%). This estimation assumed no change in frequency content between the inflows and outflows of the free-breathing data sets and that the LPA and RPA downstream flow resistances (the pulmonary vascular resistance) do not change between breath-held and free-breathing conditions. Though these assumptions are reported to hold true by Naeije and Chesler [139], calculations were still performed to assess their validity in this case.

The validity of this estimation method for these 4 missing waveforms was tested by comparing the patient-specific PA waveforms to the PA waveforms calculated using the method described above for each patient under the breath-held condition. Figure 4-3 shows the calculation of the CHOP11B BH LPA waveform compared to the patient-specific LPA waveform under the same condition.

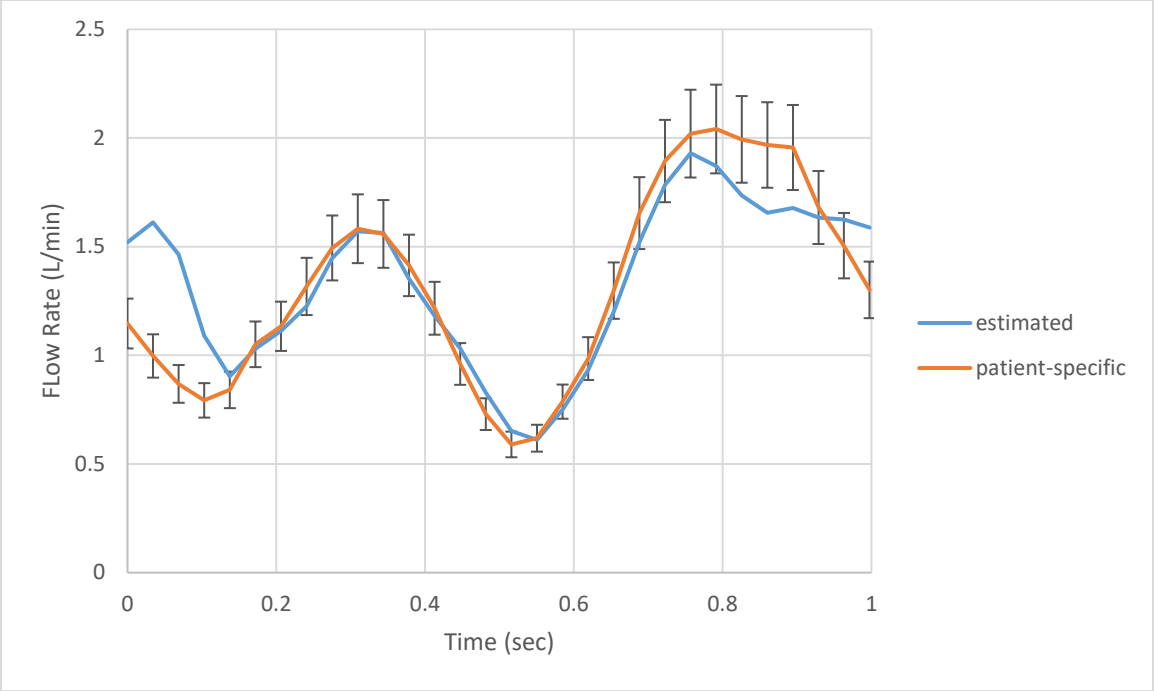

Figure 4-3: Comparison of CHOP11B BH patient-specific and estimated waveforms as verification of the missing waveforms estimation method. The error bars represent a 10% assumed MRI uncertainty interval.

4.2.1.3.2 Fourier Analysis – Decomposition of Respiratory and Cardiac Cycles

All MRI-based flow waveforms were analyzed and filtered with a custom MATLAB (The MathWorks, Inc. Natick, MA) program via Fourier analysis. The purpose of the Fourier analysis was two-fold: generalize the MRI-acquired waveforms to be periodic solutions with an integer number of respiratory/cardiac cycles, and filter out high-frequency flow waveform noise. The custom MATLAB program used a single row vector of patient-specific raw flow rate data as input, and requested the time step (in seconds) between flow rate data points from the user. With this information, the program executed MATLAB's built-in fast Fourier transform function (FFT) 1000 times, sampling different amounts of the raw data signal for each FFT calculation. These 1000 FFT calculations were then averaged to produce one single-sided amplitude spectrum. An average of so many

single-sided amplitude spectra was used to eliminate the effects of sample length on the revealed frequency content. Figure 4-4 shows an example single-sided amplitude spectrum acquired from the CHOP11B FB IVC waveform. Appendix 11.3 includes the custom MATLAB script executed.

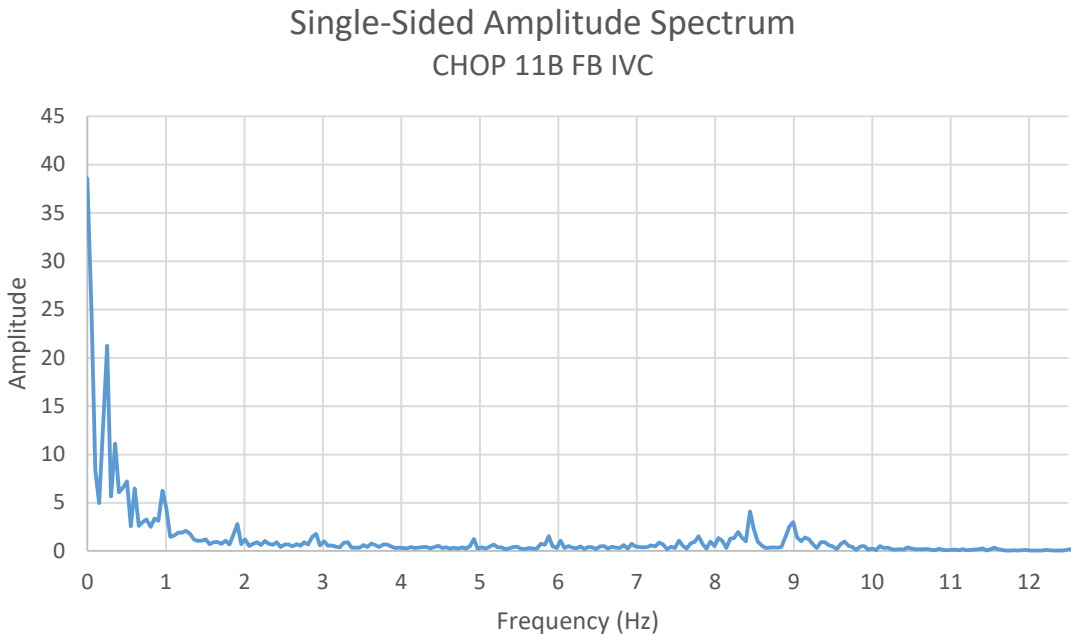

Figure 4-4: Single-sided amplitude spectrum of IVC flow for patient CHOP11B under free-breathing conditions

The single-sided amplitude spectrum was used to extract frequency content and filter the raw data. Respiratory and cardiac frequencies (and their harmonics) were identified by peaks in the single-sided amplitude spectrum. Filtering was performed by identifying the 2nd harmonic of the cardiac frequency and then excluding all frequencies greater than this frequency, as well as all other frequencies with amplitude less than the amplitude of the 2nd harmonic of the cardiac frequency. This filtering algorithm was necessary to adequately capture the amplitude variations evident in the raw flow rate data.

Figure 4-5 shows the same single-sided amplitude spectrum with the included frequencies kept highlighted.

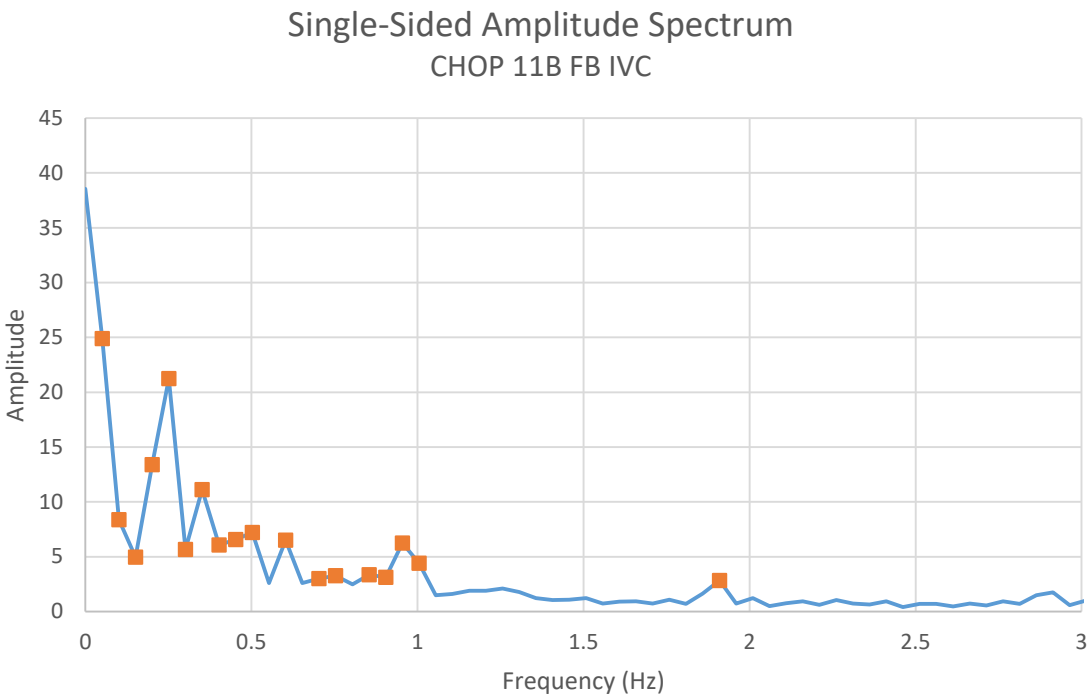

Figure 4-5: Single-sided amplitude spectrum with frequencies kept highlighted

To verify that the filtered waveform matched well with the raw MRI data, each filtered waveform was reconstructed as a sum of sine and cosine functions, as in Equation (4-1).

$$Q = A_0 + \sum_{n=1}^{k} A_n \cos(\omega_n t) + B_n \sin(\omega_n t) \qquad (4\text{-}1)$$

where Q was the filtered waveform, A_0 was the zero frequency waveform content, n was the discrete frequency number determined by the MRI sampling frequency and the raw waveform signal length, k was the total number of frequencies kept, and $\omega = 2\pi f$. A_0, A_n, B_n, and ω_n are tabulated for each vessel under each condition in Appendix 11.4.

An example comparison between the filtered waveform and the raw MRI data is shown in Figure 4-6. A correlation between the two curves below resulted in $R^2 = 0.879$.

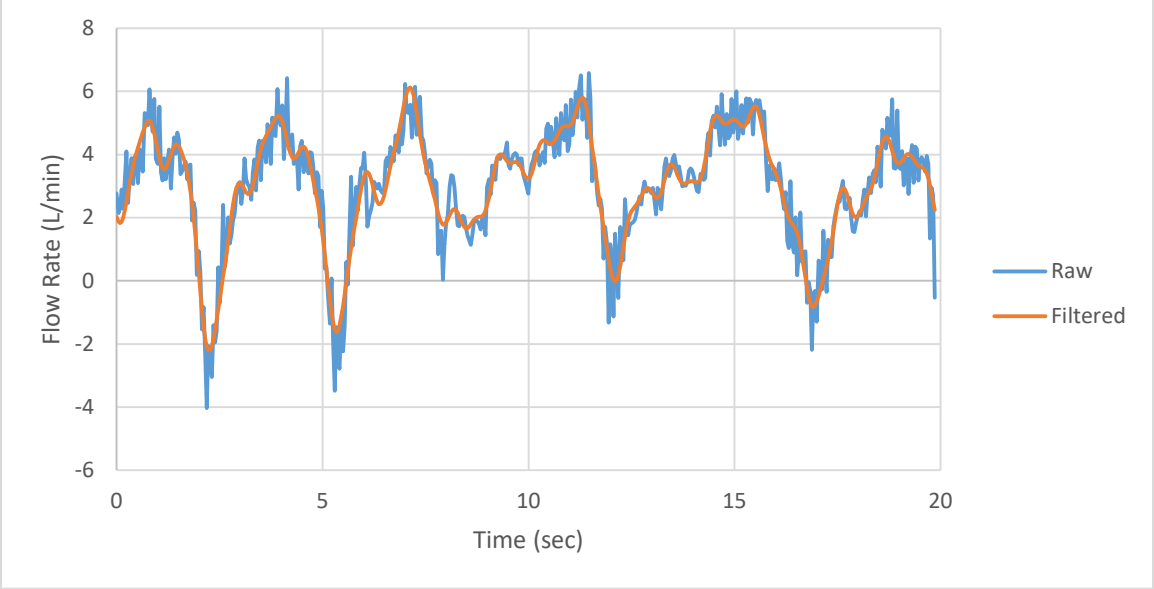

Figure 4-6: Comparison of CHOP11B FB IVC flow rate raw MRI data and post filtering procedure.

The frequency content extracted from each MRI IVC waveform was used to identify characteristic frequencies for each experimental condition. These characteristic frequencies are listed in Table 4-2.

Table 4-2: Characteristic respiration and cardiac frequencies acquired from each MRI IVC waveform for each model and condition

Model	Condition	f_{resp} (Hz)	f_{card} (Hz)
CHOP11B	BH	--	0.969
	FB	0.278	0.955
	EX	0.499	1.998
CHOP235A	BH	--	1.310
	FB	0.262	0.956
	EX	0.615	1.290

The filtered waveforms reconstructed according to Equation (4-1) served as the patient-specific waveforms to which the *in vitro* Fontan circulation model was verified.

4.2.1.4 *In Vitro* Fontan Circulation Model Verification

The *in vitro* Fontan circulation model was verified for BH, FB, and EX conditions using 2 metrics: flow waveform and TCPC model compliance.

4.2.1.4.1 Flow Waveform Verification

The *in vitro* Fontan circulation model flow waveform for each vessel was verified against the patient-specific flow waveforms established through methods in section 4.2.1.2. The model flow waveform was created through a combination of steady, gravity-driven flow and the programmable piston pump. The programmable piston pump was controlled with a comma-separated variable file via a custom LabVIEW VI. The LabVIEW VI established a constant gain to the piston waveform, which was then manually adjusted through dials on the SuperPump control box. Mean flow rate was controlled by manually adjusting the amount of gravity-drive flow passing through the various ball valves throughout the circulation model; minor model flow waveform adjustments were also made manually by adjusting the air-fluid ratio in the compliance chambers (Figure 4-1).

In general, the programmable piston pump was fed the condition-specific IVC waveform for a period of time corresponding to 4 times the lowest characteristic frequency shown in Table 4-2. The first 3 characteristic periods included data collection. The remaining characteristic cycle length was used in particle image velocimetry data collection timing, as shown in Figure 4-7.

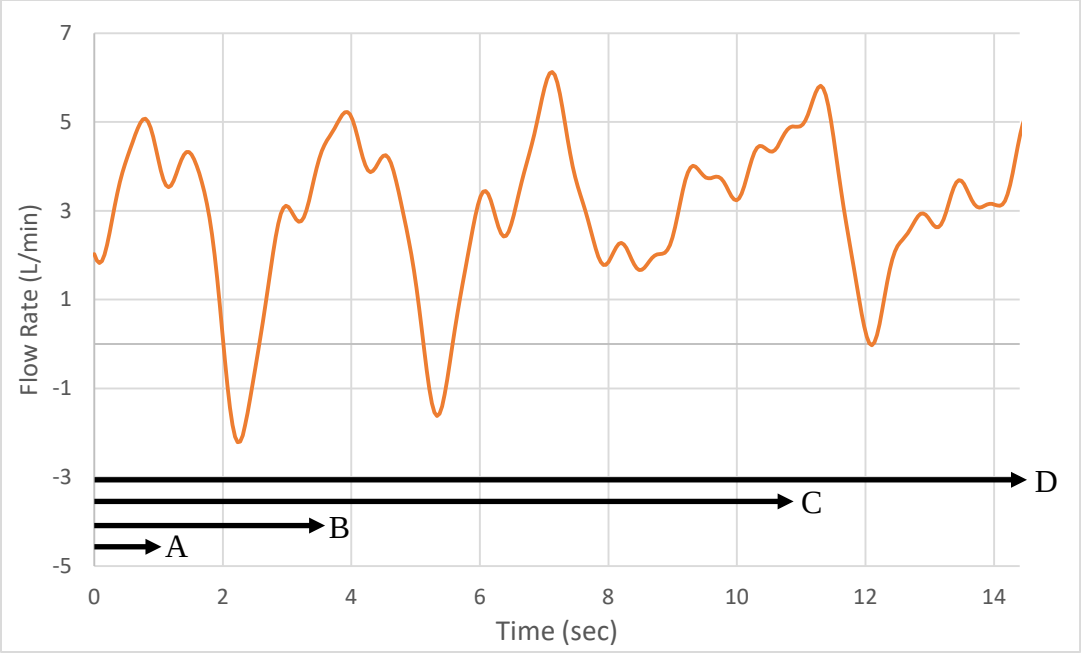

Figure 4-7: CHOP11B FB IVC flow rate waveform showing different time scales important for flow waveform verification. A, B, C, and D denote different time scales within each data acquisition; see Table 4-3.

Table 4-3 summarizes the different time scales used for each experimental condition. Note that the data collection time and total time (C and D) are rounded to the nearest 0.02 secs to accommodate a 50 Hz experimental data sampling rate.

Table 4-3: Cardiac frequency, respiratory frequency, data collection time, and total characteristic time for each experimental condition

Model	Condition	f_{card} (Hz) (A)	f_{resp} (Hz) (B)	T_{data} (secs) (C)	T_{tot} (secs) (D)
CHOP11B	BH	0.969	--	3.10	4.10
	FB	0.955	0.278	10.80	14.40
	EX	1.998	0.499	6.02	8.02
CHOP235A	BH	1.310	--	2.30	3.06
	FB	0.956	0.262	11.46	15.26
	EX	1.290	0.615	4.88	6.50

The pattern of 3 data collection cycles and 1 timing cycle was repeated at least 20 times. The 20 sets of characteristic cycles were ensemble averaged for each vessel under

each condition to establish a condition-specific *in vitro* Fontan model circulation vessel waveform. These waveforms, with their associated measurement uncertainty, were then compared to the patient-specific MRI vessel waveforms (assigned a 10% uncertainty [140]) both qualitatively and quantitatively. Quantitative comparison utilized two metrics: a ratio of the average difference between the two waveforms to the time-averaged value of the two waveforms and a time-normalized root mean square. The first error metric is shown in Equation (4-2). The second is shown in Equation (4-3).

$$\varepsilon_{avg} = \frac{2 * \overline{|Q_{model}(t) - Q_{MRI}(t)|}}{\left[\overline{Q_{model}(t)} + \overline{Q_{MRI}(t)}\right]} \tag{4-2}$$

$$\varepsilon_{rms} = \frac{\sqrt{\sum[Q_{model}(t) - Q_{MRI}(t)]^2}}{T} \tag{4-3}$$

4.2.1.4.2 TCPC Model Compliance Verification

The patient-specific flow waveforms calculated in section 4.2.1.2 were used to determine a patient-specific TCPC compliance for both CHOP11B and CHOP235A. Compliance is a bulk material property metric relating the amount of total volume deformation an object undergoes given a unit of applied pressure, and was calculated using Equation (4-4).

$$C = \frac{\Delta V}{\Delta P} \tag{4-4}$$

In order to verify that the *in vitro* TCPC model matched the patient-specific compliance both the patient-specific compliance and the existing *in vitro* TCPC compliance were necessary to determine. Then, the *in vitro* TCPC compliance had to be altered to match patient-specific compliance in a cost-effective manner. Finally, it was

necessary to confirm the resulting *in vitro* TCPC model and patient-specific compliance match. This verification process took place in five stages:

(1) The patient-specific data was analyzed to determine an *in vivo* target compliance.

(2) An arbitrary-thickness (1mm) *in vitro* model was constructed and tested to determine its compliance.

(3) The *in vitro* compliance test was reproduced computationally to determine an effective Young's modulus (E_{eff}).

(4) The model thickness was computationally iterated upon using the effective Young's modulus to determine a target model wall thickness which would match the target compliance.

(5) A new model with the computationally-derived target wall thickness was constructed and tested *in vitro* to determine if its compliance matched the target compliance from stage one.

4.2.1.4.2.1 Patient-Specific Data Analysis

Patient-specific flow waveforms were acquired from phase contrast magnetic resonance images according to the procedure detailed in section 4.2.1.1. The change in volume over the cardiac cycle was calculated by integrating the net flow in the TCPC over a cardiac cycle. Inferior vena cava (IVC) and superior vena cava (SVC) flow contributed to the TCPC volume while right pulmonary artery (RPA) and left pulmonary artery (LPA) flow subtracted from it. The volume change was defined as the minimum volume subtracted from the maximum volume. The pressure change was determined by the average pulse pressure in each of the IVC, SVC, LPA and RPA.

4.2.1.4.2.2 *In Vitro* TCPC Compliance Testing

The flexible TCPC model was constructed of a shore 30A hardness silicone material that was dip molded to the patient-specific geometry based on anatomy acquired from magnetic resonance images (MRI). The MRI data was acquired according to the protocol in section 4.2.1.1. The patient-specific anatomy was segmented from the MRI images using ITK-SNAP to produce a 3D computer surface [137]. This computational model was then 3D printed to produce the mold for silicone model production. The flexible models were manufactured by Biomedical Device Consultants Laboratories (Wheat Ridge, CO). The compliance of the manufactured model was a function of both its material properties, shape, and wall thickness. Without knowing each model's compliance *a priori*, an arbitrary thickness (1mm) model was manufactured for each patient-specific anatomy.

In vitro compliance testing was used for stages 2 and 5 of the verification method (section 4.2.1.4.2). Testing consisted of suspending the model in the physiological orientation seen from the MRI images (Figure 4-8).

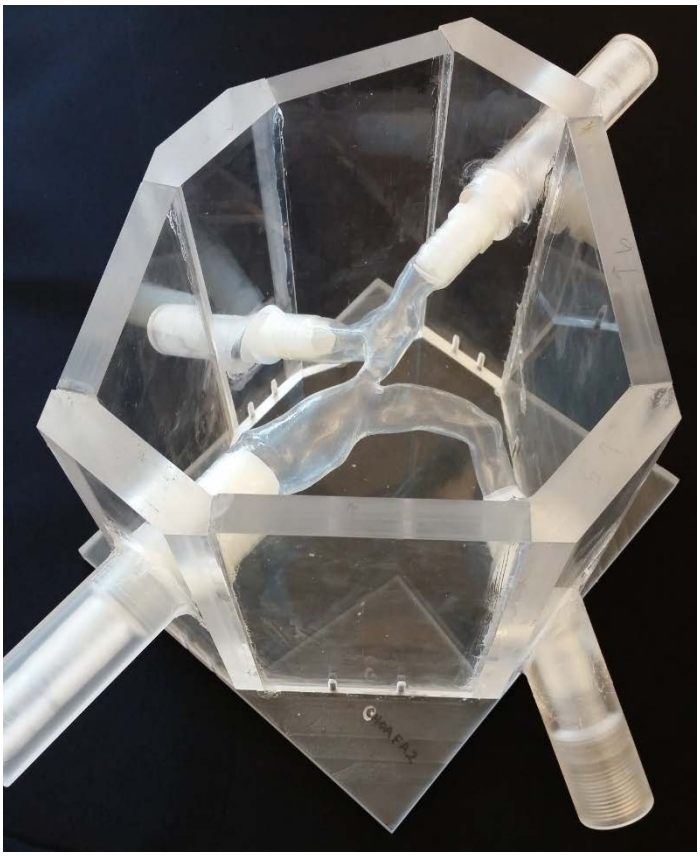

Figure 4-8: *In vitro* TCPC model suspended in physiological orientation in preparation for compliance testing

The ends of each vessel were sealed with ball valves and the TCPC was filled with a saline blood analog solution to 15 mmHg, the minimum TCPC pressure from the patient-specific catheter readings. Using a 50 cc syringe and a Harvard Apparatus PHD 2000 pump (Harvard Apparatus, Holliston, MA), a known volume of solution was injected into the system and its associated pressure change was recorded. Pressure was measured by 6199 Deltran® pressure transducers (Utah Medical Products, Inc. Midvale, UT). The injected volume was then removed from the TCPC and returned to the injection pump. Subsequent injection volumes were varied until they resulted in a 2 mmHg increase in TCPC pressure – the mean pulse pressure from the age-matched cohort. Once the appropriate injection

volume was determined, the injection/removal and pressure recording process was repeated additional 10 times to reduce measurement uncertainty.

4.2.1.4.2.3 Computational Simulations

Computational simulations were used in stages 3 and 4 of the verification method. The simulations utilized ANSYS Mechanical and Response Surface Optimization (RSM) modules (ANSYS, Inc., Canonsburg, PA).

Computational reproduction of the *in vitro* compliance testing of the arbitrary thickness (1mm) model TCPC used the same 3D computer surface model passed to the manufacturer for model production. The computational surface model was given the arbitrary (1mm) thickness within the ANSYS Mechanical module using shell181 elements. Shell181 elements were employed because of their unique ability within ANSYS Mechanical to couple to hydrostatic fluid elements (HSFLD 242) and reduce computational cost compared to a fully-coupled fluid structure interaction model. The hydrostatic fluid elements applied the same volume change over time as measured from the *in vitro* compliance test. The injected fluid was incompressible and had a density of 1000 kg/m^3. A hybrid meshing approach was used; therefore, the structure mesh contained both tetrahedral and hexahedral mesh elements. The mesh edge size was constrained to 0.001 m, and the final mesh included 23,741 elements. This mesh setup provided grid-independent results. The simulation employed a linear elastic material model with an assumed Poisson's ratio of 0.5.

Material properties determination and model thickness optimization utilized the Response Surface Optimization module in ANSYS Workbench, which achieved the optimization objective with little a priori information in a cost-effective manner. Because

this study focused on single-objective optimizations, the Screening optimization approach was used. The genetic aggregation response surface type was used because of its robustness for a wide range of applications.

4.2.2 Experimental Approach

With patient-specific verification of the *in vitro* Fontan circulation model complete per the section 4.2.1 procedures, the effect of respiration, exercise, and pulsatility on Fontan hemodynamics was more accurately examined. Table 4-4 summarizes the experimental conditions collected to study each effect for both TCPC models.

Table 4-4: Experimental conditions summary based on available patient-specific data for each independent variable examined. The * symbol denotes derived experimental conditions.

Independent Variable	Patient-Specific Data Available	Experimental Conditions
Respiration	Breath-Held Free-Breathing	Breath-Held
		Free-Breathing
Exercise Intensity	Free-Breathing Peak Exercise	Free-Breathing
		Half-Peak Exercise*
		Peak Exercise
Waveform Pulsatility	Breath-Held	Steady Breath-Held*
		Low Pulse Breath-Held*
		Breath-Held
		High Pulse Breath-Held*

A total of 7 experimental conditions were utilized based on 3 patient-specific data sets (BH, FB, EX) to study the 3 independent variables (respiration, exercise intensity, and waveform pulsatility), for each of the 2 models (CHOP11B and CHOP235A). Each model was mounted in the *in vitro* Fontan circulation model and the circulation model was then tuned to one of the experimental conditions. Each experimental condition was defined by a verified flow waveform for each vessel (section 4.2.1.4.1) and vessel-specific literature-

based mean pressure values. Bulk transient hemodynamic (pressure and flow) data was collected and particle image velocimetry was performed for each experimental condition.

The derived experimental conditions found in Table 4-4 were created to acquire more data and more fully understand the effect of each independent variable on bulk and local hemodynamics. The steady breath-held condition was defined as the same mean flow rates for each vessel (IVC, SVC, LPA, and RPA) as the patient-specific breath-held condition, but without any frequency content or pulsatility to the flow. This condition was created by turning off the programmable piston pump. The low pulse breath-held and high pulse breath-held conditions were defined by waveforms with the same mean value as the patient-specific breath-held condition, but with waveform pulsatilities that were 2 standard deviations less than or greater than the patient-specific waveform pulsatility, respectively. The cohort from which these standard deviations were derived was the 100 patients in the Cardiovascular Fluid Mechanics Fontan Database for which flow pulsatility effects were analyzed using computational fluid dynamics [10]. Pulsatility was defined as the ratio of the difference in waveform maxima over a cycle to the mean waveform value over the same time period, as seen in Equation (4-5).

$$P = \frac{Q_{max} - Q_{min}}{Q_{mean}} \tag{4-5}$$

The half-peak exercise condition was defined as having the flow waveform shape and pulsatility of the patient-specific peak exercise condition, but a mean value set at the average between the free-breathing and peak-exercise mean flow values, for each vessel. A comprehensive table summarizing key metrics for each experimental condition is found in Appendix 11.5.

Having acquired the bulk and local hemodynamic data through this experimental approach, the following sections detail the data analysis methods.

4.2.2.1 Hemodynamic Analysis

Hemodynamic data included transient pressure and flow rate waveforms acquired via the pressure and flow instrumentation discussed in section 4.1.2.1. After proper patient-specific flow waveform calculations (section 4.2.1.2), the Fontan circulation model programmable piston pump was set to the patient-specific flow waveform for each condition, at a period approximately equal to 4 times the lowest frequency found in Table 4-2. The acquired data was ensemble averaged over this condition-specific period, summarized in Table 4-5.

Table 4-5: Pulsatile piston pump cycling periods for each patient-specific condition; relate to Table 4-3

Model	Condition	T_{tot} (sec)
CHOP11B	BH	4.10
	FB	14.40
	EX	8.02
CHOP235A	BH	3.06
	FB	15.26
	EX	6.50

These periods were assigned in order to model 4 patient-specific hemodynamic cycles. Under breath-held conditions this corresponded to 4 cardiac cycles. During free-breathing and exercise conditions this corresponded to 4 respiratory cycles (and 12-18 cardiac cycles).

The ensemble-averaged pressure and flow waveforms for each vessel were used to calculate an apparent power loss for each experimental condition. The apparent power loss was derived from a control volume energy analysis assuming constant velocity profiles at both the inlet and outlet vessels, and is shown in Equation (4-6).

$$\dot{E}_{app} = \sum_{inlets} (P + \frac{1}{2}\rho\left[\frac{Q_{in}}{A}\right]^2)Q_{in} - \sum_{outlets} (P + \frac{1}{2}\rho\left[\frac{Q_{out}}{A}\right]^2)Q_{out} \quad (4\text{-}6)$$

where P is the time-averaged vessel static pressure, ρ is the fluid density (1060 $\frac{kg}{m^3}$), Q is the time-averaged vessel volumetric flow rate either in or out of the TCPC, and A is the vessel cross-sectional area. The TCPC inlets are the IVC and SVC, and the outlets are the LPA and RPA.

To adequately compare to previous publications [48] and compare between different patient-specific models, apparent power loss was indexed according to Equation (4-7).

$$iPL = \frac{\dot{E}_{app} \cdot BSA^2}{\rho Q^3} \quad (4\text{-}7)$$

where BSA is the patient's body surface area and Q is the time-averaged flow rate into the TCPC (sum of IVC and SVC flow rate).

4.2.2.2 Particle Image Velocimetry

Particle image velocimetry (PIV) is an optical flow visualization method used to obtain instantaneous velocity field measurements, from which other metrics can then be obtained. The fluid in question is seeded with tracer particles, which are assumed to follow the fluid velocity field. A laser pulsation illuminates the measurement domain, and a camera is used to capture successive images of the particles within the fluid. The camera images are then analyzed with statistical algorithms to determine the distance each particle traveled between images. Knowing the distance traveled and the time between images allows for a full velocity field calculation. Capturing particles illuminated by a laser sheet results in a

two-dimensional velocity field with two components of velocity for each particle (2D2C). Acquiring the same laser-sheet-illuminated particles with two cameras results in a two-dimensional three-component velocity field (2D3C). Spreading the laser illumination over a volume of fluid and using at least 4 cameras results in a three-dimensional three-component velocity field (3D3C).

4.2.2.2.1 Velocity Field Acquisition

This study utilized 2D3C PIV over multiple planes for each model in an attempt to more completely sample the highly three-dimensional flow fields characteristic of total cavopulmonary connections. Table 4-6 and Figure 4-9 summarize the sampling plane locations for both models.

Table 4-6: PIV sampling plane locations as measured from the base of each model's refractive index bath

Plane Number	CHOP11B Plane Height (mm)	CHOP235A Plane Height (mm)
1	110	67
2	115	71
3	120	80
4	125	86
5	130	89
6	135	93
7	140	

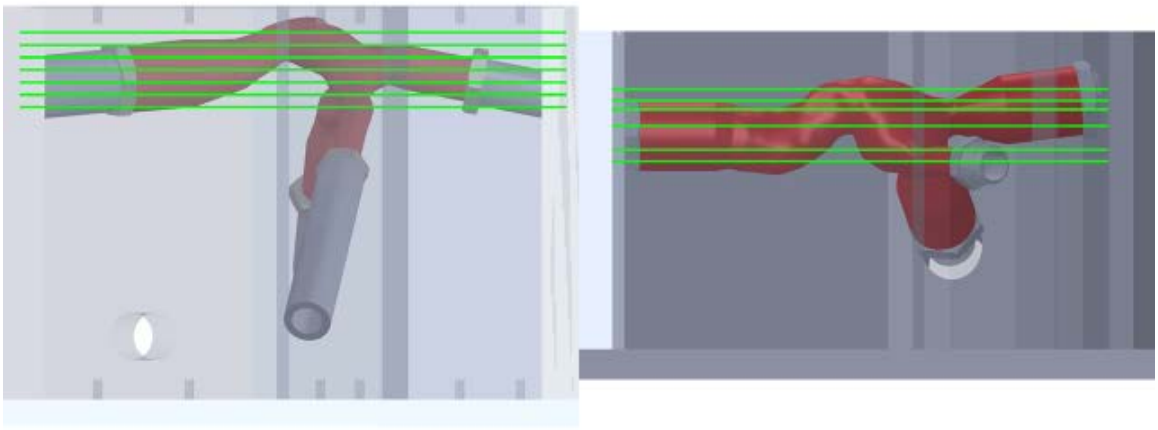

Figure 4-9: Schematic showing location of PIV sampling planes for each model. CHOP11B is on the left. CHOP235A is on the right.

Each model was positioned according to physiological orientation within an acrylic box. The box also served to hold liquid water glycerin to minimize refractive index changes throughout the system, and thereby minimize reflections. The laser-illuminated sampling planes were created by delivering a 532 nm wavelength 50 mJ pulse energy double-cavity Nd:YAG laser beam to a collimator and sheet optics via a shielded beam path. The double-cavity laser produced two laser sheet pulses, each lasting 3-5 ns. The separation between laser pulses varied from 800-2600 μs depending on the measured fluid velocity field.

PIV data were acquired for each model under each of the transient inlet experimental conditions listed in Table 4-4, as well as a steady flow inlet condition for the 4 conditions with different mean flow rates. These 20 PIV data sets are summarized in Table 4-7.

Table 4-7: Acquired PIV data set summary using IVC as representative of the changes for all TCPC vessels

Model	Condition		Mean IVC Flow Rate (L/min)	IVC Pulsatility (%)
CHOP11B	BH	Steady	2.35	0
		Patient-Specific	2.35	33.4
		Low Pulsatility	2.35	12.7
		High Pulsatility	2.35	57.5
	FB	Steady	3.07	0
		Patient Specific	3.07	84.8
	EX	Peak Steady	6.38	0
		Peak Patient-Specific	6.38	101.1
		Half-Peak Steady	4.70	0
		Half-Peak Pulsatile	4.70	93.4
CHOP235A	BH	Steady	2.36	0
		Patient-Specific	2.36	31.9
		Low Pulsatility	2.36	22.0
		High Pulsatility	2.36	38.6
	FB	Steady	2.20	0
		Patient Specific	2.20	115.2
	EX	Peak Steady	3.55	0
		Peak Patient-Specific	3.55	126.4
		Half-Peak Steady	2.88	0
		Half-Peak Pulsatile	2.88	118.4

The two frame-straddling cameras and the laser (see section 4.1.3) were triggered for each double-pulse to occur at specific points throughout each condition waveform. For example, PIV acquisition during the CHOP11B FB patient-specific condition was triggered at 57 time points over the 10.80 sec data sampling period (see Table 4-5), as shown in Figure 4-10.

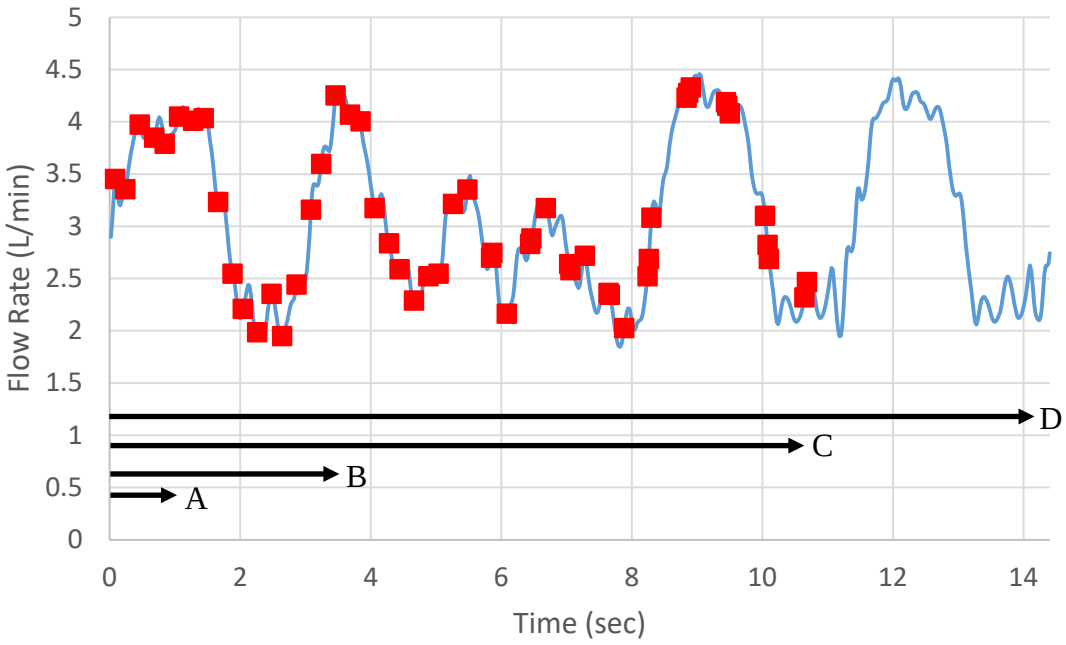

Figure 4-10: PIV data acquisition trigger points shown on the CHOP11B FB IVC flow curve as representation of PIV triggering for all conditions. A, B, C, and D denote different time scales within each data acquisition; see Table 4-3.

Though continuous triggering was synced between the Fontan circulation model and the PIV system via LabView, the command to begin PIV acquisition (and wait for the next LabView trigger) was given manually. Thus, the last ¼ of each piston pump period was left untriggered to provide an audio cue for the manual command. Table 4-8 is an extension of Table 4-3, and summarizes the PIV image triggering for each pulsatile flow condition. Table 4-8 supplies the period of time over which data was collected ($\boldsymbol{T_{data}}$) for each experimental condition, and the total number of trigger points used to sample $\boldsymbol{T_{data}}$. The period of time over which data was collected is also listed in Table 4-3 in context of the individual cardiac and respiratory frequencies of each experimental condition, as well as the total experimental condition run-time ($\boldsymbol{T_{tot}}$), which includes some time during which data collection did not take place.

Table 4-8: PIV acquisition summary for pulsatile flow conditions; relate to Table 4-3 and Table 4-4

Model	Condition	T_{data} (sec)	Trigger Points
CHOP11B	BH	3.10	31
	FB	10.80	57
	EX	6.02	61
CHOP235A	BH	2.30	27
	FB	11.46	53
	EX	4.88	22

A short study was conducted to determine the number of data cycles ($\boldsymbol{T_{data}}$) necessary for PIV velocity values to converge. The convergence study found that approximately 125 ensemble-averaged image pairs were necessary for PIV data convergence, so 150 image pairs of each triggered time point were conservatively acquired. The details of the convergence study are found in Appendix 11.6.

4.2.2.2.2 Image Calibration

Transformation from pixel-based to physical velocity values based on the acquired images required camera calibration. Camera images were calibrated using a 3-dimensioanl calibration plate 3D printed to fit the test section housing and include 1 mm diameter dots spaced 4 mm apart in one plane (XY-plane). An additional plane of dots was offset from the original plane by 2 mm in the X direction and 1 mm in the Z direction. Figure 4-11 shows a schematic rendering of a calibration plate in the test section housing.

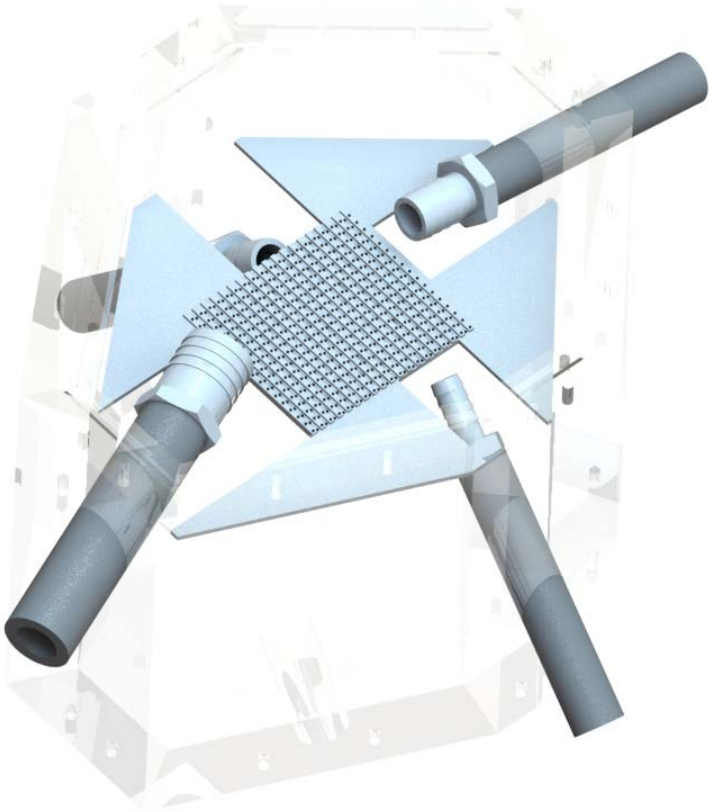

Figure 4-11: Schematic rendering of CHOP11B calibration plate in transparent test section housing

The calibration plate was placed in in the test section housing without the flexible TCPC model because the flexible model was not amenable to interior calibration. Without an interior calibration the light ray path from the calibration plate shown in Figure 4-11 could have been slightly different than that of an illuminated particle used for velocimetry calculations. Thus, a secondary self-calibration procedure was required for each data set collected. The self-calibration procedure is detailed in section 4.2.2.2.3.

LaVision DaVis software was used to acquire the calibration images for each model. Calibration images were not re-acquired for every plane of data collected because self-calibration was included as a post-image-acquisition process. Calibration images were taken while the laser sampling plane was aligned to the calibration plate to ensure accurate

laser sampling plane location. The laser sampling plane was attached to a 1-dimensional traverse which, once aligned, only permitted translation in the z-direction, normal to the test section housing baseplate.

4.2.2.2.3 PIV Self-Calibration

To account for differences in light ray paths between the illuminated particles imaged for velocimetry and the calibration plate imaged without the presence of a TCPC model, a post-acquisition PIV self-calibration procedure was employed. This procedure is a feature of the LaVision DaVis software designed to modify existing calibration settings for distortion and position differences present between calibration images and data images. The self-calibration process simply includes identification of particles or features present in both stereo images (each image coming from one of the two cameras) that are the same physical location (Figure 4-12). From this information, DaVis calculates a disparity map prediction between the two images and performs a subsequent image cross-correlation to create a complete disparity field between the two images. The calculations required to map the two images onto a shared physical space are then compared to the existing calibration parameters that perform the same function, and the existing calibration is updated with the new information.

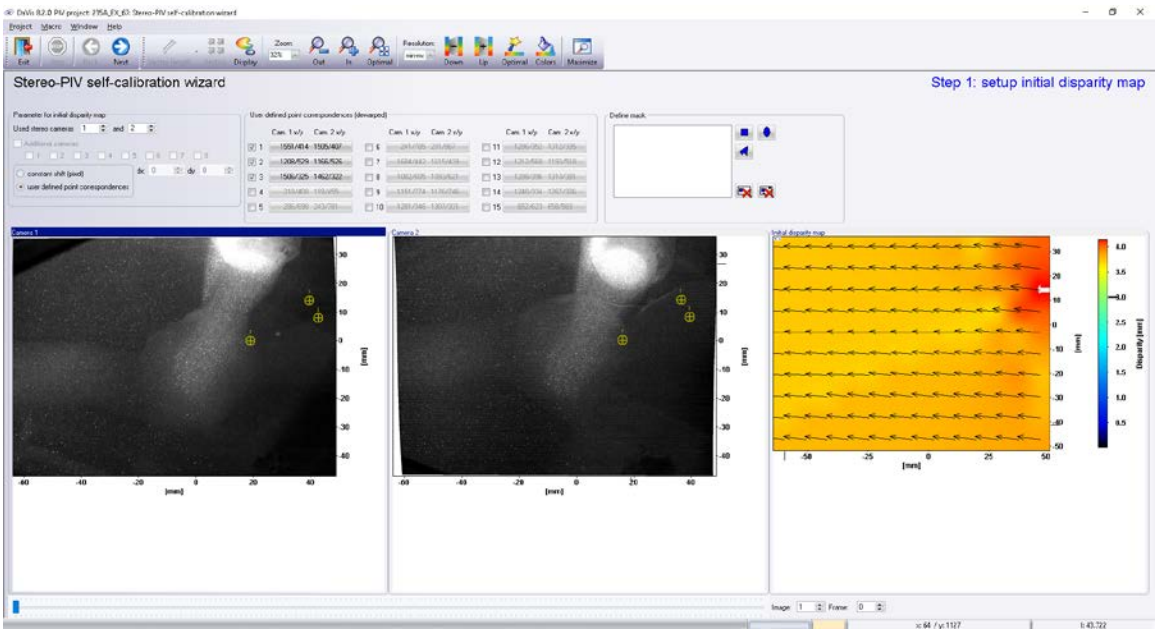

Figure 4-12: PIV self-calibration screenshot showing image feature identification and initial disparity map

4.2.2.2.4 PIV Image Processing

Image spatial cross-correlation was performed on the acquired images with DaVis software (section 4.1.3) to compute the velocity fields. The software used subpixel peak position interpolation to improve the accuracy of the displacement computation. The signal-to-noise ratio of the correlation peak was improved by using an adaptive multi-pass iterative scheme with an interrogation window overlap. A 64×64 pixel interrogation window with 50% overlap was used for the first pass while the second pass utilized a 32×32 pixel window with 75% overlap. Each camera pixel represented 7.4×7.4 $\mu m^2$of physical area. These settings resulted in a velocity vector resolution of around 1 mm. The raw images for a given time point were summed to create a time-average image which was then subtracted from each of the 150 images to remove background noise, as a pre-processing step. The background-subtracted data were then masked algorithmically based on relative spatial

intensities in order to capture only fluid motion inside the moving TCPC model walls. PIV processing was only conducted over the image remaining after masking. An applied vector range and a median filter were used to post-process each instantaneous image. All 150 instantaneous images were then time-averaged to produce a single velocity vector field for a given time point.

4.2.2.2.5 PIV Velocity Field Analysis

PIV velocity field analysis was performed using a combination of custom ParaView (Version 5.2.0, Kitware Inc., Clifton Park, NY) state machines and custom MATLAB (Version 8.6.0, MathWorks Inc., Natick MA). The processed phase-averaged velocity fields were exported from DaVis (see Section 4.2.2.2.4) and ParaView was employed to align the planes in space, interpolate the experimental data in time and space, calculate hepatic flow distribution, and determine the fluid viscous dissipation. Custom MATLAB scripts were employed to reformat and prepare data sets for each of these different analyses. The details of these processes follow, and the state machines and scripts are found in Appendix 11.7.

4.2.2.2.5.1 Plane Alignment

The processed transient velocity fields from DaVis were all assigned a unique coordinate system that, though consistent within each acquired plane, was not consistent across all planes for a given experimental condition. Thus all planes for each experimental condition (CHOP11B: 7 planes, 10 conditions; CHOP235A: 6 planes) were spatially aligned both to each other and to a static 3D patient-specific TCPC geometry according to common features found in all acquired images. The imported planes existed on a rectangular domain, so the plane alignment state machine also applied a threshold to the data to eliminate large

areas of zero velocity data. The patient-specific TCPC geometry was also assigned a 0 velocity value on its surface for future interpolation considerations. The newly-aligned velocity values were then exported as point-specific comma-separated variable files for each acquired time step. A custom MATLAB script then reformatted the planes and the TCPC geometry from individual data sets into a single, transient point cloud data set.

4.2.2.2.5.2 Spatial and Temporal Interpolation

The transient point cloud data set created by aligning the individual acquisition planes was imported into a separate custom ParaView state machine which interpolated the velocity values in both space and time. The spatial interpolation enclosed the point cloud in a rectangular prism volume with 0.5 mm x 0.5 mm x 0.5 mm resolution, and mapped velocity values from the point cloud data set to the volume with a Gaussian kernel. The Gaussian kernel considered 8 surrounding points from the point cloud data set for each mapped value in question, and points without 8 surrounding values were assigned a 0 velocity value. The enclosed rectangular prism volume was then resampled using a TCPC geometry unstructured mesh to remove all velocity values (almost entirely composed of velocity = 0) outside the TCPC physical space. At this point, the spatially interpolated unstructured mesh included velocity values only for the discrete and irregular experimental time points at which PIV data was collected. The unstructured mesh data set was then linearly temporally interpolated to a regular time step size equal to 0.1 secs. Figure 4-13 provides a flow chart summary of the interpolation process. Verification of the interpolation process accuracy using a virtual data set is described in Appendix 11.7.4.

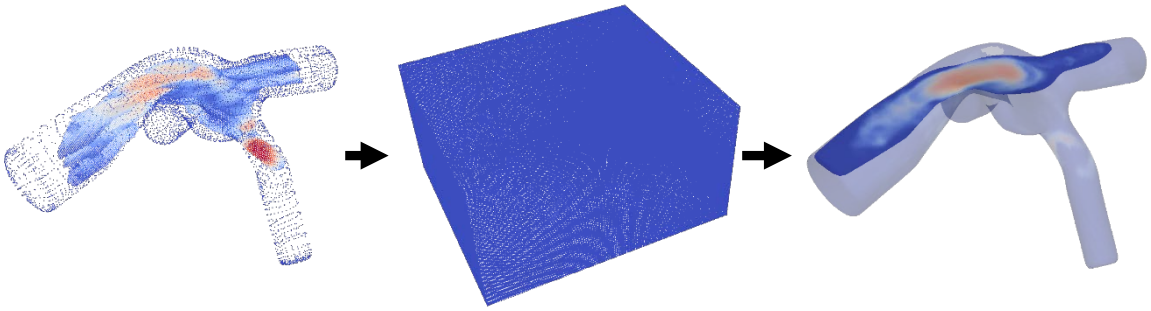

Figure 4-13: PIV velocity field interpolation process flow chart. The individual diagrams represent the aligned planes as a point cloud, the enclosed volume linear interpolation, and the final resampled data set (L to R).

4.2.2.2.5.3 Hepatic Flow Distribution Calculation

Hepatic flow distribution was determined by seeding the spatially and temporally interpolated velocity field with massless fluid particles using ParaViews ParticleTracer filter. Particle seeding took place at every data node on a cross-sectional IVC plane. Additional Lagrangian particles were added every 0.1 secs for either the cardiac or respiratory period of the experimental condition (depending on if the BH, FB, or EX condition were being analyzed). The Lagrangian particle identity, location, velocity, and time history were recorded for a total of 5 characteristic cycles (cardiac or respiratory). A custom MATLAB script then identified whether or not each particle passed through a cross-section LPA or RPA plane, or is still present in the TCPC domain yet to pass through either plane. The hepatic flow distribution was then calculated as the percent of particles passing through the LPA plane as a fraction of the total number of particles passing through either plane, as shown in Equation (4-8).

$$HFD = \frac{N_{LPA}}{N_{LPA} + N_{RPA}} * 100 \qquad (4\text{-}8)$$

4.2.2.2.5.4 Viscous Dissipation Term Calculation

The fluid viscous dissipation term was calculated for each spatially and temporally interpolated velocity field using ParaView, according to Equation (4-9).

$$\varphi = 2\left[\left(\frac{\partial u_x}{\partial x}\right)^2 + \left(\frac{\partial u_y}{\partial y}\right)^2 + \left(\frac{\partial u_z}{\partial z}\right)^2\right] + \left(\frac{\partial u_x}{\partial y} + \frac{\partial u_y}{\partial x}\right)^2 + \left(\frac{\partial u_y}{\partial z} + \frac{\partial u_z}{\partial y}\right)^2 + \left(\frac{\partial u_z}{\partial x} + \frac{\partial u_x}{\partial z}\right)^2 \quad (4\text{-}9)$$

where φ is the viscous dissipation rate per unit volume normalized by dynamic viscosity and u is the fluid velocity.

This term was both time- and space-averaged for each condition according to the condition's characteristic time scale (Table 4-8, T_{data}) to eliminate the effect of patient geometry size and time when comparing the effect of respiration, exercise, and pulsatility. Normalizing by dynamic viscosity does not affect the relationship between viscous dissipation term values because the experimental fluid was Newtonian.

For comparison between different experimental conditions, φ was also non-dimensionalized to create an indexed viscous dissipation term, $i\varphi$. Equation (4-10) details the indexed value.

$$i\varphi = \frac{\varphi \cdot BSA^3}{Q^2} \quad (4\text{-}10)$$

where BSA is the patient-specific body surface area and Q is the condition-specific average flow rate into the TCPC (sum of IVC and SVC flow).

4.2.2.3 Uncertainty Analysis

Uncertainty exists in all measurement, and is possibly the most important thing to know about a measurement. All of the uncertainty analysis that follows is performed to produce a 95% confidence interval.

4.2.2.3.1 Hemodynamic Uncertainty

The total uncertainty in hemodynamic (pressure and flow) data collected was determined using the root-sum-squares (RSS) method [141]. The RSS method for uncertainty combination is defined by Equation (4-11).

$$u_x = \sqrt{\sum_{k=1}^{K} u_k^2} \tag{4-11}$$

where u_x is the combined measurement uncertainty, and u_k is either the design-stage uncertainty, systematic uncertainty, or random uncertainty ($K = 3$). This measurement uncertainty was then propagated to other hemodynamic-based metrics (i.e. power loss) using Equations (4-12) and (4-13).

$$\theta_i = \frac{\partial R}{\partial x_{i_{x=\bar{x}}}} \; i = 1, 2, \dots, L \tag{4-12}$$

$$u_R = \left[\sum_{i=1}^{L} (\theta_i u_{\bar{x}_i})^2\right]^{1/2} \tag{4-13}$$

Equation (4-12) computes a sensitivity index, θ_i, where the hemodynamic-based metric, R, is a function of L variables, x, which each have their own uncertainty, $u_{\bar{x}_i}$. Equation (4-13) then uses the sensitivity index to weight the uncertainties of each variable contributing to the metric uncertainty. Note that the sensitivity index and the variable uncertainties are both evaluated at the variable mean value, as denoted by the over-bar.

Design-stage uncertainty was assigned via the measurement device specifications discussed in section 4.1.2.1. Systematic uncertainty was assigned based on the presence of drift, if any, between control or baseline conditions within a data collection set. In general, no drift existed in hemodynamic measurement instruments. Random uncertainty was assigned a value of twice the standard deviation of repeated measurements of the value in question. Thus, all reported uncertainty values can be considered on a 95% confidence interval.

4.2.2.3.2 Particle Image Velocimetry Uncertainty

PIV measurement uncertainty was quantified following the method outlined by Raffel, et al [142]. Error measurements were taken from the steady flow versions of the patient-specific conditions for each model. The total measurement uncertainty was divided into 3 error forms: particle lag error, ε_p, bias error, ε_b, and random error, ε_r. These individual error were calculated for a 95% confidence interval, and combined into a total error, ε_T, using the same RSS method found in Equation (4-11). All errors were calculated for each velocity component (V_x, V_y, and V_z), as both a velocity value and a percentage of the maximum velocity.

CHOP11B errors were 0.022 m/s, 0.033 m/s, and 0.046 m/s in the V_x, V_y, and V_z directions, respectively. These errors correspond to a 1.08% to 11.59% velocity magnitude error range. CHOP235A errors were 0.05 m/s, 0.033 m/s, and 0.05 m/s in the V_x, V_y, and V_z directions, respectively. These errors correspond to a 2.44% to 14.49% velocity magnitude error range. Details regarding the PIV uncertainties reported here are found in Appendix 11.8.

4.2.2.3.3 Hepatic Flow Distribution Uncertainty

The uncertainty in hepatic flow distribution calculation was determined by the difference between the calculated hepatic flow distribution and subsequent HFD calculation with a modified velocity field. The modified velocity field was determined by adding or subtracting a random value to each velocity vector component from the original HFD field. The random value added or subtracted to each velocity vector component was sampled over an interval bounded by the positive and negative value of the maximum uncertainty of that vector component from the particle image velocimetry uncertainty analysis found in section 4.2.2.3.2. For example, given an HFD value, x, for a given experimental condition with maximum PIV velocity uncertainties of U_{Vx}, U_{Vy}, and U_{Vz}, the velocity field which produces x, (Vx, Vy, and Vz) are changed to a new velocity field (Vx + rand(-$U_{Vx,}$ U_{Vx}), Vy + rand(-$U_{Vy,}$ U_{Vy}), Vz + rand(-$U_{Vz,}$ U_{Vz})). The new velocity field then produces a new HFD value, y, and the difference between the two HFD values (x-y) is set as the HFD uncertainty.

4.2.2.3.4 Viscous Dissipation Term Uncertainty

Viscous dissipation term confidence intervals were calculated by propagating the PIV uncertainties to the viscous dissipation term equations (Equation (4-9) and Equation (4-10)). The error propagation procedure followed was the same as that used in section 4.2.2.3.1, which is based on the literature [141]. All uncertainties are reported for a 95% confidence interval.

5 RESULTS

5.1 *In Vitro* Fontan Circulation Model Verification

The *in vitro* Fontan circulation model verification results stand to engender confidence in the circulation model's ability to reproduce hemodynamics on the bench-top representative of *in vivo* values. The *in vitro* Fontan circulation model verification results include both flow waveform verification and TCPC model compliance verification.

5.1.1 Flow Waveform Verification

The results from comparing patient-specific and *in vitro* Fontan circulation model waveforms are summarized in Table 5-1. The table summarizes two metrics, a ratio of the average difference between the two waveforms to the time-averaged value of the two waveforms (ε_{avg}) and a time-normalized root mean square (ε_{rms}), for each model, condition, and vessel of the data collected. Details for each of these metrics are provided in Equation (4-2) and Equation (4-3).

Table 5-1: Time-averaged and RMS error metrics for each vessel waveform under each condition and both models tested

Model	Condition	Vessel	ε_{avg}(%)	ε_{rms} (mL/s^2)
CHOP11B	BH	IVC	10.7	20.34
		SVC	4.3	2.64
		LPA	8.2	9.45
		RPA	14.8	20.19
	FB	IVC	11.2	7.51
		SVC	15.9	3.58
		LPA	9.8	4.53
		RPA	12.0	4.71
	EX	IVC	5.7	28.78
		SVC	4.9	6.67
		LPA	6.6	15.73
		RPA	6.0	20.04
CHOP235A	BH	IVC	7.8	15.97
		SVC	8.0	4.65
		LPA	5.2	2.96
		RPA	2.7	5.35
	FB	IVC	5.5	4.40
		SVC	5.1	5.21
		LPA	6.4	2.82
		RPA	6.9	9.12
	EX	IVC	9.7	19.83
		SVC	9.5	20.51
		LPA	6.3	6.17
		RPA	5.6	17.24

The greatest average difference between the patient-specific and the modeled curves occurred for the SVC of the CHOP11B patient-specific FB model at 15.9%. The

patient-specific and modelled waveforms for this vessel under this model and condition are shown in Figure 5-1.

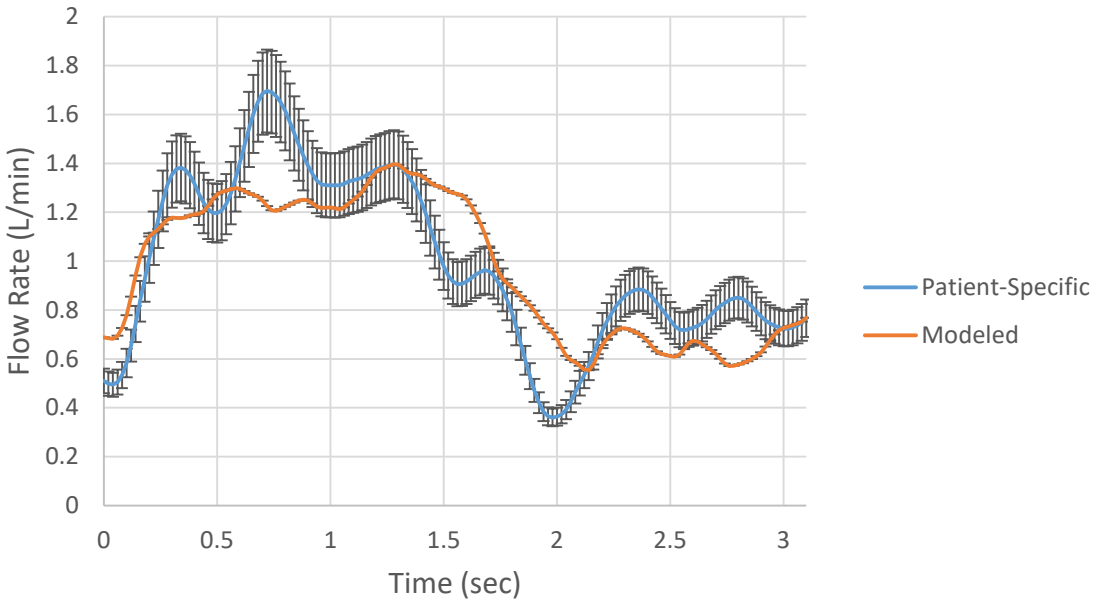

Figure 5-1: Flow rate verification for CHOP11B patient-specific FB SVC. The error bars represent a 95% confidence interval.

Figure 5-2 shows the comparison for the vessel with the greatest time-normalized root mean square error – CHOP11B patient-specific EX IVC. This vessel flow rate time-normalized root mean square value is 28.78 mL/s^2, meaning that every second the cumulative difference between the patient-specific goal and the modeled IVC flow rate

waveform is 28.78 mL/s (1.73 L/min). This value is 27.6% of the mean flow through the IVC under this experimental condition.

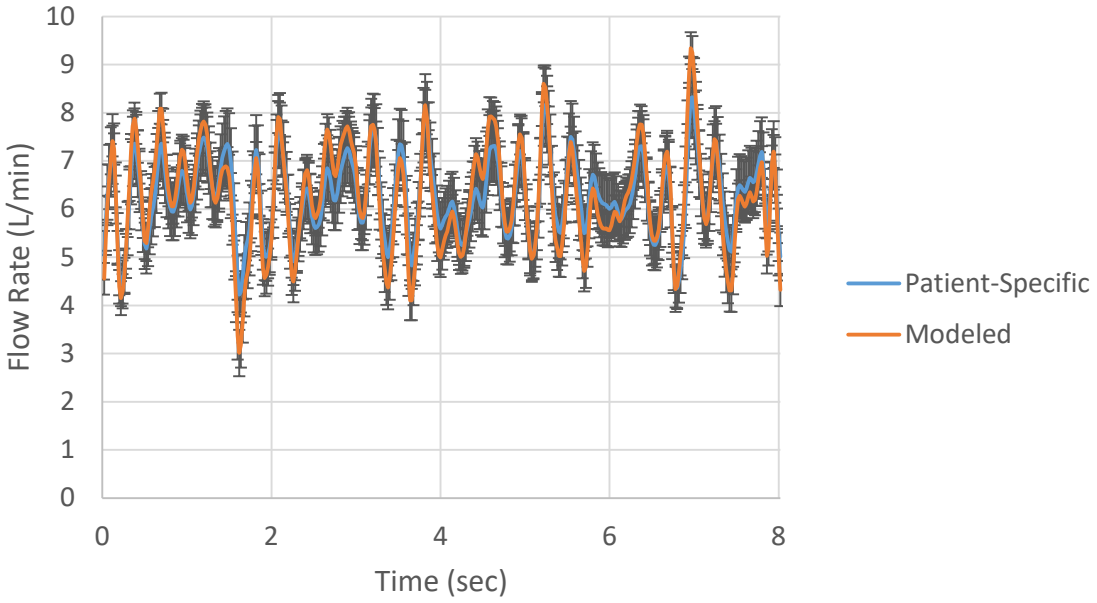

Figure 5-2: Flow rate verification for CHOP11B patient-specific EX IVC. The error bars represent a 95% confidence interval.

5.1.2 TCPC Model Compliance Verification

The results of verifying TCPC model compliance against patient-specific compliance values is broken into 3 categories: the result of patient-specific data analysis, the result of *in vitro* compliance testing, and the result of computational simulations. Patient-specific data analysis resulted in compliance target values for which the models were constructed to possess. *In vitro* compliance testing produced a pressure-volume relationship for a model of arbitrary wall thickness. Computational simulations resulted in an estimated model wall thickness to achieve patient-specific compliance, which was then verified through additional *in vitro* compliance testing.

5.1.2.1 Patient-Specific Data Analysis

The results of the patient-specific pressure and volume data analysis described in section 4.2.1.4.2 are summarized in Figure 5-3, Figure 5-4, and Table 5-2.

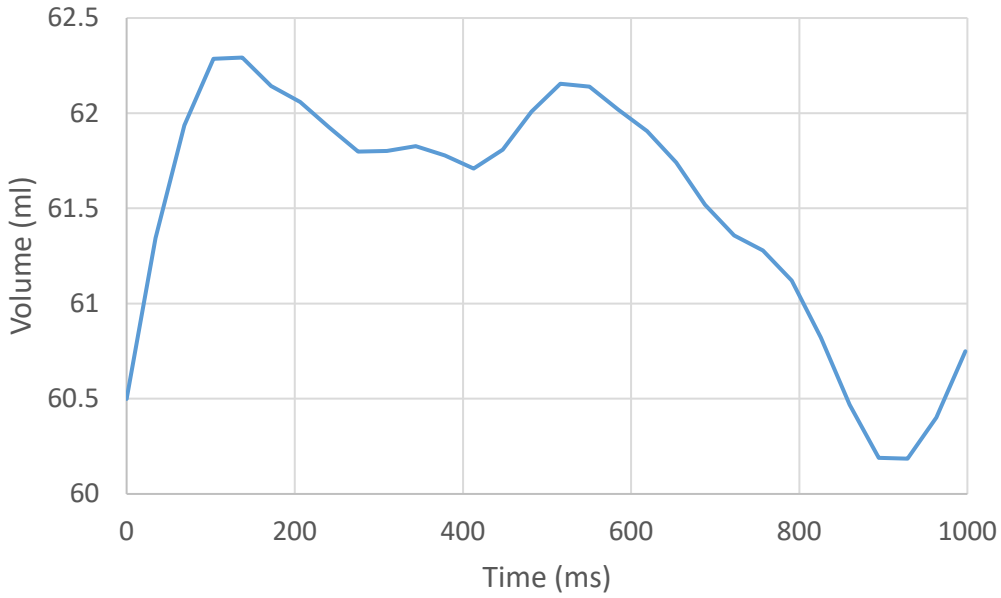

Figure 5-3: CHOP11B BH patient-specific TCPC volume as a function of time

Figure 5-3 shows patient-specific TCPC volume over a cardiac cycle for patient CHOP11B during the BH condition, as found by integrating the TCPC inflow and outflow waveforms. The maximum change in volume over this time period is 2.11 mL with a 10% uncertainty assigned for all MRI measurements [140].

Figure 5-4 shows the analysis result for patient CHOP235A, also during the breath-held condition. CHOP235A's mean volume is 109.57 mL, and CHOP11B's mean volume is 61.51 mL.

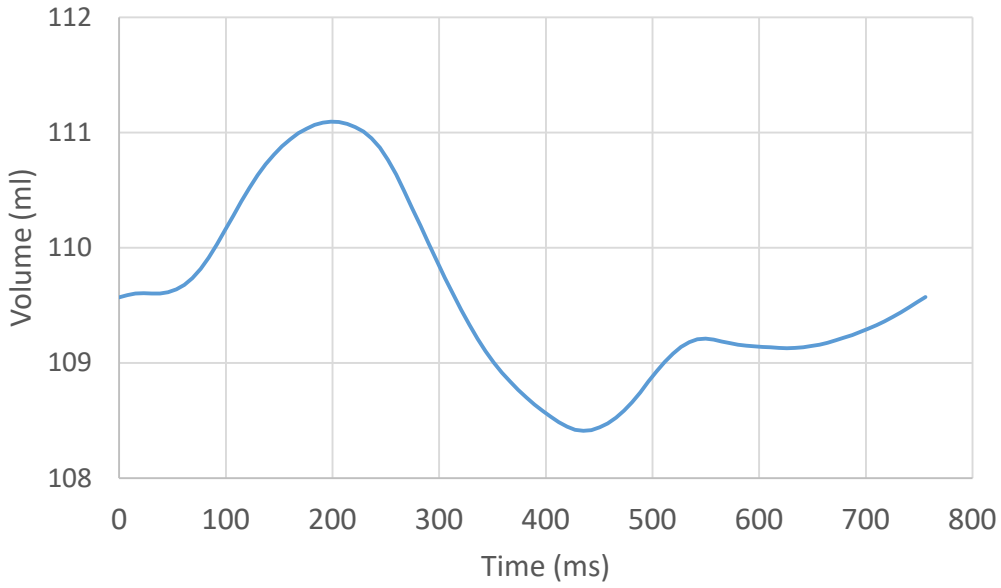

Figure 5-4: CHOP235A BH patient-specific TCPC volume as a function of time

Table 5-2 summarizes the patient-specific data analysis through displaying the pressure change values for an age-matched cohort, and ultimately the *in vivo* compliance targets. These *in vivo* compliance targets are the values for which the flexible TCPC models were designed. Given a material from the manufacture (BDC Labs) and a patient-specific geometry, the remaining variable to affect model compliance was the model wall thickness. Both *in vitro* compliance testing and computational simulation results informed this model wall thickness parameter.

Table 5-2: *In vivo* compliance target values. The uncertainties provided are for a 95% confidence interval.

Patient Number	ΔV (mL)	ΔP (mmHg)	*In Vivo* Compliance (mL/mmHg)
CHOP11B	2.11 ± 0.21	1.55 ± 0.87	1.36 ± 0.78
CHOP235A	2.68 ± 0.27		1.73 ± 0.99

5.1.2.2 *In vitro* Compliance Testing

The *in vitro* compliance testing methods covered 2 different model tests: one of arbitrary thickness where the purpose of the testing was to acquire a pressure-volume relationship and characterize material properties (step 2, section 4.2.1.4.2); and one of a defined thickness where the purpose of testing was to verify if the computational simulations estimated the proper wall thickness (step 5, section 4.2.1.4.2). The computational simulation verification was performed by comparing the *in vitro* compliance value against the patient-specific *in vivo* compliance target found in Table 5-2. Each of these two tests were performed for each of the patients (CHOP11B and CHOP235A), resulting in four *in vitro* compliance test results.

5.1.2.2.1 In vitro Compliance Testing to Characterize Material

In vitro compliance testing to characterize the material of a 1 ± 0.1 mm thick CHOP11B TCPC model found that 3.91 ± 0.08 mL (95% confidence interval) was the required injection that resulted in a 1.96 ± 0.01 mmHg change in pressure (P_1 = 15.1 ± 0.11 mmHg, P_2 = 17.1 ± 0.11 mmHg). Repeating this injection volume 10 times resulted in a 1.99 ± 0.1 mL/mmHg compliance. The 1 mm thick model was approximately 46% more compliant than the patient-specific target.

In vitro compliance testing to characterize the material of a 1 ± 0.1 mm thick CHOP235A TCPC model found that 0.51 ± 0.01 mL (95% confidence interval) was the required injection that resulted in a 2.28 ± 0.08 mmHg change in pressure (P_1 = 14.9 ± 0.14 mmHg, P_2 = 17.2 ± 0.17 mmHg). Repeating this injection volume 10 times resulted in a 0.22 ± 0.03 mL/mmHg compliance. The 1 mm thick model was approximately 87% less compliant than the patient-specific target.

These results informed step 3 of the verification process: determining an effective Young's modulus (E_{eff}) by reproducing the *in vitro* compliance test computationally.

5.1.2.2.2 In vitro Compliance Testing to Verify Computational Wall Thickness Estimate

In vitro compliance testing to verify the computational wall thickness of the 1.4 ± 0.1 mm thick CHOP11B TCPC model found that 2.69 ± 0.09 mL was the required injection that resulted in a 1.97 ± 0.02 mm Hg change in pressure (P_1 = 15.1 ± 0.21 mmHg, P_2 = 17.1 ± 0.20 mmHg). Repeating this injection volume 10 times resulted in a 1.37 ± 0.05 mL/mmHg compliance.

In vitro compliance testing to verify the computational wall thickness of the 0.38 ± 0.1 mm thick CHOP235A TCPC model found that 3.61 ± 0.19 mL was the required injection that resulted in a 2.1 ± 0.2 mm Hg change in pressure (P_1 = 15.0 ± 0.30 mmHg, P_2 = 17.1 ± 0.17 mmHg). Repeating this injection volume 10 times resulted in a 1.70 ± 0.12 mL/mmHg compliance.

5.1.2.3 Computational simulations

The first computational simulation step (step 3, section 4.2.1.4.2) sought the appropriate effective Young's modulus to achieve the measured 1 mm thick *in vitro* TCPC compliance. The procedure measured the internal TCPC pressure after injecting 4 mL of fluid. Figure 5-5 illustrates the effective Young's modulus optimization response for both CHOP11B and CHOP235A.

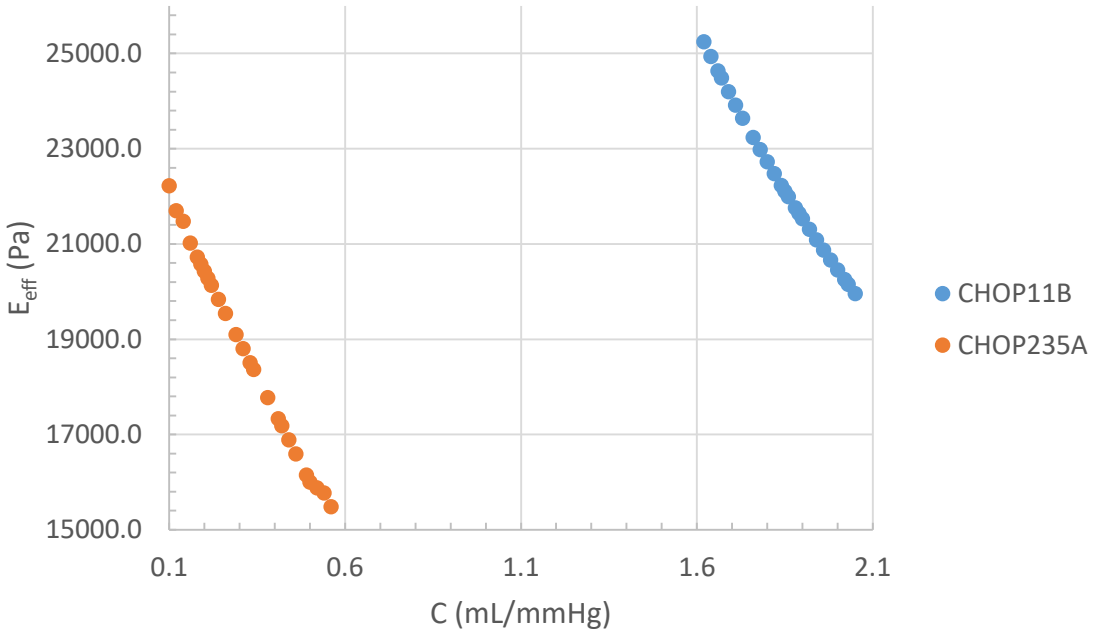

Figure 5-5: Computational analysis optimization showing effective Young's modulus as a function of the compliance.

Though almost linear, the relationships between the Young's modulus and compliance shown in Figure 5-5 for CHOP11B and CHOP235A are $E_{eff} = -12243C + 44866, R^2 = 0.9959$ and $E_{eff} = -14587C + 23384, R^2 = 0.9969$. Therefore, for CHOP11B to achieve a compliance of 1.99 mL/mmHg, the material's effective Young's modulus was calculated as 20500 Pa. For CHOP235A to achieve a compliance of 0.22 mL/mmHg, its material's effective Young's modulus was calculated as 20100 Pa.

With the resultant Young's modulus, the computational simulation then targeted the appropriate TCPC wall thickness (δ) to match the *in vivo* 1.36 mL/mmHg and 1.73 mL/mmHg target compliances from CHOP11B and CHOP235A, respectively (step 4, section 4.2.1.4.2; also see Table 5-2). The response curves are shown in Figure 5-6. Both curves are non-linear, and the power-law regression equations for the CHOP11B and

CHOP235A response curves are $\delta = 1.9C^{-0.96}, R^2 = 1$ and $\delta = 0.4975C^{-0.419}, R^2 = 1$, respectively.

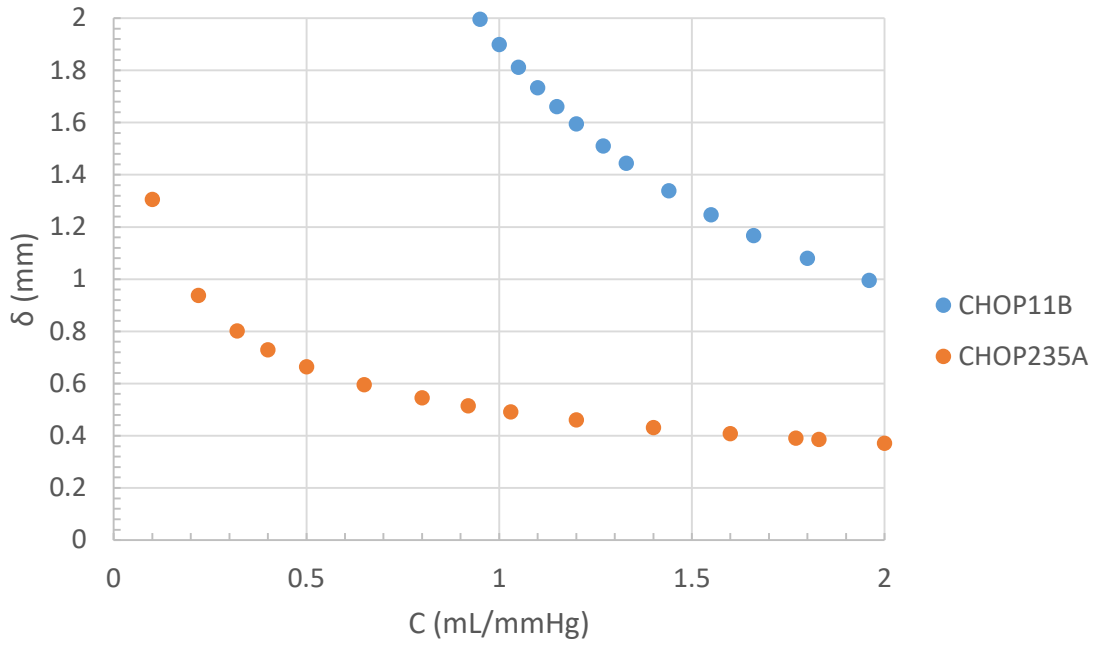

Figure 5-6: CHOP11B TCPC wall thickness vs compliance response surface

The response curves estimate a 1.41 mm and 0.40 mm TCPC wall thickness for the CHOP11B and CHOP235A models in order to match their respective target *in vivo* compliance. The *in vitro* tests verified these as proper wall thickness estimates by matching an *in vitro* compliance test of a CHOP11B TCPC model with 1.41 mm wall thickness and a CHOP235A model with 0.4 mm wall thickness to the appropriate *in vivo* target listed in Table 5-2 (see section .5.1.2.2.2).

Table 5-3 summarizes all TCPC model compliance verification results. The columns of the table correspond to the TCPC model compliance verification methods steps from section 4.2.1.4.2, which are repeated here for convenience:

(1) The patient-specific data was analyzed to determine an *in vivo* target compliance.

(2) An arbitrary-thickness (1mm) *in vitro* model was constructed and tested to determine its compliance.

(3) The *in vitro* compliance test was reproduced computationally to determine an effective Young's modulus (E_{eff}).

(4) The model thickness was computationally iterated upon using the effective Young's modulus to determine a target model wall thickness which would match the target compliance.

(5) A new model with the computationally-derived target wall thickness was constructed and tested *in vitro* to determine if its compliance matched the target compliance from stage one.

Table 5-3: TCPC model compliance verification results summary

	Step 1	Step 2	Step 3	Step 4	Step 5
Model	$\boldsymbol{C\left(\frac{\mathbf{mL}}{\mathbf{mmHg}}\right)}$	$\boldsymbol{C\left(\frac{\mathbf{mL}}{\mathbf{mmHg}}\right)}$	$\boldsymbol{E(MPa)}$	$\boldsymbol{\delta(mm)}$	$\boldsymbol{C\left(\frac{\mathbf{mL}}{\mathbf{mmHg}}\right)}$
CHOP11B	1.36 ± 0.78	1.99 ± 0.1	20.5	1.41	1.38 ± 0.1
CHOP235A	1.73 ± 0.99	0.22 ± 0.1	20.1	0.40	1.70 ± 0.1

With the *in vitro* Fontan circulation model verification results established, the study now examines effect of respiration, exercise, and pulsatility on power loss, hepatic flow distribution, and energy dissipation rate in the following sections.

5.2 Velocity Fields

The particle image velocimetry acquisition and analysis methods (section 4.2.2.2) resulted in a time-resolved three-dimensional velocity field for the patient-specific, derived, and steady experimental conditions for each model. In all, 20 three-dimensional velocity fields were collected: 3 steady flow conditions, 3 patient-specific conditions, and 4 derived conditions for each of the two models. Each velocity field contains quantitative velocity

vector component data resolved for every 0.1 seconds (100 ms) on a 0.5mm x 0.5mm x 0.5mm grid. Table 5-4 lists the experimental conditions for which three-dimensional velocity fields were collected.

Table 5-4: List of experimental conditions for which three-dimensional velocity fields were collected during this study

Model	Condition	
CHOP11B	BH	Steady
		Patient-Specific
		Low Pulsatility
		High Pulsatility
	FB	Steady
		Patient Specific
	EX	Peak Steady
		Peak Patient-Specific
		Half-Peak Steady
		Half-Peak Pulsatile
CHOP235A	BH	Steady
		Patient-Specific
		Low Pulsatility
		High Pulsatility
	FB	Steady
		Patient Specific
	EX	Peak Steady
		Peak Patient-Specific
		Half-Peak Steady
		Half-Peak Pulsatile

One purpose of collecting this velocity field data is for comparison to subsequent computational fluid dynamics (CFD) simulations hoping to validate the use of fluid-structure interaction (FSI) models. Any use of this study's velocity field results to validate a CFD FSI methodology will use quantitative results and analyses specific to the computational methodology. Hence, no CFD-relevant quantitative results of the velocity field are presented here alone because the CFD FSI simulations have yet to be performed. All 20 sets of time-resolved three-dimensional velocity fields are saved on the CFM Lab servers for use in future CFD FSI studies.

The time-resolved velocity fields are also necessary for this study because two of the three patient-relevant metrics (viscous dissipation and HFD) used in determining the effect of respiration, exercise, and pulsatility on Fontan hemodynamics are quantitative metrics derived directly from them. The third patient-relevant metric (power loss) is calculated entirely from static pressure and volumetric flow rate data. A qualitative assessment of each velocity field is useful in assigning reasoning for the changes in the power loss, viscous dissipation, and hepatic flow distribution metrics observed (sections 6.3, 6.4, 6.5, and 6.6). Therefore, the effect of respiration, exercise, and pulsatility results presentations also include qualitative comparisons of the different velocity fields involved.

Fourteen of the 20 sets of time-resolved three-dimensional velocity fields and hemodynamic results are used to show the effect of respiration, exercise, and pulsatility on the power loss, viscous dissipation and hepatic flow distribution terms. The six velocity fields acquired, but not employed are: CHOP11B FB steady, CHOP11B half-peak EX steady, CHOP11B peak EX steady, CHOP235A FB steady, CHOP235A half-peak EX steady, and CHOP235A peak EX steady. These data were collected as CFD FSI validation data sets, but were not useful in determining trends due to respiration, exercise, or pulsatility. The effect of respiration comparison utilized the patient-specific BH and FB conditions for each model, which includes multiple changes in experimental conditions based on *in vivo* patient data. The steady BH and steady FB values only include changes in mean flow rate and IVC:SVC flow ratio between conditions, which would contaminate the findings. The steady FB, steady half-peak EX, and steady peak EX values were not included in the effect of exercise comparisons for similar reasons. In contrast, the effect of pulsatility comparisons *included* the steady BH condition because all 4 conditions included

in this comparison (steady BH, low pulsatile BH, patient-specific BH, and high pulsatile BH) had effectively equal condition parameters except for pulsatility (see Appendix 11.5, Table 11-7). Appendix 11.9 includes a comprehensive results summary of all 20 experimental conditions, for completeness.

5.3 Effect of Respiration

The effect of respiration on Fontan hemodynamics is shown by comparing the BH and FB experimental conditions for both the CHOP11B and CHOP235A models. Patient-relevant metrics are derived from both the time-resolved three-dimensional velocity fields and the pressure and flow rate data for each model under these conditions. The CHOP11B BH patient-specific and FB patient-specific velocity fields are shown in Video 5-1 and Video 5-2 for qualitative comparison, respectively.

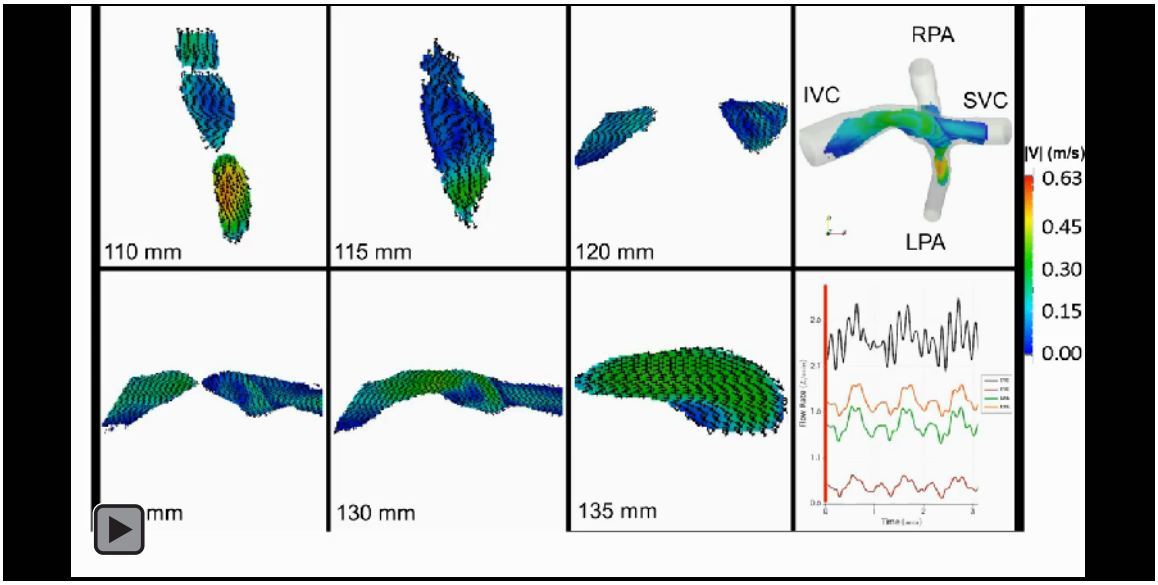

Video 5-1: CHOP11B BH patient-specific velocity fields. The black 3-component velocity vectors show velocity direction. The color provides the velocity magnitude. The upper right panel is a coronal view of the Fontan model with all planes present.

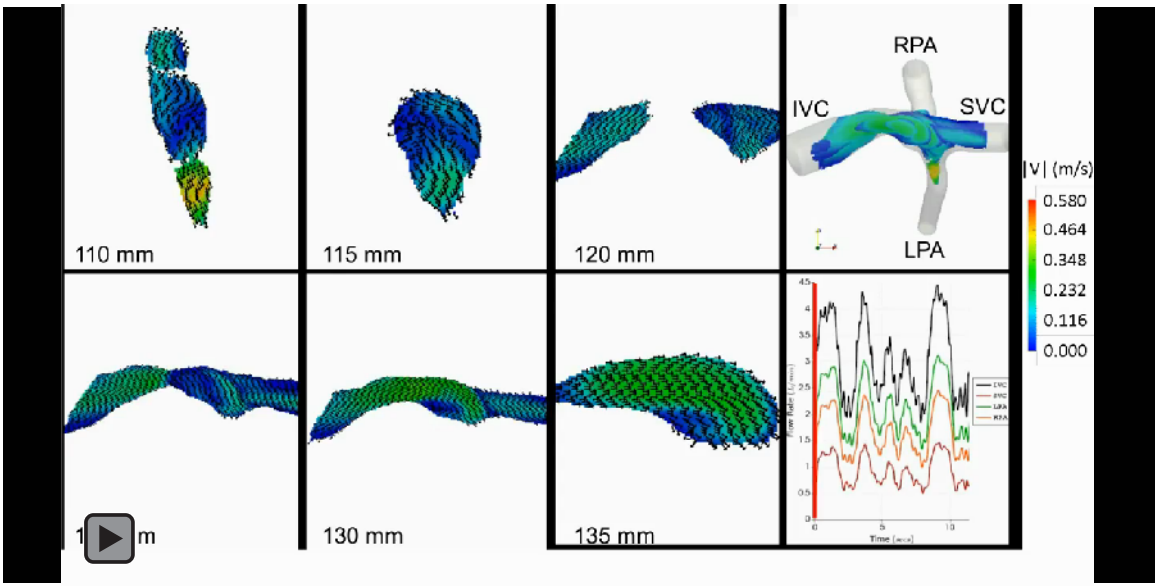

Video 5-2: CHOP11B FB patient-specific velocity fields. The black 3-component velocity vectors show velocity direction. The color provides the velocity magnitude. The upper right panel is a coronal view of the Fontan model with all planes present.

Both the CHOP11B BH patient-specific and CHOP11B FB patient-specific velocity fields show a pulsatile nature with vector magnitude and direction changing most dramatically with the cardiac cycle frequency. Both exhibit peak velocity values located in the LPA of approximately the same magnitude (~0.6 m/s). Figure 5-7 shows the qualitative IVC and SVC inflow stream collision line (red) during minimum IVC flow rates for the CHOP11B BH and CHO11B FB cases at the 130mm plane. Observing the video shows this line is relatively stable for all time points between both cases. In general, the flow fields are similar.

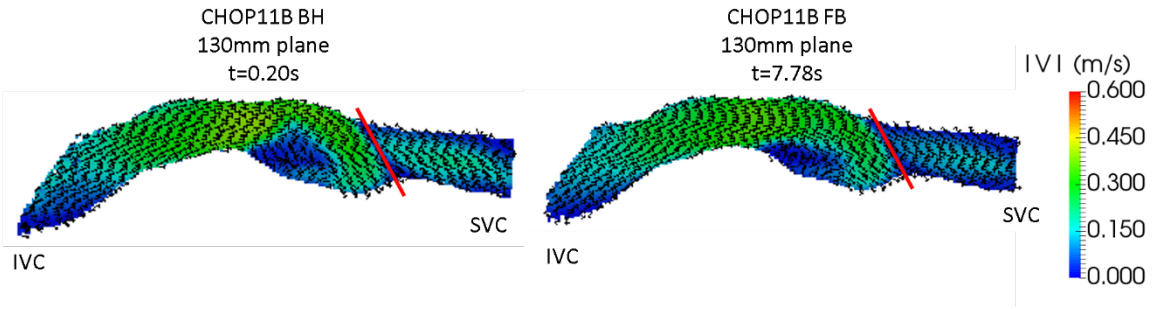

Figure 5-7: CHOP11B patient-specific BH and patient-specific FB velocity fields at the 130mm plane and minimum IVC flow rate time points. The black 3-component velocity vectors show velocity direction. The color provides the velocity magnitude.

However, there is one significant qualitative difference between the CHOP11B BH and CHOP11B FB velocity fields. Unlike the CHOP11B BH condition, the CHOP11B FB condition experiences peak and near-peak velocities in the IVC and Fontan connection regions at some time points. Figure 5-8 shows the velocity field for each case during their respective peak IVC inflow rate time points.

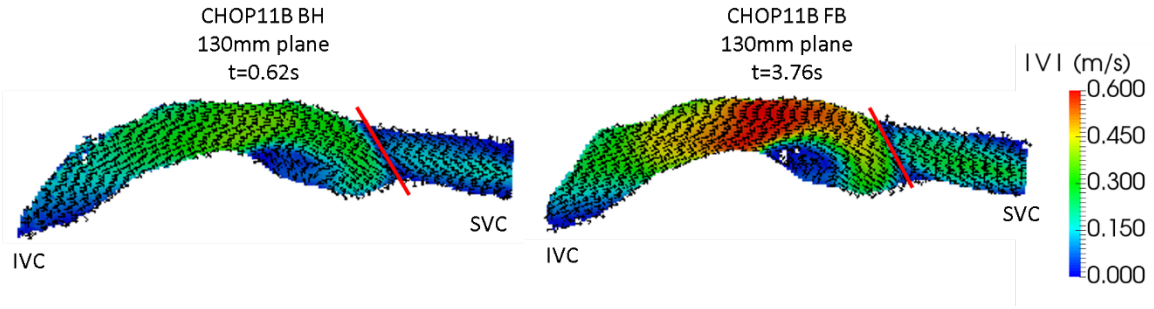

Figure 5-8: CHOP11B patient-specific BH and patient-specific FB velocity fields at the 130mm plane and peak IVC flow rate time points. The black 3-component velocity vectors show velocity direction. The color provides the velocity magnitude.

The CHOP235A BH and FB velocity fields are shown in Video 5-3 and Video 5-4, respectively.

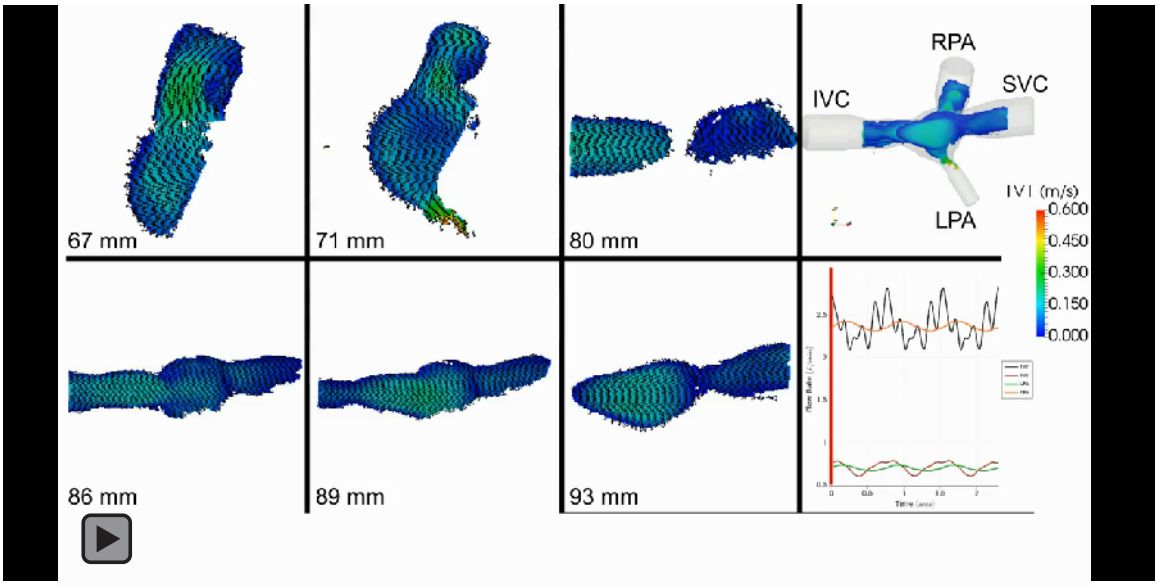

Video 5-3: CHOP235A BH patient-specific velocity fields. The black 3-component velocity vectors show velocity direction. The color provides the velocity magnitude. The upper right panel is a coronal view of the Fontan model with all planes present.

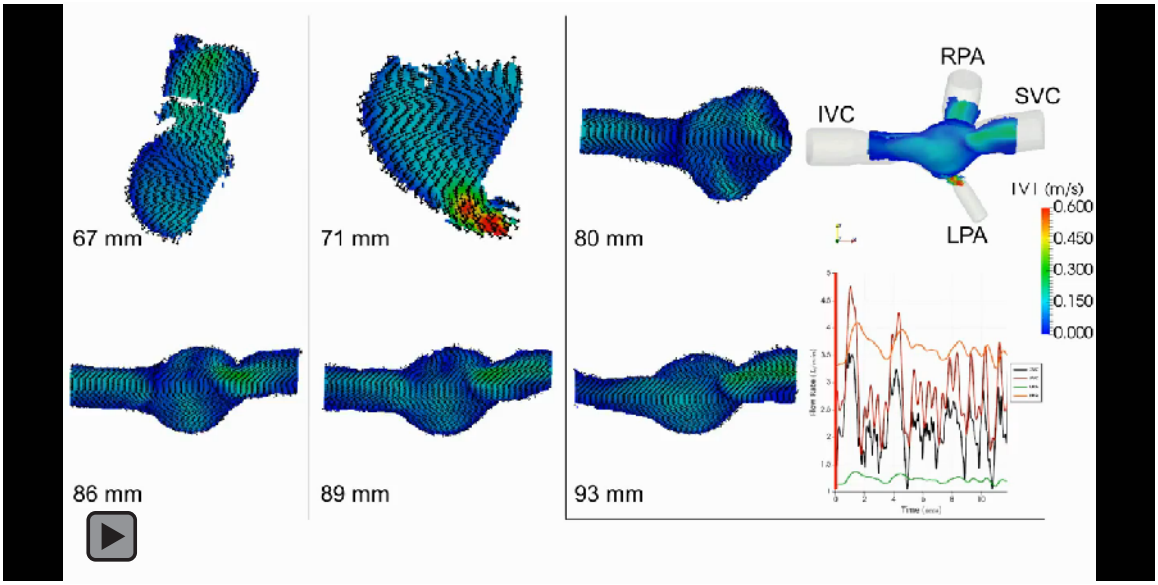

Video 5-4: CHOP235A FB patient-specific velocity fields. The black 3-component velocity vectors show velocity direction. The color provides the velocity magnitude. The upper right panel is a coronal view of the Fontan model with all planes present.

Qualitative comparison of the CHOP235A BH patient-specific and CHOP235A FB patient-specific velocity fields show more differences between them than the CHOP11B

comparison case. Though both CHOP235A velocity fields show peak velocities located in the LPA, the most noticeable difference is the higher SVC inflow velocity in the FB case. The higher SVC inflow velocity magnitude raises the SVC inflow momentum in comparison to the IVC inflow. The differences in the collision line location and shape throughout time for the FB case, as shown in Figure 5-9 and Figure 5-10, is also evidence of the higher unsteadiness the FB flow field experiences.

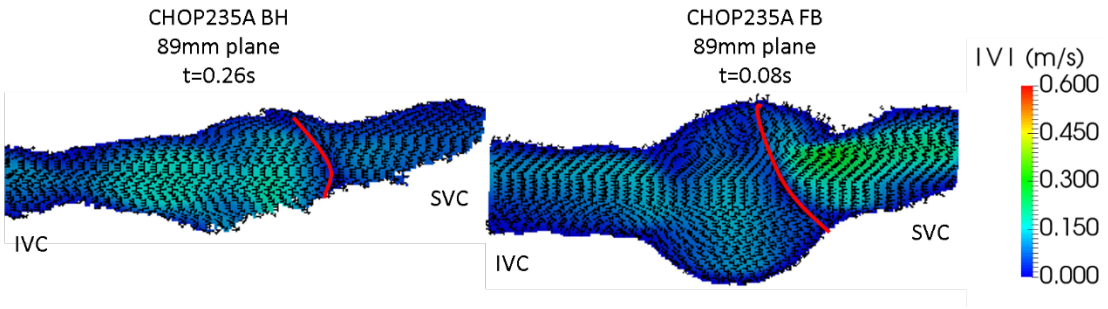

Figure 5-9: CHOP235A patient-specific BH and patient-specific FB velocity fields at the 89mm plane and minimum IVC flow rate time points. The black 3-component velocity vectors show velocity direction. The color provides the velocity magnitude.

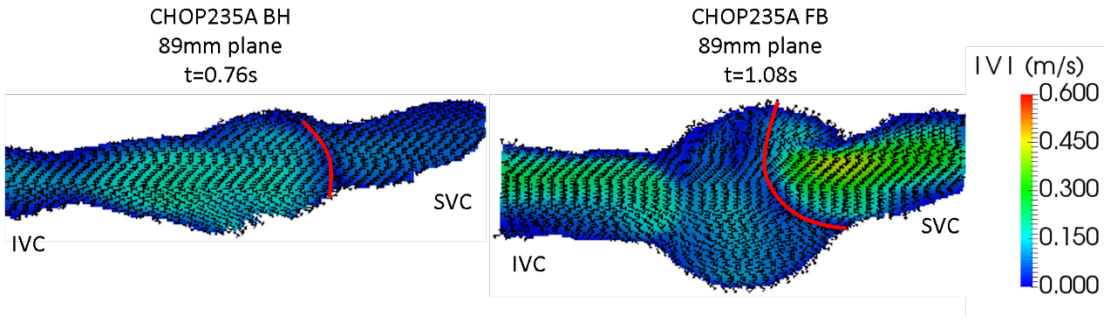

Figure 5-10: CHOP235A patient-specific BH and patient-specific FB velocity fields at the 89mm plane and peak IVC flow rate time points. The black 3-component velocity vectors show velocity direction. The color provides the velocity magnitude.

Sections 5.3.1, 5.3.2, and 5.3.3 provide further insight on the effect of respiration on Fontan hemodynamics.

5.3.1 Effect of Respiration on Power Loss

Section 4.2.2.1 and Equation (4-6) provide the specifics for a power loss metric which is related to how efficiently fluid flows through the Fontan models. Table 5-5 summarizes two power loss metrics, $\dot{E_{app}}$ and iPL, calculated for each model's BH and FB experimental conditions. Apparent power loss and indexed power loss calculation details are provided by Equations (4-6) and (4-7), respectively.

Table 5-5: Power loss values for each model at each BH and FB experimental condition

Model	Condition		$\dot{E}_{app}$ (mW)	iPL (x10^6)
CHOP11B	BH	Patient-Specific	16.3 ± 5.9	290.3 ± 128.3
	FB	Patient-Specific	55.6 ± 9.7	418.6 ± 128.2
CHOP235A	BH	Patient-Specific	18.0 ± 4.6	374.0 ± 111.1
	FB	Patient-Specific	33.8 ± 14.9	170.6 ± 79.6

The greatest apparent power loss appears for each model during the FB patient-specific case at 55.6 ± 9.7 mW (CHOP11B) and 33.8 ± 14.9 mW (CHOP235A). Both models also show that FB apparent power losses are greater than BH apparent power losses. Figure 5-11 and Figure 5-12 compare the patient-specific BH and FB indexed power loss values for CHOP11B and CHOP235A, respectively.

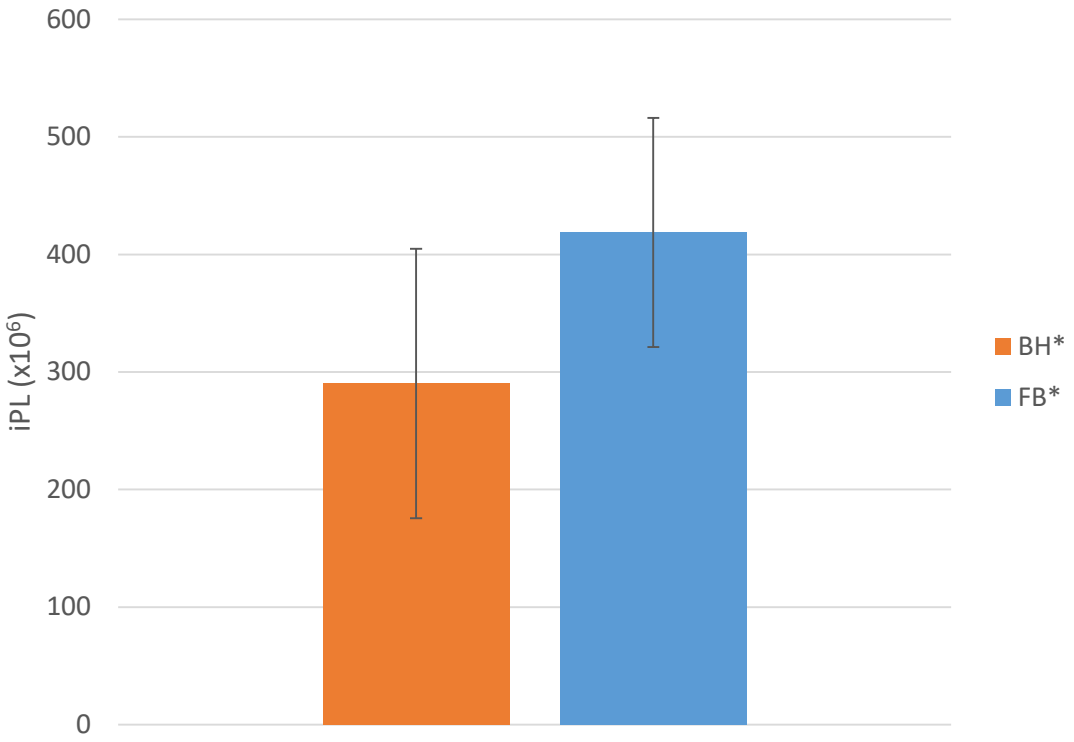

Figure 5-11: CHOP11B patient-specific indexed power loss values comparing BH and FB conditions. * denotes the patient-specific conditions. The error bars represent a 95% confidence interval.

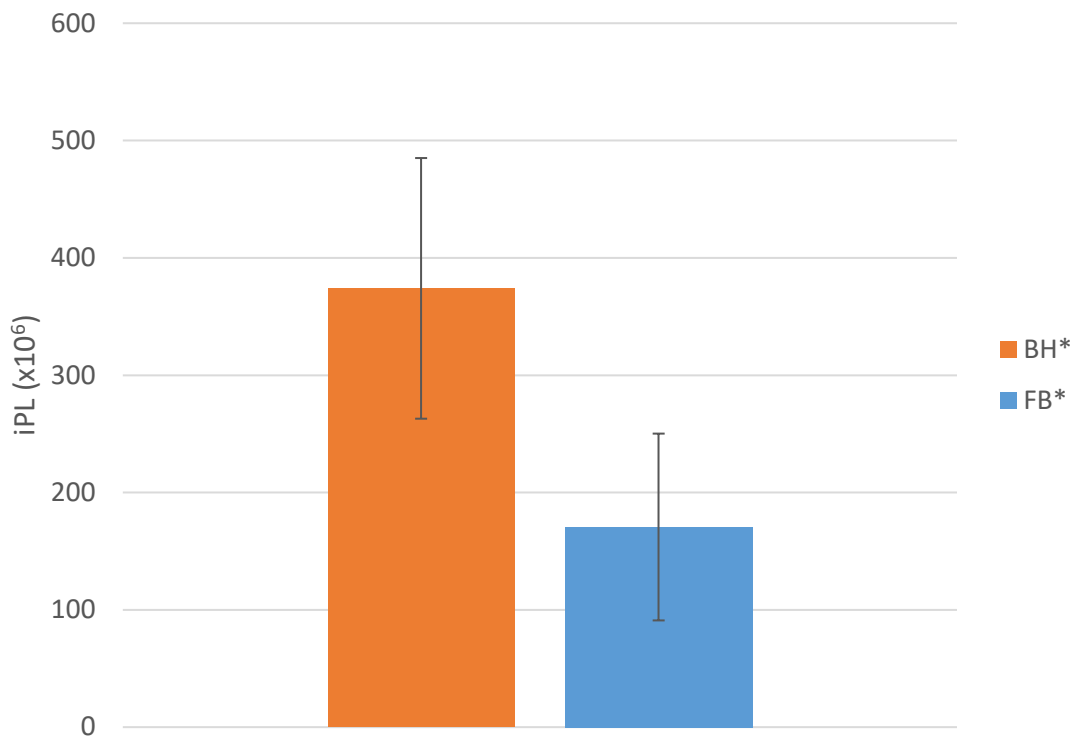

Figure 5-12: CHOP235A patient-specific indexed power loss values comparing BH and FB conditions. * denotes the patient-specific conditions. The error bars represent a 95% confidence interval.

5.3.2 Effect of Respiration on Viscous Dissipation

A viscous dissipation term was calculated for each model's BH and FB conditions, as outlined in section 4.2.2.2.5.4.. Table 5-6 summarizes φ and the indexed viscous dissipation term, $i\varphi$, for respiration effects. Equation (4-9) and Equation (4-10) detail the viscous dissipation term and the indexed viscous dissipation term.

Table 5-6: The effect of respiration on viscous dissipation terms

Model	Condition		φ (1/s^2)	$i\varphi$ (x10^{12})
CHOP11B	BH	Patient-Specific	6272.8 ± 280.6	10.66 ± 1.21
	FB	Patient-Specific	5586.53 ± 423.3	5.95 ± 0.77
CHOP235A	BH	Patient-Specific	756.3 ± 28.4	1.49 ± 0.17
	FB	Patient-Specific	533.6 ± 9.0	0.41 ± 0.04

Figure 5-13 and Figure 5-14 compare the indexed viscous dissipation term between the BH and FB patient-specific conditions for each model.

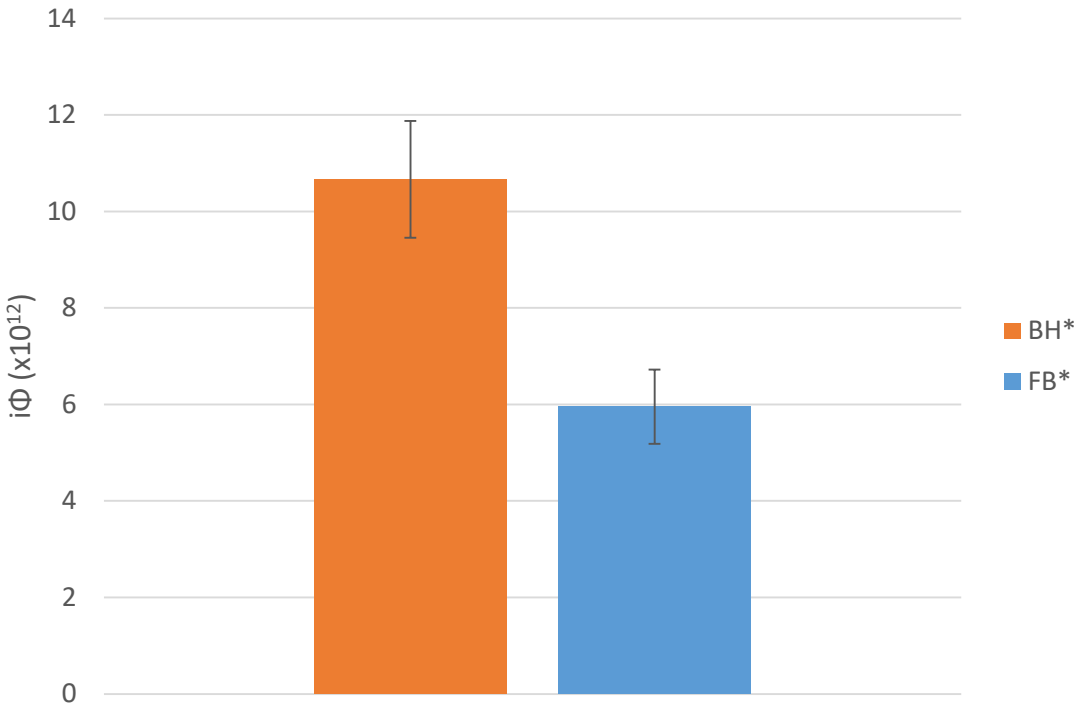

Figure 5-13: CHOP11B comparison between BH and FB patient-specific viscous dissipation term values. * denotes the patient-specific conditions. The error bars represent a 95% confidence interval.

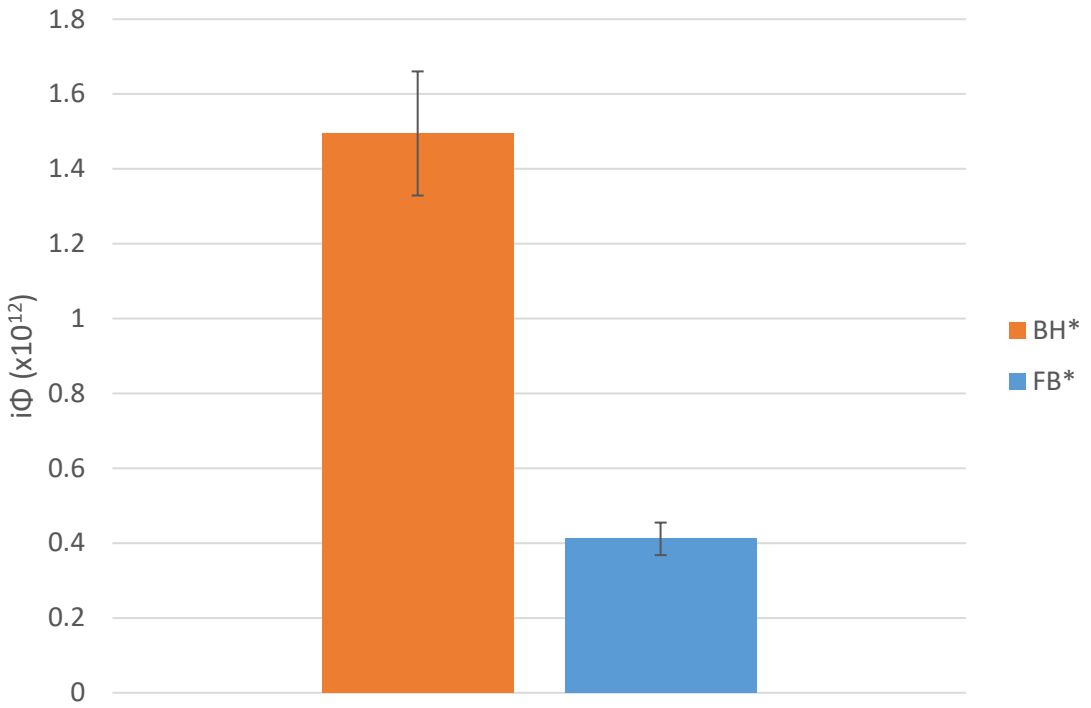

Figure 5-14: CHOP235A comparison between BH and FB patient-specific viscous dissipation term values. * denotes the patient-specific conditions. The error bars represent a 95% confidence interval.

5.3.3 Effect of Respiration on Hepatic Flow Distribution

Hepatic flow distribution (HFD) was calculated for each model's BH and FB conditions, as outlined in section4.2.2.2.5.3. Table 5-7 summarizes the effect of respiration on HFD.

Table 5-7: Effect of respiration on hepatic flow distribution

Model	Condition		HFD (%LPA)
CHOP11B	BH	Patient-Specific	61.06 ± 19.6
	FB	Patient-Specific	49.78 ± 12.0
CHOP235A	BH	Patient-Specific	54.96 ± 30.0
	FB	Patient-Specific	42.60 ± 35.9

Figure 5-15 and Figure 5-16 compare the HFD between the BH and FB patient-specific conditions for each model.

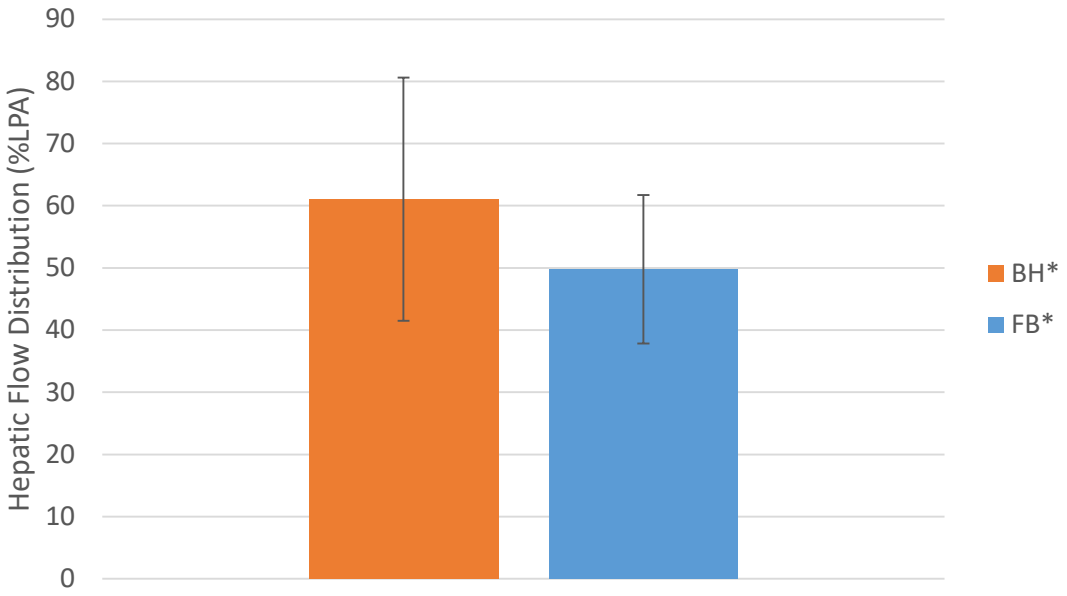

Figure 5-15: CHOP11B comparison between BH and FB patient-specific HFD values. * denotes the patient-specific conditions. The error bars represent a 95% confidence interval.

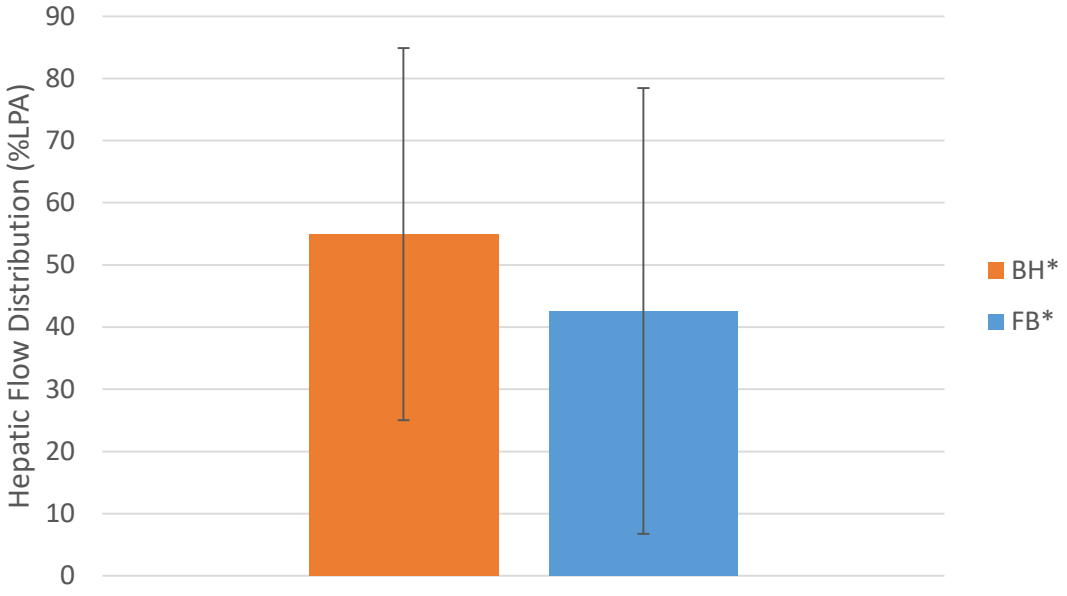

Figure 5-16: CHOP235A comparison between BH and FB patient-specific HFD values. * denotes the patient-specific conditions. The error bars represent a 95% confidence interval.

5.4 Effect of Exercise

The effect of exercise on Fontan hemodynamics is shown by comparing the patient-specific FB, patient-specific peak EX, and pulsatile half-peak EX experimental conditions for both the CHOP11B and CHOP235A models. Patient-relevant metrics are derived from both the time-resolved three-dimensional velocity fields and the pressure and flow rate data for each model under these conditions. The CHOP11B velocity fields are shown in Video 5-2 (section 5.3), Video 5-6, and Video 5-5 for qualitative comparison, respectively.

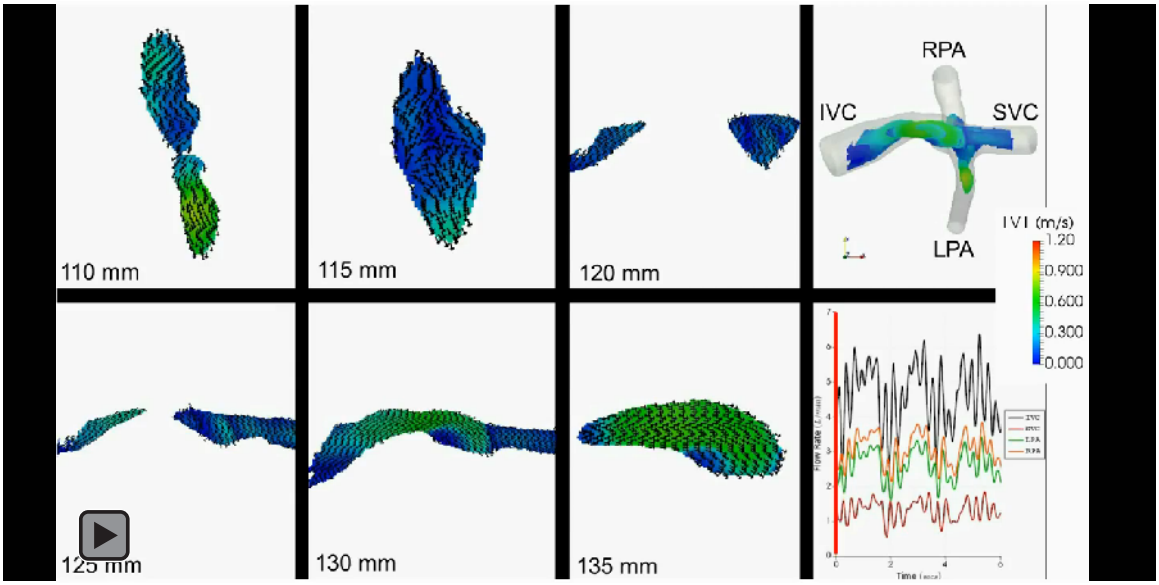

Video 5-5: CHOP11B pulsatile half-peak EX velocity fields. The black 3-component velocity vectors show velocity direction. The color provides the velocity magnitude. The upper right panel is a coronal view of the Fontan model with all planes present.

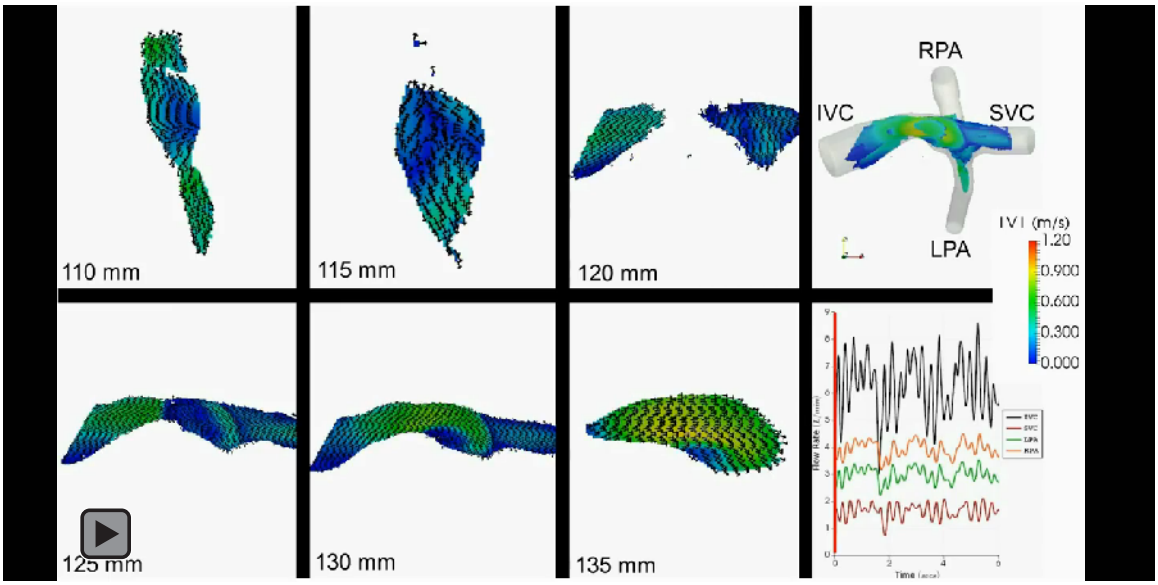

Video 5-6: CHOP11B patient-specific peak EX velocity fields. The black 3-component velocity vectors show velocity direction. The color provides the velocity magnitude. The upper right panel is a coronal view of the Fontan model with all planes present.

Qualitatively comparing the CHOP11B patient-specific FB, pulsatile half-peak EX, and patient-specific peak EX velocity fields show differences between the velocity fields. The collision line location comparison between Figure 5-17 and Figure 5-18 suggests an increase in velocity field unsteadiness from the patient-specific FB case to the pulsatile half-peak EX case, and a subsequent increase in unsteadiness from the pulsatile half-peak EX case to the patient-specific peak EX case. Video observation also appears to show more rapid velocity changes during the EX conditions than during the FB condition; a comparison also suggesting higher unsteadiness during the EX conditions. Velocity magnitude comparisons should be conducted carefully as the color bars differ for each velocity field. The patient-specific FB and pulsatile half-peak EX conditions have similar minimum velocity magnitudes at the inlets and at the Fontan connection (Figure 5-17), with higher patient-specific peak EX condition velocity values. The peak IVC flow rate time point reveals increasing velocity magnitude at the flow inlets and Fontan connection

on the 130mm plane from the patient-specific FB condition to the pulsatile half-peak EX condition. This velocity magnitude also increases from the pulsatile half-peak EX condition to the patient-specific peak EX condition.

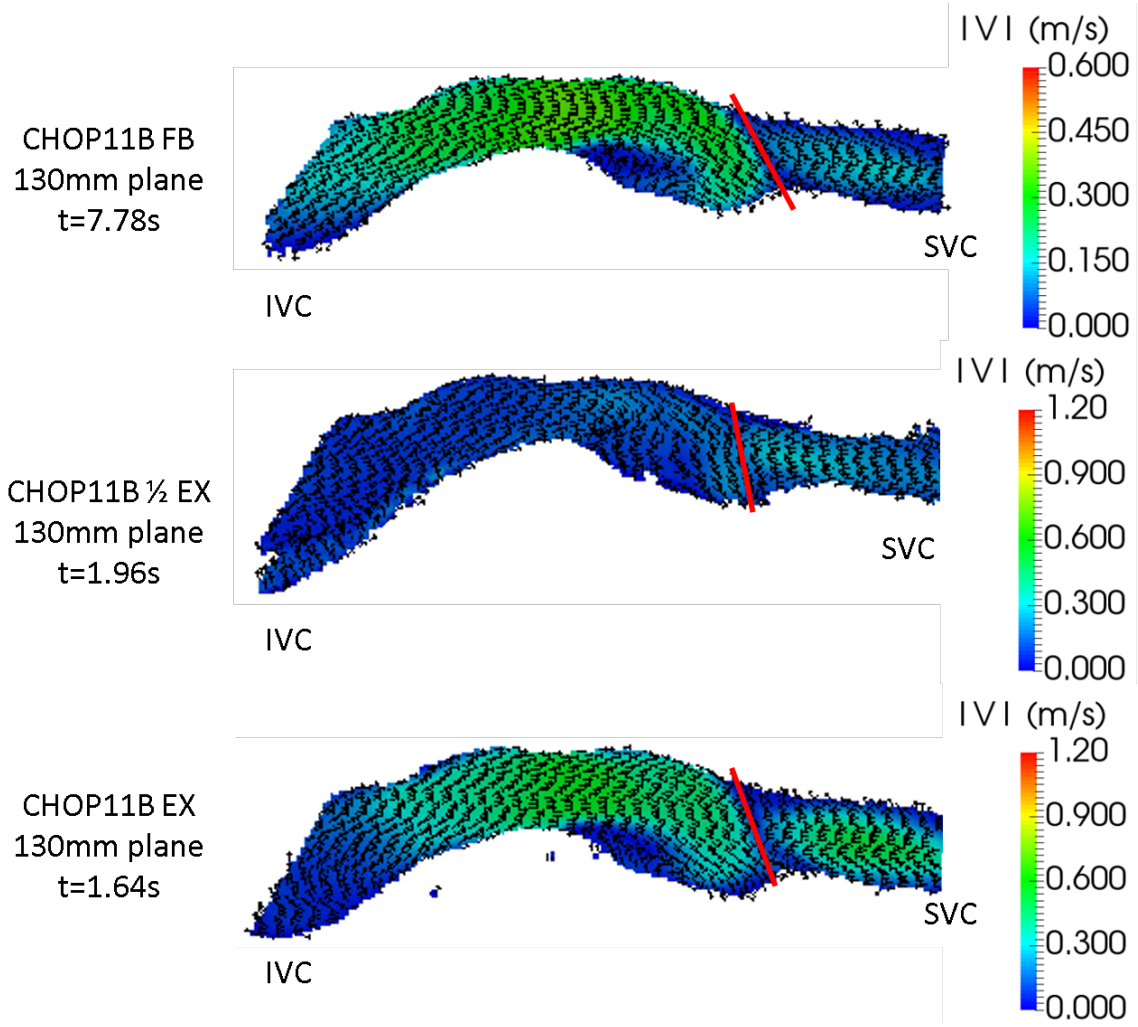

Figure 5-17: CHOP11B patient-specific FB, pulsatile half-peak EX, and patient-specific EX velocity fields at the 130mm plane and minimum IVC flow rate time points. Note the different color bars for each velocity field. The black 3-component velocity vectors show velocity direction. The color provides the velocity magnitude.

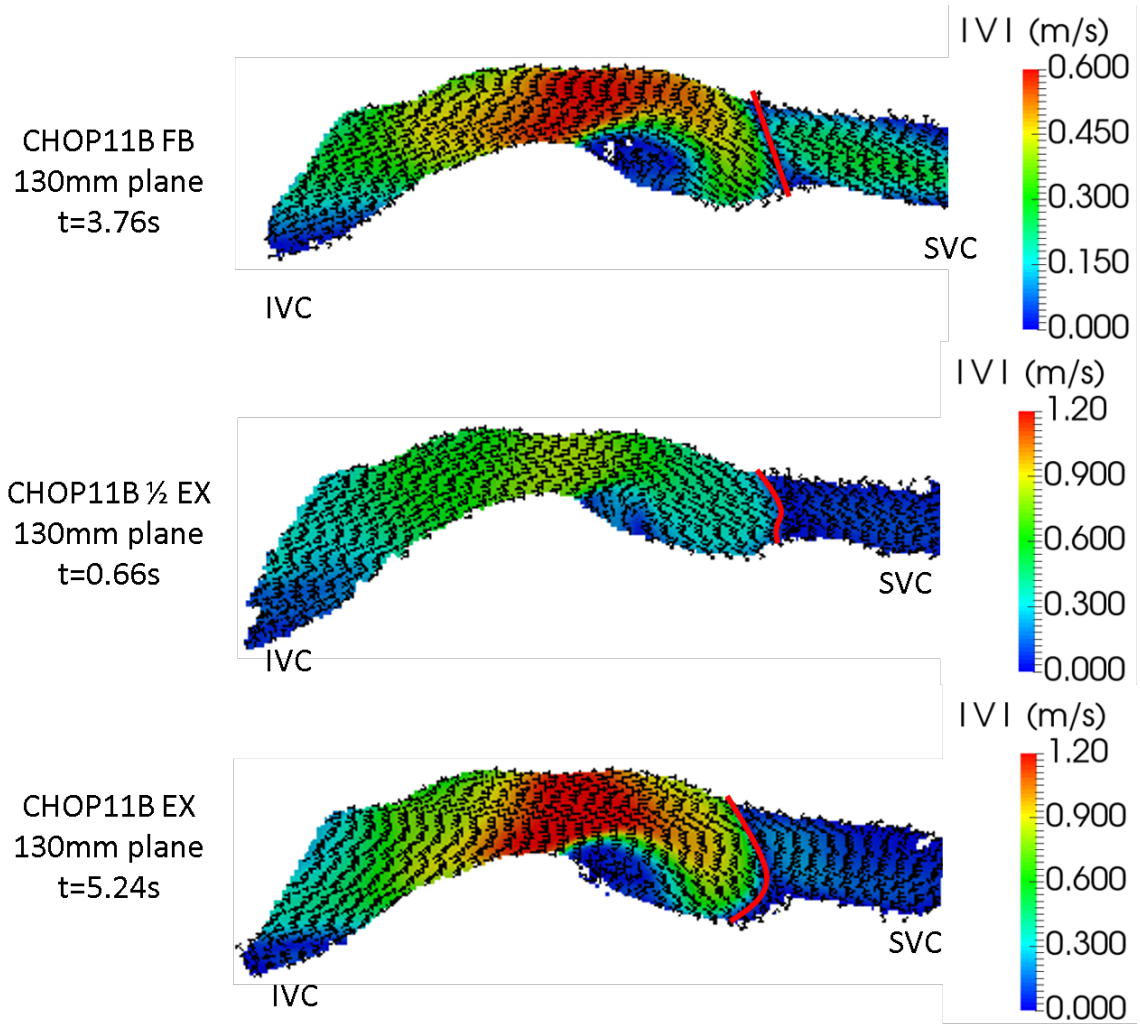

Figure 5-18: CHOP11B patient-specific FB, pulsatile half-peak EX, and patient-specific EX velocity fields at the 130mm plane and peak IVC flow rate time points. Note the different color bars for each velocity field. The black 3-component velocity vectors show velocity direction. The color provides the velocity magnitude.

The CHOP235A patient-specific FB, patient-specific peak EX, and pulsatile half-peak EX velocity fields are shown in Video 5-4 (section 5.3), Video 5-7, and Video 5-8 for qualitative comparison, respectively.

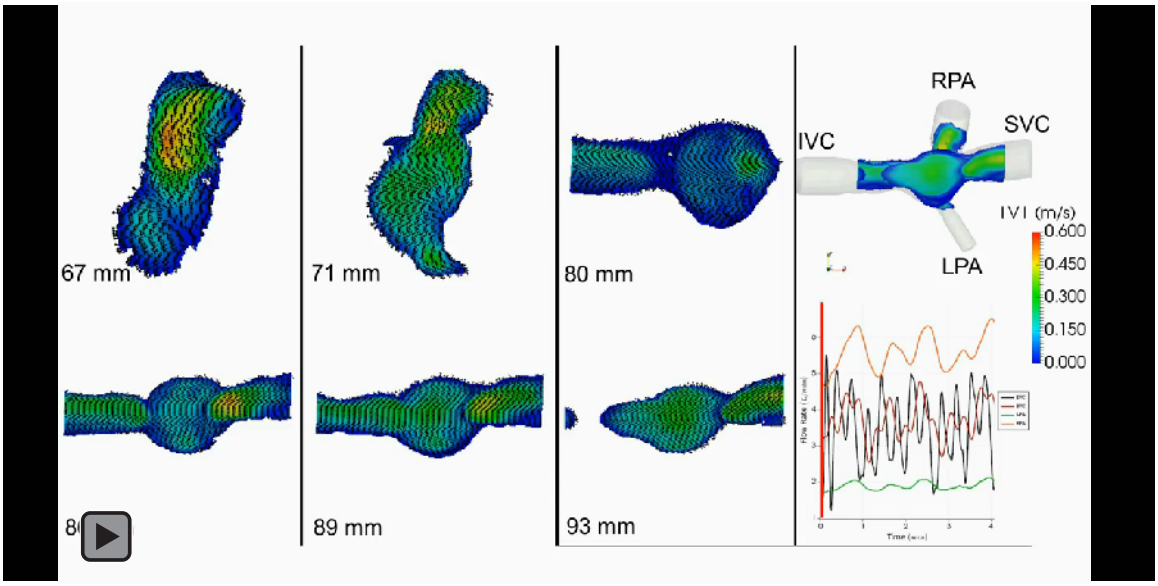

Video 5-7: CHOP235A patient-specific peak EX velocity fields. The black 3-component velocity vectors show velocity direction. The color provides the velocity magnitude. The upper right panel is a coronal view of the Fontan model with all planes present.

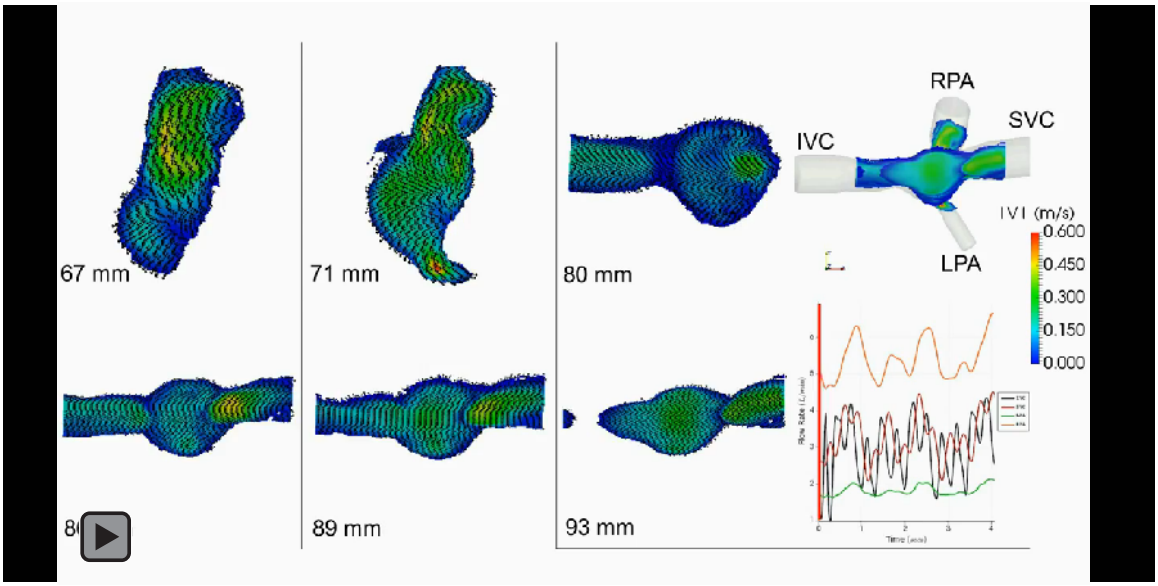

Video 5-8: CHOP235A pulsatile half-peak EX velocity fields. The black 3-component velocity vectors show velocity direction. The color provides the velocity magnitude. The upper right panel is a coronal view of the Fontan model with all planes present.

Qualitatively comparing the CHOP235A patient-specific FB, pulsatile half-peak EX, and patient-specific peak EX velocity fields shows more similarity between the

velocity fields than is present in the CHOP11B cases. The collision line comparison between Figure 5-19 and Figure 5-20 shows only slight change in shape and location between the minimum and maximum IVC flow rate time points. This qualitative finding suggests less overall unsteadiness for the CHOP235A exercise comparison conditions when compared to the CHOP11B exercise conditions. Video observation, though, shows that pulsatility is clearly present. Comparing overall velocity magnitudes between conditions shows very little change. This is not surprising, as the change in some experimental condition parameters (mean inflow rate and IVC pulsatility) between the CHOP235A patient-specific FB, pulsatile half-peak EX, and patient-specific peak EX conditions is less than the change in the same parameters for the CHOP11B patient-specific FB, pulsatile half-peak EX, and patient-specific peak EX conditions. (see Table 11-7). For example, CHOP235A mean inflow rate changes from 4.96 L/min, to 6.20 L/min, and 7.08 L/min from patient-specific FB, to pulsatile half-peak EX, and patient-specific peak EX. CHOP11B mean inflow rate changes from 4.04 L/min, to 5.95 L/min, and 7.90 L/min from patient-specific FB, to pulsatile half-peak EX, and patient-specific peak EX. Sections 5.4.1, 5.4.2, 5.4.3, and 6.4 provide further insight on the effect of exercise on Fontan hemodynamics.

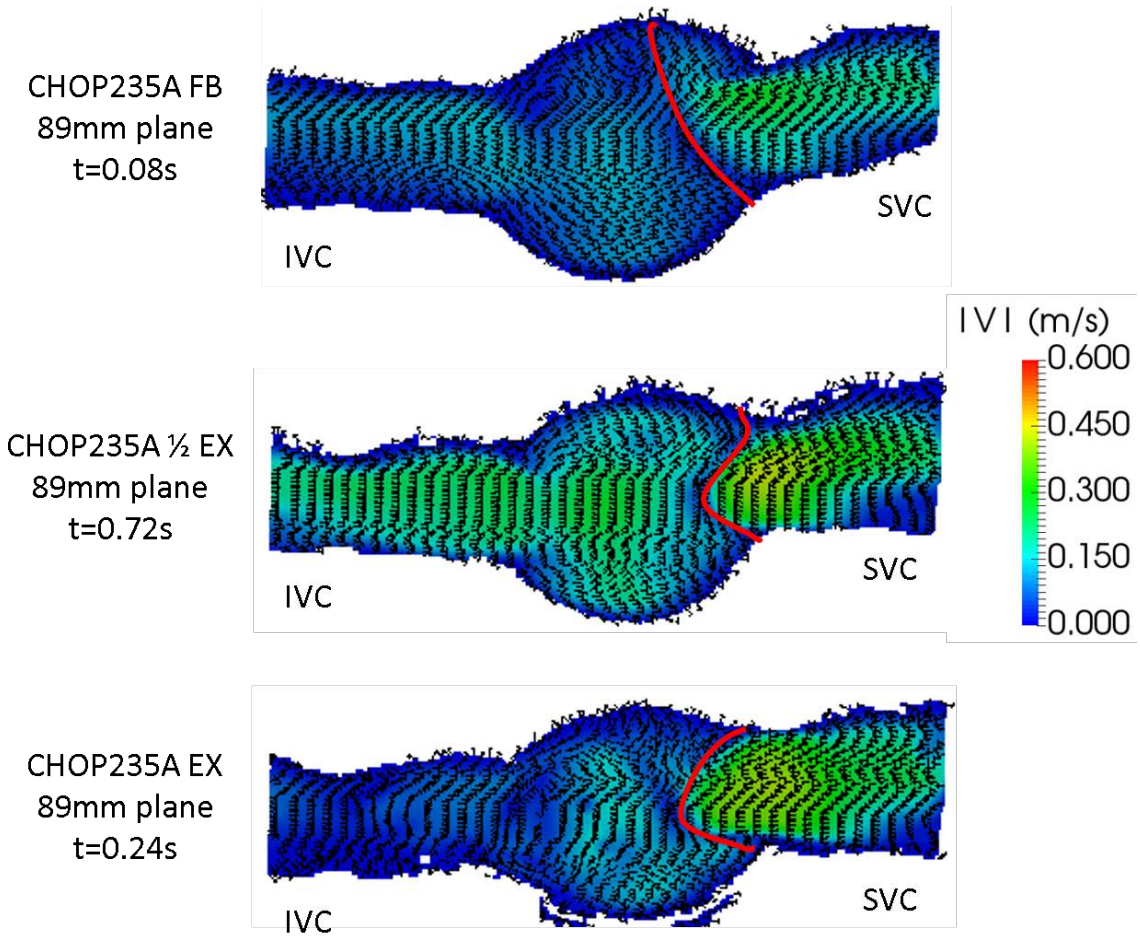

Figure 5-19: CHOP235A patient-specific FB, pulsatile half-peak EX, and patient-specific EX velocity fields at the 89mm plane and minimum IVC flow rate time points. The black 3-component velocity vectors show velocity direction. The color provides the velocity magnitude.

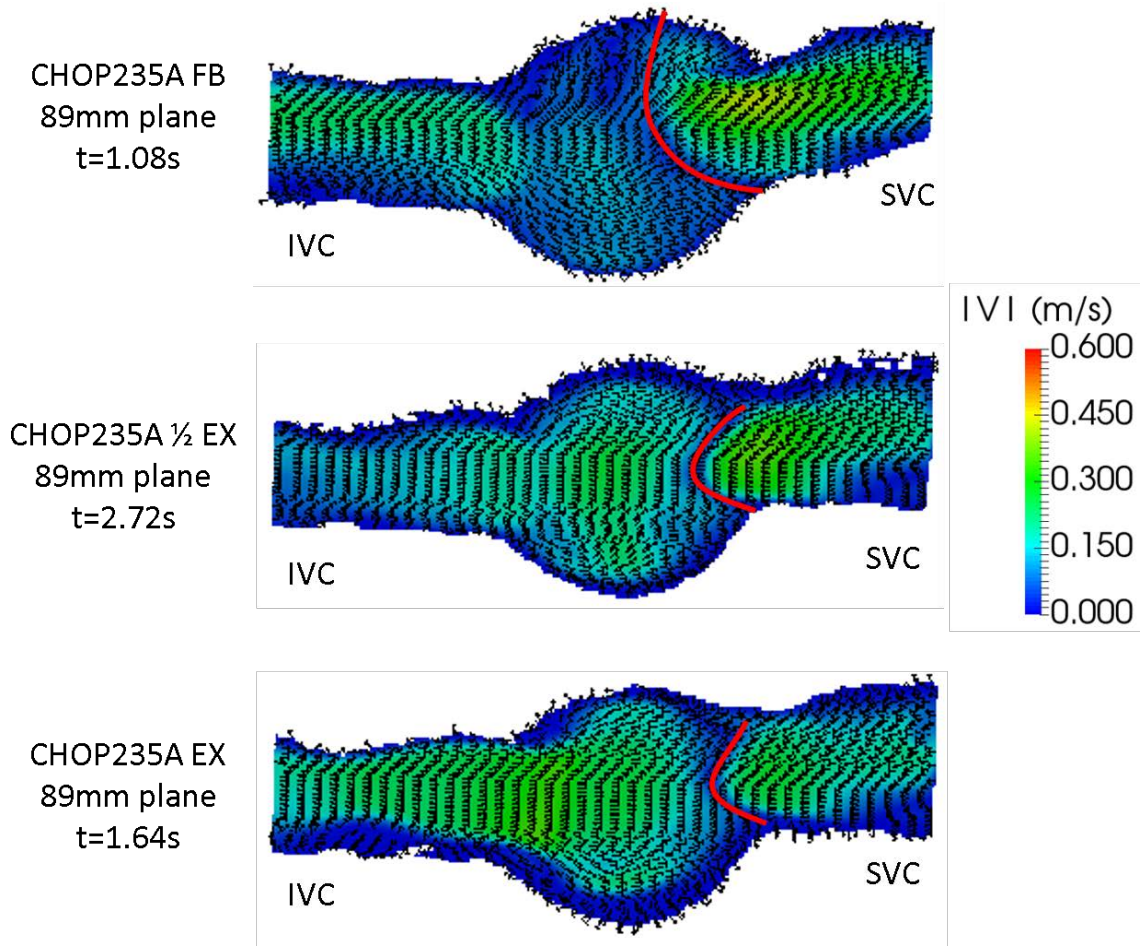

Figure 5-20: CHOP235A patient-specific FB, pulsatile half-peak EX, and patient-specific EX velocity fields at the 89mm plane and peak IVC flow rate time points. The black 3-component velocity vectors show velocity direction. The color provides the velocity magnitude.

5.4.1 Effect of Exercise on Power Loss

Comparison of $\dot{E_{app}}$ and iPL values for the patient-specific FB, patient-specific peak EX, and pulsatile half-peak EX conditions demonstrate the effect of exercise on power loss. Table 5-8 summarizes these values.

Table 5-8: Power loss values comparing FB and EX experimental conditions

Model	Condition		$\dot{E}_{app}$ (mW)	iPL (x10^6)
CHOP11B	FB	Patient-Specific	55.6 ± 9.7	418.6 ± 128.2
	EX	Half-Peak Pulsatile	96.6 ± 8.3	268.1 ± 70.9
		Peak Patient-Specific	278.5 ± 5.7	329.4 ± 82.6
CHOP235A	FB	Patient-Specific	33.8 ± 14.9	170.6 ± 79.6
	EX	Half-Peak Pulsatile	71.5 ± 9.8	185.3 ± 37.8
		Peak Patient-Specific	97.9 ± 17.1	170.6 ± 39.4

Consistent trends between both models include increasing apparent power loss from the patient-specific FB condition to the pulsatile half-peak EX condition, and a continued increase to the patient-specific peak EX condition. The same trend does not hold for indexed power loss values, which are shown further in Figure 5-21 and Figure 5-22.

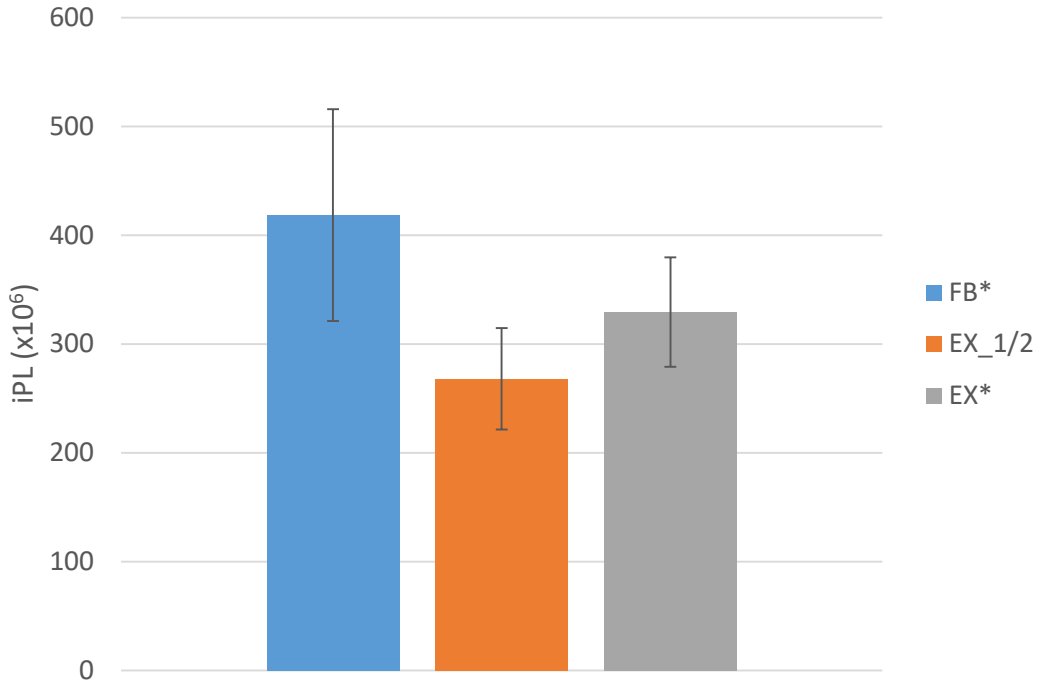

Figure 5-21: The effect of exercise on indexed power loss values for CHOP11B. The * denotes the patient-specific conditions. The error bars represent a 95% confidence interval.

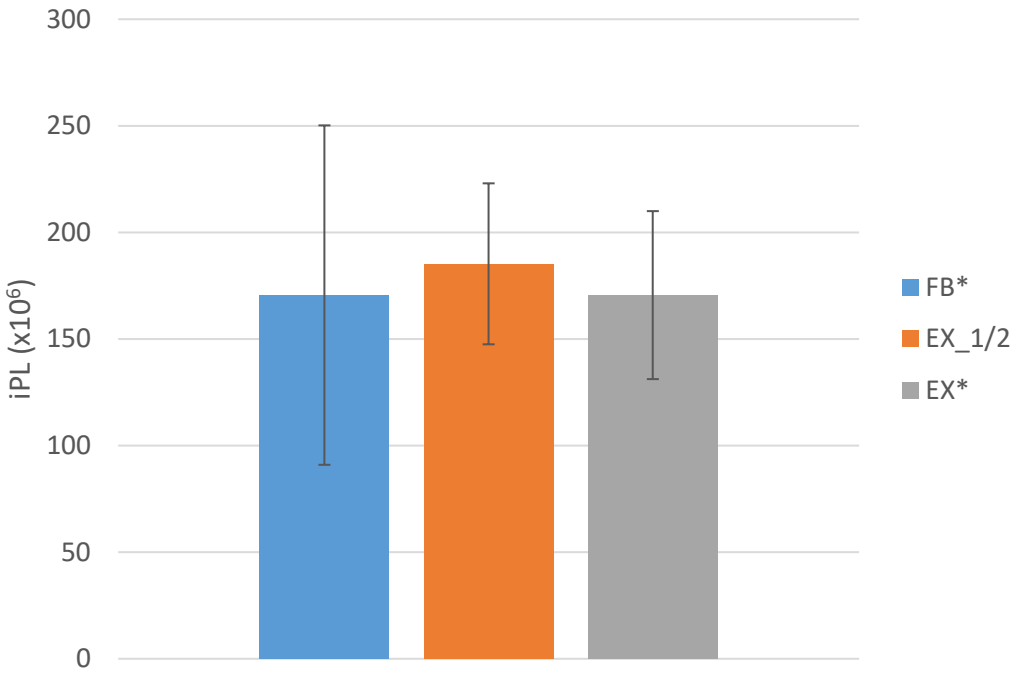

Figure 5-22: The effect of exercise on indexed power loss values for CHOP235A. The * denotes the patient-specific conditions. The error bars represent a 95% confidence interval.

5.4.2 Effect of Exercise on Viscous Dissipation

Table 5-9 summarizes the effect of exercise on viscous dissipation.

Table 5-9: The effect of exercise on viscous dissipation terms

Model	Condition		φ (1/s^2)	$i\varphi$ (x10^{12})
CHOP11B	FB	Patient-Specific	5586.53 ± 423.3	5.95 ± 0.77
	EX	Half-Peak Pulsatile	18850.3 ± 44.5	9.26 ± 0.97
		Peak Patient-Specific	33359.0 ± 527.2	9.30 ± 0.98
CHOP235A	FB	Patient-Specific	533.6 ± 9.0	0.41 ± 0.04
	EX	Half-Peak Pulsatile	742.4 ± 7.9	0.37 ± 0.04
		Peak Patient-Specific	807.9 ± 7.2	0.31 ± 0.03

Figure 5-23 and Figure 5-24 show the effect of exercise on indexed viscous dissipation for CHOP11B and CHOP235A, respectively.

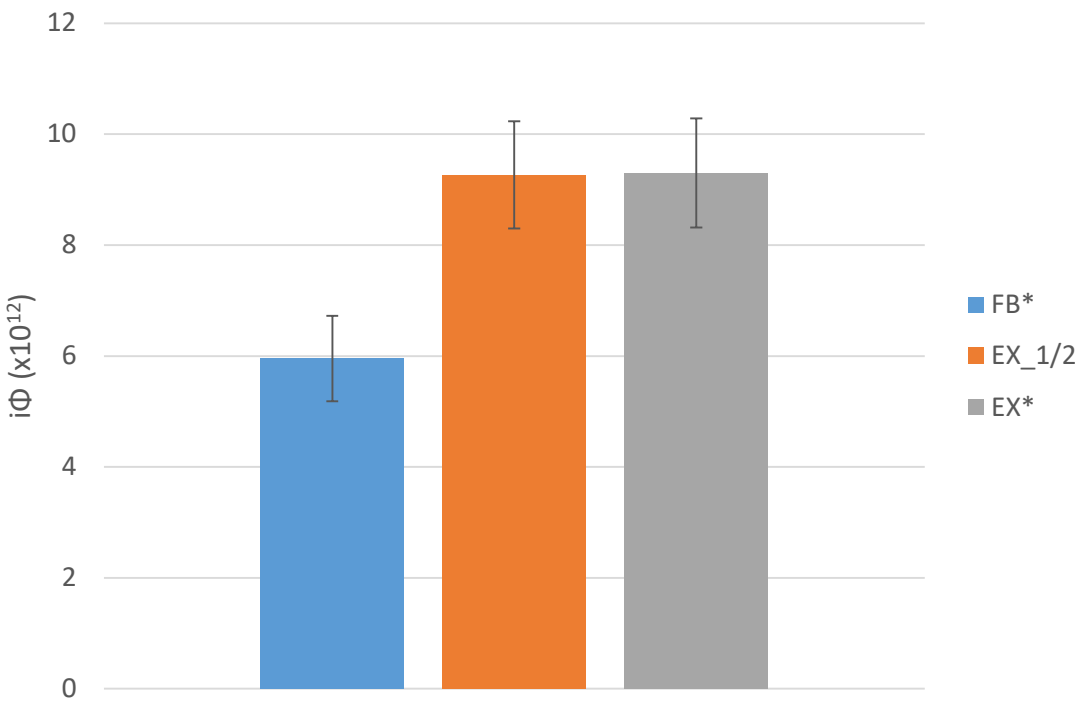

Figure 5-23: The effect of exercise on indexed viscous dissipation for CHOP11B. * denotes the patient-specific conditions. The error bars represent a 95% confidence interval.

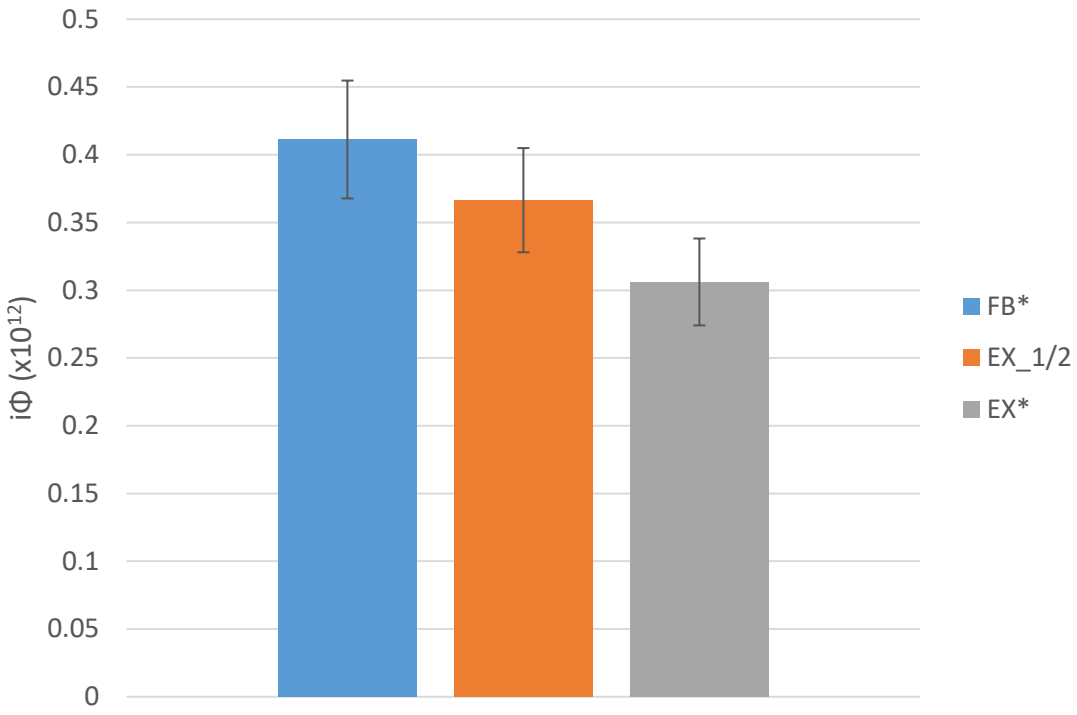

Figure 5-24: The effect of exercise on indexed viscous dissipation for CHOP235A. * denotes the patient-specific conditions. The error bars represent a 95% confidence interval.

5.4.3 Effect of Exercise on Hepatic Flow Distribution

Figure 5-25 and Figure 5-26 compare the HFD between the FB and EX experimental conditions for each model, which outlines the effect of exercise. Table 5-10 summarizes the effect of exercise on hepatic flow distribution.

Table 5-10: Effect of exercise on hepatic flow distribution

Model	Condition		HFD (%LPA)
CHOP11B	FB	Patient-Specific	49.78 ± 11.9
	EX	Half-Peak Pulsatile	45.45 ± 2.0
		Peak Patient-Specific	58.08 ± 5.3
CHOP235A	FB	Patient-Specific	40.60 ± 35.9
	EX	Half-Peak Pulsatile	20.51 ± 20.5
		Peak Patient-Specific	22.72 ± 22.7

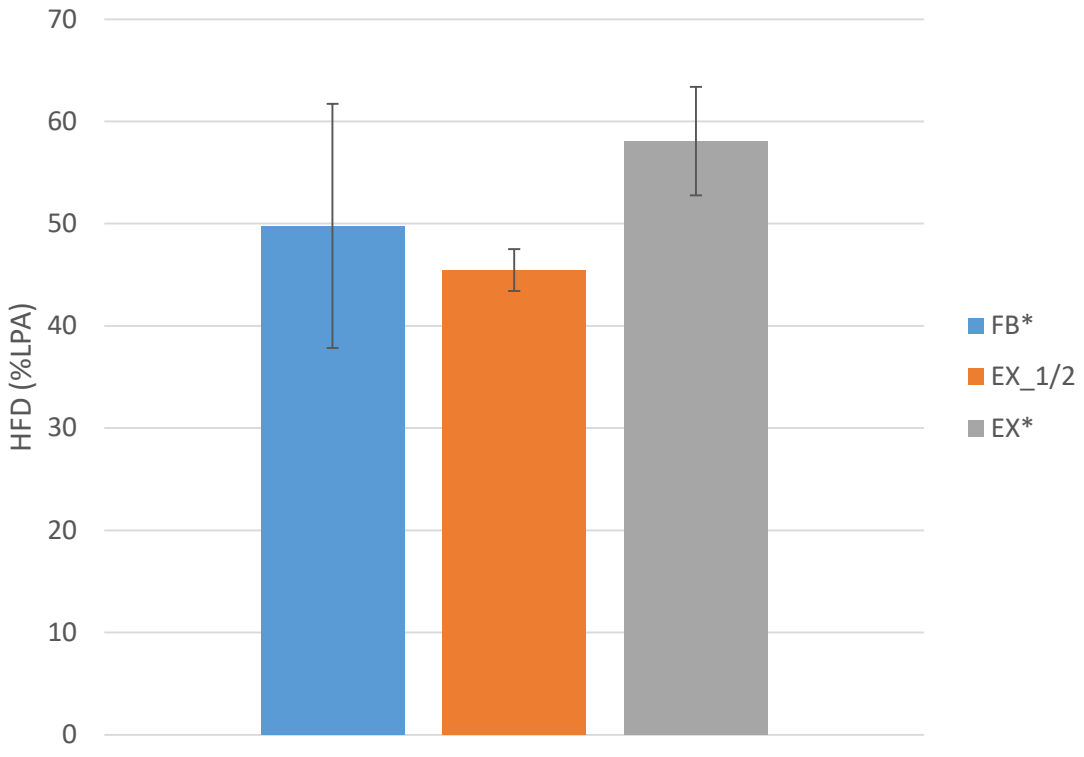

Figure 5-25: Effect of exercise on HFD for CHOP11B. * denotes the patient-specific conditions. The error bars represent a 95% confidence interval.

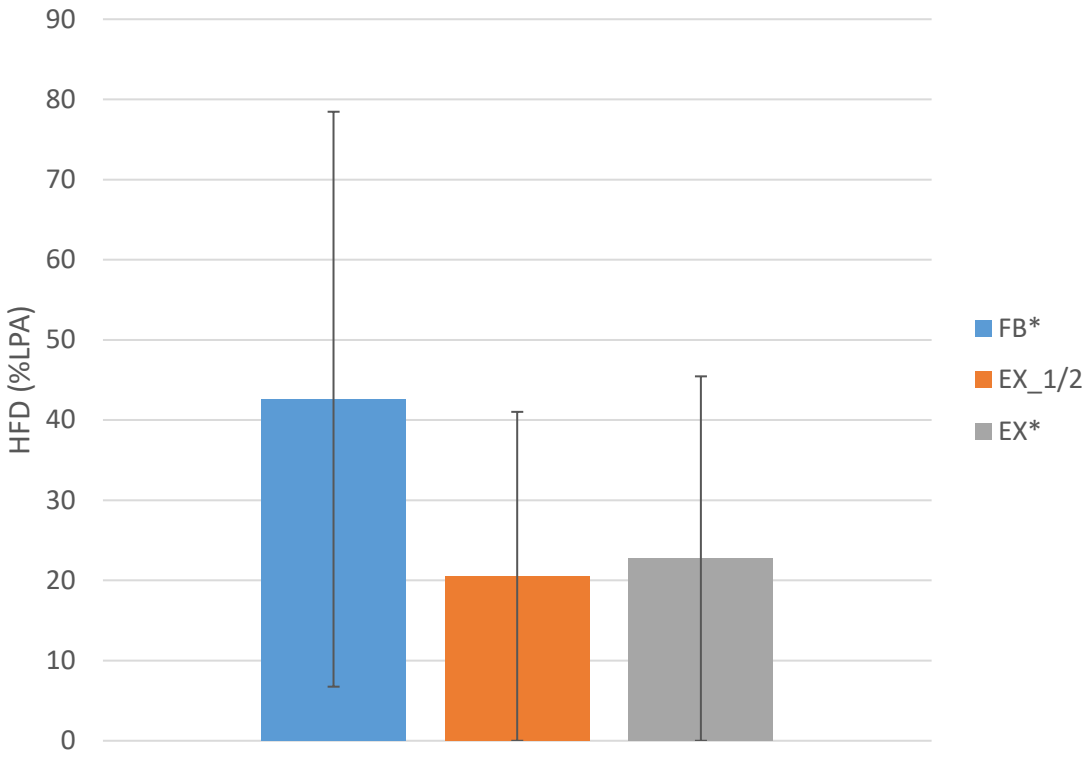

Figure 5-26: Effect of exercise on HFD for CHOP235A. * denotes the patient-specific conditions. The error bars represent a 95% confidence interval.

5.5 Effect of Pulsatility

The effect of pulsatility on Fontan hemodynamics is shown by comparing the BH steady, BH low pulsatility, BH patient-specific, and BH high pulsatility experimental conditions for both the CHOP11B and CHOP235A models. Metrics for each model are derived, in part, from the time-resolved three-dimensional velocity fields calculated from stereo PIV data. The CHOP11B velocity fields are shown in Figure 5-27, Video 5-9, Video 5-1 (section 5.3), and Video 5-10.

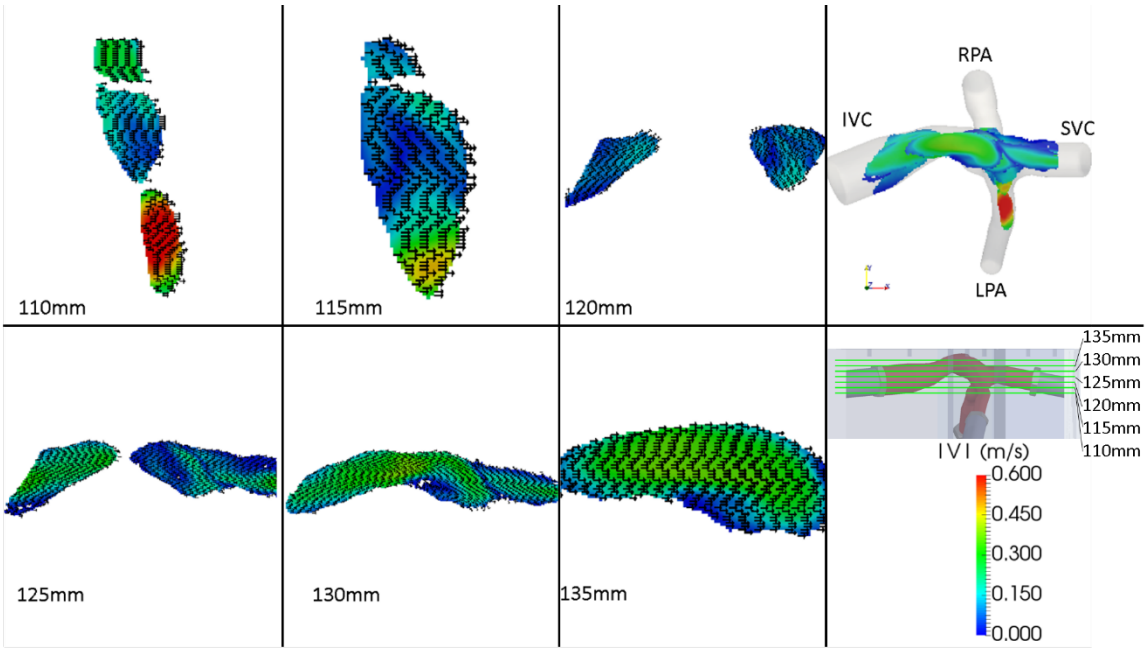

Figure 5-27: CHOP11B BH steady flow velocity fields denoted with velocity vectors and colored by velocity magnitude. The black 3-component velocity vectors show velocity direction. The color provides the velocity magnitude. The upper right panel is a coronal view of the Fontan model with all planes present.

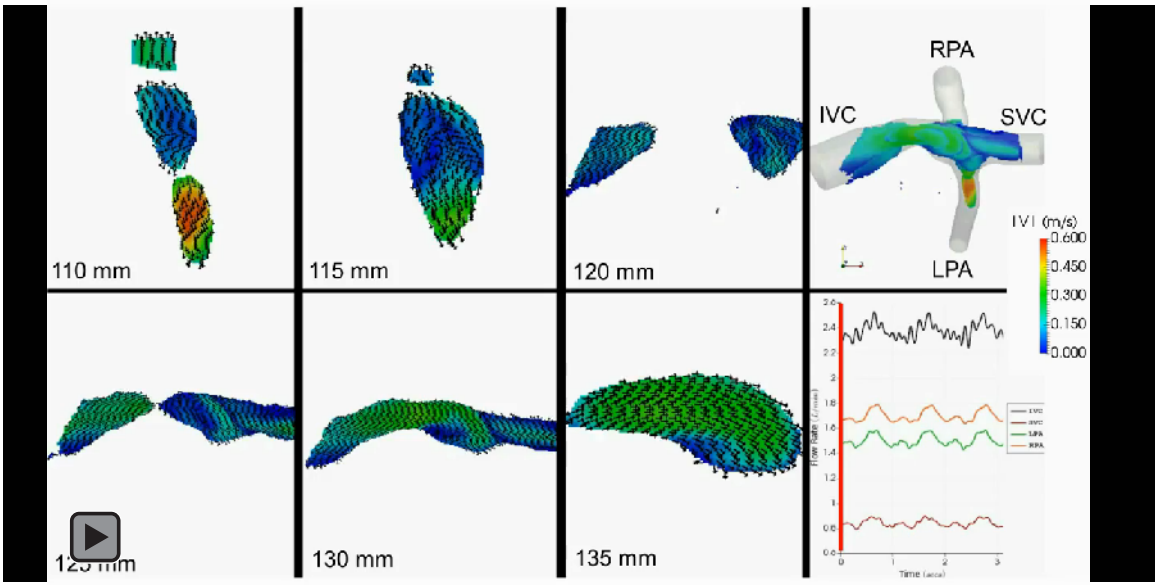

Video 5-9: CHOP11B BH low pulsatility velocity fields. The black 3-component velocity vectors show velocity direction. The color provides the velocity magnitude. The upper right panel is a coronal view of the Fontan model with all planes present.

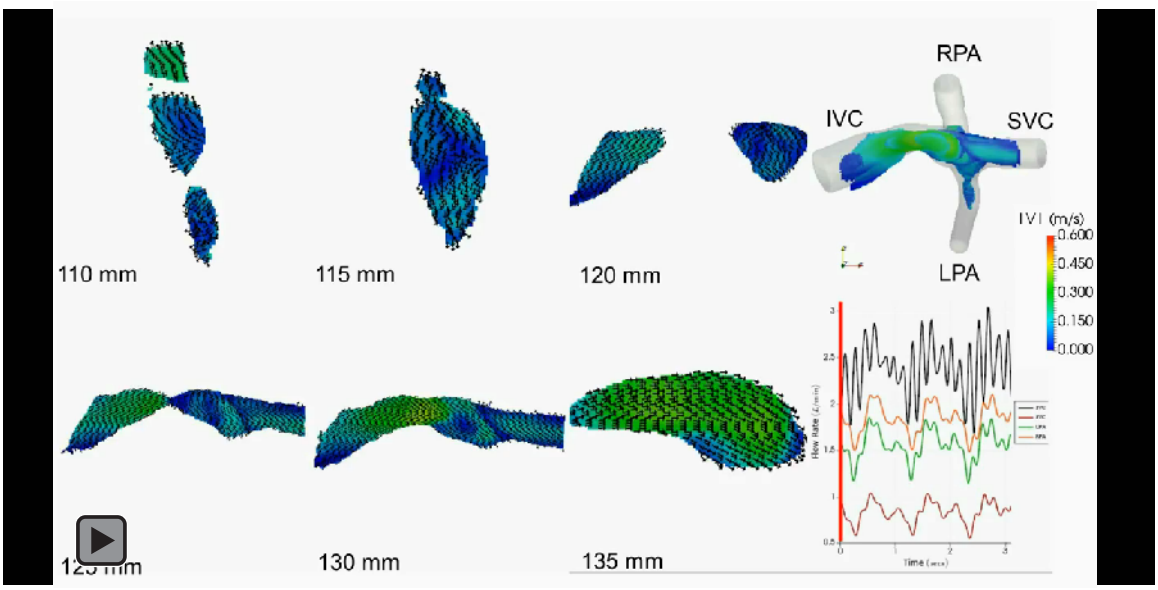

Video 5-10: CHOP11B BH high pulsatility velocity fields. The black 3-component velocity vectors show velocity direction. The color provides the velocity magnitude. The upper right panel is a coronal view of the Fontan model with all planes present.

Comparing the CHOP11B BH steady, CHOP11B BH low pulsatility, CHOP11B BH patient-specific, and CHOP11B BH high pulsatility velocity fields, little variation between the cases exists. The most prominent qualitative observation made is regarding the IVC-SVC collision line for the high pulsatility condition. Figure 5-28 and Figure 5-29 show the change in the shape of the line between the minimum and maximum peak IVC flow rate time points. This observation suggests that the high pulsatility case experiences the most unsteadiness at the center of the Fontan connection. The velocity magnitudes of all the conditions are very similar, with Figure 5-28 and Figure 5-29 showing the high pulsatility case as having greater velocity magnitude than the other cases as the IVC flow progresses into the center of the Fontan connection. Video observation highlights that the highest velocity magnitudes for all cases occurs in the LPA.

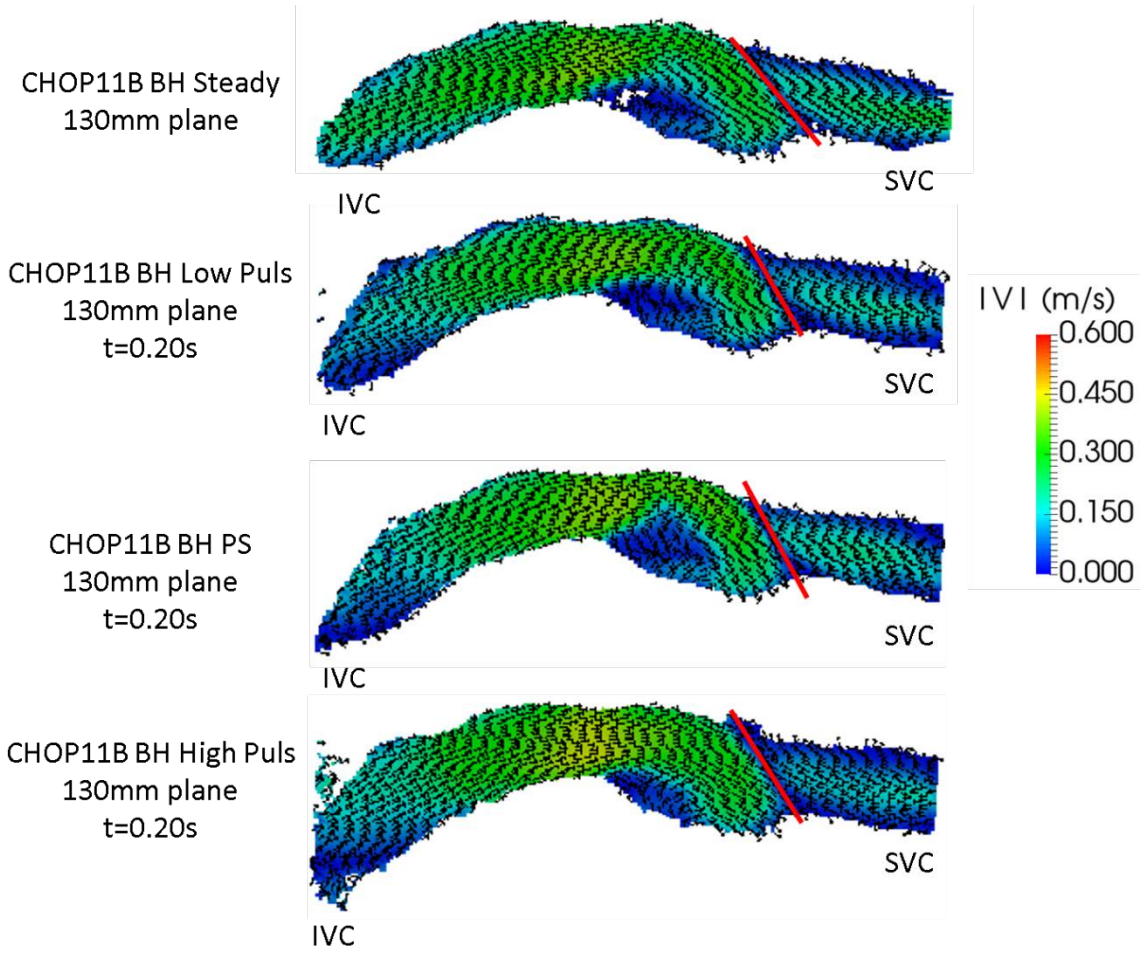

Figure 5-28: CHOP11B steady BH, low pulsatility BH, patient-specific BH, and high pulsatility BH velocity fields at the 130mm plane and minimum IVC flow rate time points. The black 3-component velocity vectors show velocity direction. The color provides the velocity magnitude.

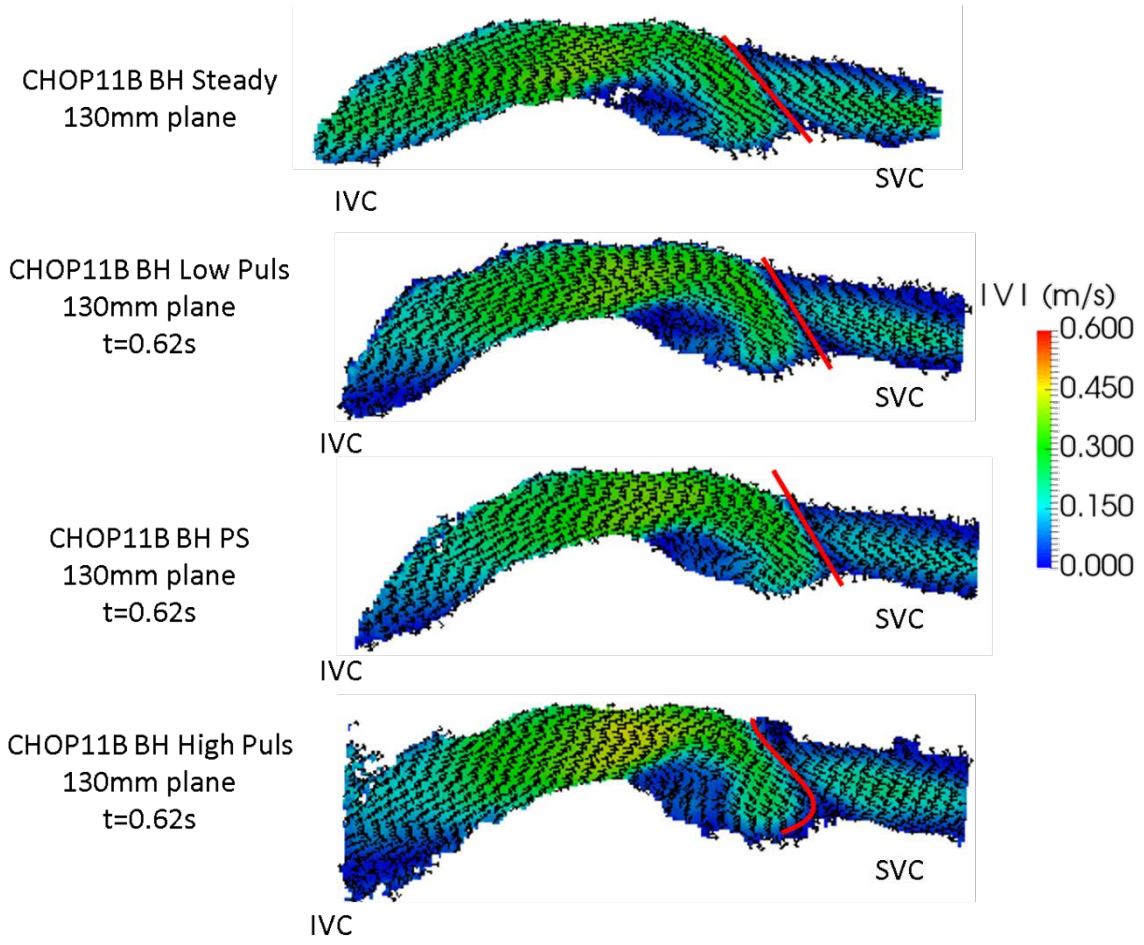

Figure 5-29: CHOP11B steady BH, low pulsatility BH, patient-specific BH, and high pulsatility BH velocity fields at the130mm plane and peak IVC flow rate time points. The black 3-component velocity vectors show velocity direction. The color provides the velocity magnitude.

The CHOP235A velocity fields are shown in Figure 5-30, Video 5-11, Video 5-3 (section 5.3), and Video 5-12.

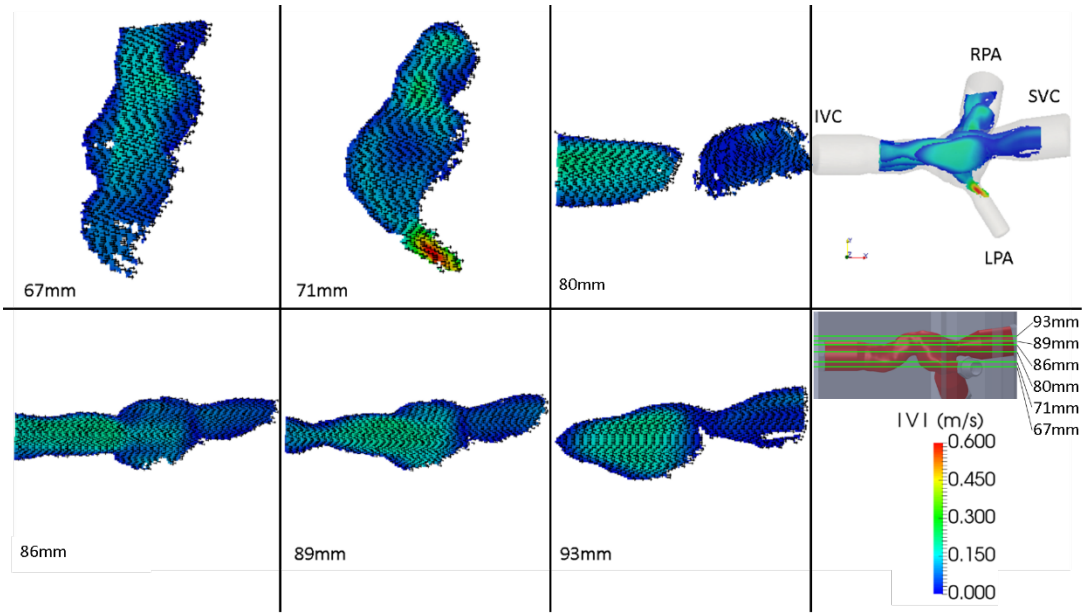

Figure 5-30: CHOP235A BH steady flow velocity fields denoted with velocity vectors and colored by velocity magnitude. The black 3-component velocity vectors show velocity direction. The color provides the velocity magnitude. The upper right panel is a coronal view of the Fontan model with all planes present.

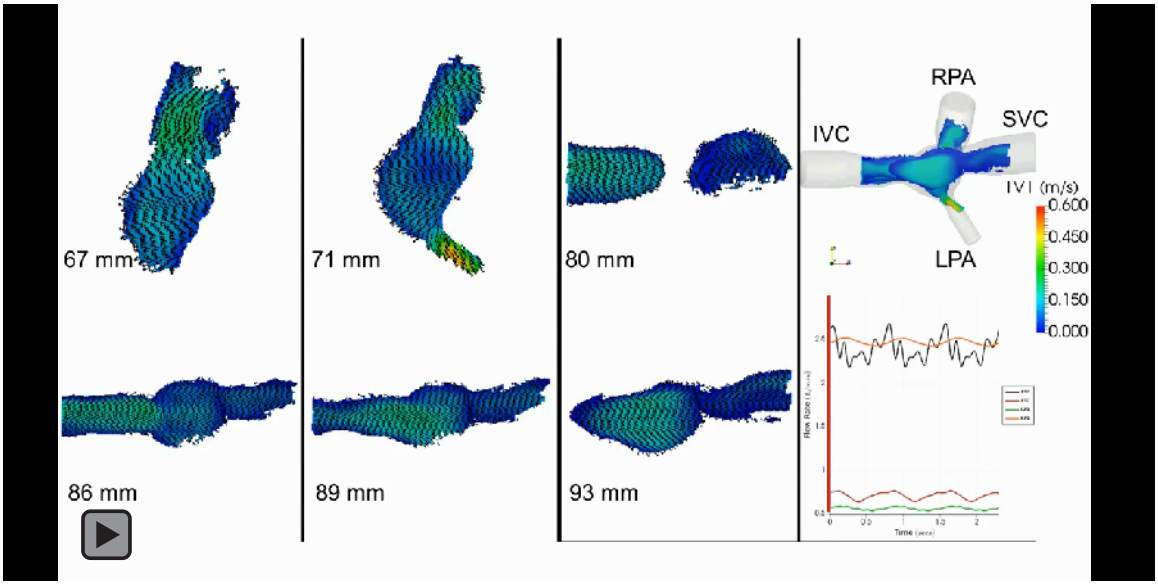

Video 5-11: CHOP235A BH low pulsatility velocity fields. The black 3-component velocity vectors show velocity direction. The color provides the velocity magnitude. The upper right panel is a coronal view of the Fontan model with all planes present.

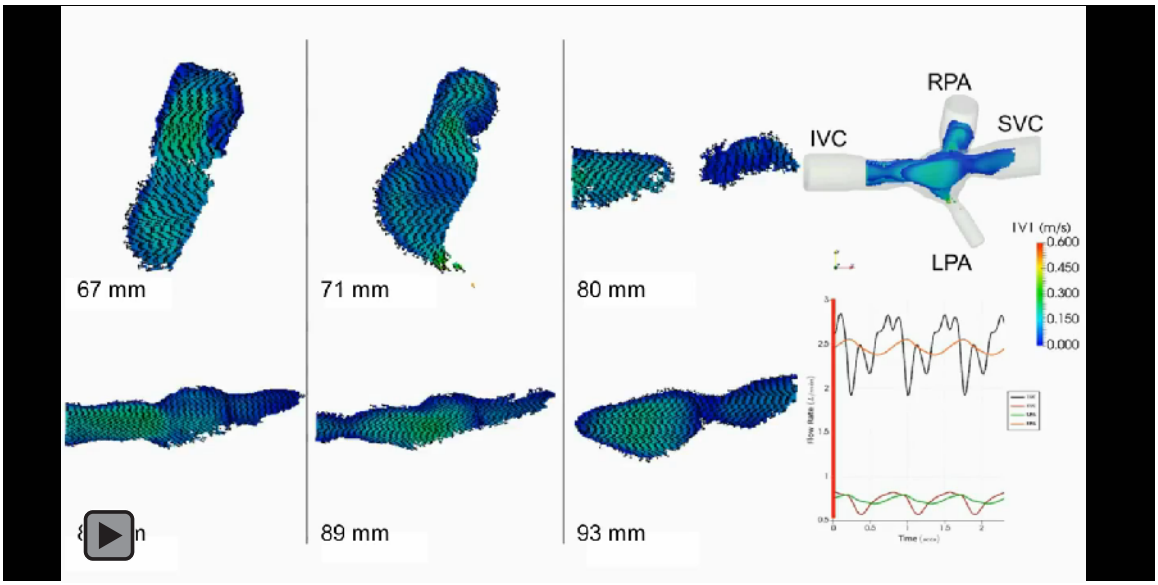

Video 5-12: CHOP235A BH high pulsatility velocity fields. The black 3-component velocity vectors show velocity direction. The color provides the velocity magnitude.

There appears no discernable qualitative difference between the IVC-SVC collision line of the CHOP235A cases shown in Figure 5-31 and Figure 5-32. In fact, when comparing the CHOP235A BH steady, CHOP235A BH low pulsatility, CHOP235A BH patient-specific, and CHOP235A BH high pulsatility velocity fields there is very little difference between any of them. This is in contrast to the CHOP11B cases, which see significant qualitative differences in the IVC-SVC collision line. This stands to reason, as the CHOP235A model compliance was greater, allowing for more pulsatile fluctuations to be absorbed by the model wall and reducing the pulsatility effect on the flow field. Table 11-7, a summary of the comprehensive experimental condition metrics, also shows that the IVC pulsatility range for the CHOP11B cases (0-57.5%) is greater than the IVC pulsatility range for the CHOP235A cases (0-38.6%). These differences also contribute to the lack of unsteadiness of the CHOP235A cases compared to the CHOP11B cases. Sections 5.5.1,

5.5.2, 5.5.3, and 6.5 provide further insight on the effect of pulsatility of Fontan hemodynamics.

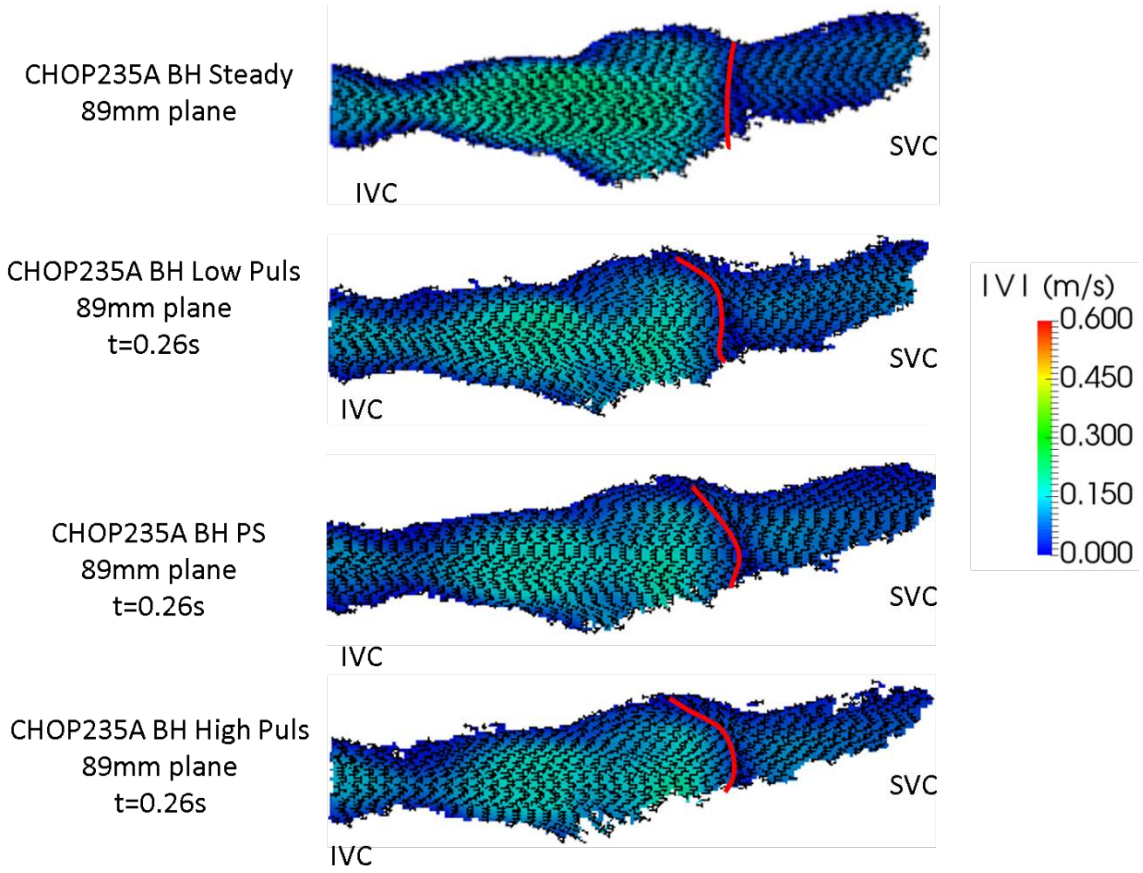

Figure 5-31: CHOP235A steady BH, low pulsatility BH, patient-specific BH, and high pulsatility BH velocity fields at the 89mm plane and minimum IVC flow rate time points. The black 3-component velocity vectors show velocity direction. The color provides the velocity magnitude.

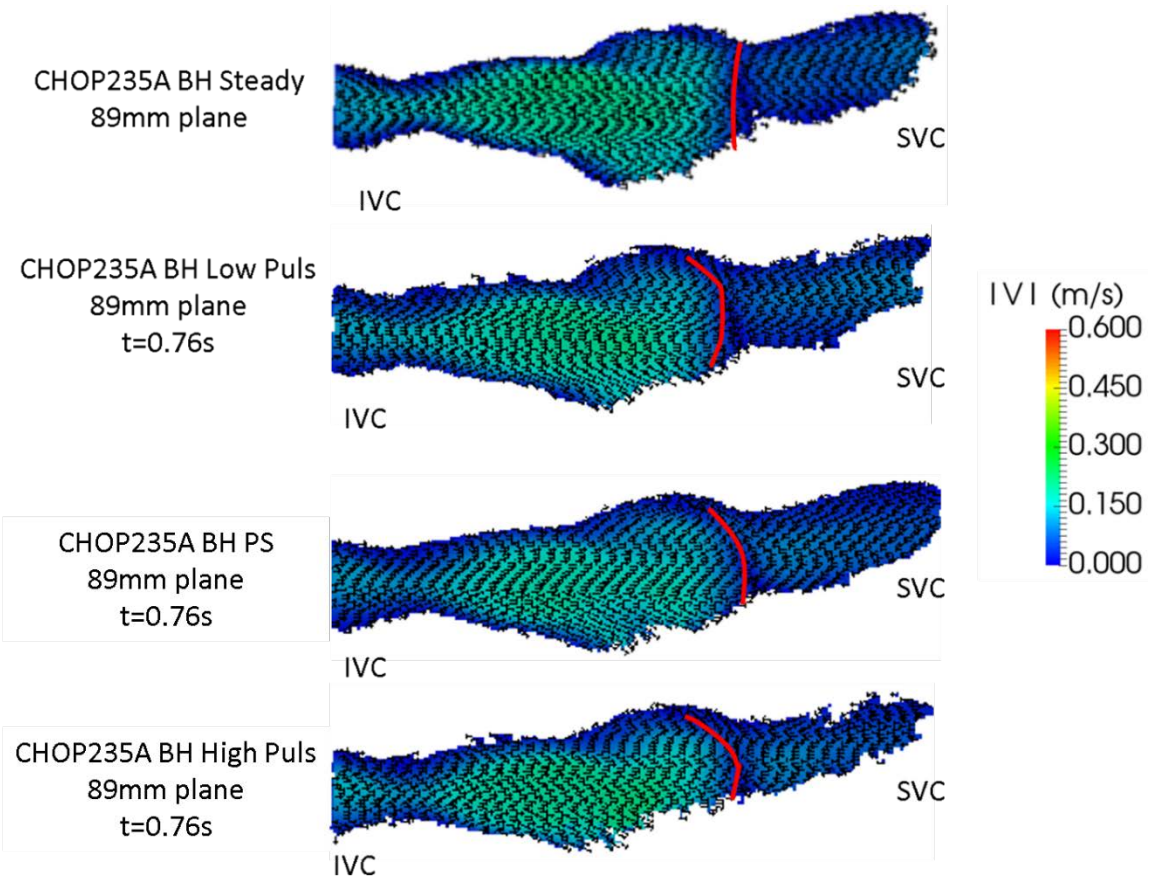

Figure 5-32: CHOP235A steady BH, low pulsatility BH, patient-specific BH, and high pulsatility BH velocity fields at the 89mm plane and peak IVC flow rate time points. The black 3-component velocity vectors show velocity direction. The color provides the velocity magnitude.

5.5.1 Effect of Pulsatility on Power Loss

Comparison of $\dot{E_{app}}$ and iPL values for all of the BH experimental conditions illustrates the effect of pulsatility on power loss. Table 5-11 summarizes these values.

Table 5-11: Power loss values for all BH experimental conditions

Model	Condition		$\dot{E}_{app}$ (mW)	iPL (x10^6)
CHOP11B	BH	Steady	6.9 ± 3.0	114.7 ± 57.3
		Low Pulsatility	7.2 ± 3.0	125.0 ± 60.8
		Patient-Specific	16.3 ± 5.9	290.3 ± 128.3
		High Pulsatility	20.6 ± 7.5	360.8 ± 159.7
CHOP235A	BH	Steady	8.8 ± 3.2	182.2 ± 71.8
		Low Pulsatility	9.9 ± 4.9	206.2 ± 107.9
		Patient-Specific	18.0 ± 4.6	374.0 ± 111.1
		High Pulsatility	26.9 ± 7.0	501.5 ± 150.8

Apparent power loss increases with pulsatility for both models, as does indexed power loss. The indexed power loss values are further shown in Figure 5-33 and Figure 5-34.

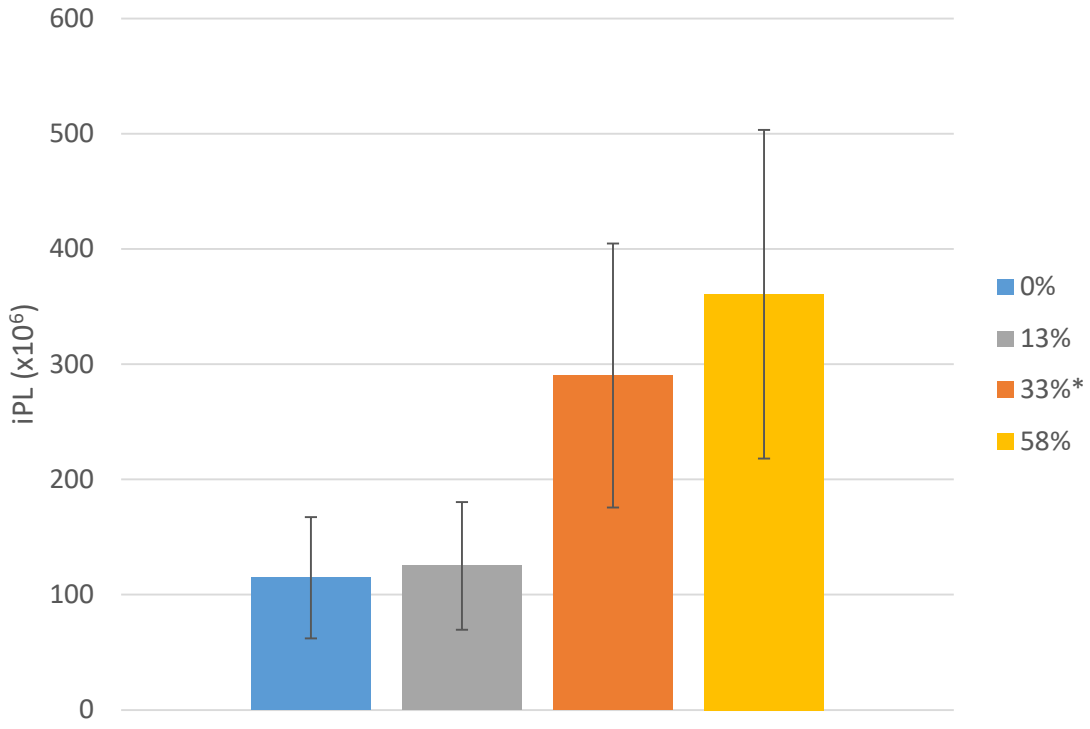

Figure 5-33: The effect of pulsatility on indexed power loss values for CHOP11B. * denotes the patient-specific condition. The error bars represent a 95% confidence interval.

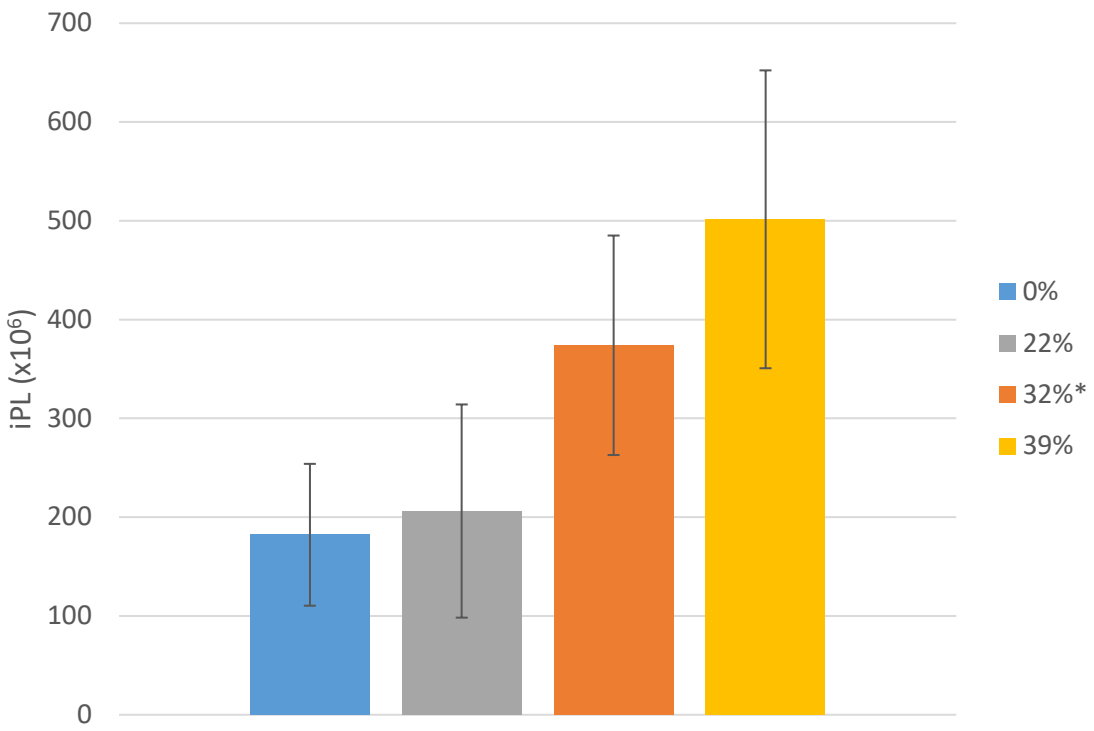

Figure 5-34: The effect of pulsatility on indexed power loss values for CHOP235A. * denotes the patient-specific condition. The error bars represent a 95% confidence interval.

5.5.2 Effect of Pulsatility on Viscous Dissipation

Table 5-12 summarizes the effect of pulsatility on viscous dissipation.

Table 5-12: The effect of pulsatility on viscous dissipation terms

Model	Condition		φ (1/s^2)	$i\varphi$ (x10^{12})
CHOP11B	BH	Steady	7442.6 ± 143.9	12.08 ± 1.28
		Low Pulsatility	5535.3 ± 48.9	9.28 ± 0.97
		Patient-Specific	6272.8 ± 280.6	10.66 ± 1.21
		High Pulsatility	7392.0 ± 347.3	12.43 ± 1.42
CHOP235A	BH	Steady	1225.4 ± 36.8	2.42 ± 0.26
		Low Pulsatility	743.6 ± 108.6	1.48 ± 0.26
		Patient-Specific	756.3 ± 28.4	1.49 ± 0.17
		High Pulsatility	789.0 ± 17.6	1.45 ± 0.16

Figure 5-35 and Figure 5-36 show the effect of exercise on indexed viscous dissipation for CHOP11B and CHOP235A, respectively.

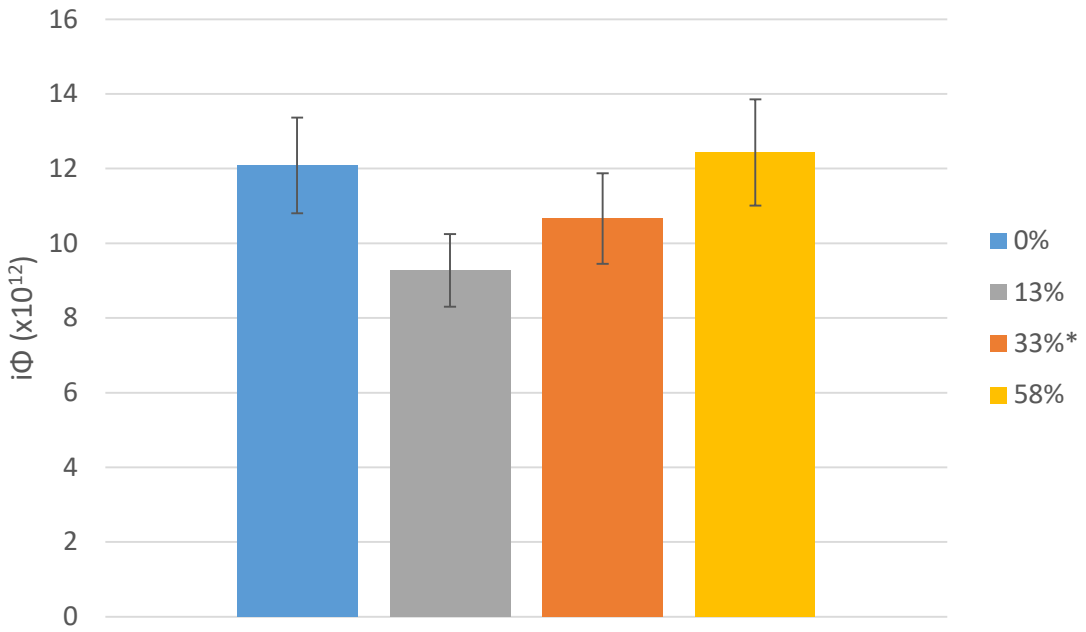

Figure 5-35: The effect of pulsatility on indexed viscous dissipation for CHOP11B. * denotes the patient-specific condition. The error bars represent a 95% confidence interval.

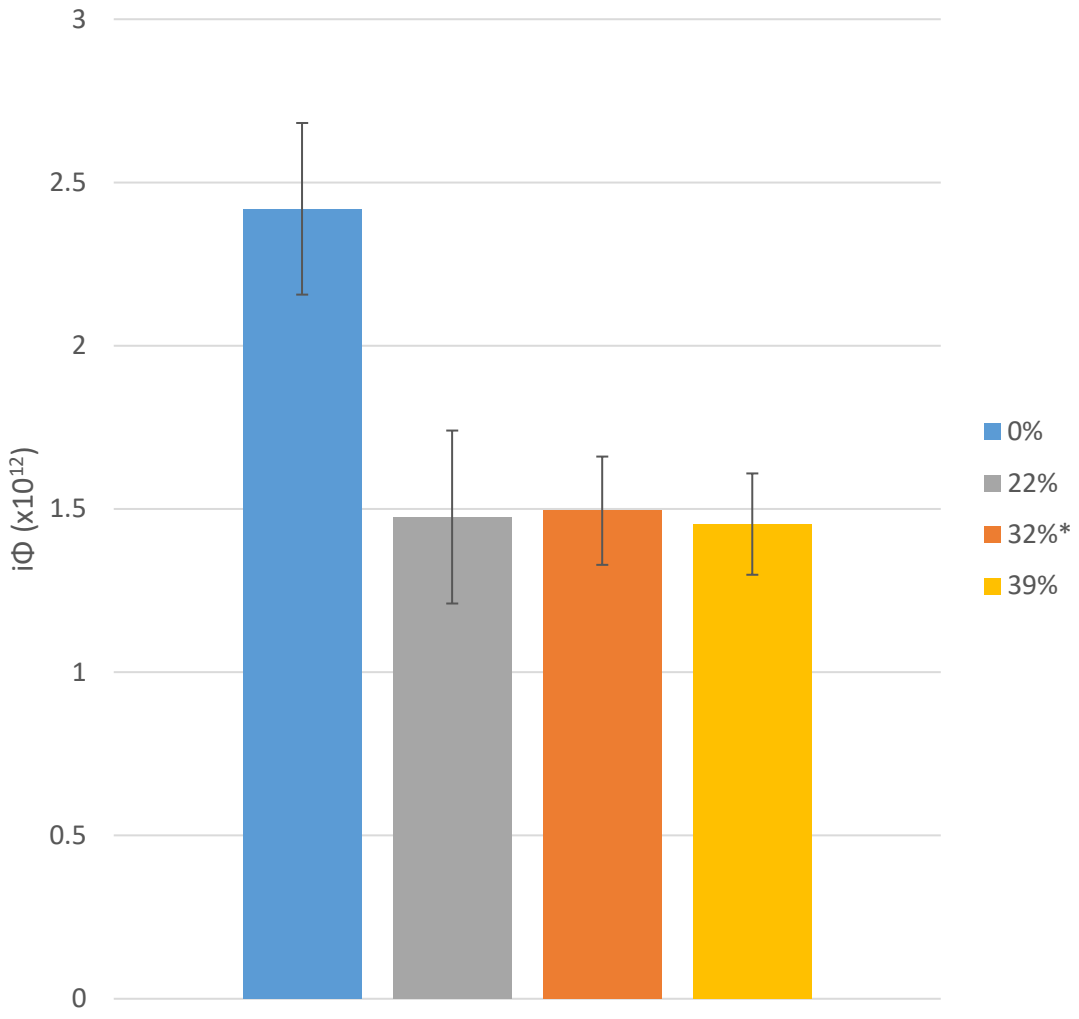

Figure 5-36: The effect of pulsatility on indexed viscous dissipation for CHOP235A. * denotes the patient-specific condition. The error bars represent a 95% confidence interval.

5.5.3 Effect of Pulsatility on Hepatic Flow Distribution

Figure 5-37 and Figure 5-38 compare the HFD between all BH experimental conditions for CHOP11B and CHOP235A, respectively. This comparison outlines the effect of pulsatility on hepatic flow distribution. Table 5-13 summarized the effect of pulsatility on HFD.

Table 5-13: The effect of flow pulsatility on hepatic flow distribution

Model	Condition		HFD (%LPA)
CHOP11B	BH	Steady	53.85 ± 8.9
		Low Pulsatility	71.94 ± 12.0
		Patient-Specific	61.06 ± 19.6
		High Pulsatility	56.49 ± 6.6
CHOP235A	BH	Steady	40.0 ± 25.7
		Low Pulsatility	58.93 ± 41.1
		Patient-Specific	54.96 ± 30.0
		High Pulsatility	63.86 ± 36.0

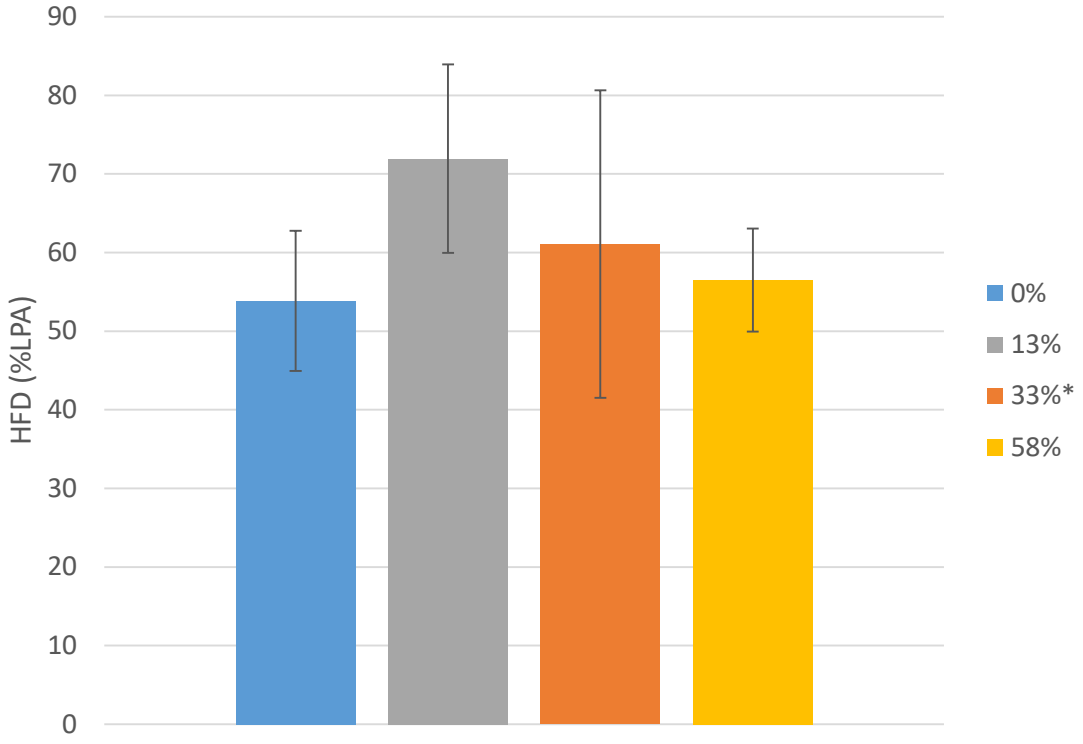

Figure 5-37: The effect of pulsatility on HFD for CHOP11B. * denotes the patient-specific condition. The error bars represent a 95% confidence interval.

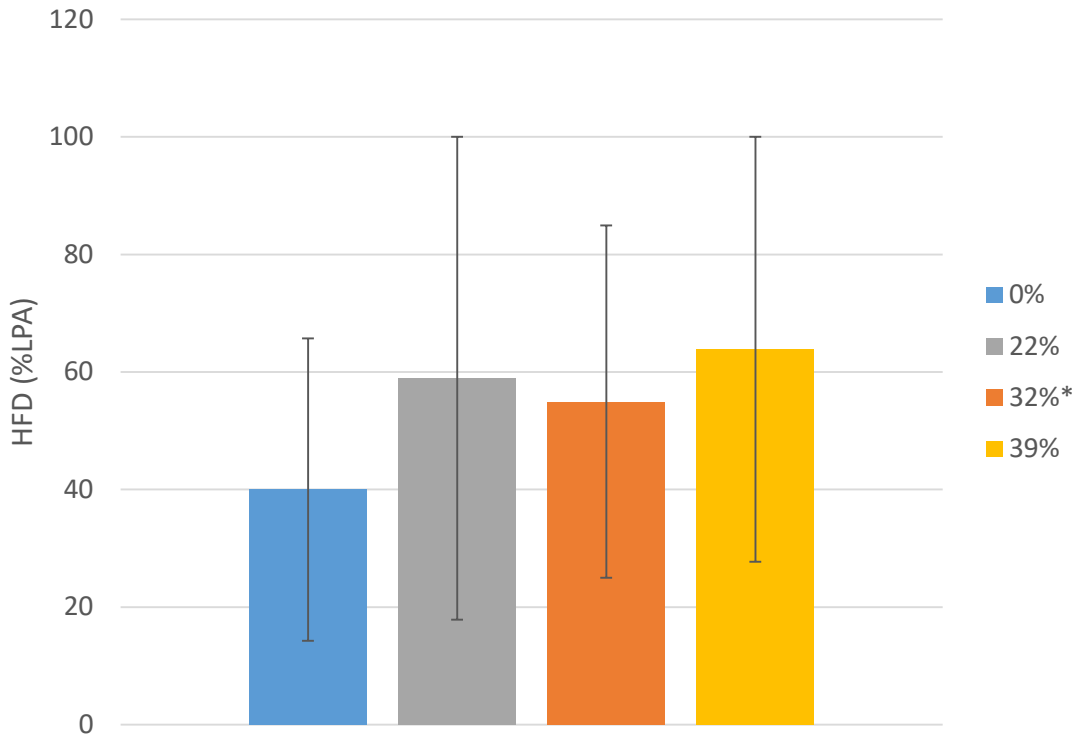

Figure 5-38: The effect of pulsatility on HFD for CHOP235A. * denotes the patient-specific condition. The error bars represent a 95% confidence interval.

6 DISCUSSION

6.1 *In Vitro* Fontan Circulation Model Verification

The *in vitro* Fontan circulation model results presented in section 5.1 show good agreement between the *in vivo* flow rates and the modeled flow rates for each condition tested, as well as matching of each model's compliance to its respective *in vivo* target compliance. The flow rate waveform agreement in section 5.1.1 is characterized using two metrics: a ratio of the average difference between the two waveforms to the time-averaged value of the two waveforms (ε_{avg}) and a time-normalized root mean square (ε_{rms}) only to fully characterize the error. The ratio of the average difference between the two waveforms to the time-averaged value of the two waveforms (ε_{avg}) provides time-independent information that can be used to compare error between conditions, but does not characterize the complete set of possible differences between two waveforms. For example, consider a 1 L/min steady flow rate waveform compared to a pulsatile flow rate waveform (i.e. sine curve) with a time-average value equal to 1 L/min. The average difference ratio value (ε_{avg}) between the two waveforms is 0, but the two waveforms are clearly different. In summary, the average difference ratio value (ε_{avg}) characterizes the bias between the two waveforms, and the time-normalized root mean square (ε_{rms}) quantifies how accurately the *in vitro* Fontan circulation model mimics patient-specific flow rate waveforms. The time-independent nature of ε_{rms} maintains its ability for cross-condition comparison.

No one vessel consistently demonstrated a lower average error than any other vessel across multiple experimental conditions, and there was no discernable pattern when examining the errors between conditions. In general, the EX conditions for both models

had higher ε_{rms} values, but the highest ε_{avg}values are found for the CHOP11B FB condition. Overall, the ε_{avg} values ranged from 2.7% for the CHOP235A BH RPA flow waveform to 15.9% for the CHOP11B FB SVC flow waveform. The ε_{rms} values ranged from 2.64 mL/s^2 for the CHOP11B BH SVC flow waveform to 28.78 mL/s^2 for the CHOP11B EX IVC flow waveform. Comparing the two models shows slightly better flow waveform agreement for the CHOP235A model than for the CHOP11B model. The average ε_{avg} and ε_{rms} values for CHOP235A across all vessels at all conditions was 6.6% and 9.52 mL/s^2, respectively. The average ε_{avg} and ε_{rms} values for CHOP11B across all vessels at all conditions was 9.2% and 11.40 mL/s^2, respectively.

Examination of the error results from the flow waveform verification suggests some insights. The fact that EX conditions had generally higher ε_{rms} values and that the EX conditions also had the highest flow pulsatilities suggests that ε_{rms} scales with flow pulsatility. However, the FB conditions had the next highest pulsatility values, but have generally lower ε_{rms} than BH conditions, so the relationship of ε_{rms} to flow condition must be multi-factorial. Overall, the observed errors are comparable to the 5% error reported for the only similar mock circulatory system reported in the literature [27]. The details of this system are provided in the subsequent paragraphs.

The TCPC model compliance verification results found in section 5.1.2 demonstrated good agreement between the *in vivo* patient-specific target and *in vitro* model compliance with a computationally-derived wall thickness. The TCPC model verification process included numerous steps out of necessity in order to properly verify the compliance value. The calculated *in vivo* target compliance values (Table 5-2), that were subsequently successfully matched by the *in vitro* TCPC models, have substantially higher compliance

than the only other known *in vitro* flexible TCPC model from Vukicevic et al [38]. Table 6-1 shows the compliance values for the TCPC models in this study compared to the study from Vukicevic et al.

Table 6-1: Compliance value comparison between this thesis and the only other known *in vitro* Fontan study that employed a patient-specific flexible TCPC model

Study	Model	Compliance (mL/mmHg)
Thesis	CHOP11B	1.36 ± 0.78
Thesis	CHOP235A	1.73 ± 0.99
Vukicevic et al	--	0.28

The only similar mock circulatory system that includes a patient-specific flexible TCPC model is the product of the Modeling of Congenital Hearts Alliance (MOCHA), a multi-institutional collaboration including experimental modeling, computational modeling, and clinical research experts. The system MOCHA employs is a physical lumped parameter model with 4 major branches of the circulatory system: the upper body, lower body, splanchnic, and pulmonary circulations (Figure 6-1).

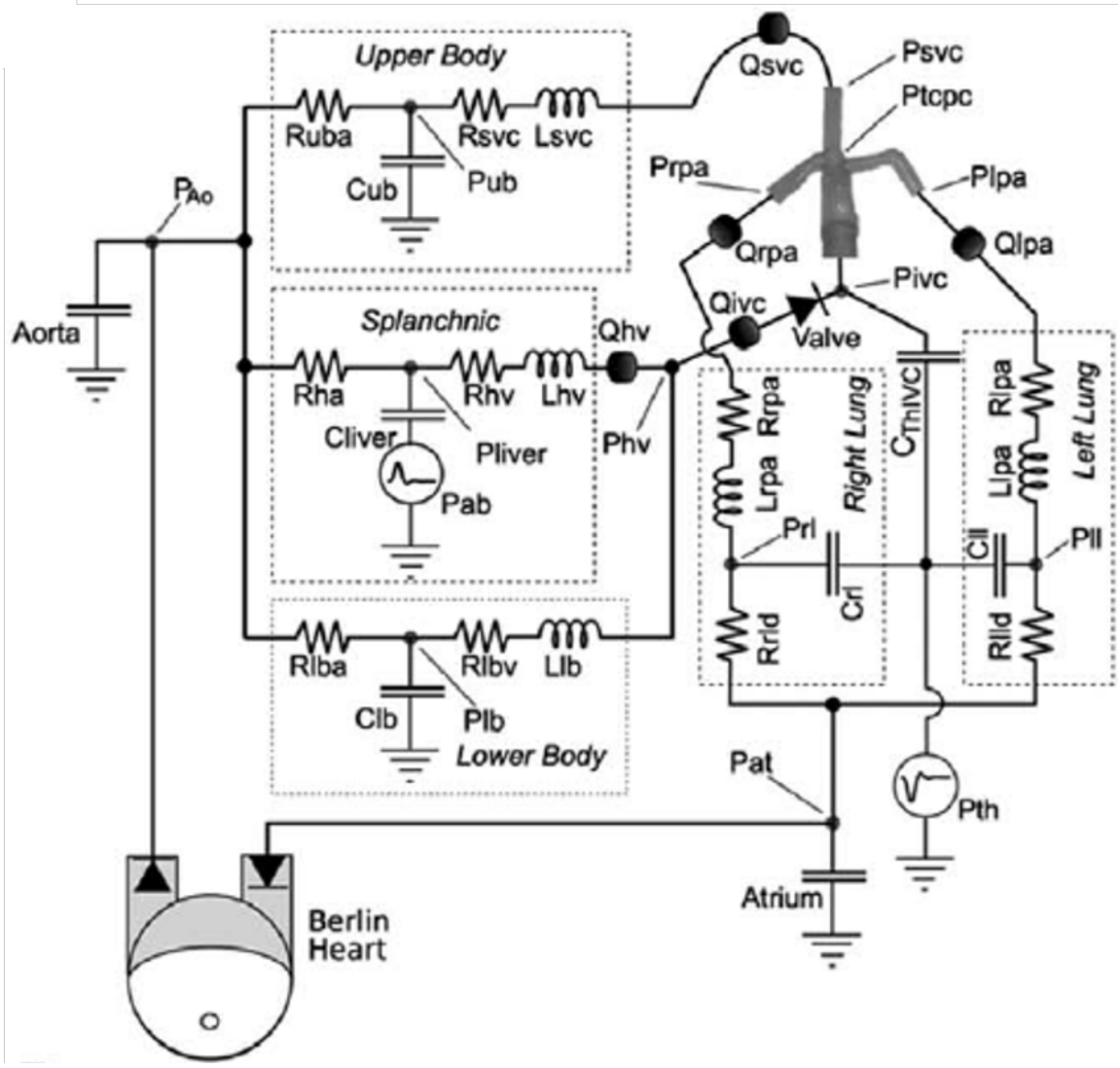

Figure 6-1: Schematic representation of MOCHA in vitro Fontan circulation model [38].

The MOCHA *in vitro* Fontan circulation model employs a Berlin Heart (Berlin Heart GmbH, Berlin, Germany) as the driving pressure to create an aortic waveform. The aortic waveform is then modified via resistance (R) and compliance (C) elements to create the necessary patient specific waveforms at the TCPC test section. Inertance (L) is shown in the schematic, but is affected only by the total mass of the modeling fluid. Flow changes due to thoracic pressure (Pth) are supplied via a pneumatic pump to the IVC, and are independent of the aortic flow provided by the Berlin Heart.

To date, studies from the MOCHA group's *in vitro* Fontan circulation model employed either rigid-walled TCPC models, or flexible TCPC models with arbitrary material properties [27,32,37,38]. The most recent study by Vukicevic et al sought to control retrograde flow in Fontan patients due to respiration effects with a one-way bioprosthetic valve [38]. The study employed a patient-specific flexible TCPC model, but the material properties / compliance value of the model is only stated, never justified:

> "*The TCPC test section is a patient-specific geometry based on MR images and realized using a thin-walled (1 ± 0.2 mm), compliant (C ~ 0.28 ml/mm Hg) silicone phantom (Shelley Medical Imaging, London, Ontario).*"

Without proper TCPC model compliance, the MOCHA group mock circulatory system matches pressure and flow waveforms by adjusting compliance values at other locations throughout the Fontan circulation model (i.e. Clb, Cliver). This allows the study to maintain TCPC model inlet and outlet pressure and flow waveform accuracy (global metrics), but does not guarantee an accurate internal TCPC flow field. The TCPC model verification methods outlined in the current thesis are an effort to establish both global and local flow accuracy.

The *in vivo* patient-specific TCPC volume vs time curves shown in Figure 5-3 and Figure 5-4 help to place the importance of proper TCPC compliance modeling in context. Examination of these figures reveals the average TCPC volume change over one cardiac cycle to be 2.4 mL. Based on the two available patient geometries, the relative range of this volume change is between 2.5 and 3.5% of the total TCPC volume. With such small dynamic change over a cardiac cycle, one might not expect large variations in the metrics calculated between steady and pulsatile flow conditions. Yet, large variations were found

to exist. Table 5-11, for example, shows a 136% change in apparent power loss and a 153% change in indexed power loss between the CHOP11B BH steady and CHOP11B BH patient-specific conditions. These large changes in flow-based metrics without significant TCPC deformation suggests that properly modeled compliance affects TCPC fluid dynamics more drastically than intuitive.

This fluid dynamic effect under different physiological and derived experimental conditions is the subject of discussion in sections 6.3, 6.4, and 6.5. These sections each show significant trends, which can only be considered as reliable as the accuracy of the *in vitro* Fontan circulation model employed. Ultimately, the addition of a compliance-verified flexible TCPC model to an *in vitro* Fontan circulation system is a novel step toward more accurate *in vitro* modeling. Though the TCPC does not deform a large percentage over a cardiac or respiratory cycle, the fluid dynamic effects are significant, and patient-relevant metrics are notably altered.

The potential impact of properly *in vitro* Fontan circulation modeling on the results found from studying the effects of respiration, exercise, and pulsatility on Fontan hemodynamics cannot be understated. Any limitations or inaccuracies found in the *in vitro* Fontan circulation model will be propagated to the hemodynamic results. These limitations are addressed in section 7.1, and should be carefully considered when drawing general conclusions from the results. Future studies should look to eliminate these limitations, where possible.

6.2 Experimental Conditions

The examination of the effects of respiration, exercise, and pulsatility on Fontan hemodynamics used patient-specific data acquired from MRI. Table 6-2 provides a summary of the experimental conditions collected, for clarity.

Table 6-2: List of experimental conditions collected during this study. Patient-specific conditions were based directly on MRI acquisitions, and are bolded.

Model	Condition	
CHOP11B	BH	Steady
		Patient-Specific
		Low Pulsatility
		High Pulsatility
	FB	Steady
		Patient Specific
	EX	Peak Steady
		Peak Patient-Specific
		Half-Peak Steady
		Half-Peak Pulsatile
CHOP235A	BH	Steady
		Patient-Specific
		Low Pulsatility
		High Pulsatility
	FB	Steady
		Patient Specific
	EX	Peak Steady
		Peak Patient-Specific
		Half-Peak Steady
		Half-Peak Pulsatile

By themselves, examination of the results collected from only the patient-specific experimental conditions allowed for understanding the effect of respiration and exercise on Fontan hemodynamics. However, studying only the patient-specific experimental conditions limits the study's ability to isolate flow field characteristics and assign physical reasoning to the changes in the calculated metrics. For example, power loss, viscous dissipation, and HFD changes due to respiration effects cannot be attributed to a single factor. The multiple factors involved include, but are not limited to: flow waveform

frequency content, flow waveform pulsatility, mean TCPC flow (sum of IVC and SVC flow), inflow ratio (ratio of IVC flow rate to SVC flow rate), and outflow ratio (ratio of LPA flow rate to RPA flow rate). In addition, each experimental condition is patient-specific, meaning that the changes in each of these factors between the BH and FB conditions for CHOP11B were not the same as the changes seen in these factors for CHOP235A.

In an effort to create more generalizable results and clarify the physical reasoning for the hemodynamic changes seen, several artificial physiological conditions were included in the study. These derived experimental conditions include both steady and pulsatile flow scenarios, and are also listed in Table 6-2. Adding these derived experimental conditions to the study allows for the isolation of pulsatility effects on Fontan hemodynamics, the results of which are more generalizable and have broader application. The effect of respiration and effect of exercise results remain patient-specific because the changes in flow metrics describing these physiological changes are patient-dependent. The additional experimental conditions, specifically the steady flow conditions, also provide a simpler flow field usable as a "first-step" CFD simulation validation.

6.3 Effect of Respiration

The effect of respiration on Fontan connection hemodynamics was evidenced by comparisons between the BH and FB patient-specific physiological conditions. as several studies exist reporting the role of respiration in Fontan hemodynamics [27,42,126,135] and on cardiac filling [41]. However, these studies report a global respiration effect (ratio of Fontan flow rates during inspiration to the expiration flow rate). In contrast, the current study examined the local effect of respiration physiology, and considered the cumulative

physiological change without separating the respiratory period into inspiration and expiration phases.

This local effect of respiration was quantified by the power loss, viscous dissipation, and hepatic flow distribution terms (indexed and non-indexed) described in section 4.2.2. All of the metrics are listed for 2 experimental conditions for each model: BH patient-specific and FB patient-specific. Comparing the BH and FB steady conditions isolates the effect of mean flow rate changes between the two physiological conditions. Comparisons between the BH and FB patient-specific cases include all physiological effects of respiration (flow rate changes, pulsatility changes, frequency content changes, etc.). The following paragraphs first identify the power loss, viscous dissipation, and hepatic flow distribution trends resulting from the effect of respiration. The results and trends are then compared to existing literature data. The final paragraphs give physical reasoning and explanation for the trends shown.

6.3.1 Data Trends

The apparent power loss ($\dot{E_{app}}$) and indexed power loss (iPL) metrics listed in Table 5-5 demonstrate observable an observable trend. The patient-specific FB $\dot{E_{app}}$ values are greater than the corresponding BH values for both models. However, the FB iPL values are not always greater than the BH iPL values, as CHOP235A shows a decrease in iPL from BH to FB conditions for both steady and patient-specific considerations.

The viscous dissipation term (φ) and indexed viscous dissipation term ($i\varphi$) listed in Table 5-6 also demonstrate trends. Both φ and $i\varphi$ show a consistent decrease from steady flow to the patient-specific condition across both models and during both BH and FB scenarios. Both φ and $i\varphi$ also show increased values during FB conditions when compared

to BH conditions during steady and patient-specific cases, except for the CHOP235A patient-specific comparison.

The hepatic flow distribution (HFD) metric shown in Figure 5-15 and Figure 5-16 shows a consistent decrease in percent hepatic flow to the LPA from the patient-specific BH condition to the patient-specific FB condition.

6.3.2 Literature Comparison

Of the metrics calculated in this study (power loss, viscous dissipation, and hepatic flow distribution), only the power loss metric has been quantified for changes dues to respiration to date in the literature. Liu et al report a 150% increase in apparent power loss when respiration is added to a single rigid-wall CFD simulation [124]. This result is consistent with this study's trend. Though not peer-reviewed, the PhD dissertation by Tsz Ling Elaine Tang directly compared apparent power loss and indexed power loss values from 9 CFD simulation that used patient-specific pulsatile flow boundary conditions and patient-specific rigid-wall Fontan connection anatomies [143]. Tang found that free-breathing apparent power loss values exceeded breath-held apparent power loss for each of the 9 patient simulated. This finding is consistent with the results from this study. Tang also found that indexed power loss was not consistently higher or lower when respiration was added; another trend consistent with the data from this study. Other contemporary studies include power loss calculations while simulating or modeling Fontan connection flows under free-breathing conditions, but do not directly compare the effect of respiration on power loss [15,44,45]. The order of magnitude of the apparent power loss values found in these studies coincides with the results from this study. Overall, the data from this study compares well with data from the literature.

6.3.3 Physical Reasoning

Table 6-3 provides a comprehensive view of the experimental conditions used for this comparison, and can be used to assess reasoning behind the power loss, viscous dissipation, and hepatic flow distribution trends previously noted.

Examination of the table shows an interesting comparison between the BH and FB conditions. Four metrics ($\dot{E_{app}}$, iPL, φ, and $i\varphi$) all increasing in value from BH to FB conditions, except for iPL and $i\varphi$ during the CHOP235A BH to FB transition. Examination of Table 6-3 shows that FB conditions have higher mean inflow rates than BH conditions, and consistent flow ratios (both IVC:SVC and LPA:RPA) except when comparing the CHOP235A BH and FB IVC:SVC flow ratio. Adding to this fact the knowledge that the iPL and $i\varphi$ are indexed to account for changes in mean inflow rate suggests a fundamental difference in the CHOP235A BH and FB flow fields. The change in IVC:SVC flow ratio between these conditions suggests a shift in the collision point of the inflowing flow streams relative to the TCPC geometry which creates less flow power lost and less energy dissipated due to viscosity.

The decreasing HFD trend from the patient-specific BH to the patient-specific FB is counter-intuitive when the experimental conditions are considered because the LPA:RPA flow ratio increases under these same conditions for both models. The CHOP11B model increases from 45.9% to 56.4%, and the CHOP235A model LPA:RPA flow ratio increases less, from 23.0% to 25.3%. These model flow ratio increases may not be practically different when flow rate measurement uncertainties are considered. Regardless, with more of the total flow exiting through the LPA, one would think that a higher percent of the IVC flow (HFD) would traverse this path as well. However, the data

shows otherwise. This counterintuitive result is easily explained for the CHOP235A model by a drastic decrease in IVC:SVC flow ratio. The change in IVC:SVC flow ratio for CHOP235A from the patient-specific BH to the patient-specific FB condition is from 76.8% to 43.8%. Using these values and the mean inflow rate for the same conditions we see that the mean IVC flow *decreases* between the BH and FB condition, even though the total mean inflow rate *increases*. At the same time, the SVC flow drastically increases, shifting the mass balance between the two inflow streams and causing the counterintuitive result. The changes between patient-specific BH and FB conditions for CHOP11B are less dramatic, yet it still shows the same decrease in HFD with an increase in LPA:RPA flow ratio. This result is not uncommon, and simply shows that HFD is a Lagrangian metric manifest as the accumulation of the entire velocity vector field time history [144]. Time-averaged experimental condition parameters do not capture this time history, so using them to predict or understand HFD results should be done with caution.

Table 6-3: Comprehensive experimental conditions summary for the effect of respiration on Fontan hemodynamics.

Model	Condition		Mean Inflow Rate (IVC+SVC) (L/min)	IVC:SVC Flow Ratio (%)	LPA:RPA Flow Ratio (%)	IVC Pulsatility (%)
CHOP11B	BH	Patient-Specific	3.2	75.1	45.9	33.4
	FB	Patient-Specific	4.04	76.3	56.4	84.8
CHOP235A	BH	Patient-Specific	3.10	76.8	23.0	31.9
	FB	Patient-Specific	4.96	43.8	25.3	115.2

6.4 Effect of Exercise

The effect of exercise on Fontan connection hemodynamics is shown by comparison between the FB and EX patient-specific and derived physiological conditions. It is well known that Fontan patients experience lower exercise capacity than their healthy peers, with reasons attributed to reduced cardiorespiratory functional capacity [43,48,71,128,145]. Yet few studies have closely examined the local TCPC velocities during exercise, with the hope that improved surgical and medical techniques may improve Fontan patient exercise capacity. The comparison of patient-specific FB, pulsatile half-peak EX, and patient-specific peak EX experimental conditions include all the physiological changes that occur during exercise. These physiological changes include, but are not limited to: mean flow rate, flow rate peak frequency, flow rate frequency content, flow rate pulsatility, IVC:SVC flow ratio, and LPA:RPA flow ratio. The following paragraphs first identify the power loss, viscous dissipation, and hepatic flow distribution trends resulting from the effect of exercise comparison conditions. The results and trends are then compared to existing literature data. The final paragraphs give physical reasoning and explanation for the trends shown.

6.4.1 Data Trends

The apparent power loss metric listed in Table 5-8 includes a consistent trend. The $\dot{E_{app}}$ values increased consistently from the FB patient-specific condition to the half-peak pulsatile EX condition, and from the half-peak pulsatile EX condition to the peak patient-specific EX condition. However, iPL, which accounts for differences in mean flow and patient-size, did not show any consistent trend, much less the same trend as $\dot{E_{app}}$.

The viscous dissipation term (φ) listed in Table 5-9 showed the same trend as that seen by $\dot{E_{app}}$ in Table 5-8; both values increase consistently from the FB patient-specific condition to the half-peak pulsatile EX condition, and from the half-peak pulsatile EX condition to the peak patient-specific EX condition.

The hepatic flow distribution (HFD) metric shown in Figure 5-25 and Figure 5-26 shows no consistent trend with changes in exercise intensity.

6.4.2 Literature Comparison

Of the three metrics calculated in this study, only changes in power loss due to exercise effects is also present in the current literature. Marsden et al report the apparent power loss calculated for two patients whose hemodynamics are simulated using computational fluid dynamics with rigid wall boundary conditions [15]. The study simulates a resting, free-breathing condition with a mean IVC flow rate equal to 1.2 L/min, and then increases IVC flow rate by increments of 1.2 L/min for each of three different exercise levels (light exercise, moderate exercise, and heavy exercise). Cardiac and respiratory frequency are also increased during the exercise simulations. Table 6-4 shows the results from the Marsden et al study.

Table 6-4: The effect of exercise level on apparent power loss from Marsden et al [15]

Exercise Level	Patient A $\dot{E}_{app}$ (mw)	Patient B $\dot{E}_{app}$ (mw)
Rest	6.7	13.9
Light Exercise	19.5	51.6
Moderate Exercise	44.8	87.4
Heavy Exercise	89.3	169.4

The apparent power loss results from Marsden et al are of the same order of magnitude with this study's apparent power loss values, and also agree with this study's apparent power loss trends.

PhD thesis work by Tang compared Fontan connection anatomy metrics to apparent power loss and indexed power loss values calculated from steady flow rigid-wall CFD simulations for both rest and exercise mean flow rates. Of the two cohorts used, 11 patients were the same between the same between the steady FB and steady EX simulations. Comparing these results showed that steady FB apparent power loss was less than steady EX apparent power loss for each patient. Indexed power loss did not hold the same trend. Four of the 11 patients showed a decrease in indexed power loss the steady FB simulation to the steady EX simulation. These trends hold with the data shown in this study.

Overall, the data shown in this study compares well with data from the literature.

6.4.3 Physical Reasoning

Table 6-5 provides a comprehensive view of the experimental conditions used for the effect of exercise comparison. Examination of these experimental conditions can be used to assess some reasoning behind the power loss and viscous dissipation.

The $\dot{E_{app}}$ trend where values increase consistently from the FB patient-specific condition to the half-peak pulsatile EX condition, and from the half-peak pulsatile EX condition to the peak patient-specific EX condition corresponds to increasing mean inflow rates (cardiac output) for the same conditions, across both models. Thus, the increase in mean inflow rate seems the most likely candidate to explain this increase in apparent power loss. Likewise, the φ trend, which follows the same pattern, can be attributed to changes in the mean inflow rate (cardiac output) as well.

No other power loss, viscous dissipation, or hepatic flow distribution trends hold with any IVC:SVC flow ratio, LPA:RPA flow ratio, or IVC pulsatility trends shown in Table 6-5. This suggests that the changes in power loss, viscous dissipation, and hepatic flow distribution functions of a single experimental condition variable. Instead, it is more likely that these hemodynamic metrics are results of a multi-variate cumulative effect which may not even be limited to the experimental condition variables listed. Other factors could include biological changes due to increased exercise intensity (vascular resistance changes, oxygen consumption levels, etc.)

That being said, there is an interesting trend within the experimental condition variables alone. As the IVC:SVC flow ratio increases the LPA:RPA flow ratio decreases for the CHOP11B model. This same trend does not hold for CHOP235A, and suggests something about the CHOP11B geometry and fluid dynamics which encourages IVC flow to proceed down the RPA.

Table 6-5: Comprehensive experimental conditions summary for the effect of exercise on Fontan hemodynamics.

Model	Condition		Mean Inflow Rate (IVC+SVC) (L/min)	IVC:SVC Flow Ratio (%)	LPA:RPA Flow Ratio (%)	IVC Pulsatility (%)
CHOP11B	FB	Patient-Specific	4.04	76.3	56.4	84.8
	EX	Peak Patient-Specific	7.90	79.3	43.1	101.1
		Half-Peak Pulsatile	5.95	77.8	46.1	93.4
CHOP235A	FB	Patient-Specific	4.96	43.8	25.3	115.2
	EX	Peak Patient-Specific	7.08	48.2	25.3	126.4
		Half-Peak Pulsatile	6.20	47.4	25.1	118.4

The power loss data shown here are in agreement with previous data from the Georgia Tech Cardiovascular Fluid Mechanics Lab relating power loss to Fontan patient exercise capacity. Figure 6-2 shows this study's data superimposed on data from Khiabani et al [48]. The ratio of peak EX $\dot{E_{app}}$ to the patient-specific FB $\dot{E_{app}}$ follows the same relationship to the ratio of the peak EX mean inflow rate to the patient-specific FB mean inflow rate as the previously published data. This engenders confidence in stating that CHOP235A enjoys greater exercise capacity than CHOP11B, as CHOP11B has the greater indexed power loss values.

Table 6-6: Superposition of this study's data on previously published data from Khibani et al [48]

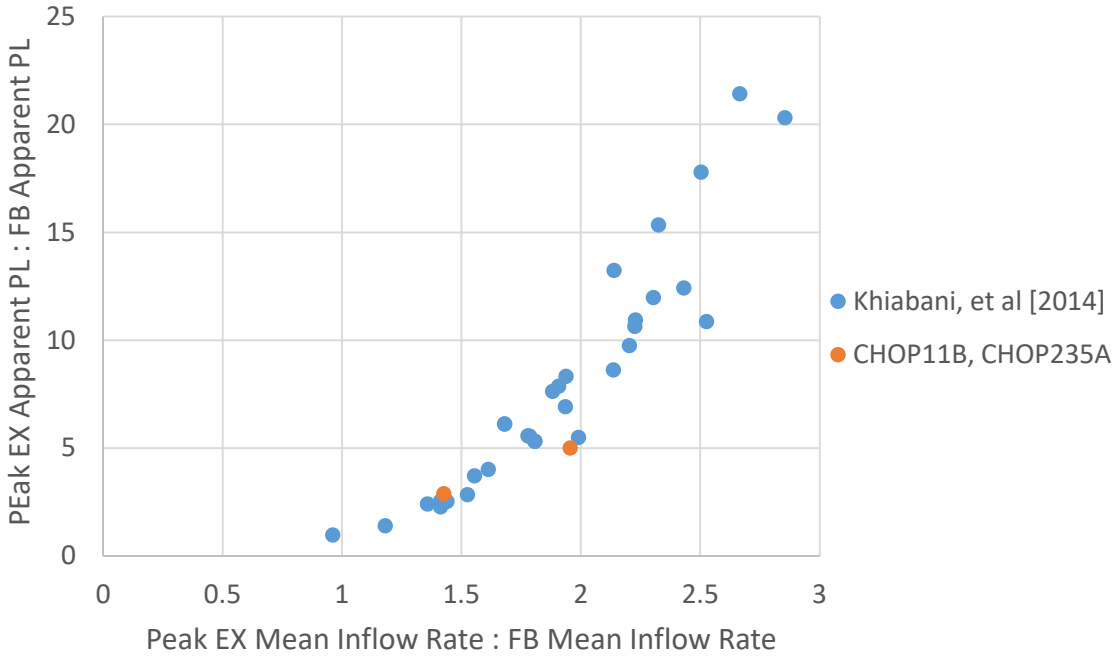

Figure 6-2: Superposition of this study's data on previously published data from Khibani et al [48]

6.5 Effect of Pulsatility

The effect of pulsatility on Fontan connection hemodynamics is shown by comparison between the patient-specific and derived BH experimental conditions. Flow pulsatility is established as an important parameter in Fontan patient pulmonary vasculature, as it plays a role in vasodilation and pulmonary vascular resistance [146]. The relationship between pulsatility and Fontan connection hemodynamics, though, has yet to be fully established, and, therefore, connections to pulmonary arteriovenous malformations and exercise capacity are weak. This study examines the local effect of pulsatility on Fontan hemodynamics in an effort to further inform the importance of restoring physiological pulsatility to Fontan patients.

The comparison of steady BH, low pulsatile BH, patient-specific BH, and high pulsatile BH experimental conditions does not include any true physiological changes. The only physiologically accurate condition is the patient-specific BH scenario. Instead, these conditions artificially change the flow waveform pulsatility without significantly altering any other flow waveform variables. This fact allows these results to be more generally applicable. The following paragraphs first identify the power loss, viscous dissipation, and hepatic flow distribution trends resulting from the effect of pulsatility comparison conditions. The results and trends are then compared to existing literature data. The final paragraphs give physical reasoning and explanation for the trends shown.

6.5.1 Data Trends

The $\dot{E}_{app}$ and iPL metrics listed in Table 5-11 show a consistent trend. Both $\dot{E}_{app}$ and iPL increase with increasing IVC flow waveform pulsatility. To explore this

relationship, a comprehensive list of the experimental condition values are listed in Table 6-7.

Table 6-7: Comprehensive experimental conditions summary for the effect of pulsatility on Fontan hemodynamics.

Model	Condition		Mean Inflow Rate (IVC+SVC) (L/min)	IVC:SVC Flow Ratio (%)	LPA:RPA Flow Ratio (%)	IVC Pulsatility (%)
CHOP11B	BH	Steady	3.28	73.9	46.9	0
		Patient-Specific	3.2	75.1	45.9	33.4
		Low Pulsatility	3.22	73.8	46.9	12.7
		High Pulsatility	3.21	74.1	45.9	57.5
CHOP235A	BH	Steady	3.10	79.0	23.5	0
		Patient-Specific	3.10	76.8	23.0	31.9
		Low Pulsatility	3.09	77.0	18.6	22.0
		High Pulsatility	3.21	77.3	23.1	38.6

The CHOP11B $\dot{E_{app}}$ and iPL increase with increasing IVC flow waveform pulsatility is more linear than the same relationship for CHOP235A, as seen in Figure 6-3 and Figure 6-4.

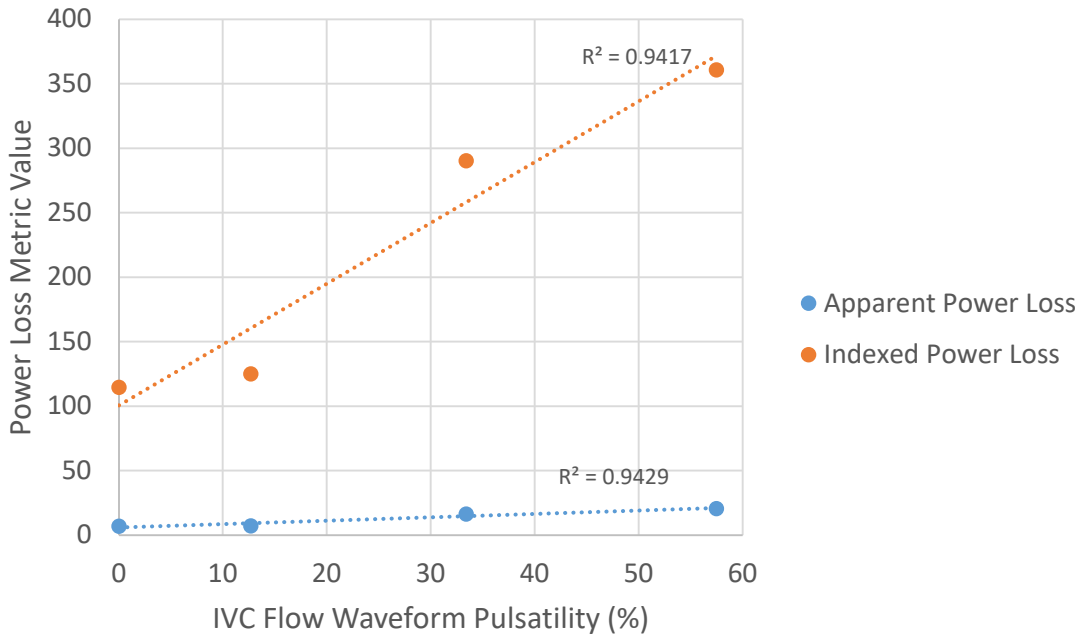

Figure 6-3: CHOP11B relationship between power loss metrics and IVC waveform pulsatility

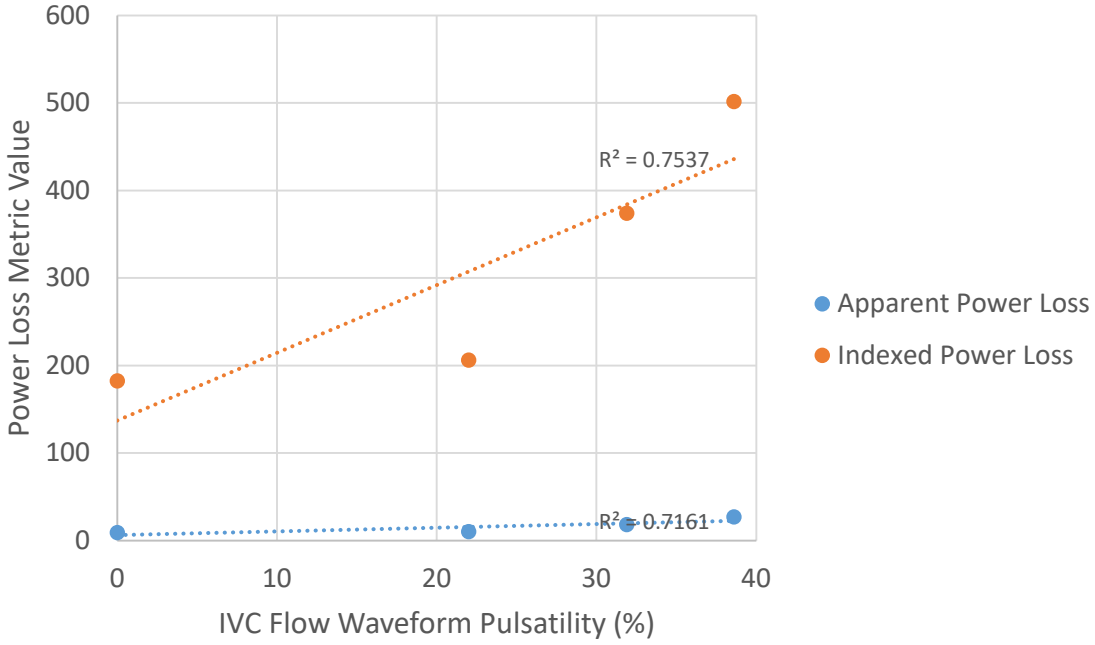

Figure 6-4: CHOP235A relationship between power loss metrics and IVC waveform pulsatility

Both Figure 6-3 and Figure 6-4 show that the increase in iPL value with increasing IVC flow waveform pulsatility is greater than the increase in the $E_{app}^{\cdot}$ value. This is most likely due to the effect of mean flow rate on each metric's relationship to pulsatility.

Table 5-12 shows an interesting trend for both φ and $i\varphi$. Though with different absolute values, both of these metrics show an increase in value with increasing pulsatility *not including* the steady flow experimental condition. The steady flow condition for both models possesses high φ and $i\varphi$ values compared to the pulsatile conditions, and is the maximum value in each case except for the CHOP11B $i\varphi$ set wherein the steady flow condition value is exceeded by the high pulsatility value (IVC flow pulsatility = 57.5%).

6.5.2 Literature Comparison

Contrary to the effect of respiration and the effect of exercise results, both power loss changes and hepatic flow distribution changes due to pulsatility effects are found in the literature for comparison. The most applicable literature comparison comes from Khiabani et al, who calculated apparent power loss from the computational fluid dynamics simulations from 24 patient-specific breath-held pulsatile and steady flow conditions using rigid wall anatomies [147]. This study found that the percent difference in apparent power loss between the pulsatile and steady flow conditions increased non-linearly with an increase in weighted pulsatility index, a wholistic Fontan connection pulsatility term where the pulsatility of each vessel (IVC, SVC, LPA, and RPA) is weighted by that vessel's flow rate. Another study by Wei et al assess the usefulness of steady versus pulsatile patient-specific breath-held conditions for use in surgical planning cases across 101 patients [148]. This study shows that a difference in indexed power loss between the pulsatile and steady conditions is statistically dependent on the flow pulsatility, and increases with increasing

pulsatility. The difference in hepatic flow distribution between the pulsatile and steady flow conditions is not statistically dependent on the pulsatility index. These findings by Wei et al coincide with this study's trends.

6.5.3 Physical Reasoning

The trend where both $\dot{E_{app}}$ and iPL increase with increasing pulsatility is widely attributed to the increase in overall fluid dynamic unsteadiness that occurs with increasing pulsatility. Increasing pulsatility effectively increases the instantaneous velocity gradients present in the TCPC flow field. High velocity gradients result in higher momentum losses, which are manifest as a monotonically increasing $\dot{E_{app}}$ and iPL trend.

The non-monotonic trend seen between φ and $i\varphi$ suggests there is a fundamental difference between steady flow and pulsatile flow as seen by the viscous dissipation term. Equation (4-9) reminds us that the viscous dissipation term is based on spatial velocity gradients. During steady flow these spatial velocity gradients do not change in time. During pulsatile flow the spatial velocity gradients are changing based on the transient velocity profile changes. It is these transient velocity profile changes that create the decreased spatial gradients, and hence the decreased viscous dissipation between the steady and low pulsatility cases. Then, as the pulsatility increases, the peak velocity in the transient velocity profile becomes greater, increasing the spatial velocity profiles, and causing the increasing viscous dissipation with pulsatility.

Further details of this phenomena are best explained with a simple example: the Womersley solution to the Navier-Stokes equations [149]. Pulsatile flow in a straight tube results in a Womersley velocity profile, as shown in Figure 6-5

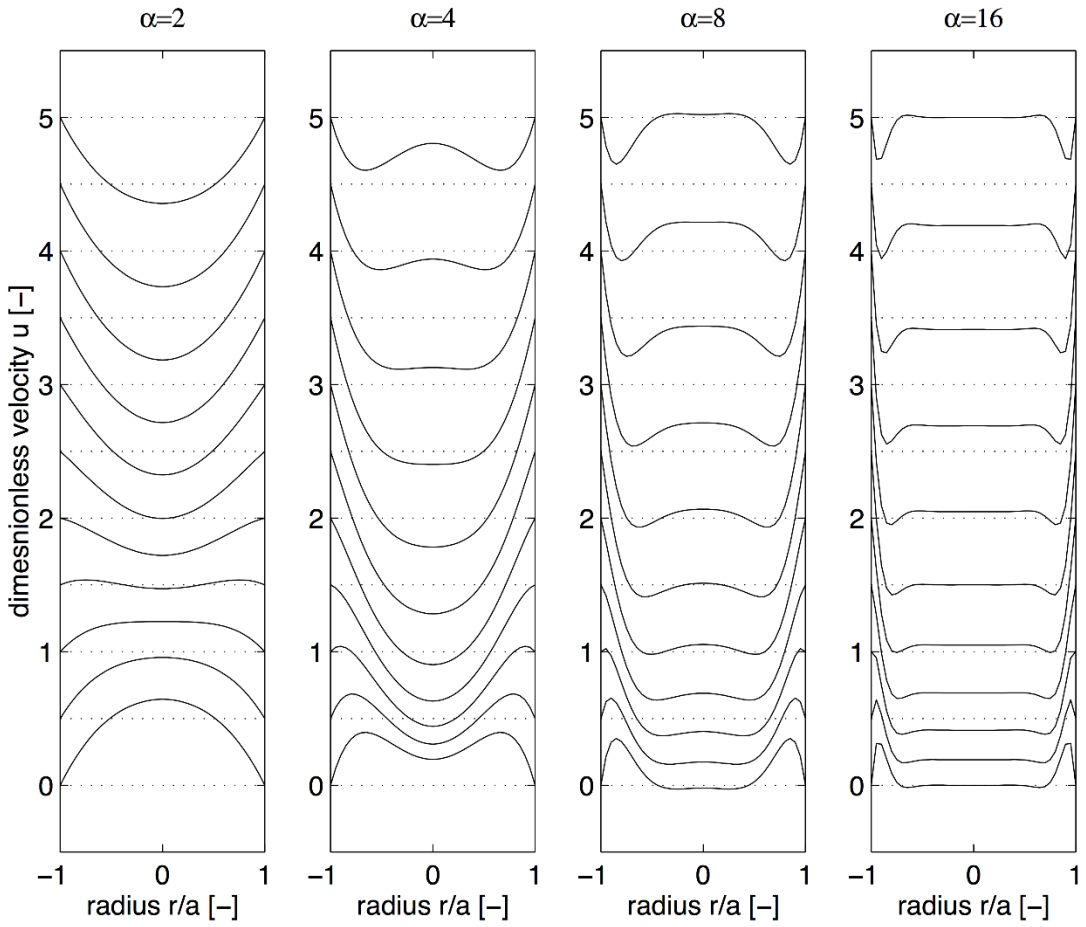

Figure 6-5: Womersley velocity profiles at different Womersley numbers, α

The velocity profiles during the Womersley solution change in time, as shown by the different rows of velocity profiles in the figure. The shape of the velocity profile is determined by the Womersley number, α, shown in Equation (6-1).

$$\alpha = \frac{\omega L^2}{\nu} \tag{6-1}$$

where ω is the angular frequency of the pulsatility, L is a characteristic length scale (vessel diameter), and ν is the fluid kinematic viscosity.

Figure 6-5 clearly shows that the spatial gradients of a pulsatile flow are different (and less than) the spatial gradients of a steady, Poiseuille, flow profile. This is the cause of the drop in viscous dissipation from the steady BH condition to the BH low pulsatility

condition seen in Figure 5-35 and Figure 5-36. Increasing pulsatility then increases the peak velocity of each of these transient profiles without affecting α. This increases the magnitude of the velocity profile extremes, but does not change its shape. Increasing the magnitude of the velocity while maintaining shape increases the spatial velocity magnitude. This is the reason for the increase in viscous dissipation with increased pulsatility, once pulsatility is present, as seen in Figure 5-35. Figure 5-36 does not see the same increase because the CHOP235A pulsatility does not change much between the BH low pulsatility and BH high pulsatility conditions (Table 6-7), and the effect falls within the measurement uncertainty bounds. Table 6-8 includes the Womersley number for the conditions exploring pulsatility effects.

Table 6-8: The effect of pulsatility on viscous dissipation terms, including IVC pulsatility and Womersley number, α

Model	Condition		φ (1/s^2)	$i\varphi$ (x10^{12})	IVC Pulsatility (%)	α
CHOP11B	BH	Steady	7442.6 ± 143.9	12.08 ± 1.28	0	-
		Patient-Specific	6272.8 ± 280.6	10.66 ± 1.21	33.4	19.9
		High Pulsatility	7392.0 ± 347.3	12.43 ± 1.42	12.7	19.9
		Low Pulsatility	5535.3 ± 48.9	9.28 ± 0.97	57.5	19.9
CHOP235A	BH	Steady	1225.4 ± 36.8	2.42 ± 0.26	0	-
		Patient-Specific	756.3 ± 28.4	1.49 ± 0.17	31.9	23.1
		High Pulsatility	789.0 ± 17.6	1.45 ± 0.16	22.0	23.1
		Low Pulsatility	743.6 ± 108.6	1.48 ± 0.26	38.6	23.1

Figure 6-6 shows the comparison of an instantaneous velocity magnitude profile from the CHOP11B BH High Pulsatility PIV acquisition at the 130mm plane, sampled in the IVC to a steady state analytical velocity profile with the same mass flow rate, and an apparent power loss assumed velocity profile. The blunted parabolic profile of the experimental data suggests Womersley-type flow characteristics within the IVC. This proves the existence of a fundamentally different flow profile existing between the steady state and pulsatile experimental conditions. The comparison of the experimental data to the

steady state analytical solution shows spatial velocity gradient differences that give rise to the change in the viscous dissipation term value from steady state to any of the pulsatile experimental conditions. The apparent power loss line is equal to the average velocity because $Q = \bar{V} \cdot A$, where Q is the volumetric flow rate, $\bar{V}$ is the average velocity, and A is the cross-sectional area. It is clearly a different velocity profile than the measured profile. The apparent power loss profile will not change

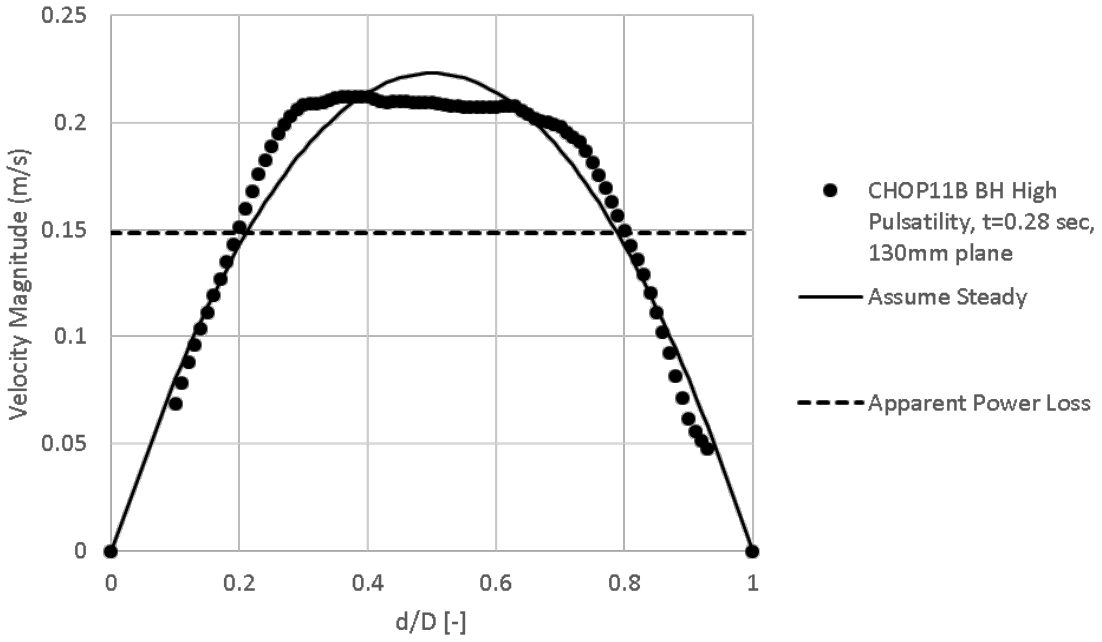

Figure 6-6: Velocity vector x-component versus normalized radius plotted for the CHOP235A patient-specific BH condition, sampled from the IVC on the 89mm plane.

6.6 Comparing Viscous Dissipation and Power Loss

Careful consideration of the flow physics within the TCPC draws question toward this study's calculation of a viscous dissipation term in addition to a power loss term. A thermodynamic perspective of the flow collision process occurring within the TCPC identifies viscous dissipation as the only source of lost energy (entropy). So, if calculated correctly, $\dot{E}_{app}$ and φ (as well as iPL and $i\varphi$) should always show the same trend, making

a viscous dissipation term calculation redundant. In fact, this intuition is so strong that some studies have calculated a volume-integrated viscous dissipation rate instead of $\dot{E}_{app}$ with the assumption they are equal [150–152]. However, $\dot{E}_{app}$ and φ (and iPL and $i\varphi$) do not show the same trend due to respiration or pulsatility effects. A thorough derivation of both $\dot{E}_{app}$ and φ reveals the reasoning behind the trend discrepancy and highlights important issues related to these two terms in the Fontan hemodynamics research field.

6.6.1 Control Volume Energy Analysis

The apparent power loss term used in this study, $\dot{E}_{app}$, comes from a control volume energy analysis of the TCPC. The derivation that follows closely aligns with Munson, Young, and Okiishi [153].

The first law of thermodynamics for a system states that the time rate of increase of the total stored energy of the system is equal to the sum of the net time rate of energy addition by heat transfer into the system and the net time rate of energy addition by work transfer into the system. This is represented symbolically in Equation (6-2):

$$\frac{\partial}{\partial t}\int_V \rho e \, dV + \int_{CS} \rho e \, \vec{U} \cdot \vec{n} \, dA = \dot{Q}_{in} + \dot{W}_{in} \tag{6-2}$$

where e is the intensive total energy, $\vec{U}$ is the fluid velocity vector, $\vec{n}$ is a unit vector normal (outward) to the control surface (cs), $\dot{Q}_{in}$ is the extensive heat rate added to the control volume, and $\dot{W}_{in}$ is the extensive work rate added to the control volume. The intensive total energy, e, is related to the intensive internal energy, $\hat{u}$, the intensive kinetic energy, $U^2/2$, and the intensive potential energy, gz, by Equation (6-3):

$$e = \hat{u} + gz + \frac{V^2}{2} \tag{6-3}$$

The work term, $\dot{W}_{in}$, is broken into several forms of work by Equation (6-4):

$$\dot{W}_{in} = \dot{W}_{in,shaft} + \dot{W}_{in,press} + \dot{W}_{in,viscous} \tag{6-4}$$

where $\dot{W}_{in,shaft}$ is the net shaft work rate into the system (i.e. via turbine), $\dot{W}_{in,press}$ is the net pressure work into the system acting on all the control surfaces, and $\dot{W}_{in,viscous}$ is the net viscous work rate into the system due to stress tangential to the control surfaces. Both $\dot{W}_{in,press}$ and $\dot{W}_{in,viscous}$ definitions are provided in Equation (6-5) and Equation (6-6), respectively:

$$\dot{W}_{in,press} = -\int_{CS} p(\vec{U} \cdot \vec{n})\, dA \tag{6-5}$$

$$\dot{W}_{in,viscous} = \int_{CS} \vec{\tau} \cdot \vec{U}\, dA \tag{6-6}$$

where p is the hydrostatic fluid pressure and $\vec{\tau}$ is the shear stress vector.

Substituting Equations (6-3), (6-4), (6-5), and (6-6) into (6-2) results in Equation (6-7):

$$\begin{aligned} \frac{\partial}{\partial t}\int_V \rho\left(\hat{u} + gz + \frac{U^2}{2}\right) dV + \int_{CS}\left(\hat{u} + gz + \frac{U^2}{2}\right)\rho\vec{U} \cdot \vec{n}\, dA \\ = \dot{Q}_{in} \\ + \int_{CS} \vec{\tau} \cdot \vec{U}\, dA - \int_{CS} p\left(\vec{U} \cdot \vec{n}\right) dA + \dot{W}_{in,shaft} \end{aligned} \tag{6-7}$$

The power (energy rate) lost during the TCPC flow process is equal to the sum of the time rate of internal energy change and the heat rate out of the control volume. Isolating these terms on the left-hand side of the energy balance results in Equation (6-8):

$$\dot{E}_{loss} = \dot{W}_{in,shaft} + \int_{CS} \vec{\tau} \cdot \vec{U}\, dA - \int_{CS} \left(gz + \frac{U^2}{2} + \frac{P}{\rho} \right) \rho \vec{U} \cdot \vec{n}\, dA - \frac{\partial}{\partial t} \int_V \rho \left(gz + \frac{U^2}{2} \right) dV \quad (6\text{-}8)$$

Equation (6-8) is most general form of power loss, and is mathematically equal to the volume integral of the viscous dissipation rate. Yet, $\dot{E}_{loss} \neq \dot{E}_{app}$, and this has led to several problems with power loss.

6.6.2 Power Loss Problems

One problem with power loss as a Fontan connection hemodynamic metric stems from the assumptions made to calculate a power loss term. Apparent power loss, $\dot{E}_{app}$, was developed on simpler Fontan circulation models where most of these assumptions were valid. Subsequent Fontan circulation models, including the model in this study, include complexities that invalidate these assumptions, but $\dot{E}_{app}$ is still used because it relates to patient outcomes. This causes confusion as to the physical meaning of $\dot{E}_{app}$ and its comparison to viscous dissipation.

In order to arrive at $\dot{E}_{app}$ from $\dot{E}_{loss}$ the following assumptions are made:

(1) No shaft work is present on the system control surface

$$\dot{W}_{in,shaft} = 0$$

(2) No viscous work is present in the system

$$\int_{CS} \vec{\tau} \cdot \vec{U}\, dA = 0$$

(3) The control volume does not change in time

$$\frac{\partial}{\partial t}\int_{V} \rho\left(gz + \frac{U^2}{2}\right) dV = 0$$

(4) There is no change in elevation between control surfaces

$$\int_{CS}\left(gz + \frac{U^2}{2} + \frac{P}{\rho}\right)\rho\vec{U}\cdot\vec{n}\,dA = \int_{CS}\left(\frac{U^2}{2} + \frac{P}{\rho}\right)\rho\vec{U}\cdot\vec{n}\,dA$$

(5) The velocity profile at the control surfaces is constant

$$\vec{U}\cdot\vec{n} = \frac{Q}{A}$$

The validity of these assumptions varies depending on the complexity of the system under consideration. Assuming no shaft work is present is almost always perfectly valid. The question of negligible viscous work is more complex. Examination of Equation (6-6) shows negligible viscous work can exist when either (1) the shear stress vector is extremely small, (2) the velocity vector is extremely small, or (3) the shear stress vector and velocity vector are orthogonal to one another. Proper control volume selection can usually create a situation where any one of these 3 situations occurs. However, if the TCPC inflow and outflow control surfaces are not perfectly orthogonal to the TCPC inflow and outflow velocity field, respectively, then the viscous work cannot be considered zero. Non-orthogonal control surfaces are most likely to occur at the outflows where the velocity fields is unknown prior to control surface definition. The third assumption, that the control volume does not change in time, is only valid for rigid wall studies, and is the first assumption that cannot be accounted for in an *in vivo* setting. The fourth assumption, that there is no change in elevation (or no gravity influence) between control surfaces is probably not representative of the patient's lifestyle, but can be considered valid during an *in vivo* study, as patient-specific data is collected in the supine position. Similarly, as long

as the *in vitro* study or *in silico* simulation does not include gravity effects, this assumption is valid. The fifth, and final, assumption is never valid, as even a steady flow, rigid-walled, idealized anatomy Fontan circulation model system produces spatially-varying velocity profiles at the control surfaces. Spatially-varying profiles occur anytime the fluid domain includes a no-slip condition and flow. Each of these assumptions contributes to the confused physical meaning behind $\dot{E}_{app}$ as a power loss metric.

Another issue with power loss is that it requires static pressure measurements for calculation. Static pressure values are not difficult to acquire for *in vitro* or *in silico* studies, but are not typically available for Fontan patients. Extensive catheterization is required to obtain pressure values at all of the TCPC inlets and outlets, and such invasive procedures are typically avoided. One particularly important limitation associated with the inability to acquire *in vivo* power loss values is the subsequent inability to verify *in vitro* and *in silico* power loss values against patient-specific *in vivo* data. Without verification, the knowledge from *in vitro* and *in silico* power loss correlations to patient outcomes will always be limited.

Ultimately, though $\dot{E}_{app}$ loses physical meaning from assumptions and requires an invasive pressure measurement that restricts its calculation during *in vivo* studies, it is still valuable for its correlations to patient outcomes . For pure statistical purposes, $\dot{E}_{app}$ can be related to patient outcomes without any physical understanding; it is simply a number. So, any solution to the lost physical meaning and required static pressure power loss problems must maintain correlations to patient outcomes to be truly useful.

The following analysis examines the viscous dissipation term acquired in this study as a solution to the previously stated power loss problems

6.6.3 Viscous Dissipation as a Solution to Power Loss Problems

In order to act as a solution to the present power loss problems, viscous dissipation must meet three requirements: (1) maintain physical meaning by employing no invalid assumptions, (2) require only values measureable in the clinic, and (3) relate with current power loss values, $\dot{E}_{app}$, to maintain correlations to patient outcomes. Analysis of viscous dissipation as a solution to the power loss problems begins with its derivation from a differential energy conservation analysis.

6.6.3.1 Differential Energy Analysis

The viscous dissipation term used in this study, φ, comes from a differential energy conservation analysis. The first law of thermodynamics, restated from section 6.6.1, is that the time rate of increase of the total stored energy of the system is equal to the sum of the net time rate of energy addition by heat transfer into the system and the net time rate of energy addition by work transfer into the system. The differential work rate transferred into the system is broken into work done by pressure forces normal to the surface (Equation (6-9)), work done by shear forces tangential to the surface (Equation(6-10)) and body forces (Equation (6-11)).

$$d\dot{w}_p = \left(-p\vec{I} \cdot \vec{U}\right) dV \tag{6-9}$$

$$d\dot{w}_s = \nabla \cdot \left(\underline{\tau} \cdot \vec{U}\right) dV \tag{6-10}$$

$$d\dot{w}_b = \rho\vec{f} \cdot \vec{U}\, dV \tag{6-11}$$

where p is the static pressure, $\vec{I}$ is the identity vector, $\vec{U}$ is the velocity vecotry, $\underline{\tau}$ is the symmetric shear stress tensory, and $\vec{f}$ is a body force (gravity) per unit mass.

The differential heat rate transferred into the system is broken into volumetric heating (Equation (6-12)) and thermal conduction heating (Equation (6-13)) components.

$$d\dot{Q}_v = \rho \dot{q}_v \, dV \tag{6-12}$$

$$d\dot{Q}_c = -(\nabla \cdot \dot{q}_c) dV \tag{6-13}$$

where $\dot{q}_v$ is a term representing heat added to the entire volume per unit mass (i.e. due to radiation or a chemical reaction), and $\dot{q}_c$ is the conductive heat vector.

The differential total energy rate increase of the system is defined in Equation (6-14).

$$d\dot{e} = \rho \frac{D}{Dt}\left(\hat{u} + \frac{U^2}{2}\right) dV \tag{6-14}$$

where e is the total energy, $\hat{u}$ is the intensive internal energy, and $\frac{U^2}{2}$ is the intensive kinetic energy. The potential energy contribution for this analysis is considered as part of the body forces term (Equation (6-11)).

Constructing Equations (6-9) through (6-14) to meet the first law of thermodynamics results in Equation (6-15):

$$\rho \frac{D}{Dt}\left(\hat{u} + \frac{U^2}{2}\right) = \rho \dot{q}_v - (\nabla \cdot \dot{q}_c) - \left(p\vec{I} \cdot \vec{U}\right) + \nabla \cdot \left(\underline{\tau} \cdot \vec{U}\right) + \rho \vec{f} \cdot \vec{V} \tag{6-15}$$

Similar to section 6.6.1, the sum of the change in internal energy and the heat rate leaving the system are equal to the power lost. These terms are isolated on the left-hand side of Equation (6-15) by subtracting the differential kinetic energy rate (Equation (6-16)) from both sides.

$$\rho \frac{D}{Dt}\left(\frac{V^2}{2}\right) = -\vec{U} \cdot \nabla p + \vec{U} \cdot \left(\nabla \cdot \underline{\tau}\right) + \rho \vec{f} \cdot \vec{V} \tag{6-16}$$

Equation (6-17) results, and defines the differential power lost in the Fontan connection.

$$\dot{e}_{loss} = -p\left(\nabla \cdot \vec{U}\right) + \underline{\tau} : \nabla \vec{U} \tag{6-17}$$

Assuming the fluid in question is Newtonian allows for a relationship between the shear stress vector and the velocity, which can then be substituted into Equation (6-17).

$$\begin{aligned} \dot{e}_{loss} = -p\left(\frac{\partial u_x}{\partial x} + \frac{\partial u_y}{\partial y} + \frac{\partial u_z}{\partial z}\right) \\ + \mu\left[2\left(\frac{\partial u_x}{\partial x}\right)^2 + 2\left(\frac{\partial u_y}{\partial y}\right)^2 + 2\left(\frac{\partial u_z}{\partial z}\right)^2\right. \\ + \left(\frac{\partial u_x}{\partial y} + \frac{\partial u_y}{\partial x}\right)^2 + \left(\frac{\partial u_x}{\partial z} + \frac{\partial u_z}{\partial x}\right)^2 \\ \left. + \left(\frac{\partial u_y}{\partial z} + \frac{\partial u_z}{\partial y}\right)^2\right] - \frac{2}{3}\mu\left(\frac{\partial u_x}{\partial x} + \frac{\partial u_y}{\partial y} + \frac{\partial u_z}{\partial z}\right)^2 \end{aligned} \tag{6-18}$$

Equation (6-18) is simplified by assuming incompressible flow , which leaves Equation (6-19):

$$\begin{aligned} \dot{e}_{loss} = \mu\varphi = \mu\left[2\left(\frac{\partial u}{\partial x}\right)^2 + 2\left(\frac{\partial v}{\partial y}\right)^2 + 2\left(\frac{\partial w}{\partial z}\right)^2 + \left(\frac{\partial u}{\partial y} + \frac{\partial v}{\partial x}\right)^2\right. \\ \left. + \left(\frac{\partial u}{\partial z} + \frac{\partial w}{\partial x}\right)^2 + \left(\frac{\partial v}{\partial z} + \frac{\partial w}{\partial y}\right)^2\right] \end{aligned} \tag{6-19}$$

Thus we see that the product of the viscous dissipation term, φ, and the dynamic viscosity is equal to the true power loss per unit volume. Integration of this product will result in $\dot{E}_{loss}$, the same quantity derived in section 6.6.1. The viscous dissipation term

derivation included no invalid assumptions, so it maintains its physical meaning and fulfills solution requirement (1).

The viscous dissipation term, φ, found in Equation (6-19) is measureable in the clinic. Unlike apparent power loss, the viscous dissipation term does not require static pressure to be calculated. This avoids any need for invasive measurement, which is preferentially avoided for *in vivo* measurements. The only measurement that the viscous dissipation term requires is a time-resolved velocity field, the spatial gradients of which compose all terms in the viscous dissipation equation. Time-resolved blood velocity fields are potentially available via 4D MRI technology [154,155]. The research of 4D MRI technology to improve its accuracy and availability in the clinic is underway [152]. Thus, the viscous dissipation term, φ, fulfills solution requirement (2) by being a clinically measureable quantity.

6.6.3.2 Statistical Analysis

An analysis of whether φ fulfills the final solution requirement of relating to apparent power loss, and thus relating to patient outcomes, was conducted through statistical comparison of φ and $\dot{E}_{app}$ values. Indexed power loss and the indexed viscous dissipation term were also compared, for completeness. The statistical comparison of φ to $\dot{E}_{app}$ and φ to iPL employed values calculated from two different methods, an *in silico* method and an *in vitro* method. The *in silico* method values were used to relate power loss and viscous dissipation values for a single condition across multiple patients, and used similar TCPC modeling techniques to that which exists in the current literature. The *in vitro* method values were used to relate power loss and viscous dissipation for two patients across multiple conditions, and used TCPC modeling techniques closer to physiological realities.

The *in silico* methods for acquiring the viscous dissipation and power loss values provided time-resolved three-dimensional velocity fields and static pressure values through the use of ANSYS Fluent 17.0 (ANSYS, Inc. Canonsburg, PA). The coupled solver scheme was employed to solve to continuity and linearized momentum equations simultaneously. Temporal and spatial discretizations employed second-order schemes, and warped-face gradient correction was employed to improve gradient calculation accuracy. The simulation was conducted on polyhedral meshes, converted from an unstructured tetrahedral mesh. Mesh size was $0.05\ x\ \overline{D_{vessel}}$, where $\overline{D_{vessel}}$ is the average diameter of all TCPC inlets and outlets. Boundary layer zones were created to improve numerical accuracy near the walls. The boundary layer zone was filled with three uniform prismatic boundary meshes equal to 1/3 the size of the surrounding elements. These mesh parameters were previously established as creating mesh-independent results [121]. Flow extensions equal to 10 times the vessel diameter in length were added to all inlets and outlets. User-defined functions were used to apply fully-developed time-varying velocity profiles at the inlets. Time step size was set at 0.001 seconds to ensure the Flow Courant number was ~ 0.1. The vessel walls were assumed rigid, and the fluid was assumed Newtonian with density equal to 1060 kg-m^{-3} and dynamic viscosity equal to 3.5x10^{-3} Pa-s.

The power loss ($\dot{E}_{app}$ and iPL) and viscous dissipation (φ and $i\varphi$) terms were calculated from the CFD solution, and analyzed statistically. Table 6-9 summarizes the values used for the statistical comparison of φ to $\dot{E}_{app}$ and $i\varphi$ to iPL. The patient-specific data used in the CFD simulations were chosen from the Cardiovascular Fluid Mechanics Lab Fontan Database Patients were selected to include mean inflow and outflow (cardiac

output) values spanning the range of all patients within the data base. Patients with more than 2 inlets (IVC and SVC) or more than two outlets (LPA and RPA) were excluded.

Table 6-9: Values used for multi-patient, single condition viscous dissipation and power loss relationship analysis. PS - patient-specific.

Model	Condition		$\dot{E}_{app}$ (mW)	iPL (x10^6)	φ (1/s^2)	$i\varphi$ (x10^{12})
202B	BH	PS	11.00	41.82	54215.03	49.56
89B			3.50	9.64	6749.47	3.14
82B			5.15	21.03	27635.55	11.66
39C			3.68	78.66	37593.52	49.64
23B			2.60	28.02	11902.93	12.80
21A			1.89	22.20	15862.29	12.05
18A			0.55	4.99	8199.43	1.95
128A			0.86	4.15	9312.65	2.45
88B			4.61	26.58	23561.35	19.83
33B			3.75	41.50	11642.50	17.68

The data were analyzed for normality within each variable using the Shapiro-Wilk test within IBM SPSS Statistics (IBM, Inc., Armonk, NY). Indexed power loss and the viscous dissipation term were found to be normally distributed, but apparent power loss and indexed viscous dissipation were not. Accordingly, Spearman's correlation test was used to explore the relationships between both the viscous dissipation term and apparent power loss, and indexed viscous dissipation and indexed power loss, respectively.

Both relationships showed a significant statistical correlation. The correlation coefficient for the apparent power loss and viscous dissipation term comparison was $r = 0.709$ ($p = 0.022$). The indexed viscous dissipation and indexed power loss comparison results in an $r = 0.952$ correlation coefficient ($p<0.001$). This result fulfills the third solution requirement (section 6.6.3). With all three requirements fulfilled, viscous

dissipation (the $i\varphi$ and φ terms) can be considered adequate solutions to the existing power loss problems.

The strong correlation between the power loss and viscous dissipation terms from the *in silico* methods is at least partially due to the CFD modelling assumptions. Of the 5 assumptions made to arrive at $\dot{E}_{app}$ listed in section 6.6.2, 3 of them were made in the *in silico* methods. The 3 assumptions made were: assumption (1): no shaft word was present in the system, assumption (3): the control volume did not change in time, and assumption (4): there was no change in elevation between control surfaces. To test the usefulness of viscous dissipation as a solution to the power loss problems under a more general system, power loss and viscous dissipation values were also collected and statistically analyzed under *in vitro* methods.

The *in vitro* methods employed to produce values for the *in vitro* statistical analysis were those described in section 4.2.2. The viscous dissipation terms calculations under these methods only assumed two of the 5 assumptions listed in section 6.6.2: assumption (1) that no shaft work was present in the system and assumption (4) that there was no elevation change between control surfaces. The major difference between the *in vitro* and *in silico* methods was the use of flexible walls for the *in vitro* analysis. Table 6-10 summarizes the power loss and viscous dissipation values from the *in vitro* methods used for statistical analysis.

Table 6-10: Values used for multi-condition viscous dissipation and power loss relationship analysis. Puls - pulsatile; PS - patient-specific

Model	Condition		$\dot{E}_{app}$ (mW)	iPL (x10^6)	φ (1/s^2)	$i\varphi$ (x10^{12})
11B	BH	Low Puls	7.2	125.0	5535.3	9.28
		PS	16.3	290.3	6272.8	10.66
		High Puls	20.6	360.8	7392.0	12.43
	FB	PS	55.6	418.6	5586.5	5.95
	EX	Peak PS	278.5	329.4	33359.0	9.30
		Half-Peak Puls	96.6	268.1	18850.3	9.26
235A	BH	Low Puls	9.9	206.2	743.6	1.45
		PS	18.0	374.0	756.3	1.48
		High Puls	26.9	501.5	789.0	1.49
	FB	PS	33.8	170.6	533.6	0.41
	EX	Peak PS	97.9	170.6	807.9	0.31
		Half-Peak Puls	71.5	185.3	742.4	0.37

The data used for the viscous dissipation and power loss relationship analysis did not include any steady state (0% pulsatility) values. The steady state condition was excluded because of the fundamentally different trend seen in the effect of pulsatility on viscous dissipation data (section 6.5).

The data were analyzed for normality within each variable using the Shapiro-Wilk test within IBM SPSS Statistics. Only indexed power loss was found to be normally distributed. Accordingly, Spearman's correlation test was then used to explore the relationships between both the viscous dissipation term and apparent power loss, and indexed viscous dissipation and indexed power loss, respectively.

Neither relationship showed a significant statistical correlation, but the relationship between indexed viscous dissipation and indexed power loss showed a trend. The correlation coefficient for the apparent power loss and viscous dissipation term comparison is $r = 0.322$, which is statistically insignificant ($p = 0.308$). The indexed viscous

dissipation and indexed power loss comparison results include an $r = 0.518$ correlation coefficient that is trending toward statistical significance ($p = 0.084$).

The relationships between the power loss and viscous dissipation terms from the *in vitro* method are less strong as the relationships between the terms from the *in silico* methods for two reasons. First, the *in vitro* method viscous dissipation terms calculations does not include the rigid wall assumption, but the power loss calculations do. The influence of a moving wall weakens the correlation between the two metrics. Second, the *in vitro* method experimental conditions span two different patients and multiple physiological conditions per patient, but the *in silico* method relates metrics from multiple patients (n=10) at only one physiological condition. The indexed viscous dissipation and indexed power loss comparison shows a stronger relationship than the non-indexed viscous dissipation and apparent power loss comparison for both methods because indexing the variables accounts for some patient-specific and physiological condition differences.

7 LIMITATIONS

7.1 *In Vitro* Fontan Circulation Model Verification

The purpose of the *in vitro* Fontan circulation model verification aspects of this study are to characterize the model against *in vivo* patient-specific data. This verification is a relatively standard engineering process of defining what is known and what is uncertain when comparing data sets. Thus, there are no limitations in the verification method itself.

That being said, the *in vitro* Fontan circulation model itself is not without its limitations. The intent of the model is to reproduce Fontan connection hemodynamics both in the global circulatory system and in the local total cavopulmonary connection (TCPC). The most notable limitation is in the use of a bulk compliance metric to characterize the *in vivo* TCPC material properties. In reality, the *in vivo* TCPC is a mixture of heterogeneous living tissue types (arterial and venous) and artificial graft material for the IVC connection. Representing these vessels with a homogenous, linear elastic material with a single compliance value belies the complexity of the *in vivo* solid dynamics. Of course, these solid dynamics are in direct contact with, and affect the blood fluid dynamics creating different *in vitro* flow fields than those which may exist and are recorded in this study. Both the viscous dissipation and hepatic flow distribution metrics calculated in the study are directly based on the *in vitro* flow fields, so these metrics could be affected. However, the homogeneous flexible TCPC models used do still deform dynamically under pulsatile flows, and are the most physiologically accurate models used in this field of study, to date.

The *in vitro* Fontan circulation model is also limited in that it cannot replicate Fontan circulatory system remodeling or growth based on hemodynamic conditions. Though this limitation does not impact the influence of any of the effects of respiration,

exercise, or pulsatility on Fontan connection hemodynamics directly, the secondary effects of global circulation differences on Fontan connection hemodynamics are not considered. For example, increasing pulsatility consistently increases both apparent power loss and indexed power loss in this study. Research suggests that the presence of pulsatility in Fontan flows affects pulmonary system vasodilation. With larger pulmonary blood vessels, pulmonary vascular resistance drops, and an increase in single ventricle diastolic filling is implied. If the single ventricle fills more it will also eject more blood with every systolic stroke, increasing cardiac output. This increased cardiac output manifests itself at the Fontan connection as an increase in either IVC or SVC inflow, and a possible change in the IVC:SVC flow ratio. The *in vivo* circulatory system will iterate on this process until reaching homeostasis, but the *in vitro* model never replicates the change in pulmonary vascular resistance. This limitation is only applicable to the derived experimental conditions (high pulsatility, low pulsatility, and half-peak exercise), as the patient-specific physiological experimental conditions were set according to *in vivo* data that assumes the patient is in a homeostatic circulatory system condition. Ultimately, this effect is secondary and its changes to the Fontan connection are considered insignificant when compared to the primary effects.

Though it did not limit accuracy, the five step process used to verify the flexible TCPC model compliance (section 4.2.1.4.2) was tedious and time-consuming. In a sense, this process is limited in the number of models produced in a given amount of time. Technically, step 1 of the process could have been eliminated through the use of a more sophisticated finite element analysis (FEA) computational model. The information provided from step 1 is the compliance of an arbitrarily thick model given with the silicone

model material properties. A more advanced FEA model could have used the volume and pressure change information from the *in vivo* data available, combined with material properties from the silicone material, to estimate a desired wall thickness resulting in the patient-specific compliance. This methodological change should be considered if a larger number of compliance-matched flexible TCPC models are to be constructed.

The final limitation of the *in vitro* Fontan circulation model is concerning the use of the BH anatomical data as the baseline model shape. This selection assumes that the BH anatomical data holds the TCPC stress-free state, which is most acceptable when performing analyses only based on the BH condition. The pulsatility data collected in this study, for example, can validly use this assumption. However, it is possible that the introduction of respiration and/or a switch to exercise conditions introduced a different baseline, mean pressure in the chest cavity. This would mean that employing the BH model shape during those conditions eliminates its validity as a stress-free model. This could cause unpredictable changes to local wall deformations that may affect each of the metrics calculated. The use of condition-specific models rather than just patient-specific flexible TCPC models was not pursued due to time and cost. Future considerations of TCPC wall deformation (most probably in the case of CFD FSI analyses) should carefully consider and define the TCPC stress-free state for each patient-specific condition.

7.2 PIV Velocity Field Analysis

The most notable limitation related to the PIV velocity field analysis is due to the PIV acquisition method itself. Without the ability to collect volumetric particle image velocimetry data, stereoscopic PIV data at sparsely spaced planes is the next best acquisition technique. The limitations in analyzing the resultant volumetric velocity field

from the stereoscopic PIV data are housed in the volumetric and temporal interpolation necessary to fill in missing data.

The linear temporal interpolation employed between the PIV-acquired time points may not be representative of the temporal velocity behavior. Fluid dynamics possesses inherently non-linear physics, so the potential exists that a non-linear temporal interpolation scheme may more accurately represent the temporal velocity field changes. This limitation affects the viscous dissipation and hepatic flow distribution metrics calculated from the transient velocity field data sets (pulsatile and patient-specific data sets), but only in so far as the absolute values of these metrics are concerned. Comparisons between these metrics should still hold, as the temporal interpolation method is kept the same for all transient experimental conditions.

The volumetric interpolation method employed a static TCPC unstructured mesh to resample the enclosed rectangular prism, and defines a 0 (zero) velocity value on the TCPC unstructured mesh surface. This resampling and 0 (zero) velocity boundary definition is necessary to define the TCPC model boundary location and use the location to interpolate velocity values not lying in the PIV-acquired planes. However, the TCPC unstructured mesh is static, which means it does not deform with the deforming planes. To guarantee that the static TCPC unstructured mesh never over-wrote velocity data in the PIV-acquired plane locations, the mesh was offset by 2 mm outward at every surface. This method most directly affects the velocity gradients near the wall, which then affects the viscous dissipation metrics most drastically.

The hepatic flow distribution calculation, which is based on the PIV velocity fields, is calculated by seeding an IVC cross-sectional plane evenly with respect to space. This

even seeding distribution assumes that the hepatic factor, which originates upstream of the IVC in the liver, is perfectly well-mixed in the bloodstream by the time it reaches this seeding plane. A more accurate HFD calculation can be conducted if the anatomical model includes both the hepatic veins (hepatic factor input/source) and the IVC are included before their confluence. Unfortunately, including these vessels was not standard of care or part of the MRI data acquisition protocol used for the retrospective data set on which the models in this study were based.

8 CONCLUSIONS

The Fontan procedure is the standard palliative treatment for single ventricle congenital heart defects. Though early outcomes are successful, long-term complications exist. These complications and patient outcomes are related to Fontan connection local and global hemodynamics. The evidence for these relationships exist based on *in vivo*, *in vitro*, and computational studies, some of which assumed rigid-wall Fontan connection models. This study developed an *in vivo* compliance-verified Fontan connection model as the basis for a set of *in vitro* Fontan connection hemodynamics experiments exploring the effects of respiration, exercise, and pulsatility on Fontan hemodynamics. The hypothesis of the study is that respiration, exercise, and pulsatility each affect Fontan hemodynamic metrics related to patient outcomes. The conclusions from each of the study aspects are included in the following sections.

8.1 Fontan Circulation *In Vitro* Modelling

This study successfully developed an *in vivo* compliance-verified Fontan connection model for use in an *in vitro* Fontan circulation. Development included analysis of patient-specific MRI data to calculate the *in vivo* compliance, and iterative *in vitro* compliance testing using computational simulations to determine material properties. The completed *in vitro* Fontan circulation matched target *in vivo* flow conditions within an acceptable percentage, as quantified by two different error metrics. Both these patient-specific flow conditions based on MRI data and derived flow conditions were used as experiments from which bulk hemodynamic and local velocity fields were collected. The collected data was analyzed for the effect of respiration, exercise, and pulsatility on Fontan hemodynamic metrics related to patient outcomes.

8.2 Respiration and Fontan Hemodynamics

The effect of respiration on Fontan hemodynamics was assessed for two different patient-specific Fontan connection models. The respiration effect for each model was assessed by comparing and contrasting a patient-specific breath-held experimental condition to a patient-specific free-breathing experimental condition. Velocity fields were compared qualitatively, and the following quantitative metrics were also compared: apparent power loss, indexed power loss, a viscous dissipation term, indexed viscous dissipation, and hepatic flow distribution.

The results of the respiration comparison showed some consistent trends. Apparent power loss consistently increases with added respiration. Also, hepatic flow distribution consistently decreases with the added influence of respiration. Indexed power loss, the viscous dissipation term, and indexed viscous dissipation did not show consistent trends. All three of these metrics showed an increase in value when respiration effects were added for the first patient-specific model (CHOP11B), but then showed a decreased value for the second model (CHOP235A).

The trends found in this study are important to understand for Fontan patient well-being. Though highly patient-specific and with some quantifiable error, trends showing a decrease in hepatic flow distribution when respiration effects are considered can affect clinical understanding surrounding pulmonary arteriovenous malformations. This shunting across the capillary bed coincides with, and is attributed to, uneven hepatic flow distribution in Fontan patients. Thus, depending on the MRI protocol used for HFD analysis, the results may be increased over the true patient's flow distribution value.

Regardless of trends, the use of free-breathing versus breath-held flow conditions affects all of the hemodynamic metrics calculated in this study. The importance of accurately modeling the patient-specific physiology with proper anatomy, flexibility, and FB versus BH flow boundary conditions cannot be understated.

8.3 Exercise and Fontan Hemodynamics

The effect of exercise on Fontan hemodynamics was assessed for two different patient-specific Fontan connection models. The exercise effect for each model was assessed by comparing and contrasting a patient-specific free-breathing experimental condition to a derived half-peak exercise experimental condition and a patient-specific peak exercise experimental condition. Velocity fields were compared qualitatively, and the following quantitative metrics were also compared: apparent power loss, indexed power loss, a viscous dissipation term, indexed viscous dissipation, and hepatic flow distribution.

The results of the exercise comparison showed some consistent trends. Both apparent power loss and the viscous dissipation term increase consistently from the free-breathing patient-specific condition to the derived half-peak exercise condition, and from the derived half-peak exercise condition to the patient-specific peak exercise condition. Indexed power loss, indexed viscous dissipation, and hepatic flow distribution did not show consistent trends.

The most notable Fontan patient outcome related to exercise is the finding that increased indexed power loss under resting conditions correlates with decreased exercise capacity [48]. There is no established correlation precedent between resting, free-breathing indexed power loss and peak exercise power loss. The results of this study contribute to this lack of correlation. Exercise intensity level undoubtedly has an influence on both

global and local Fontan hemodynamics, but the relationship is complicated. This is not surprising, as changing from resting, free-breathing to exercise conditions includes changes in mean inflow rate, IVC:SVC inflow ratio, LPA:RPA outflow ratio, waveform pulsatility, waveform frequency content, and likely several other parameters. With simultaneous changes to so many physiologic variables, it is not surprising that the relationship with the output metrics is more complicated than can be currently determined.

Regardless of trends, the use of different exercise flow conditions affects all of the hemodynamic metrics calculated in this study. The importance of accurately modeling the patient-specific exercise physiology with proper anatomy, flexibility, and flow boundary conditions cannot be understated.

8.4 Pulsatility and Fontan Hemodynamics

The effect of pulsatility on Fontan hemodynamics was assessed for two different patient-specific Fontan connection models. The pulsatility effect for each model was assessed by comparing and contrasting a derived steady flow breath-held experimental condition to a derived low pulsatility breath-held experimental condition, a patient-specific breath-held experimental condition, and a derived high pulsatility breath-held experimental condition. Velocity fields were compared qualitatively, and the following quantitative metrics were also compared: apparent power loss, indexed power loss, a viscous dissipation term, indexed viscous dissipation, and hepatic flow distribution.

The results of the pulsatility comparison showed some consistent trends. Both apparent power loss and indexed power loss increase consistently with increasing pulsatility. The viscous dissipation term and indexed viscous dissipation also increase in value with increasing pulsatility, but only when the steady flow case (0% pulsatility) is not

considered. This complicated trend is attributed to the fundamental fluid dynamics difference between a steady flow velocity profile and the velocity profile of a pulsatile flow. Hepatic flow distribution showed no consistent trend with changing pulsatility.

These results help this study conclude that all Fontan connection hemodynamic assessments and calculations under pulsatile flow conditions with flexible model walls should be performed using pulsatile conditions. Time-averaged flow conditions are an inaccurate assessment of power loss, viscous dissipation, and hepatic flow distribution metrics under the model conditions used in this study. Previous Fontan hemodynamic models without the use of flexible walls concluded that the error introduced by assuming time-averaged conditions was small [147,148]. However, the relationship between the steady flow value and the pulsatile value for each of these metrics with a flexible wall model is too complicated and contains too much variability to base life-changing decisions on a steady flow assumption and account for pulsatile flow with a simple correlation.

Regardless of trends, the use of different flow pulsatility conditions affects all of the hemodynamic metrics calculated in this study. The importance of accurately modeling the patient-specific physiology with proper anatomy, flexibility, and flow boundary conditions – including pulsatility – cannot be understated.

8.5 Viscous Dissipation Relationship to Power Loss

A comparison between viscous dissipation and power loss as hemodynamic metrics was conducted, exploring the problems power loss faces as an adequate metric for future studies.

Viscous dissipation is an adequate solution to the problems present with the power loss as a hemodynamic metric because it maintains physical meaning, is calculable from

clinically-available data, and it is relatable to patient outcomes through statistical relationships to apparent power loss. The viscous dissipation term derivation from differential conservation of energy analysis showed that a volume-integrated viscous dissipation term was equal to the true power lost in the TCPC without any invalid assumptions. The viscous dissipation terms calculated in this study were derived from a time-resolved three-dimensional velocity fields, and do not require pressure measurements. Both the non-indexed and indexed viscous dissipation term are statistically relatable to apparent power loss and indexed power loss, respectively, for the *in silico* BH patient-specific condition across multiple patients. Thus, the indexed viscous dissipation term from this study should be added to future studies as an additional hemodynamic metric.

9 RECOMMENDATIONS AND FUTURE WORK

9.1 Recommendations

This study on the effects of respiration, exercise, and pulsatility on *in vitro* Fontan hemodynamics is by no means all-inclusive or final. It does not answer every question. In fact, quite the opposite is true. Regardless, there are some lessons learned from this study that are important toward the future directions of the field.

First, the study findings conclusively recommend the use of flexible-walled TCPC models when analyzing Fontan hemodynamics. Admittedly, the Fontan models used in this study were homogeneous, and the study results are not directly compared to results from rigid-walled models to determine its relative importance to other factors (anatomy, flow conditions, etc.). However, the ability to adequately model Fontan connection flows with acceptable error proves that flexible modelling is possible. The *in vivo* information undoubtedly states that flexible modelling is required. So, flexible modelling should be adopted. The next step along this vein is to account for the heterogeneous nature of the *in vivo* Fontan connection. The main obstacle in employing a heterogeneous model in this study was the optical access required for the PIV data collection.

Second, this study's findings recommend careful attention be paid to the physiological condition behind all Fontan hemodynamic analyses. The tremendous variability in velocity fields produced by the different experimental conditions in this study result in large changes in patient-relevant outcomes. Though not always explicitly visualized, these velocity field variations will be present for any *in vivo*, *in vitro*, or *in silico* studies. Thus, all studies should note the general finding that small changes in Fontan

connection boundary conditions can have large effects on patient-relevant metrics, and take extra care in assigning and characterizing these conditions.

Third, this study advocates for the continued use of the viscous dissipation term as an important metric potentially relatable to patient outcomes. The apparent power loss metric established in the literature is a construct of the Bernoulli equation assuming steady flow and constant control surface boundary conditions. These assumptions break down in the presence of pulsatile flow (see section 6.5). Conducting future studies using only apparent power loss and indexed power loss as efficiency-related metrics may confound future findings and patient outcome relationships. As engineering procedures advance to include more complex patient-specific modeling the metrics to relate findings from these models and simulations to patient outcomes must include the effect of the modeling advancements, or else the extra effort to advance the model provides very little clinical impact.

9.2 Future Work

Future work examining Fontan hemodynamics relatable to patient outcomes should include efforts to overcome some of the limitations from this study.

The first limitation to address is the simplified material properties this study used to characterize TCPC compliance. The most advanced work toward modelling the heterogeneous nature of the TCPC exists in a study from Long et al [45]. Without the optical access requirement of an *in vitro* study seeking velocity field information, Long et al was able to assign different material properties according to the computational mesh spatial location. Long et al then performed fluid structure interaction simulations and drew

conclusions on the influence of variable wall properties. What remains is verification of the Long et al model, both from a material property and fluid dynamics perspective.

The second limitation to address is the inability to assess long-term Fontan circulation changes with the current *in vitro* model. This limitation also exists for the current computational and animal Fontan circulation models. Adding chronic outcomes to these models will require an extensive understanding of Fontan circulation growth and remodeling, which is currently not well understood. This understanding will, most likely, require an extensive, long-term clinical data collection study encompassing several years to decades. The most promising source of retrospective data may be The Australian and New Zealand Fontan Registry, an extensive database of thousands of Fontan patients spanning decades.

The third limitation to address is the stereoscopic PIV and volumetric interpolation methods used to acquire the volumetric velocity fields. The post-acquisition plane alignment and interpolation introduce uncertainties which can possibly be decreased if a volumetric PIV method were followed instead. Tracking the TCPC wall motion to replace the static boundary used in the spatial and temporal interpolation method will also improve velocity field accuracy.

The final limitation to be addressed by future work is to acquire PIV data which includes the hepatic veins. This eliminates the need to assume that the hepatic factor is evenly distributed at the seeding plane location for hepatic flow distribution calculations.

Ultimately, Fontan circulation *in vitro* modeling needs to advance each of the above listed areas because of its pivotal role in addressing biomedical engineering issues related to patient outcomes. The advancement of medical technology, either through medical

device development or medical procedural changes, is best accomplished through the multi-prong approach of *in vivo*, *in vitro*, computational, animal testing, and clinical trials. *In vitro* tests play a pivotal role in providing a middle ground between *in vivo*, animal testing, and clinical trials, which provide limited information about true physiology, and computational models, which provide almost boundless information about a modelled physiology. The middle ground consists of true physics (fluid dynamics, solid mechanics, etc.) of a modelled physiology useful for repeatable testing that provides more information (can be examined more invasively) than *in vivo* studies, but less information than computational studies. Thus, the key to every *in vitro* study and its effectiveness in furthering medical technology is in its modelling limitations. By identifying and eliminating these limitations, *in vitro* studies will continue to play a pivotal role in biomedical engineering.

With as many modelling limitations overcome as possible, the next stage for Fontan patients in general is to transition from a palliative to a curative procedure. The underlying issue for all Fontan patients is their fundamentally different circulatory system. The lack of a pulmonary support pump leads to the numerous comorbidities and complications they endure [156]. One future avenue for eliminating these complications is to provide a mechanical pump. Mechanical pumps already exist as ventricular assist devices (VADs) for congestive heart failure patients, and studies exist examining some existing VAD designs for efficacy in the Fontan connection [104,157]. Significant obstacles regarding growth and remodeling, flow pulsatility, VAD preload requirements, and Fontan connection afterload remain before existing VADs can be used in Fontan patients. These should be the subject of future work in order to most quickly impact Fontan patients.

10 FUNDING SOURCES

This study was funded by an NIH R01 grant (HL098252) focused on the effect of Fontan hemodynamics on patient outcomes, as well as Dr. Ajit Yoganthan's discretionary funds.

APPENDIX A: LABVIEW VIRTUAL INSTRUMENT

The LabVIEW virtual instrument used to control the pulsatile piston pump, trigger imaging systems, and record pressure and flow measurements was composed of an active waveform display on the left-hand side and various control panels on the right with different display, calculations, calibration, and output settings. Figure 11-1 shows the panel with display settings. Figure 11-2 shows the panel with calculations settings. Figure 11-3 shows the panel with calibration settings. Figure 11-4 shows the panel with output settings.

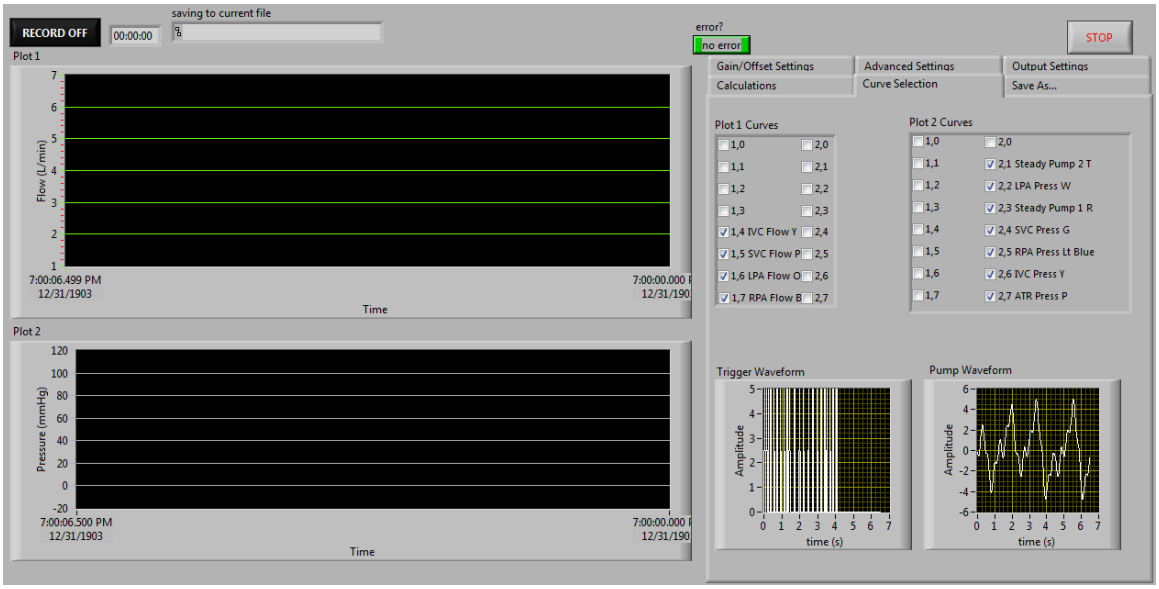

Figure 11-1: LabVIEW virtual instrument with plot display settings panel. The Plot 1 and Plot 2 curves settings are used to display different channels in the plots on the left. The two plots in the lower right display the analog output signals generated by the virtual instrument.

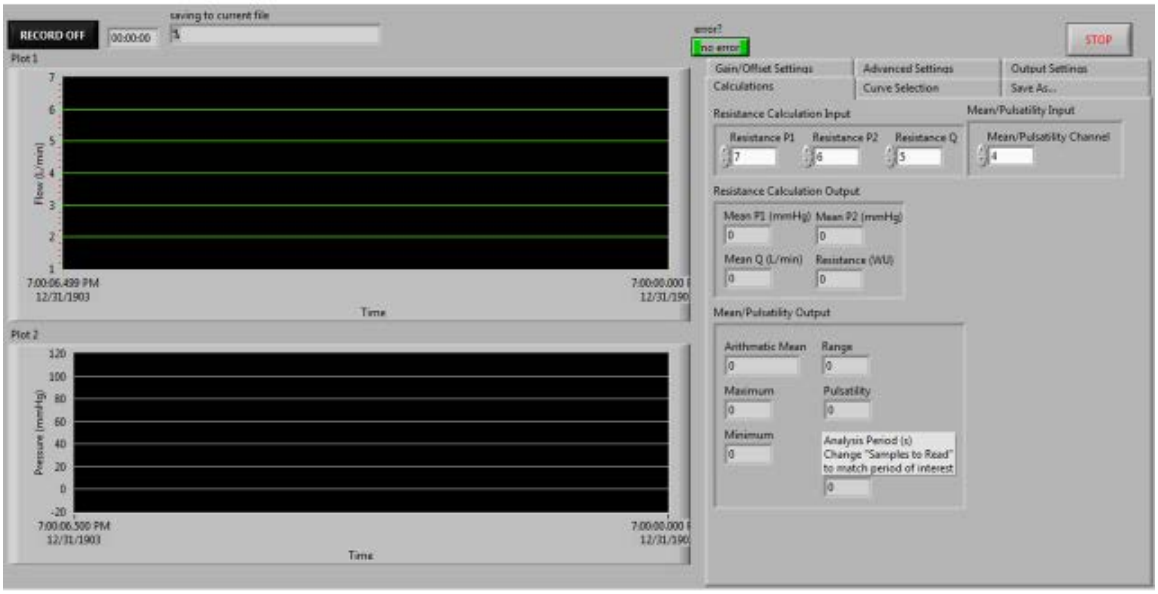

Figure 11-2: LabVIEW virtual instrument with calculations settings panel. The Resistance Calculation Input and Mean/Pulsatility Channel boxes are used to specify the input channel number (0-15) for the calculations displayed below. The analysis period displays the time, in seconds, over which the calculated numbers take place.

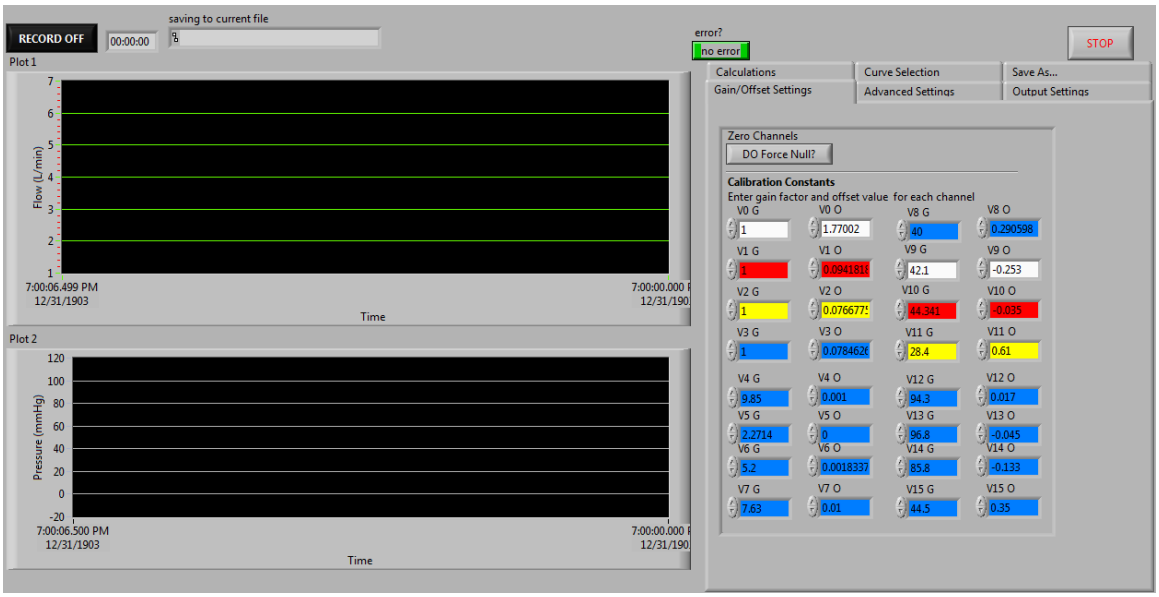

Figure 11-3: LabVIEW virtual instrument with calibration settings panel. This panel is used to specify the linear relationship between the analog input signal (V) and its respective metric value (L/min or mmHg) using a gain (G) and offset (O) for each channel. The DO Force Null? button can be used to force all readings to zero by modification of their respective offset values. All values can also be altered manually.

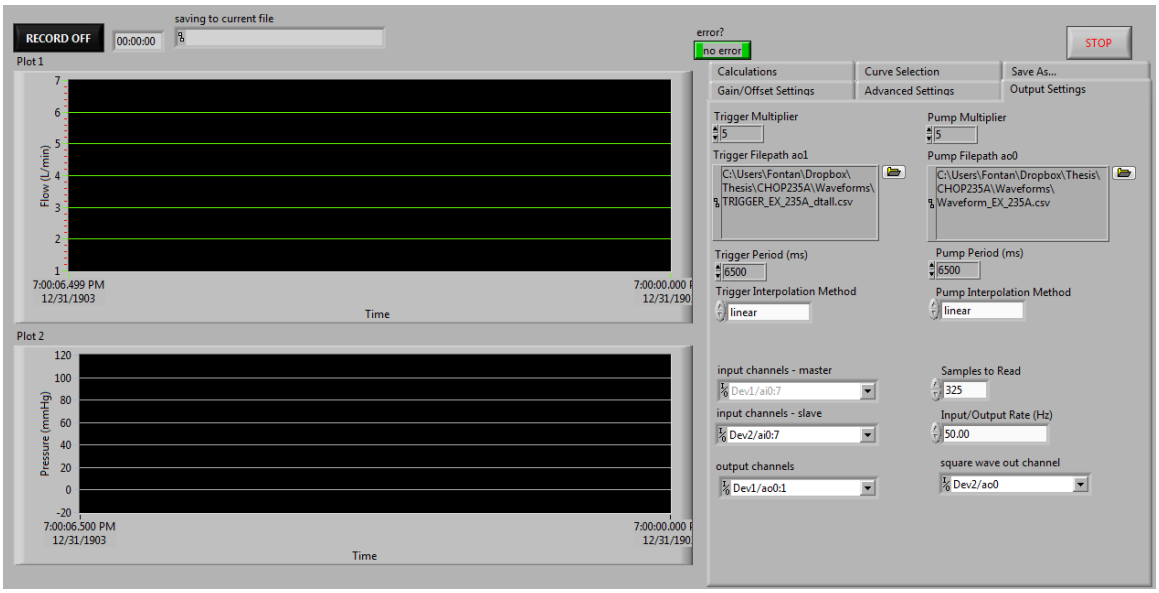

Figure 11-4: LabVIEW virtual instrument with output settings panel. The trigger and pump filepath boxes specify the custom waveform file location (.csv format) on the computer hard drive. The multiplier and period boxes (above and below) specify the custom waveform amplitude gain and time period, respectively. The input and output channels boxes specify the DAQ devices and channels used. The Input/Output Rate box specifiys the data sampling and created waveform frequency. The Samples to Read box specifies the number of samples (at the Input/Output Rate box frequency) to use when calculating metrics and displaying plots on the left.

APPENDIX B: SEGMENT FLOW ANALYSIS

The following content is chapter 22 from the Medviso Segment v1.9 user's manual. This chapter addresses flow analysis and was used in the acquisition of patient-specific flow data.

22 Flow Analysis

This functionality may depend on your MRI scanner. Currently it has been tested using Siemens, Philips and GE scanners.

When flow image stacks are displayed, the screen should now similar to what is shown in Figure 34. On the left image panel the magnitude image is shown and on the right image panel the phase image is shown. When a flow image stack is selected a white frame around both the magnitude image and phase image is drawn in the thumbnail preview area. This helps to keep track of which phase images belongs to which magnitude images.

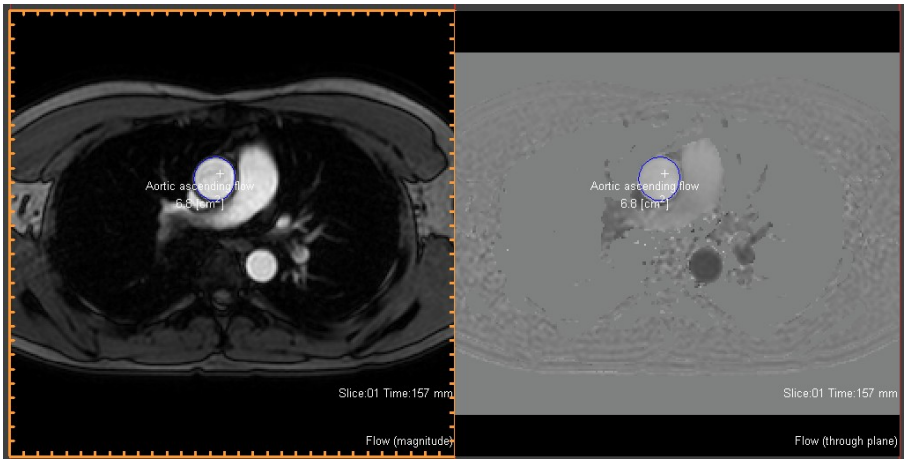

Figure 34: Example of main GUI in flow mode.

22.1 Automatic segmentation of flow ROI's

The suggested method is to select the ROI tool  . Then draw a rough outline of the vessel contour. Thereafter start the automated vessel tracking and refine. This is done by pressing Ctrl-T.

Another method to automatically segment a vessel is to drag the center cursor (white +) to the approximate center of the desired vessel and press Ctrl-G, or Auto delineate a vessel under the Segmentation→ROI and Flow Tools menu. The vessel is automatically delineated and you are asked for an appropriate label. Deleting, renaming, recoloring the region of interest is described in Chapter 17. If you are not satisfied with the ROI there are two methods that can be applied.

22.1.1 Refine

Refine operation operates on the current time frame or all time frames depending on the single frame mode checkbox. Short key for the refine function is Ctrl-R. You need to have the ROI pen active when using the hot key. Refine on all time frames is particularly useful if the vessel is fairly round and not too close to other surrounding tissue.

22.1.2 Refine and propagate

Start at the first time frame of the time series. If pleased with the result simply use the right arrow key on the keyboard to proceed to next time frame. When you find a time frame where you are not pleased with the segmentation use the ROI pen to adjust the contour or use the refine option Ctrl-R with the single frame mode checkbox enabled. Continue by propagating the contour by pressing Ctrl-F.

22.1.3 Shrink flow ROI

If the RIO is outside the vessel then it might be advantageous to shrink the ROI followed by one or more refine operations. Shrink flow ROI is found under the Segmentation menu and the submenu ROI and Flow tools.

22.2 Plotting the result of the flow analysis

The flow plotting utility is started by using the icon  or by using the function Plot flow curves under the Flow menu. An example of the graphical user interface is shown in Figure 35.

In the upper right area of the GUI you can select which parameter to plot. The volumes presented in Volume panel of the GUI represents flow integrated between the two vertical red bars. These bar can interactively be moved with the mouse to control the range of the integration. Forward volume is the volume of the flow integrated only over the time frames where the net flow is positive (forward). Backward volume is the volume of the flow integrated only over the time frames where the net flow is negative (back- ward). This should be contrasted to the flow parameter Forward/Backward that plots simultaneously the flow that goes forward and backward of the region of interest. Note that there can be significant backward flow in one time frame even though the net flow is forward in that very time frame. An example on the latter is shown in Figure 36. The sum of the two curves is the same as the net flow that is shown in Figure 35.

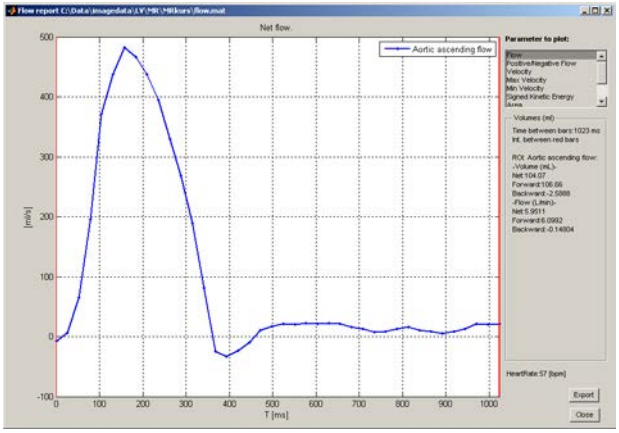

Figure 35: Example of flow plotting GUI. Plotting parameter can be selected in the upper right corner of the GUI. The flow integration is performed between the two red bars.

It is also possible to plot the Velocity over time, and this is shown in Figure 37. The ’error bars’ denote the standard deviation of all pixels in the ROI of that particular time frame.

Another possibility is to plot the max or min velocity in the ROI over time. It is also possible to plot the radius and diameter over time. The radius are calculated as; what diameter need a circular vessel have to have the same area as the area of the ROI. The option Signed Kinetic Energy calculates the kinetic energy in the blood assuming standard density of the blood.

The final possibility is to plot a 3D profile of the velocity distribution of the vessel. This can be plotted for all time frames at once or only a single time frame that later can be stepped forward/backward in time. An example of the 3D plot is shown in Figure 38.

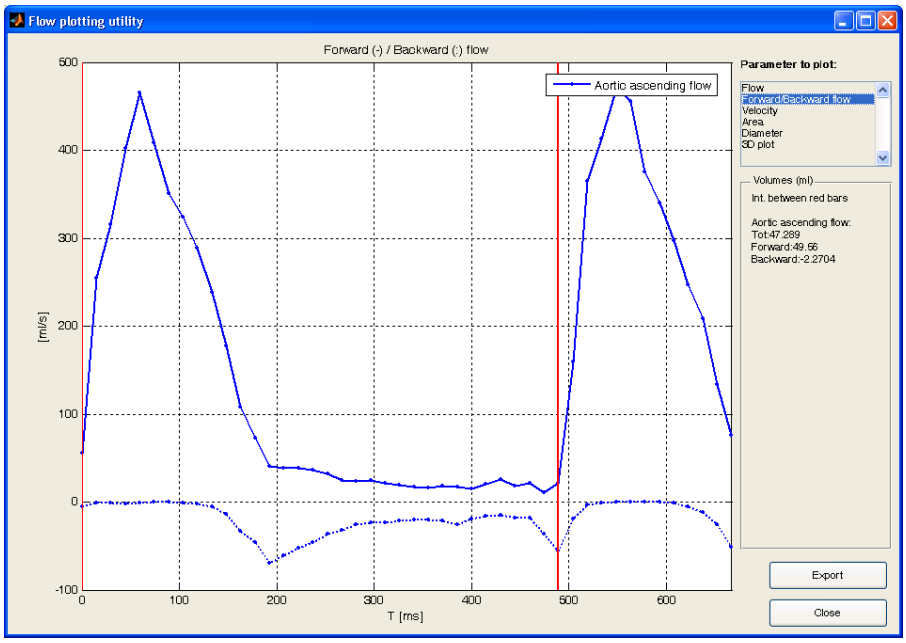

Figure 36: Example of plotting of backwards and forward flow simultaneously. The sum of the two curves will be the net flow showed in Figure 35.

22.3 Compensating for eddy current effects

To get accurate flow measurements it is important to compensate for concomitant field effects such as eddy currents, and Maxwell effects. Ideally Maxwell effects should be compensated for directly on the MRI scanner since it can be analytically calculated. Consult your MRI vendor for details about how this is implemented in your scanner. Note that when compensating for eddy current effects the image stack should not be cropped upon loading, since the algorithm need phase information of static tissue in the chest wall to function properly.

The graphical user interface for compensating for eddy current effects is shown in Figure 39.

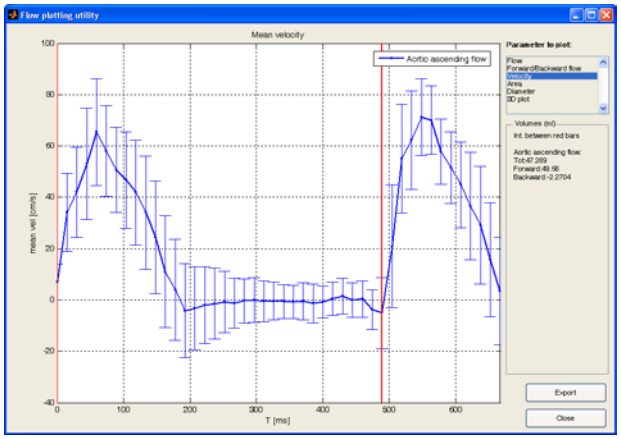

Figure 37: Example of plotting of velocity over time. The ’error’ bars shown the standard deviation of the pixels within the ROI over time.

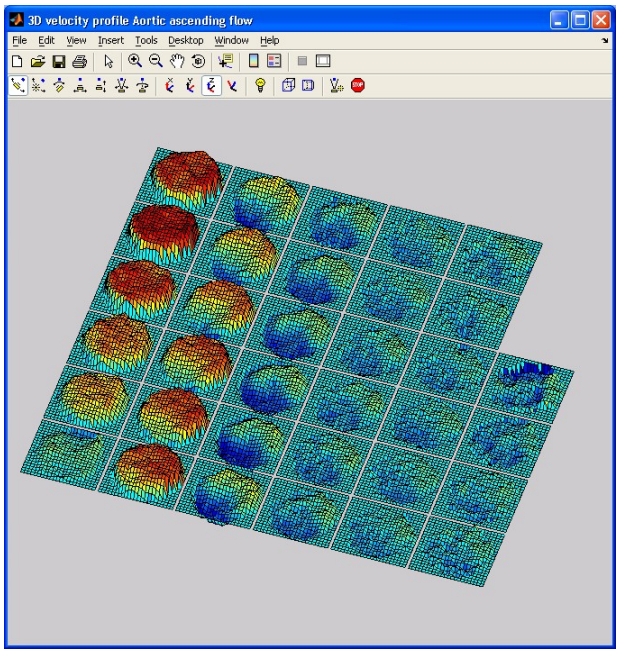

Figure 38: Example of plotting of a 3D profile of the velocity distribution.

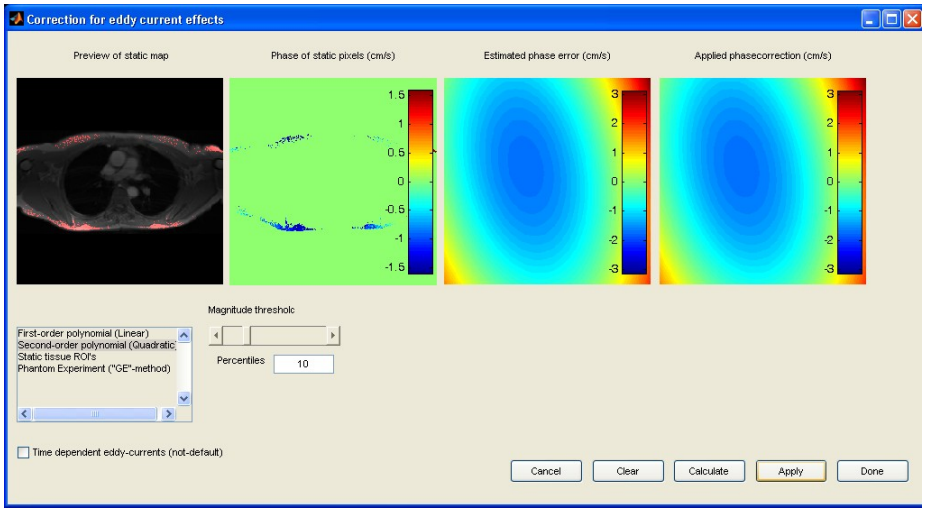

Figure 39: Example graphical user interface for compensating of concomitant field effects. In the left the identified static tissue is the displayed, and in the middle panel the corresponding phase for these pixels is shown, and in the right panel the resulting phase correction is shown.

You can select model order, and clear the phase correction. When you are pleased with the phase correction press Apply to proceed. The function automatically finds stationary parts in the image by selecting a percentage of the pixels whose standard deviation of the phase over time is smallest. The fraction of pixels taken can be controlled

by the edit box Percentile. The image is divided into four quadrants and the algorithm to find stationary pixels is applied to each quadrant separately. This is done to ensure that there are about the same number of pixels from each quadrant. Pixels taken as stationary tissue are shown as red dots in the magnitude image. The Magnitude slider controls what magnitude the pixels need to have before being labeled as stationary. By selecting the mode of operation as Static tissue ROI then ROI's that are labeled Static tissue are taken as stationary areas. This is particularly useful when doing phantom experiments, since the automated identification of static areas fails in cases with stationary row. The mode of operation Phantom Experiment (GE-method) automatically finds a row image stacks that have the same scanning parameters this useful when a static tissue have been scanned in the same position as the patient as recommended by GE for eddy current compensation. For usage, see paper by Alex Chernobelsky et al. [10].

22.4 Phase unwrapping

In cases were the velocity in the blood is higher than the VENC the velocities can wrap around. Under certain conditions these phase wraps can be uncovered and phase unwrapping can be performed to retrieve the correct velocities. The graphical user interface for the phase unwrapping tool is shown in Figure 40

The Show ROI pixels checkbox shows the pixels that are used in the ROI in a red color. This is useful when one want to know exactly what pixels are included in the ROI. The Use Magnitude Mask checkbox is used when one want to limit the automated phase unwrapping only in pixels that have a magnitude over a certain threshold.

22.4.1 Automated Unwrapping

The automated phase unwrapping algorithm works on a pixel by pixel basis and operates along the temporal dimension. It looks for pixels where the phase appears to have wrapped once up and once down. Therefore the algorithm will fail for a biphasic velocity profile if phase wrapping occurs at both phases. Furthermore, it only considers single wrap arounds (i.e the phase is assumed to have wrapped once).

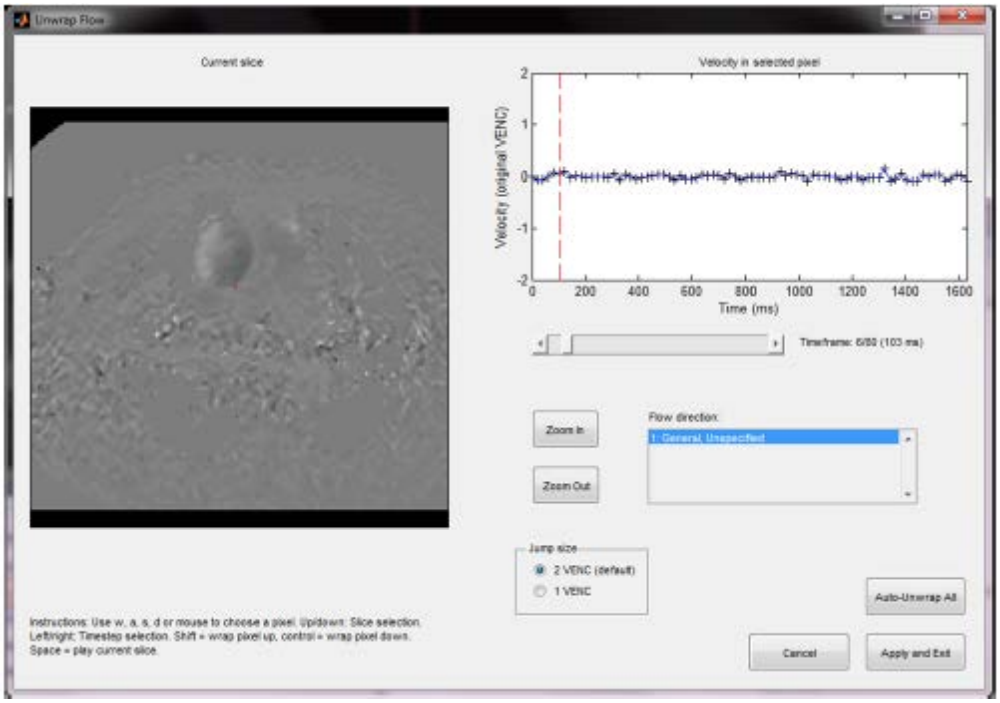

Figure 40: Example of the graphical user interface for phase unwrapping. The left image panel shows the original phase, and the right image panel shows the unwrapped phase. The long slider adjusts the current time frame.

22.5 Creating angio and velocity magnitude images

It is possible to create a so called angio image that is the magnitude image times the velocity magnitude. This is available under the Flow menu and Create Angio. If you have more than one velocity encoding direction it is possible to create a velocity magnitude image that is the square root of the sum of squares of all velocity directions (velocity magnitude).

22.6 Coupling magnitude and flow images

If magnitude and flow image stacks have been loaded into Segment without being coupled to each other, it is possible to couple them using the Couple Magnitude/Phase Flow Image Stacks from the Flow menu. Available magnitude and phase image stacks are then identified and coupled using heuristics.

APPENDIX C: CUSTOM FFT MATLAB SCRIPT

The following custom-built MATLAB script was used to determine the frequency content of a *in vivo* flow data provided for each patient (CHOP11B and CHOP235A):

```
clear all
close all
clc

load waveforms_2016_05_27.mat

%% Frequency Analysis of Each Vessel Signal

% pull in the individual vessel data to be analyzed
data = rpa_ex;                                  % data for specific vessel
N = length(data);                                  % number of discrete data
points
Dt = 0.02002004;                                % time step size (secs) USER
INPUT!
T = N*Dt ;                                      % total time
ffreq = 2*pi/T ;                                % fundamental frequency
t = linspace(0,T,N) ;                           % time vector
f = (1/Dt)*(0:(N/2))/N';                        % frequncy domain
k=0:(N/2-1);                                    % frequency counter
omega=k*ffreq;                                  % in units of rads/sec

% perform a single fft on the entire data
ftilde = data;                                  % re-cast the data
ftilde(1) = (data(1)+data(end))/2 ;
ftilde(end) = [] ;

Fone = fft(ftilde,N) ;                          % perform fft

P2tilde = abs(Fone/N);                          % 2-sided spectrum
P1tilde = P2tilde(1:N/2+1);
P1tilde(2:end-1) = 2*P1tilde(2:end-1);      % single-sided spectrum

h(3) = figure(3);
plot(f,P1tilde)

% perform a BUNCH of ffts on data subsets, and we'll average the result
num = 1000;                                     % number of ffts
P1_sum = 0;                                      % initialize power spectrum
vector
Y_sum = 0;                                             % initialize Foureir
coefficients vector
fft_store = cell(2,num);

% initialize fft store cells
for i = 1:num
    r = rand();
```

```
    begin = floor(1+(N/2-1)*r);           % set random beginning between
1 and N/2
    data_subset = data(begin:end);

    fhat = data_subset;                    % re-cast the data
    fhat(1) = (data_subset(1)+data_subset(end))/2 ;
    fhat(end) = [] ;

    F = fft(fhat,N) ;                      % perform fft

    P2 = abs(F/N);                         % 2-sided spectrum
    P1 = P2(1:N/2+1);
    P1(2:end-1) = 2*P1(2:end-1);           % single-sided spectrum

    fft_store{1,i} = P1;                   % store power spectra
    fft_store{2,i} = F;                    % store fft values

    P1_sum = P1_sum + P1;                  % sum all of the power spectra
vectors to get average later
end

P1_avg = P1_sum./num;                      % average power spectrum

h(1) = figure(1);
plot(f,P1_avg)                             % plot single sided amplitude
spectrum
title('Single-Sided Amplitude Spectrum of X(t)')
xlabel('f (Hz)')
ylabel('|P1(f)|')

% L = 10;
% fapprox = A(1)*ones(size(t));
% for k=1:L
%   %             fapprox   =   fapprox   +   A(k+1)*cos(omega(k+1)*t)   +
B(k+1)*sin(omega(k+1)*t);
% end

% ask for user input
in  =  input('Enter  the  TOTAL  number  of  frequencies  to  be  kept,  NOT
including the zero frequency: ');

freqs = zeros(in,1);
locs = zeros(in,1);

for i = 1:in
    h(1) = figure(1);
    plot(f,P1_avg)
    title('Single-Sided Amplitude Spectrum of X(t)')
    xlabel('f (Hz)')
    ylabel('|P1(f)|')

    datacursormode on
    dcm_obj = datacursormode(h(1));
```

```
    display('Click peak to save frequency, then press Return.')
    pause                                   % Wait while the user does
this.

    c_info = getCursorInfo(dcm_obj);
    freqs(i) = c_info.Position(1);           % store frequencies to be
kept
    locs(i) = find(freqs(i) == f,1);         % store index location of
these frequencies in the frequency vector
end

% Use the coefficients from the SINGLE fft calc rather than the averaged
% The averaged power spectrum from the multiple FFTs was used simpley to
% see the frequency content easier. Averaging out all the Fourier
% coefficients in this case will ruin our reconstruction of the data, so
we
% must only use the single fft calculation when reconstructing.

A = 2*real(Fone)/N;                         % cosine coefficients
A(1)= A(1)/2 ;
B =-2*imag(Fone)/N;                         % sine coefficients

fapprox = A(1)*ones(size(t));
for l=1:length(locs)
    k = locs(l);
    fapprox = fapprox + A(k)*cos(omega(k)*t) + B(k)*sin(omega(k)*t);
end

h(2) = figure(2);
plot(t,data)
hold on
plot(t,fapprox)
```

APPENDIX D: VESSEL FREQUENCY CONTENT

This appendix includes tables of the coefficients and frequencies extracted from MRI flow data that serve as filtered patient-specific waveforms to which the *in vitro* Fontan circulation model was verified. Relate to section 4.2.1.2.

Table 11-1: CHOP11B BH patient-specific pulsatility frequency content

CHOP11B BH				
n	**A_n (cos terms)**	**B_n (sin terms)**	**$\omega_n = 2\pi f_n$**	**f_n (Hz)**
0	37.837	0	0	0
1	2.304	-2.497	6.088	0.969
2	-7.924	0.477	12.177	1.938
3	0.627	0.819	18.265	2.907
4	-0.822	1.172	24.353	3.876
5	-2.062	2.238	30.442	4.845
6	-1.480	2.872	36.530	5.814
7	-0.344	3.352	42.619	6.783
8	0.246	2.915	48.707	7.752
9	0.954	2.706	54.795	8.721
10	1.454	2.581	60.884	9.690
11	2.096	2.197	66.972	10.659
12	2.550	1.736	73.060	11.628
13	2.691	1.149	79.149	12.597
14	2.878	0.575	85.237	13.566

Table 11-2: CHOP11B FB patient-specific pulsatility frequency content

CHOP11B FB				
n	**A_n (cos terms)**	**B_n (sin terms)**	**$\omega_n = 2\pi f_n$**	**f_n (Hz)**
0	50.375	0	0	0
1	-4.813	-4.400	0.316	0.050
2	2.677	1.383	0.631	0.100
3	3.504	4.249	0.947	0.151
4	14.725	-1.822	1.263	0.201
5	6.551	-16.413	1.579	0.251
6	2.128	13.751	1.894	0.301
7	-15.924	8.483	2.210	0.352
8	-10.958	0.580	2.526	0.402
9	3.678	0.118	2.841	0.452
10	-6.173	-5.486	3.157	0.502
12	-1.710	-7.448	3.788	0.603
14	3.439	5.029	4.420	0.703
15	-4.146	4.101	4.736	0.754
17	1.726	0.813	5.367	0.854
18	-5.982	2.089	5.683	0.904
19	-0.832	-8.075	5.998	0.955
20	-2.278	-4.941	6.314	1.005
38	-2.202	-2.765	11.997	1.909

Table 11-3: CHOP11B EX patient-specific pulsatility frequency content

CHOP11B EX				
n	A_n (cos terms)	B_n (sin terms)	$\omega_n = 2\pi f_n$	f_n (Hz)
0	113.674	0	0	0
1	1.727	3.643	0.628	0.100
2	6.386	1.914	1.255	0.200
3	5.828	-0.630	1.883	0.300
4	15.475	-0.305	2.511	0.400
5	-5.059	-3.756	3.138	0.499
6	-0.411	6.525	3.766	0.599
7	-6.485	8.694	4.394	0.699
9	5.267	-8.727	5.649	0.899
10	-9.308	7.242	6.277	0.999
16	3.191	-12.134	10.043	1.598
18	-2.898	-1.988	11.298	1.798
20	2.863	-9.624	12.554	1.998
21	8.266	-4.831	13.181	2.098
23	2.001	-5.120	14.437	2.298
28	1.231	-4.773	17.575	2.797
29	-3.975	8.856	18.203	2.897
30	3.734	-3.922	18.831	2.997
31	-6.584	-2.595	19.458	3.097
38	4.615	3.482	23.852	3.796
39	1.084	-14.482	24.480	3.896
45	9.331	-13.327	28.246	4.495
46	9.824	-3.824	28.874	4.595
47	15.164	6.212	29.501	4.695
48	-16.751	23.731	30.129	4.795
49	17.739	-6.014	30.757	4.895
50	-2.113	-8.036	31.384	4.995
51	0.899	-10.293	32.012	5.095
53	1.424	-6.000	33.268	5.295

Table 11-4: CHOP235A BH patient-specific pulsatility frequency content

CHOP235A BH				
n	A_n (cos terms)	B_n (sin terms)	$\omega_n = 2\pi f_n$	f_n (Hz)
0	38.984	0.000	0.000	0.000
1	4.351	5.884	8.231	1.310
2	-1.425	4.381	16.462	2.620
3	-3.603	-2.625	24.693	3.930
4	-2.619	-0.965	32.924	5.240
5	-0.509	0.421	41.154	6.550
6	-0.440	-0.621	49.385	7.860
7	-0.292	0.064	57.616	9.170
8	-0.628	0.523	65.847	10.480
9	-0.489	0.074	74.078	11.790
10	-0.396	0.539	82.309	13.100
11	-0.578	0.698	90.540	14.410
12	-0.647	0.480	98.771	15.720
13	-0.462	0.601	107.001	17.030
14	-0.494	0.733	115.232	18.340
15	-0.493	0.599	123.463	19.650
16	-0.344	0.666	131.694	20.960
17	-0.292	0.803	139.925	22.270
18	-0.367	0.750	148.156	23.580
19	-0.238	0.788	156.387	24.890
20	-0.210	0.844	164.618	26.200
21	-0.238	0.807	172.849	27.510
22	-0.181	0.896	181.079	28.820
23	-0.112	0.863	189.310	30.130
24	-0.084	0.784	197.541	31.440
25	-0.001	0.812	205.772	32.750
26	0.056	0.825	214.003	34.060
27	0.110	0.818	222.234	35.370
28	0.156	0.822	230.465	36.680
29	0.160	0.794	238.696	37.990
30	0.236	0.779	246.927	39.300
31	0.331	0.752	255.157	40.610
32	0.349	0.717	263.388	41.920
33	0.412	0.708	271.619	43.230
34	0.457	0.701	279.850	44.540
35	0.486	0.650	288.081	45.850
36	0.548	0.634	296.312	47.159

37	0.580	0.612	304.543	48.469
38	0.601	0.568	312.774	49.779
39	0.645	0.526	321.004	51.089
40	0.681	0.492	329.235	52.399
41	0.696	0.442	337.466	53.709
42	0.730	0.395	345.697	55.019
43	0.766	0.367	353.928	56.329
44	0.762	0.313	362.159	57.639
45	0.783	0.250	370.390	58.949
46	0.805	0.210	378.621	60.259
47	0.804	0.164	386.852	61.569
48	0.825	0.118	395.082	62.879
49	0.821	0.057	403.313	64.189

Table 11-5: CHOP235A FB patient-specific pulsatility frequency content

CHOP235A FB				
n	A_n (cos terms)	B_n (sin terms)	$\omega_n = 2\pi f_n$	f_n (Hz)
0	36.608	0.000	0.000	0.000
1	5.728	-0.053	0.316	0.050
2	3.087	-0.866	0.632	0.101
3	4.376	2.969	0.949	0.151
4	2.224	-0.825	1.265	0.201
5	20.811	-2.485	1.581	0.252
6	5.354	0.788	1.897	0.302
7	1.617	3.956	2.213	0.352
8	-1.709	4.807	2.530	0.403
9	-4.188	2.118	2.846	0.453
10	9.423	-0.191	3.162	0.503
11	0.474	0.706	3.478	0.554
12	-2.738	1.448	3.794	0.604
13	-3.801	0.440	4.111	0.654
14	-3.950	-3.431	4.427	0.705
15	0.109	-1.452	4.743	0.755
16	-0.743	-2.669	5.376	0.856
17	-0.201	-2.125	5.692	0.906
18	-1.282	-6.756	6.008	0.956
19	-7.525	-0.333	6.324	1.007
20	0.362	2.960	6.640	1.057
21	-0.746	2.745	6.957	1.107
22	4.086	1.236	7.273	1.157
23	2.552	-1.052	7.589	1.208
24	-2.413	-0.192	8.538	1.359
25	0.496	-2.150	10.119	1.610
26	-3.135	-2.063	12.332	1.963
27	-0.545	2.687	12.648	2.013
28	0.985	2.785	28.142	4.479
29	2.198	0.843	28.459	4.529
30	0.678	-2.241	29.724	4.731

Table 11-6: CHOP235A EX patient-specific pulsatility frequency content

CHOP235A EX				
n	**A_n (cos terms)**	**B_n (sin terms)**	**$\omega_n = 2\pi f_n$**	**f_n (Hz)**
0	77.981	0.000	0.000	0.000
1	-13.317	6.851	0.624	0.099
2	-6.536	0.440	1.247	0.199
3	-12.169	6.102	1.871	0.298
4	17.338	-7.174	2.495	0.397
5	-29.383	-2.079	3.119	0.496
6	29.857	23.892	3.742	0.596
7	2.262	24.937	4.366	0.695
8	12.264	0.184	4.990	0.794
9	10.817	-7.215	5.613	0.893
10	10.168	0.211	6.861	1.092
11	-18.086	-2.376	8.108	1.290
12	2.268	-13.457	18.087	2.879
13	3.095	8.715	24.948	3.971

APPENDIX E: COMPREHENSIVE EXPERIMENTAL CONDITIONS

The following table, Table 11-7, provides a comprehensive list of metrics describing the experimental conditions conducted in this study. These metrics are derived from the hemodynamic results.

Table 11-7: Comprehensive table of experimental conditions metrics

Model	Condition		Mean Inflow Rate (IVC+SVC) (L/min)	IVC:SVC Flow Ratio (%)	LPA:RPA Flow Ratio (%)	IVC Pulsatility (%)
CHOP11B	BH	Steady	3.28	73.9	46.9	0
		Patient-Specific	3.2	75.1	45.9	33.4
		Low Pulsatility	3.22	73.8	46.9	12.7
		High Pulsatility	3.21	74.1	45.9	57.5
	FB	Steady	3.9	75.8	47.4	0
		Patient-Specific	4.04	76.3	56.4	84.8
	EX	Peak Steady	8.21	77.6	43.5	0
		Peak Patient-Specific	7.90	79.3	43.1	101.1
		Half-Peak Steady	6.08	78.5	47.0	0
		Half-Peak Pulsatile	5.95	77.8	46.1	93.4
CHOP235A	BH	Steady	3.10	79.0	23.5	0
		Patient-Specific	3.10	76.8	23.0	31.9
		Low Pulsatility	3.09	77.0	18.6	22.0
		High Pulsatility	3.21	77.3	23.1	38.6
	FB	Steady	4.96	43.9	25.1	0
		Patient-Specific	4.96	43.8	25.3	115.2
	EX	Peak Steady	6.98	52.6	22.7	0
		Peak Patient-Specific	7.08	48.2	25.3	126.4
		Half-Peak Steady	6.22	47.3	26.8	0
		Half-Peak Pulsatile	6.20	47.4	25.1	118.4

APPENDIX F: PIV ACQUISITION IMAGE CONVERSION STUDY

The purpose of this short study was to determine the number of images required to insure velocity field convergence of PIV data. The velocity field data is acquired over a transient flow profile at specific time points (see Figure 4-10 for example), and then ensemble averaged over several flow profile cycles. The number of cycles (with one image pair per cycle) required to converge the ensemble average velocity field is the quantity in question. If an adequate number of images is not acquired, the resulting ensemble velocity field data is inaccurate. However, acquiring an excessive number of cycles increases acquisition time and required data storage space.

The number of cycles over which to acquire images for each time point was determined by collecting a large number of images for a representative time point and iteratively processing an increasing number of these images until changes in the ensemble average velocity field became increasingly small. The processing method conducted for this convergence study was the same as for all PIV processed images, as outlined in section 4.2.2.2.4. The representative time point chosen was from the CHOP11B Peak Exercise condition during maximum IVC inflow. This point was chosen because it was the maximum Reynolds number across all data acquisition conditions, and thus possessed the most potential for time-dependent inconsistencies. Convergence analysis was conducted by collecting 200 image pairs at this time point, and subtracting the processed velocity field of the 200 image pairs from an increasing number of processed image pairs in 25 image increments. The resulting velocity field then included a velocity difference at each spatial location (see Figure 11-5) , which was summed across all locations.

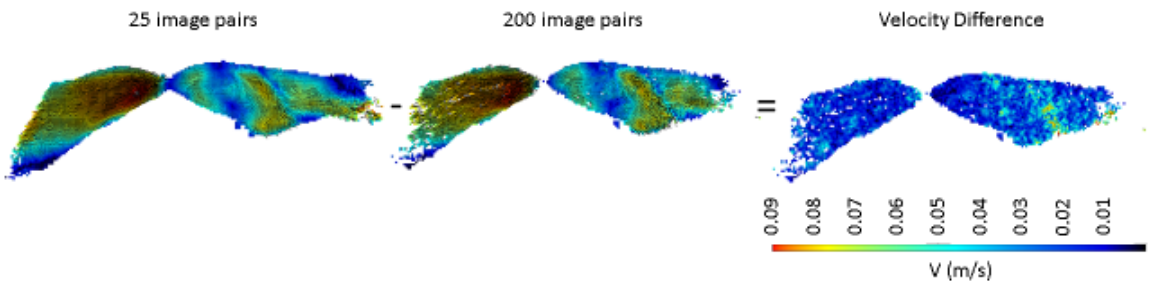

Figure 11-5: PIV image convergence study example calculation of velocity difference

The ensemble average velocity field was considered converged when the velocity difference equaled zero. Figure 11-6 displays the total velocity difference value for each number of image pairs calculated, for each image sampling plane of the model.

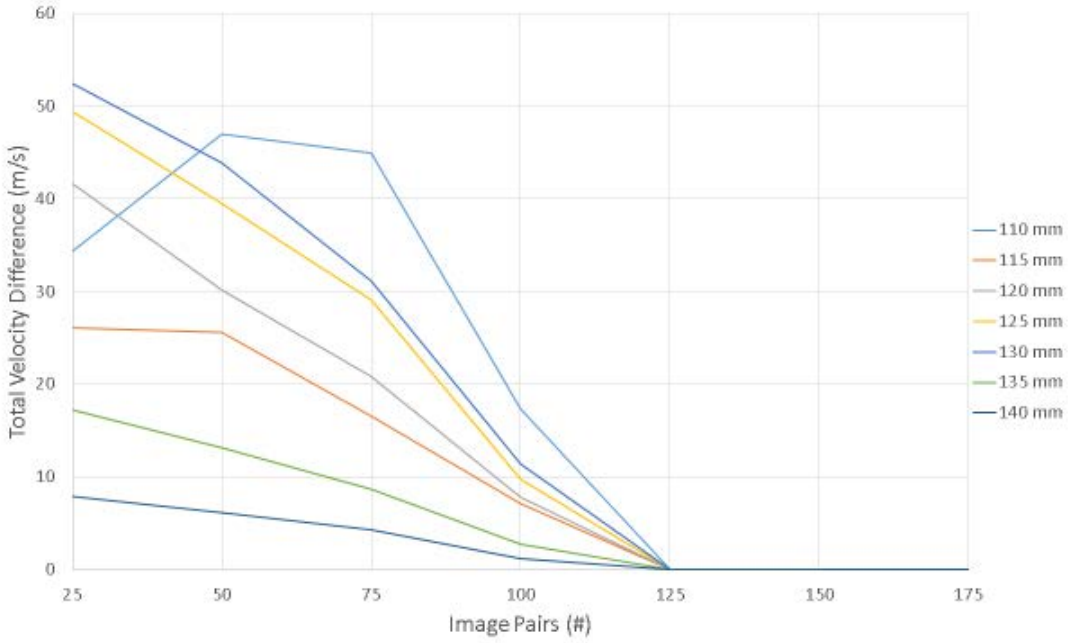

Figure 11-6: Total velocity difference value for each convergence study calculation

The results of the convergence study show that each PIV measurement plane possesses ensemble average velocity field convergence at 125 image pairs. Thus, the PIV acquisition was set at 150 image pairs for conservative purposes.

APPENDIX G: PIV VELOCITY FIELD ANALYSIS STATE MACHINES AND SCRIPTS

G.1 Plane Alignment

The plane alignment ParaView state machine used for PIV velocity field analysis methods in section 4.2.2.2.5.1 was copied and saved for each condition analyzed. A screen shot of the state machine in use for the CHOP11B BH patient-specific pulsatility condition is shown in Figure 11-7.

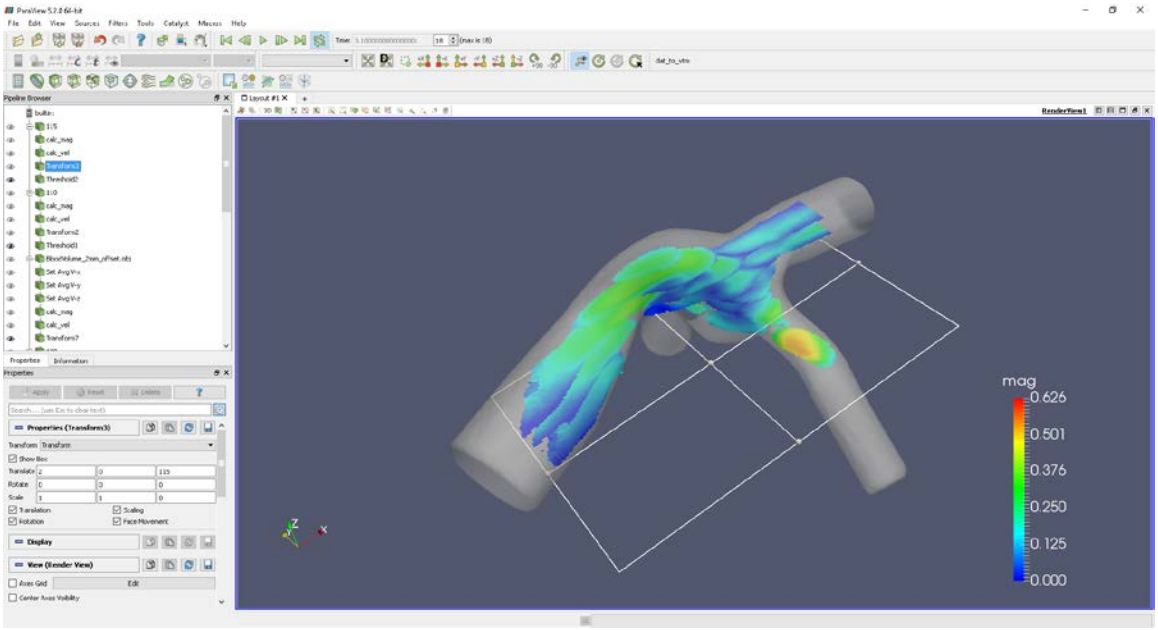

Figure 11-7: AlignPlanes.pvsm screenshot showing the mechanism for aligning the planes of an acquisition in space

G.2 Concatenate Points

The following custom MATLAB script takes the velocity data points on each plane and the TCPC model and concatenates them together into a single data set.

```
% Concatenate Planes and TCPC
% This script takes the aligned experimental planes and TCPC surface and
% combines their point files into a single point file, for each time step
```

```
% Creates the CSV file series named "AllPoints" for import into Paraview

clear all
clc
%% User Input

FolderLoc = 'Z:\PIV\11B\BH_EX_PK\BH_Puls_High_PostProcessing\saves\';
LastFileNum = 44;
PlaneNames = {'110', '115', '120', '125', '130', '135', '140'};
filenameMid='0.';
filenamePostfix='.csv';

TCPCfilename = 'tcpc.0.csv';

WriteNamePrefix = 'AllPoints_';
WriteNamePostfix = '.csv';

%%
for i = 1:LastFileNum+1
    AllPoints = [];
    FileNum = i-1;
    for j = 1:length(PlaneNames);
        PlaneName = PlaneNames{j};
        FileName                                                    =
strcat(PlaneName,filenameMid,num2str(FileNum,'%d'),filenamePostfix);
        CSV = csvread(FileName,1,3);
        AllPoints = [AllPoints; CSV];
    end
    % Add TCPC to each time step and make sure that the matrix saved has
    % unique rows
    AllPointsTime = AllPoints;
    TCPCfile = strcat(FolderLoc,TCPCfilename);
    TCPCCSV = csvread(TCPCfile,1,6);
    AllPointsTime = [AllPointsTime; TCPCCSV];
    AllPointsTime = unique(AllPointsTime, 'Rows');

    % allocate names for table
    Vx = AllPointsTime(:,1);
    Vy = AllPointsTime(:,2);
    Vz = AllPointsTime(:,3);
    Mag = AllPointsTime(:,4);
    PointsX = AllPointsTime(:,5);
    PointsY = AllPointsTime(:,6);
    PointsZ = AllPointsTime(:,7);

    % Create a table from the saved arrays
    T = table(Vx, Vy, Vz, Mag, PointsX, PointsY, PointsZ);

    % Save the table as a CSV file for import into Paraview
    SaveName                                                    =
strcat(FolderLoc,WriteNamePrefix,num2str(FileNum,'%d'),WriteNamePostfix
);
    writetable(T,SaveName);
```

```
    % display time step just finished
    TimeStep = i-1
end
```

G.3 Spatial and Temporal Interpolation

The spatial and temporal interpolation ParaView state machine used for PIV velocity field analysis methods in section 4.2.2.2.5.1 was copied and saved for each condition analyzed. A screen shot of the state machine in use for the CHOP11B BH patient-specific pulsatility condition is shown in Figure 11-8.

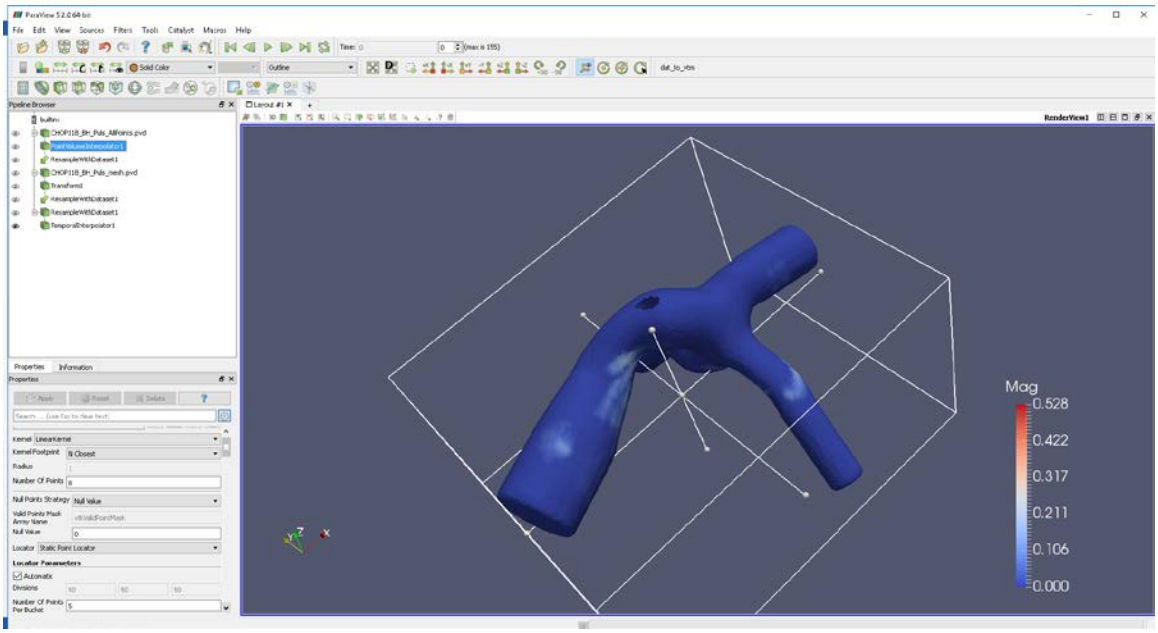

Figure 11-8: Interpolate.pvsm screenshot showing the spatial interpolation filter properties

G.4 Spatial Interpolation Verification

The spatial interpolation scheme described in section 4.2.2.2.5.2 was verified for accuracy using a virtual data set. The virtual data set consisted of computational fluid dynamics (CFD) results of an idealized TCPC anatomy. The CFD results included velocity and pressure values dispersed on a 3-dimensional mesh. Velocity magnitude was selected as the comparison metric. The verification process consisted of sampling the virtual data set with 6 slices normal to the z-direction. These slices then underwent the same spatial

interpolation scheme described in section 4.2.2.2.5.2, as if they were the experimentally-collected PIV slices. The true virtual data set and the interpolated virtual data set were then sampled at a z-normal plane not equal to any of the 6 z-normal planes used in the interpolation.

Qualitative comparison of the true and interpolated data sets shows excellent fluid flow structure agreement, as seen in Figure 11-9.

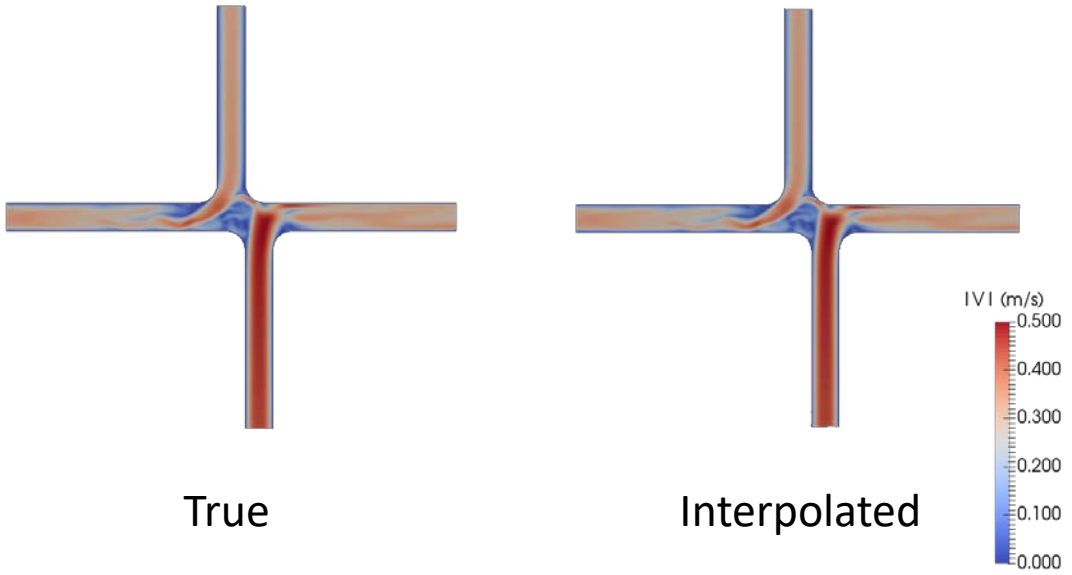

Figure 11-9: Qualitative comparison on true and interpolated data for spatial interpolation verification

G.5 Hepatic Flow Distribution Calculation

Hepatic flow distribution was calculated in a ParaView state machine employing the PIV velocity field analysis methods in section 4.2.2.2.5.1, and was copied and saved for each condition analyzed. A screen shot of the state machine in use for the CHOP11B BH patient-specific pulsatility condition is shown in Figure 11-11. Figure 11-10 shows a quantitative comparison of the two data, which was determined by subtracting the velocity magnitude values of the interpolated data from the true data.

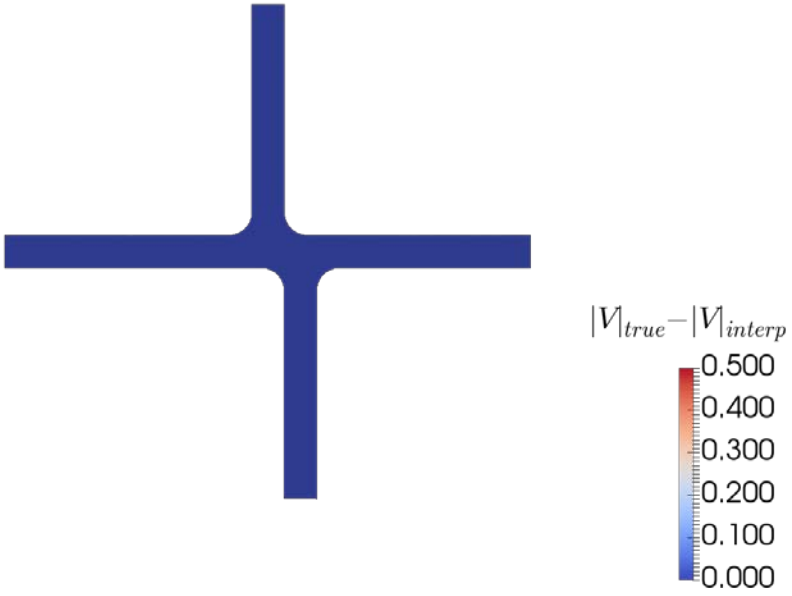

Figure 11-10: Quantitative comparison of true and interpolated data toward verification of the spatial interpolation scheme used.

Summing the velocity magnitude difference between each data set resulted in an interpolation error of less than 1%. Thus, the spatial interpolation scheme used is considered verified.

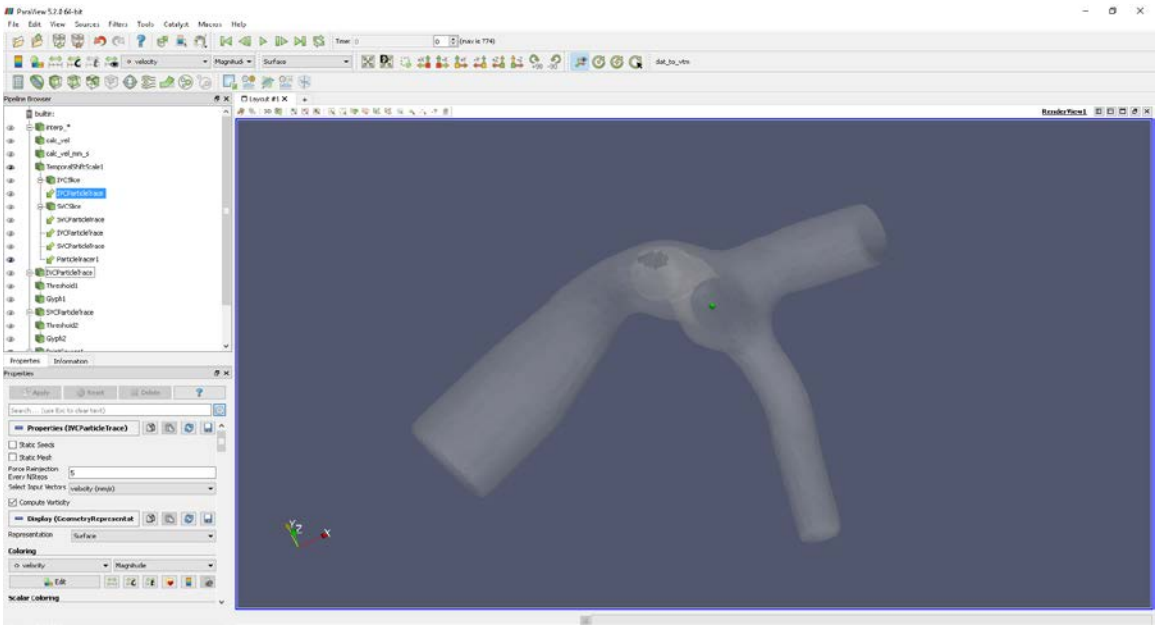

Figure 11-11: HFD.pvsm screenshot showing the particle tracer filter properties

G.6 Viscous Dissipation Term Calculation

The viscous dissipation rate term was calculated in a ParaView state machine employing the PIV velocity field analysis methods in section 4.2.2.2.5.1, and was copied and saved for each condition analyzed. A screen shot of the state machine in use for the CHOP11B BH patient-specific pulsatility condition is shown in Figure 11-12.

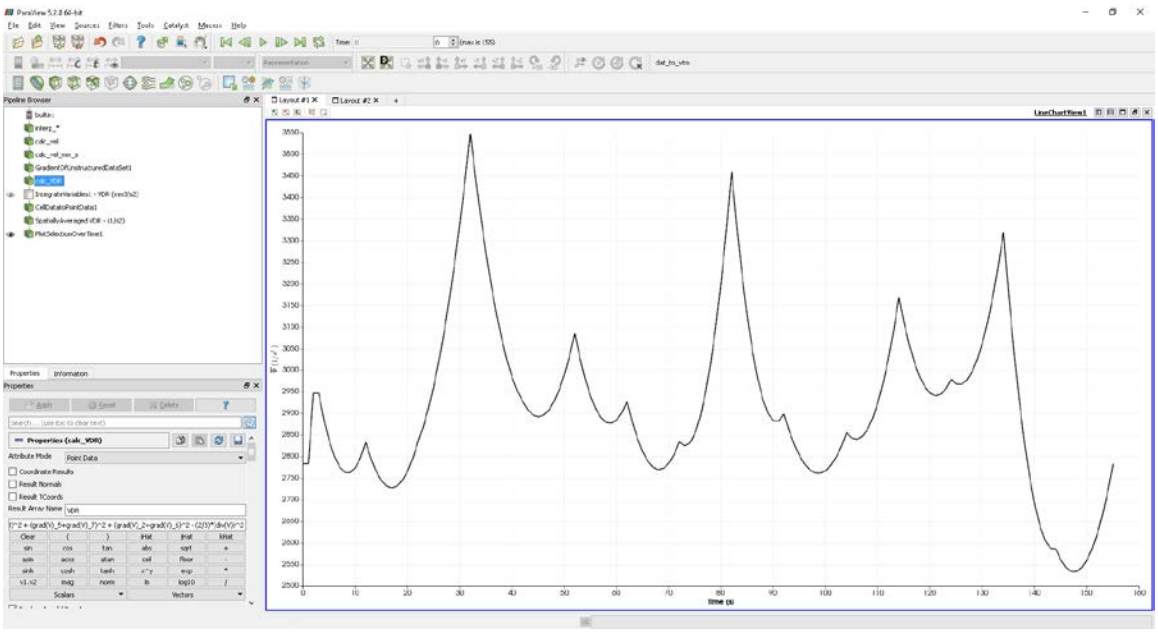

Figure 11-12: VD.pvsm screenshot showing the viscous dissipation rate calculator filter properties

APPENDIX H: PIV UNCERTAINTY DETAILS

PIV measurement uncertainty was quantified following the method outlined by Raffel, et al [142]. Error measurements were taken from the steady flow versions of the patient-specific conditions for each model. The total measurement uncertainty was divided into 3 error forms: particle lag error, ε_p, bias error, ε_b, and random error, ε_r. These individual error were calculated for a 95% confidence interval, and combined into a total error, ε_T, using the same RSS method found in Equation (4-11). All errors were calculated for each velocity component (V_x, V_y, and V_z), as both a velocity value and a percentage of the maximum velocity.

Particle lag error considers the tracer particle relaxation time, τ_s, compared to the velocity field characteristic time, τ_f . The particle relaxation time is estimated in [142], and the estimation is found in Equation (11-1).

$$\tau_s = \frac{d^2}{\upsilon} \tag{11-1}$$

where d is the particle diameter and υ is the fluid kinematic viscosity. When compared to the velocity field characteristic time (calculated from the smallest physical diameter and the maximum velocity for each model over all conditions), the τ_f: τ_s ratio is on the order of $1x10^{-10}$. Physically, there is this order of time delay between when the fluid changes and when the particle is affected by these changes. Thus, the particle lag error is considered negligible. Particle lag error is considered equal to 0 for all total error calculations.

Bias error was determined by plotting the probability density function of the instantaneous velocity data. By binning the velocity distributions in varying size, the maximum pixel fraction where peak locking effects may exist was recorded, and equated

to the direction-specific bias error. Random error was evaluated as ten percent of the particle image diameter (in pixels), again, according to [142].

Table 11-8 and Table 11-9 summarize the PIV error calculations for CHOP11B. Table 11-10 and Table 11-11 summarize the PIV error calculations for CHOP235.

Table 11-8: CHOP11B PIV error metrics acquired from processed data. These metrics were used in error calculations shown in the next table

Condition		Plane (mm)	D (px)	PL_x (px)	PL_y (px)	PL_z(px)	$V_{max,x}$ (m/s)	$V_{max,y}$ (m/s)	$V_{max,z}$ (m/s)	Conversion (px/m/s)
BH	Steady	110	0.950	0.333	0.333	0.500	0.193	0.627	0.077	25.977
		115	0.950	0.333	0.333	0.500	0.216	0.457	0.078	25.978
		120	0.950	0.333	0.500	0.500	0.133	0.157	0.069	31.750
		125	0.975	0.032	0.032	0.500	0.329	0.151	0.055	28.864
		130	1.000	0.071	0.071	0.500	0.386	0.203	0.090	23.091
		135	1.100	0.200	0.032	0.500	0.377	0.164	0.081	23.091
		140	1.100	0.032	0.032	0.167	0.304	0.193	0.038	23.091
FB	Steady	110	0.900	0.032	0.032	0.032	0.112	0.322	0.099	43.296
		115	0.875	0.250	0.250	0.333	0.150	0.271	0.094	31.750
		120	0.925	0.032	0.032	0.500	0.167	0.201	0.083	31.750
		125	0.975	0.032	0.032	0.500	0.343	0.170	0.066	31.750
		130	1.025	0.032	0.032	0.333	0.466	0.182	0.053	31.750
		135	1.100	0.032	0.032	0.032	0.457	0.207	0.045	23.091
		140	1.100	0.032	0.032	0.250	0.382	0.239	0.059	21.648
EX	Peak Steady	110	1.075	0.032	0.032	0.032	0.337	0.836	0.199	18.762
		115	1.025	0.032	0.032	0.500	0.274	0.572	0.156	18.761
		120	1.050	0.032	0.032	0.500	0.503	0.410	0.209	15.875
		125	1.025	0.032	0.032	0.500	0.701	0.314	0.108	15.875
		130	1.125	0.032	0.032	0.500	0.823	0.334	0.090	15.875
		135	1.500	0.032	0.032	0.333	0.771	0.373	0.082	15.875
		140	1.400	0.333	0.333	0.500	0.562	0.350	0.073	15.875

Table 11-9: CHOP11B PIV error calculations

Condition		Plane (mm)	$\varepsilon_{bias,x}$ (m/s)	$\varepsilon_{bias,y}$ (m/s)	$\varepsilon_{bias,z}$ (m/s)	ε_{rand} (m/s)	$\varepsilon_{tot,x}$ (m/s)	$\varepsilon_{tot,y}$ (m/s)	$\varepsilon_{tot,z}$ (m/s)	$\varepsilon_{tot,mag}$ (m/s)	$\varepsilon_{tot,x}$ (%)	$\varepsilon_{tot,y}$ (%)	$\varepsilon_{tot,z}$ (%)	$\varepsilon_{tot,mag}$ (%)
BH	Steady	110	0.013	0.013	0.019	0.004	0.013	0.013	0.020	0.027	6.913	2.128	25.444	4.118
		115	0.013	0.013	0.019	0.004	0.013	0.013	0.020	0.027	6.177	2.920	25.117	5.318
		120	0.010	0.016	0.016	0.003	0.011	0.016	0.016	0.025	8.208	10.210	23.232	11.594
		125	0.001	0.001	0.017	0.003	0.004	0.004	0.018	0.018	1.081	2.356	32.089	5.012
		130	0.003	0.003	0.022	0.004	0.005	0.005	0.022	0.023	1.379	2.622	24.536	5.239
		135	0.009	0.001	0.022	0.005	0.010	0.005	0.022	0.025	2.622	3.027	27.372	5.913
		140	0.001	0.001	0.007	0.005	0.005	0.005	0.009	0.011	1.633	2.572	22.758	3.076
FB	Steady	110	0.001	0.001	0.001	0.002	0.002	0.002	0.002	0.004	1.972	0.686	2.231	1.077
		115	0.008	0.008	0.010	0.003	0.008	0.008	0.011	0.016	5.562	3.078	11.547	4.953
		120	0.001	0.001	0.016	0.003	0.003	0.003	0.016	0.017	1.848	1.535	19.295	6.054
		125	0.001	0.001	0.016	0.003	0.003	0.003	0.016	0.017	0.943	1.903	24.310	4.295
		130	0.001	0.001	0.010	0.003	0.003	0.003	0.011	0.012	0.726	1.860	20.724	2.382
		135	0.001	0.001	0.001	0.005	0.005	0.005	0.005	0.009	1.086	2.398	11.032	1.707
		140	0.001	0.001	0.012	0.005	0.005	0.005	0.013	0.015	1.386	2.216	21.385	3.228
EX	Peak Steady	110	0.002	0.002	0.002	0.006	0.006	0.006	0.006	0.010	1.775	0.716	3.006	1.122
		115	0.002	0.002	0.027	0.005	0.006	0.006	0.027	0.028	2.090	1.001	17.439	4.346
		120	0.002	0.002	0.031	0.007	0.007	0.007	0.032	0.034	1.376	1.688	15.399	4.934
		125	0.002	0.002	0.031	0.006	0.007	0.007	0.032	0.034	0.966	2.156	29.770	4.325
		130	0.002	0.002	0.031	0.007	0.007	0.007	0.032	0.034	0.896	2.207	35.871	3.800
		135	0.002	0.002	0.031	0.009	0.010	0.010	0.033	0.036	1.254	2.591	40.101	4.139
		140	0.021	0.021	0.031	0.009	0.023	0.023	0.033	0.046	4.052	6.507	44.805	6.891

Table 11-10: CHOP235A PIV error metrics acquired from processed data. These metrics were used in error calculations shown in the next table

Condition		Plane (mm)	D (px)	PL_x (px)	PL_y (px)	PL_z(px)	$V_{max,x}$ (m/s)	$V_{max,y}$ (m/s)	$V_{max,z}$ (m/s)	Conversion (px/m/s)
BH	Steady	67	1.15	0.5	0.5	0.5	0.113	0.154	0.09	29.048
		71	1.43	0.5	0.5	0.5	0.413	0.498	0.152	15.524
		80	1.175	0.5	0.5	0.5	0.216	0.078	0.039	29.048
		86	1.1	0.5	0.5	0.5	0.203	0.058	0.031	29.048
		89	1.2	0.5	0.5	0.5	0.207	0.083	0.021	29.048
		93	1.125	0.5	0.5	0.5	0.196	0.6	0.018	29.048
		67	1.125	0.0323	0.03226	0.0667	0.113	0.211	0.063	34.857
FB	Steady	71	1.067	0.5	0.03226	0.5	0.675	0.591	0.155	10.167
		80	1.075	0.5	0.03226	0.0323	0.198	0.309	0.2	37.765
		86	1.067	0.3333	0.03226	0.1667	0.264	0.179	0.147	34.857
		89	1.167	0.5	0.03226	0.1111	0.314	0.15	0.096	34.857
		93	1.22	0.5	0.03226	0.5	0.359	0.303	0.167	31.953
		67	1.075	0.5	0.5	0.5	0.339	0.515	0.161	17.429
		71	1.075	0.5	0.5	0.5	0.415	0.0457	0.142	17.429
EX	Peak Steady	80	0.975	0.5	0.5	0.5	0.283	0.153	0.109	34.857
		86	1.05	0.5	0.5	0.5	0.406	0.177	0.065	34.857
		89	1.1	0.5	0.2	0.5	0.37	0.338	0.199	34.857
		93	1.133	0.5	0.33333	0.5	0.331	0.124	0.095	34.857
		67	1.15	0.5	0.5	0.5	0.113	0.154	0.09	29.048
		71	1.43	0.5	0.5	0.5	0.413	0.498	0.152	15.524
		80	1.175	0.5	0.5	0.5	0.216	0.078	0.039	29.048

Table 11-11: CHOP235A PIV error calculations

Condition		Plane (mm)	$\varepsilon_{bias,x}$ (m/s)	$\varepsilon_{bias,y}$ (m/s)	$\varepsilon_{bias,z}$ (m/s)	ε_{rand} (m/s)	$\varepsilon_{tot,x}$ (m/s)	$\varepsilon_{tot,y}$ (m/s)	$\varepsilon_{tot,z}$ (m/s)	$\varepsilon_{tot,mag}$ (m/s)	$\varepsilon_{tot,x}$ (%)	$\varepsilon_{tot,y}$ (%)	$\varepsilon_{tot,z}$ (%)	$\varepsilon_{tot,mag}$ (%)
BH	Steady	67	0.017	0.017	0.017	0.004	0.018	0.018	0.018	0.031	15.630	11.469	19.625	14.488
		71	0.032	0.032	0.032	0.009	0.033	0.033	0.033	0.058	8.111	6.727	22.039	8.731
		80	0.017	0.017	0.017	0.004	0.018	0.018	0.018	0.031	8.186	22.669	45.338	13.147
		86	0.017	0.017	0.017	0.004	0.018	0.018	0.018	0.031	8.682	30.387	56.853	14.306
		89	0.017	0.017	0.017	0.004	0.018	0.018	0.018	0.031	8.552	21.327	84.294	13.687
		93	0.017	0.017	0.017	0.004	0.018	0.018	0.018	0.031	9.002	2.941	98.018	4.839
		67	0.001	0.001	0.002	0.003	0.003	0.003	0.004	0.006	2.971	1.591	5.955	2.445
FB	Steady	71	0.049	0.003	0.049	0.010	0.050	0.011	0.050	0.072	7.450	1.855	32.443	7.903
		80	0.013	0.001	0.001	0.003	0.014	0.003	0.003	0.014	6.840	0.962	1.486	3.393
		86	0.010	0.001	0.005	0.003	0.010	0.003	0.006	0.012	3.803	1.787	3.862	3.408
		89	0.014	0.001	0.003	0.003	0.015	0.003	0.005	0.016	4.691	2.316	4.815	4.384
		93	0.016	0.001	0.016	0.004	0.016	0.004	0.016	0.023	4.487	1.303	9.645	4.637
		67	0.029	0.029	0.029	0.006	0.029	0.029	0.029	0.051	8.656	5.698	18.226	7.976
		71	0.029	0.029	0.029	0.006	0.029	0.029	0.029	0.051	7.071	64.209	20.664	11.525
EX	Peak Steady	80	0.014	0.014	0.014	0.003	0.015	0.015	0.015	0.025	5.164	9.552	13.408	7.452
		86	0.014	0.014	0.014	0.003	0.015	0.015	0.015	0.025	3.610	8.281	22.550	5.671
		89	0.014	0.006	0.014	0.003	0.015	0.007	0.015	0.022	3.970	1.937	7.381	4.039
		93	0.014	0.010	0.014	0.003	0.015	0.010	0.015	0.023	4.443	8.145	15.482	6.318
		67	0.017	0.017	0.017	0.004	0.018	0.018	0.018	0.031	15.630	11.469	19.625	14.488
		71	0.032	0.032	0.032	0.009	0.033	0.033	0.033	0.058	8.111	6.727	22.039	8.731
		80	0.017	0.017	0.017	0.004	0.018	0.018	0.018	0.031	8.186	22.669	45.338	13.147

APPENDIX I: COMPREHENSIVE RESULTS SUMMARY

Table 11-12 includes a summary of all experimental conditions and results collected for all 20 time-resolved three-dimensional velocity field and hemodynamic data sets.

Table 11-12: Comprehensive results summary for all 20 time-resolved three-dimensional velocity field and hemodynamic data sets. Note the uncertainties represent a 95% confidence interval.

Model	Condition		$\dot{E}_{app}$ (mW)	iPL (x10^6)	φ (1/s^2)	$i\varphi$ (x10^{12})	HFD (%LPA)
CHOP11B	BH	Steady	6.9 ± 3.0	114.7 ± 57.3	7442.6 ± 143.9	12.08 ± 1.28	53.85 ± 8.9
		Patient-Specific	16.3 ± 5.9	290.3 ± 128.3	6272.8 ± 280.6	10.66 ± 1.21	61.06 ± 19.6
		Low Pulsatility	7.2 ± 3.0	125.0 ± 60.8	5535.3 ± 48.9	9.28 ± 0.97	71.94 ± 12.0
		High Pulsatility	20.6 ± 7.5	360.8 ± 159.7	7392.0 ± 347.3	12.43 ± 1.42	56.49 ± 6.6
	FB	Steady	30.3 ± 5.7	294.4 ± 71.0	11495.7 ± 258.5	13.05 ± 1.36	63.06 ± 14.3
		Patient-Specific	55.6 ± 9.7	418.6 ± 128.2	5586.53 ± 423.3	5.95 ± 0.77	49.78 ± 12.0
	EX	Peak Steady	290.0 ± 3.9	304.2 ± 46.2	16100.5 ± 258.5	4.14 ± 0.43	56.33 ± 5.4
		Peak Patient-Specific	278.5 ± 5.7	329.4 ± 82.6	33359.0 ± 527.2	9.30 ± 0.98	58.08 ± 5.3
		Half-Peak Steady	75.2 ± 7.6	195.4 ± 35.5	7332.0 ± 258.5	3.45 ± 0.36	50.29 ± 2.0
		Half-Peak Pulsatile	96.6 ± 8.3	268.1 ± 70.9	18850.3 ± 44.5	9.26 ± 0.97	45.45 ± 2.0
CHOP235A	BH	Steady	8.8 ± 3.2	182.2 ± 71.8	1225.4 ± 36.8	2.42 ± 0.26	40.00 ± 25.7
		Patient-Specific	18.0 ± 4.6	374.0 ± 111.1	756.3 ± 28.4	1.49 ± 0.17	54.96 ± 30.0
		Low Pulsatility	9.9 ± 4.9	206.2 ± 107.9	743.6 ± 108.6	1.48 ± 0.26	58.93 ± 41.1
		High Pulsatility	26.9 ± 7.0	501.5 ± 150.8	789.0 ± 17.6	1.45 ± 0.16	63.86 ± 36.0
	FB	Steady	15.3 ± 6.5	77.2 ± 34.8	1714.96 ± 47.9	1.32 ± 0.14	43.75 ± 42.0
		Patient-Specific	33.8 ± 14.9	170.6 ± 79.6	533.6 ± 9.0	0.41 ± 0.04	42.60 ± 35.9
	EX	Peak Steady	88.3 ± 7.8	147.9 ± 26.5	390.4 ± 8.1	0.15 ± 0.02	33.33 ± 33.3
		Peak Patient-Specific	97.9 ± 17.1	170.6 ± 39.4	807.9 ± 7.2	0.31 ± 0.03	22.72 ± 22.7
		Half-Peak Steady	49.7 ± 4.6	130.2 ± 23.1	323.5 ± 7.3	0.16 ± 0.02	21.43 ± 21.4
		Half-Peak Pulsatile	71.5 ± 9.8	185.3 ± 37.8	742.4 ± 7.9	0.37 ± 0.04	20.51 ± 20.5

REFERENCES

[1] Fontan, F., and Baudet, E., 1971, “Surgical repair of tricuspid atresia,” Thorax, **26**(3), pp. 240–8.

[2] Dick, M., Fyler, D. C., and Nadas, A. S., 1975, “Tricuspid atresia: clinical course in 101 patients.,” Am. J. Cardiol., **36**(3), pp. 327–37.

[3] d’Udekem, Y., Iyengar, A. J., Cochrane, A. D., Grigg, L. E., Ramsay, J. M., Wheaton, G. R., Penny, D. J., and Brizard, C. P., 2007, “The Fontan Procedure: Contemporary Techniques Have Improved Long-Term Outcomes,” Circulation, **116**(11_suppl), p. I-157-I-164.

[4] D’Udekem, Y., Iyengar, A. J., Galati, J. C., Forsdick, V., Weintraub, R. G., Wheaton, G. R., Bullock, A., Justo, R. N., Grigg, L. E., Sholler, G. F., Hope, S., Radford, D. J., Gentles, T. L., Celermajer, D. S., and Winlaw, D. S., 2014, “Redefining Expectations of Long-Term Survival After the Fontan Procedure: Twenty-Five Years of Follow-Up From the Entire Population of Australia and New Zealand,” Circulation, **130**(11_suppl_1), pp. S32–S38.

[5] Rychik, J., 2003, “Complications After the Fontan Operation,” Hypoplastic Left Heart Syndrome, Springer US, pp. 347–359.

[6] Khairy, P., and Mercier, L.-A., 2008, “Late Complications Following the Fontan Operation,” Diagnosis and Management of Adult Congenital Heart Disease, Elsevier, pp. 104–109.

[7] Rychik, J., 2016, “The Relentless Effects of the Fontan Paradox,” Semin. Thorac. Cardiovasc. Surg. Pediatr. Card. Surg. Annu., **19**(1), pp. 37–43.

[8] Prêtre, R., Häussler, A., Bettex, D., and Genoni, M., 2008, “Right-Sided Univentricular Cardiac Assistance in a Failing Fontan Circulation,” Ann. Thorac. Surg., **86**(3), pp. 1018–1020.

[9] Ensley, A. E., Lynch, P., Chatzimavroudis, G. P., Lucas, C. W., Sharma, S., and Yoganathan, A. P., 1999, “Toward designing the optimal total cavopulmonary connection: an in vitro study,” Ann. Thorac. Surg., **68**(4), pp. 1384–90.

[10] Haggerty, C. M., Restrepo, M., Tang, E., de Zélicourt, D. A., Sundareswaran, K. S., Mirabella, L., Bethel, J., Whitehead, K. K., Fogel, M. A., and Yoganathan, A. P., 2014, “Fontan Hemodynamics from 100 Patient-Specific Cardiac Magnetic Resonance Studies: A Computational Fluid Dynamics Analysis,” J. Thorac. Cardiovasc. Surg., **148**(4), pp. 1481–1489.

[11] Whitehead, K. K., Pekkan, K., Kitajima, H. D., Paridon, S. M., Yoganathan, A. P., and Fogel, M. A., 2007, “Nonlinear power loss during exercise in single-ventricle patients after the Fontan: insights from computational fluid dynamics.,” Circulation, **116**(11 Suppl), pp. I165-71.

[12] Hebson, C. L., McCabe, N. M., Elder, R. W., Mahle, W. T., McConnell, M., Kogon, B. E., Veledar, E., Jokhadar, M., Vincent, R. N., Sahu, A., and Book, W. M., 2013, “Hemodynamic phenotype of the failing Fontan in an adult population.,” Am. J. Cardiol., **112**(12), pp. 1943–7.

[13] Opotowsky, A. R., Halpern, D. G., Kulik, T. J., Systrom, D. M., Wu, F., Optowsky, A. R., Halpern, D. G., Kulik, T. J., Systrom, D. M., and Wu, F., 2014, “Inadequate Venous Return as a Primary Cause For Fontan Circulatory Limitation,” J. Hear. Lung Transplant., **33**(11), pp. 1–6.

[14] Rychik, J., and Goldberg, D. J., 2014, “Late Consequences of the Fontan Operation,” Circulation, **130**(17), pp. 1525–1528.
[15] Marsden, A. L., Vignon-Clementel, I. E., Chan, F. P., Feinstein, J. A., and Taylor, C. A., 2007, “Effects of exercise and respiration on hemodynamic efficiency in CFD simulations of the total cavopulmonary connection.,” Ann. Biomed. Eng., **35**(2), pp. 250–63.
[16] Kung, E., Perry, J. C., Davis, C., Migliavacca, F., Pennati, G., Giardini, A., Hsia, T.-Y., and Marsden, A. L., 2014, “Computational Modeling of Pathophysiologic Responses to Exercise in Fontan Patients.,” Ann. Biomed. Eng., **43**(6), pp. 1335–1347.
[17] Sughimoto, K., Okauchi, K., Zannino, D., Brizard, C. P., Liang, F., Sugawara, M., Liu, H., and Tsubota, K., 2015, “Total Cavopulmonary Connection is Superior to Atriopulmonary Connection Fontan in Preventing Thrombus Formation: Computer Simulation of Flow-Related Blood Coagulation,” Pediatr. Cardiol., **36**(7), pp. 1436–1441.
[18] Marsden, A. L., and Feinstein, J. A., 2015, “Computational modeling and engineering in pediatric and congenital heart disease,” Curr. Opin. Pediatr., **27**(5), pp. 587–596.
[19] de Zélicourt, D. A., Marsden, A. L., Fogel, M. A., and Yoganathan, A. P., 2010, “Imaging and patient-specific simulations for the Fontan surgery: Current methodologies and clinical applications,” Prog. Pediatr. Cardiol., **30**(1–2), pp. 31–44.
[20] Migliavacca, F., Dubini, G., Bove, E. L., and de Leval, M. R., 2003, “Computational Fluid Dynamics Simulations in Realistic 3-D Geometries of the Total Cavopulmonary Anastomosis: The Influence of the Inferior Caval Anastomosis,” J. Biomech. Eng., **125**(6), p. 805.
[21] Tang, E., and Yoganathan, A. P., 2015, “Optimizing hepatic flow distribution with the Fontan Y-graft: Lessons from computational simulations,” J. Thorac. Cardiovasc. Surg., **149**(1), pp. 255–256.
[22] Khunatorn, Y., Shandas, R., DeGroff, C. G., and Mahalingam, S., 2003, “Comparison of In Vitro Velocity Measurements in a Scaled Total Cavopulmonary Connection with Computational Predictions,” Ann. Biomed. Eng., **31**(7), pp. 810–822.
[23] de Zélicourt, D. A., Pekkan, K., Wills, L., Kanter, K. R., Forbess, J. M., Sharma, S., Fogel, M. A., and Yoganathan, A. P., 2005, “In vitro flow analysis of a patient-specific intraatrial total cavopulmonary connection.,” Ann. Thorac. Surg., **79**(6), pp. 2094–102.
[24] Santhanakrishnan, A., Maher, K. O., Tang, E., Khiabani, R. H., Johnson, J., and Yoganathan, A. P., 2013, “Hemodynamic effects of implanting a unidirectional valve in the inferior vena cava of the Fontan circulation pathway: an in vitro investigation.,” Am. J. Physiol. Heart Circ. Physiol., **305**(10), pp. H1538-47.
[25] Dur, O., Lara, M., Arnold, D., Vandenberghe, S., Keller, B. B., DeGroff, C. G., and Pekkan, K., 2009, “Pulsatile in vitro simulation of the pediatric univentricular circulation for evaluation of cardiopulmonary assist scenarios.,” Artif. Organs, **33**(11), pp. 967–76.
[26] Kim, Y. H., Walker, P. G., Fontaine, A. A., Panchal, S., Ensley, A. E., Oshinski, J.,

Sharma, S., Ha, B., Lucas, C. L., Yoganathan, A. P., Oshinkski, J., Sharma, S., Ha, B., Lucas, C. L., and Yoganathan, A. P., 1995, "Hemodynamics of the Fontan Connection: An In-Vitro Study," J. Biomech. Eng., **117**(4), p. 423.

[27] Vukicevic, M., Chiulli, J. A., Conover, T. A., Pennati, G., Hsia, T.-Y., and Figliola, R. S., 2013, "Mock circulatory system of the fontan circulation to study respiration effects on venous flow behavior.," ASAIO J., **59**(3), pp. 253–60.

[28] Sharma, S., Goudy, S., Walker, P., Panchal, S., Ensley, A. E., Kanter, K. R., Tam, V., Fyfe, D., and Yoganathan, A. P., 1996, "In vitro flow experiments for determination of optimal geometry of total cavopulmonary connection for surgical repair of children with functional single ventricle.," J. Am. Coll. Cardiol., **27**(5), pp. 1264–9.

[29] Corno, A. F., Vergara, C., Subramanian, C., Johnson, R. A., Passerini, T., Veneziani, A., Formaggia, L., Alphonso, N., Quarteroni, A., and Jarvis, J. C., 2010, "Assisted Fontan procedure: animal and in vitro models and computational fluid dynamics study," Interact. Cardiovasc. Thorac. Surg., **10**(5), pp. 679–684.

[30] Rodefeld, M. D., Boyd, J. H., Myers, C. D., LaLone, B. J., Bezruczko, A. J., Potter, A. W., and Brown, J. W., 2003, "Cavopulmonary assist: circulatory support for the univentricular fontan circulation," Ann. Thorac. Surg., **76**(6), pp. 1911–1916.

[31] Chopski, S. G., Downs, E. A., Haggerty, C. M., Yoganathan, A. P., and Throckmorton, A. L., 2011, "Laser flow measurements in an idealized total cavopulmonary connection with mechanical circulatory assistance.," Artif. Organs, **35**(11), pp. 1052–64.

[32] Figliola, R. S., Giardini, A., Conover, T. A., Camp, T. A., Biglino, G., Chiulli, J. A., and Hsia, T.-Y., 2010, "In Vitro Simulation and Validation of the Circulation with Congenital Heart Defects.," Prog. Pediatr. Cardiol., **30**(1–2), pp. 71–80.

[33] Gerdes, A., Kunze, J., Pfister, G., and Sievers, H.-H. H., 1999, "Addition of a small curvature reduces power losses across total cavopulmonary connections.," Ann. Thorac. Surg., **67**(6), pp. 1760–4.

[34] Walker, P. G., Howe, T. T., Davies, R. L., Fisher, J., and Watterson, K. G., 2000, "Distribution of hepatic venous blood in the total cavo-pulmonary connection: an in vitro study," Eur. J. Cardio-Thoracic Surg., **17**(6), pp. 658–665.

[35] Chopski, S. G., Rangus, O. M., Moskowitz, W. B., and Throckmorton, A. L., 2014, "Experimental Measurements of Energy Augmentation for Mechanical Circulatory Assistance in a Patient-Specific Fontan Model.," Artif. Organs, **38**(9), pp. 791–799.

[36] Mondésert, B., Marcotte, F., Mongeon, F.-P., Dore, A., Mercier, L.-A., Ibrahim, R., Asgar, A., Miro, J., Poirier, N., and Khairy, P., 2013, "Fontan Circulation: Success or Failure?," Can. J. Cardiol., **29**(7), pp. 811–20.

[37] Vukicevic, M., Conover, T. A., Zhou, J., Hsia, T.-Y., and Figliola, R. S., 2012, "In Vitro Study of Pulmonary Vascular Resistance in Fontan Circulation with Respiration Effects," Proceedings of the ASME 2012 Summer Bioengineering Conference, Fajardo, Puerto Rico, pp. 1–2.

[38] Vukicevic, M., Conover, T. A., Jaeggli, M., Zhou, J., Pennati, G., Hsia, T.-Y., and Figliola, R. S., 2014, "Control of respiration-driven retrograde flow in the subdiaphragmatic venous return of the Fontan circulation," ASAIO J., **60**(4), pp. 21–23.

[39] Penny, D. J., and Redington, A. N., 1991, "Doppler echocardiographic evaluation

of pulmonary blood flow after the Fontan operation: the role of the lungs.," Br. Heart J., **66**(5), pp. 372–4.

[40] Körperich, H., Barth, P., Gieseke, J., Müller, K., Burchert, W., Esdorn, H., Kececioglu, D., Beerbaum, P., and Laser, K. T., 2014, "Impact of respiration on stroke volumes in paediatric controls and in patients after Fontan procedure assessed by MR real-time phase-velocity mapping," Eur. Heart J. Cardiovasc. Imaging, pp. 1–12.

[41] Van De Bruaene, A., Claessen, G., La Gerche, A., Kung, E., Marsden, A. L., De Meester, P., Devroe, S., Bogaert, J., Claus, P., Heidbuchel, H., Budts, W., and Gewillig, M., 2015, "Effect of respiration on cardiac filling at rest and during exercise in Fontan patients: A clinical and computational modeling study," IJC Hear. Vasc., **9**, pp. 100–108.

[42] Hsia, T.-Y. Y., Khambadkone, S., Redington, A. N., Migliavacca, F., Deanfield, J. E., Leval, M. R. De, and de Leval, M. R., 2000, "Effects of Respiration and Gravity on Infradiaphragmatic Venous Flow in Normal and Fontan Patients," Circulation, **102**(III), pp. 148–153.

[43] Hjortdal, V. E. V. E., Emmertsen, K., Stenbøg, E. V, Fründ, T., Schmidt, M. R., Kromann, O., Sørensen, K. E., Pedersen, E. M., and Sorensen, K. E., 2003, "Effects of Exercise and Respiration on Blood Flow in Total Cavopulmonary Connection: A Real-Time Magnetic Resonance Flow Study," Circulation, **108**(10), pp. 1227–31.

[44] Baretta, A., Corsini, C., Marsden, A. L., Vignon-Clementel, I. E., Hsia, T.-Y., Dubini, G., Migliavacca, F., and Pennati, G., 2012, "Respiratory effects on hemodynamics in patient-specific CFD models of the Fontan circulation under exercise conditions," Eur. J. Mech. - B/Fluids, **35**, pp. 61–69.

[45] Long, C. C., Hsu, M.-C. C., Bazilevs, Y., Feinstein, J. A., and Marsden, A. L., 2012, "Fluid – structure interaction simulations of the Fontan procedure using variable wall properties," Int. j. numer. method. biomed. eng., **28**, pp. 513–527.

[46] Dur, O., Kocyildirim, E., Soran, O., Wearden, P. D., Morell, V. O., DeGroff, C. G., and Pekkan, K., 2012, "Pulsatile venous waveform quality affects the conduit performance in functional and 'failing' Fontan circulations," Cardiol. Young, **22**(3), pp. 251–62.

[47] Tang, E., Haggerty, C. M., Khiabani, R. H., de Zélicourt, D. A., Kanter, J., Sotiropoulos, F., Fogel, M. A., and Yoganathan, A. P., 2013, "Numerical and experimental investigation of pulsatile hemodynamics in the total cavopulmonary connection.," J. Biomech., **46**(2), pp. 373–82.

[48] Khiabani, R. H., Whitehead, K. K., Han, D., Restrepo, M., Tang, E., Bethel, J., Paridon, S. M., Fogel, M. A., and Yoganathan, A. P., 2014, "Exercise capacity in single-ventricle patients after Fontan correlates with haemodynamic energy loss in TCPC.," Heart, pp. 1–5.

[49] Duvernois, V., Marsden, A. L., and Shadden, S. C., 2013, "Lagrangian analysis of hemodynamics data from FSI simulation," Int. j. numer. method. biomed. eng., **29**(4), pp. 445–461.

[50] Wang, R., Lacour-Gayet, F. G., Lanning, C. J., Hunter, K. S., and Shandas, R., 2007, "Patient-Specific Fluid Structure Interaction Simulation Applied to Evaluating Hemodynamics Within the Total Cavopulmonary Connection," Proceedings of the ASME 2007 Summer Bioengineering Conference, Keystone,

Colorado, pp. 4–5.
[51] Mirabella, L., Haggerty, C. M., Passerini, T., Piccinelli, M., Powell, A. J., Del Nido, P. J., Veneziani, A., Yoganathan, A. P., and Nido, P. J. Del, 2013, "Treatment planning for a TCPC test case: A numerical investigation under rigid and moving wall assumptions," Int. j. numer. method. biomed. eng., **29**(2), pp. 197–216.
[52] Hoffman, J. I. E., and Kaplan, S., 2002, "The incidence of congenital heart disease," J. Am. Coll. Cardiol., **39**(12), pp. 1890–1900.
[53] Rychik, J., Goldberg, D. J., and Dodds, K., 2010, "Long-term results and consequences of single ventricle palliation," Prog. Pediatr. Cardiol., **29**(1), pp. 19–23.
[54] O'Leary, P. W., 2002, "Prevalence, clinical presentation and natural history of patients with single ventricle," Prog. Pediatr. Cardiol., **16**(1), pp. 31–38.
[55] Dean, P. N., Hillman, D. G., McHugh, K. E., and Gutgesell, H. P., 2011, "Inpatient costs and charges for surgical treatment of hypoplastic left heart syndrome," Pediatrics, **128**(5), pp. e1181-6.
[56] Norwood, W. I., Lang, P., Casteneda, A. R., and Campbell, D. N., 1981, "Experience with operations for hypoplastic left heart syndrome.," J. Thorac. Cardiovasc. Surg., **82**(4), pp. 511–9.
[57] Ohye, R. G., Sleeper, L. a, Mahony, L., Newburger, J. W., Pearson, G. D., Lu, M., Goldberg, C. S., Tabbutt, S., Frommelt, P. C., Ghanayem, N. S., Laussen, P. C., Rhodes, J. F., Lewis, A. B., Mital, S., Ravishankar, C., Williams, I. a, Dunbar-Masterson, C., Atz, A. M., Colan, S., Minich, L. L., Pizarro, C., Kanter, K. R., Jaggers, J., Jacobs, J. P., Krawczeski, C. D., Pike, N., McCrindle, B. W., Virzi, L., and Gaynor, J. W., 2010, "Comparison of shunt types in the Norwood procedure for single-ventricle lesions.," N. Engl. J. Med., **362**(21), pp. 1980–1992.
[58] Sano, S., Ishino, K., Kado, H., Shiokawa, Y., Sakamoto, K., Yokota, M., and Kawada, M., 2004, "Outcome of Right Ventricle–to–Pulmonary Artery Shunt in First-Stage Palliation of Hypoplastic Left Heart Syndrome: A Multi-Institutional Study," Ann. Thorac. Surg., **78**(6), pp. 1951–1958.
[59] Kreutzer, G. O., Galíndez, E., Bono, H., De Palma, C., Laura, J. P., Galindez, E., Bono, H., Palma, C. de, Laura, J. P., Galíndez, E., Bono, H., De Palma, C., and Laura, J. P., 1973, "An operation for the correction of tricuspid atresia.," J. Thorac. Cardiovasc. Surg., **66**(4), pp. 613–21.
[60] Dobell, A. R. C., Trusler, G. A., Smallhorn, J. F., and Williams, W. G., 1986, "Atrial Thrombi after the Fontan Operation," Ann. Thorac. Surg., **42**(6), pp. 664–667.
[61] Mair, D. D., Puga, F. J., and Danielson, G. K., 1992, "Late functional status of survivors of the Fontan procedure performed during the 1970s.," Circulation, **86**(5 Suppl), p. II106-9.
[62] de Leval, M. R., Kilner, P. J., Gewillig, M. H., Bull, C., and Leval, M. R. De, 1988, "Total cavopulmonary connection: a logical alternative to atriopulmonary connection for complex Fontan operations. Experimental studies and early clinical experience.," J. Thorac. Cardiovasc. Surg., **96**(5), pp. 682–695.
[63] Balaji, S., Gewillig, M., Bull, C., de Leval, M. R., and Deanfield, J. E., 1991, "Arrhythmias after the Fontan procedure. Comparison of total cavopulmonary connection and atriopulmonary connection.," Circulation, **84**(5 Suppl), p. III162-7.

[64] Stewart, R. D., Pasquali, S. K., Jacobs, J. P., Benjamin, D. K., Jaggers, J., Cheng, J., Mavroudis, C., and Jacobs, M. L., 2012, "Contemporary Fontan Operation: Association Between Early Outcome and Type of Cavopulmonary Connection," Ann. Thorac. Surg., **93**(4), pp. 1254–1261.

[65] Mair, D. D., Puga, F. J., and Danielson, G. K., 2001, "The Fontan procedure for tricuspid atresia: early and late results of a 25-year experience with 216 patients.," J. Am. Coll. Cardiol., **37**(3), pp. 933–9.

[66] Stamm, C., Friehs, I., Mayer, J. E., Zurakowski, D., Triedman, J. K., Moran, A. M., Walsh, E. P., Lock, J. E., Jonas, R. A., and del Nido, P. J., 2001, "Long-term results of the lateral tunnel Fontan operation," J. Thorac. Cardiovasc. Surg., **121**(1), pp. 28–41.

[67] Khairy, P., Fernandes, S. M., Mayer, J. E., Triedman, J. K., Walsh, E. P., Lock, J. E., and Landzberg, M. J., 2008, "Long-term survival, modes of death, and predictors of mortality in patients with Fontan surgery.," Circulation, **117**(1), pp. 85–92.

[68] Nakano, T., Kado, H., Tatewaki, H., Hinokiyama, K., Oda, S., Ushinohama, H., Sagawa, K., Nakamura, M., Fusazaki, N., and Ishikawa, S., 2015, "Results of extracardiac conduit total cavopulmonary connection in 500 patients," Eur. J. Cardio-Thoracic Surg., **48**(6), pp. 1–9.

[69] Anderson, P. A. W., Sleeper, L. A., Mahony, L., Colan, S. D., Atz, A. M., Breitbart, R. E., Gersony, W. M., Gallagher, D., Geva, T., Margossian, R., McCrindle, B. W., Paridon, S., Schwartz, M., Stylianou, M., Williams, R. V., and Clark, B. J., 2008, "Contemporary Outcomes After the Fontan Procedure," J. Am. Coll. Cardiol., **52**(2), pp. 85–98.

[70] Ohuchi, H., Negishi, J., Noritake, K., Hayama, Y., Sakaguchi, H., Miyazaki, A., Kagisaki, K., and Yamada, O., 2014, "Prognostic Value of Exercise Variables in 335 Patients after the Fontan Operation : A 23-year Single-center Experience of Cardiopulmonary Exercise Testing," Congenit. Heart Dis., **10**(2), pp. 105–116.

[71] Hjortdal, V. E., Christensen, T. D., Larsen, S. H., Emmertsen, K., and Pedersen, E. M., 2008, "Caval blood flow during supine exercise in normal and Fontan patients.," Ann. Thorac. Surg., **85**(2), pp. 599–603.

[72] Driscoll, D. J., Danielson, G. K., Puga, F. J. F. J., Schaff, H. V., Heise, C. T., and Staats, B. A., 1986, "Exercise tolerance and cardiorespiratory response to exercise after the Fontan operation for tricuspid atresia or functional single ventricle," J. Am. Coll. Cardiol., **7**(5), pp. 1087–1094.

[73] Goldberg, D. J., Shaddy, R. E., Ravishankar, C., and Rychik, J., 2011, "The failing Fontan: etiology, diagnosis and management," Expert Rev. Cardiovasc. Ther., **9**(6), pp. 785–793.

[74] Mori, M., Aguirre, A. J., Elder, R. W., Kashkouli, A., Farris, A. B., Ford, R. M., and Book, W. M., 2014, "Beyond a broken heart: circulatory dysfunction in the failing Fontan.," Pediatr. Cardiol., **35**(4), pp. 569–79.

[75] Mertens, L., Hagler, D. J., Sauer, U., Somerville, J., and Gewillig, M. H., 1998, "Protein-losing enteropathy after the Fontan operation: an international multicenter study," J. Thorac. Cardiovasc. Surg., **115**(5), pp. 1063–73.

[76] Al-Biltagi, M., Al-Kouatli, A., Al-Ata, J., Jamjoom, A., and Abouzeid, H., 2015, "Thrombosis of Extra-cardiac Fontan, an Institutional Experience," Cardiol. Angiol. An Int. J., **3**(4), pp. 192–202.

[77] Lindsay, I., Johnson, J., Everitt, M. D., Hoffman, J., and Yetman, A. T., 2014, "Impact of Liver Disease After the Fontan Operation," Am. J. Cardiol., **115**(2), pp. 249–252.
[78] Srivastava, D., Preminger, T., Lock, J. E., Mandell, V., Keane, J. F., Mayer, J. E., Kozakewich, H., and Spevak, P. J., 1995, "Hepatic Venous Blood and the Development of Pulmonary Arteriovenous Malformations in Congenital Heart Disease," Circulation, **92**(5), pp. 1217–1222.
[79] Hebert, A. H., Jensen, A. S., Mikkelsen, U. R., Idorn, L., Sorensen, K. E., Thilen, U., Hanseus, K., and Sondergaard, L., 2014, "Hemodynamic Causes for Exercise Intolerance in Fontan Patients," J. Am. Coll. Cardiol., **63**(12), p. A500.
[80] John, A. S., 2015, "Fontan Repair of Single Ventricle Physiology," Cardiol. Clin., **33**(4), pp. 559–569.
[81] Redington, A. N., 2014, "Low cardiac output due to acute right ventricular dysfunction and cardiopulmonary interactions in congenital heart disease (2013 Grover Conference series)," Pulm. Circ., **4**(2), pp. 191–199.
[82] Vallecilla, C., Khiabani, R. H., Trusty, P., Sandoval, N., Fonarow, G. C., Carlos Briceño, J., Yoganathan, A. P., Fogel, M., Carlos Briceño, J., and Yoganathan, A. P., 2015, "Exercise capacity in the bidirectional Glenn physiology: Coupling cardiac index, ventricular function and oxygen extraction ratio," J. Biomech., **48**(10), pp. 1997–2004.
[83] Patel, J. K., Loomes, K. M., Goldberg, D. J., Mercer-Rosa, L., Dodds, K., and Rychik, J., 2016, "Early Impact of Fontan Operation on Enteric Protein Loss," Ann. Thorac. Surg., **101**(3), pp. 1025–1030.
[84] Ostrow, A. M., Freeze, H., and Rychik, J., 2006, "Protein-losing enteropathy after fontan operation: investigations into possible pathophysiologic mechanisms.," Ann. Thorac. Surg., **82**(2), pp. 695–700.
[85] Shachar, G. B., Fuhrman, B. P., Wang, Y., Lucas, R. V., and Lock, J. E., 1982, "Rest and exercise hemodynamics after the Fontan procedure," Circulation, **65**(6), pp. 1043–1048.
[86] Nakazawa, M., Nakanishi, T., Okuda, H., Satomi, G., Nakae, S., Imai, Y., and Takao, A., 1984, "Dynamics of right heart flow in patients after Fontan procedure," Circulation, **69**(2), pp. 306–312.
[87] Forsdick, V., Iyengar, A. J., Carins, T., Gentles, T. L., Weintraub, R. G., Celermajer, D. S., and D'Udekem, Y., 2015, "Unsatisfactory Early and Late Outcomes After Fontan Surgery Delayed to Adolescence and Adulthood," Semin. Thorac. Cardiovasc. Surg., **27**(2), pp. 168–174.
[88] Ly, M., Roubertie, F., Kasdi, R., Chatti, S., Vergnat, M., Luu, D., Le Bret, E., Roussin, R., Capderou, A., and Belli, E., 2014, "The Modified Fontan Procedure With Use of Extracardiac Conduit in Adults: Analysis of 32 Consecutive Patients," Ann. Thorac. Surg.
[89] François, K., Vandekerckhove, K., De Groote, K., Panzer, J., De Wolf, D., De Wilde, H., and Bové, T., 2015, "Current outcomes of the bi-directional cavopulmonary anastomosis in single ventricle patients: analysis of risk factors for morbidity and mortality, and suitability for Fontan completion," Cardiol. Young, pp. 1–10.
[90] Stanton, R. E., Lurie, P. R., Lindesmith, G. G., and Meyer, B. W., 1981, "The fontan

procedure for tricuspid atresia.," Circulation, **64**(2 Pt 2), p. II140-6.

[91] Petrossian, E., Reddy, V. M., McElhinney, D. B., Akkersdijk, G. P., Moore, P., Parry, a J., Thompson, L. D., and Hanley, F. L., 1999, "Early results of the extracardiac conduit Fontan operation.," J. Thorac. Cardiovasc. Surg., **117**(4), pp. 688–96.

[92] Ford, R. M., Book, W. M., and Spivey, J. R., 2014, "Liver Disease Related to the Heart," Transplant. Rev.

[93] Stiller, B., Riedel, F., Paul, K., and van Landeghem, F. K. H., 2002, "Plastic Bronchitis in Children with Fontan Palliation: Analogue to Protein Losing Enteropathy?," Pediatr. Cardiol., **23**, pp. 90–94.

[94] Panthee, N., Murakami, A., Ando, M., Takaoka, T., and Ono, M., 2014, "Fontan Failure and Thrombosis of Total Cavo-Pulmonary Connection Conduit," J Nepal Med Assoc, **52**(194), pp. 819–821.

[95] Ovroutski, S., Nordmeyer, S., Miera, O., Ewert, P., Klimes, K., Kühne, T., and Berger, F., 2012, "Caval flow reflects Fontan hemodynamics: quantification by magnetic resonance imaging.," Clin. Res. Cardiol., **101**(2), pp. 133–8.

[96] Song, M. K., Bae, E. J., Kwon, B. S., Kim, G. B., Noh, C. Il, Choi, J. Y., Kim, W. H., Lee, J. R., and Kim, Y. J., 2015, "Intra-atrial reentrant tachycardia in Adult Patients after Fontan Operation," Int. J. Cardiol., **187**, pp. 157–163.

[97] Klimes, K., Abdul-Khaliq, H., Ovroutski, S., Hui, W., Alexi-Meskishvili, V., Spors, B., Hetzer, R., Felix, R., Lange, P. E., Berger, F., and Gutberlet, M., 2007, "Pulmonary and caval blood flow patterns in patients with intracardiac and extracardiac Fontan: a magnetic resonance study.," Clin. Res. Cardiol., **96**(3), pp. 160–7.

[98] Yu, J. J., Yun, T., Yun, S.-C., Im, Y. M., Lee, S. C., Shin, H. J., Ko, H. K., Park, J.-J., Seo, D.-M., Kim, Y.-H., Ko, J.-K., and Park, I.-S., 2013, "Low pulmonary vascular compliance predisposes post-Fontan patients to protein-losing enteropathy," Int. J. Cardiol., **165**(July 2010), pp. 454–457.

[99] Brancaccio, G., Carotti, A., D'Argenio, P., Michielon, G., and Parisi, F., 2003, "Protein-losing enteropathy after Fontan surgery: resolution after cardiac transplantation," J. Hear. Lung Transplant., **22**(4), pp. 484–486.

[100] Mori, M., Hebson, C. L., Shioda, K., Elder, R. W., Rodriguez, F., Jokhadar, M., McCabe, N., Kogon, B. E., McConnell, M., Sahu, A., and Book, W. M., 2015, "Catheter-Measured Hemodynamics of Adult Fontan Circulation: Association With Major Adverse Event," Acc, American College of Cardiology Foundation, p. A537.

[101] Grattan, M., and Mertens, L., 2015, "Mechanics of the Functionally Univentricular Heart—How Little Do We Understand and Why Does It Matter?," Can. J. Cardiol.

[102] Sundareswaran, K. S., Pekkan, K., Dasi, L. P., Whitehead, K. K., Sharma, S., Kanter, K. R., Fogel, M. A., and Yoganathan, A. P., 2008, "The total cavopulmonary connection resistance: a significant impact on single ventricle hemodynamics at rest and exercise," Am. J. Physiol. Heart Circ. Physiol., **295**(6), pp. H2427-35.

[103] Pekkan, K., Frakes, D. H., de Zélicourt, D. A., Lucas, C. W., Parks, W. J., and Yoganathan, A. P., 2005, "Coupling Pediatric Ventricle Assist Devices to the Fontan Circulation: Simulations with a Lumped-Parameter Model," ASAIO J., **51**(5), pp. 618–628.

[104] Haggerty, C. M., Fynn-Thompson, F., McElhinney, D. B., Valente, A. M.,

Saikrishnan, N., del Nido, P. J., and Yoganathan, A. P., 2012, “Experimental and Numeric Investigation of Impella Pumps as Cavopulmonary Assistance for a Failing Fontan.,” J. Thorac. Cardiovasc. Surg., **144**(3), pp. 563–9.

[105] Di Molfetta, A., Amodeo, A., Fresiello, L., Trivella, M. G., Iacobelli, R., Pilati, M., and Ferrari, G., 2015, “Simulation of Ventricular, Cavo-Pulmonary, and Biventricular Ventricular Assist Devices in Failing Fontan,” Artif. Organs, **39**(7), pp. 550–558.

[106] Fogel, M. A., Khiabani, R. H., and Yoganathan, A. P., 2013, “Imaging for Pre-Intervention Planning: Pre and Post-Fontan Procedures,” Circ. Cardiovasc. Imaging, **6**(6), pp. 1092–1101.

[107] Restrepo, M., Luffel, M., Sebring, J., Kanter, K. R., Del Nido, P. J., Veneziani, A., Rossignac, J., and Yoganathan, A. P., 2014, “Surgical Planning of the Total Cavopulmonary Connection: Robustness Analysis.,” Ann. Biomed. Eng., (i).

[108] Yang, W., 2012, “Surgical Design for the Fontan Procedure Using Computational Fluid Dynamics and Derivative-Free Optimization,” University of California, San Diego.

[109] Galdi, G. P., Rannacher, R., Robertson, A. M., and Turek, S., 2008, Hemodynamical Flows: Modeling, Analysis and Simulation, Birkhauser.

[110] Arbia, G., 2014, “Multiscale modeling of blood flow in the context of congenital heart disease,” University of Pierre and Marie Curie.

[111] Marsden, A. L., and Esmaily-Moghadam, M., 2015, “Multiscale Modeling of Cardiovascular Flows for Clinical Decision Support,” Appl. Mech. Rev., **67**(3), p. 30804.

[112] Taylor, C. A., and Figueroa, C. A., 2009, “Patient-specific modeling of cardiovascular mechanics.,” Annu. Rev. Biomed. Eng., **11**, pp. 109–34.

[113] Watrous, R. L., and Chin, A. J., 2014, “Model-Based Comparison of the Normal and Fontan Circulatory Systems: Part I: Development of a General Purpose, Interactive Cardiovascular Model,” World J. Pediatr. Congenit. Hear. Surg., **5**(3), pp. 372–384.

[114] Marsden, A. L., Bazilevs, Y., Long, C. C., and Behr, M., 2014, “Recent advances in computational methodology for simulation of mechanical circulatory assist devices,” Wiley Interdiscip. Rev. Syst. Biol. Med., p. n/a-n/a.

[115] Delorme, Y. T., Anupindi, K., Kerlo, A. E. A.-E. M., Shetty, D. A., Rodefeld, M. D., Chen, J., and Frankel, S. H., 2013, “Large Eddy Simulation of Powered Fontan Hemodynamics,” J. Biomech., **46**(2), pp. 408–22.

[116] Esmaily Moghadam, M., Vignon-Clementel, I. E., Figliola, R. S., Marsden, A. L., and Esmaily-Moghadam, M., 2013, “A modular numerical method for implicit 0D/3D coupling in cardiovascular finite element simulations,” J. Comput. Phys., **244**, pp. 63–79.

[117] Koeken, Y., Arts, T., and Delhaas, T., 2012, “Simulation of the Fontan circulation during rest and exercise.,” Conf. Proc. IEEE Eng. Med. Biol. Soc., **2012**, pp. 6673–6.

[118] DeGroff, C. G., 2008, “Modeling the Fontan circulation: where we are and where we need to go.,” Pediatr. Cardiol., **29**(1), pp. 3–12.

[119] Masters, J. C., Ketner, M., Bleiweis, M. S., Mill, M., Yoganathan, A., and Lucas, C. L., 2004, “The Effect of Incorporating Vessel Compliance in a Computational

Model of Blood Flow in a Total Cavopulmonary Connection (TCPC) with Caval Centerline Offset," J. Biomech. Eng., **126**(6), p. 709.

[120] DeGroff, C. G., Birnbaum, B., Shandas, R., Orlando, W., and Hertzberg, J. R., 2005, "Computational simulations of the total cavo-pulmonary connection: insights in optimizing numerical solutions.," Med. Eng. Phys., **27**(2), pp. 135–46.

[121] Wang, C., Pekkan, K., de Zélicourt, D. A., Horner, M., Parihar, A., Kulkarni, A., and Yoganathan, A. P., 2007, "Progress in the CFD modeling of flow instabilities in anatomical total cavopulmonary connections.," Ann. Biomed. Eng., **35**(11), pp. 1840–56.

[122] Takizawa, K., Bazilevs, Y., Tezduyar, T. E., Long, C. C., Marsden, A. L., and Schjodt, K., 2014, "Patient-Specific Cardiovascular Fluid Mechanics Analysis with the ST and ALE-VMS Methods," pp. 71–102.

[123] Baretta, A., Corsini, C., Yang, W., Vignon-Clementel, I. E., Marsden, A. L., Feinstein, J. A., Hsia, T.-Y. T.-Y. T.-Y., Dubini, G., Migliavacca, F., Pennati, G., and Modeling of Congenital Hearts Alliance (MOCHA) Investigators, 2011, "Virtual surgeries in patients with congenital heart disease: a multi-scale modelling test case," Philos. Trans. R. Soc. A Math. Phys. Eng. Sci., **369**(1954), pp. 4316–4330.

[124] Liu, J. J., Qian, Y., Sun, Q., Liu, J. J., and Umezu, M., 2013, "Use of computational fluid dynamics to estimate hemodynamic effects of respiration on hypoplastic left heart syndrome surgery: total cavopulmonary connection treatments.," Sci. World J., **2013**, p. 131597.

[125] Honda, T., Itatani, K., Takanashi, M., Kitagawa, A., Ando, H., Kimura, S., Nakahata, Y., Oka, N., Miyaji, K., and Ishii, M., 2016, "Contributions of Respiration and Heartbeat to the Pulmonary Blood Flow in the Fontan Circulation," Ann. Thorac. Surg.

[126] Khiabani, R. H., Whitehead, K., Losse, J., Fogel, M., and Yoganathan, A., 2014, "The Effects of Respiration on Flow in the Fontan Pathway Using Real Time Phase Contrast Magnetic Resonance Imaging At Resting Conditions," J. Am. Coll. Cardiol., **63**(12), p. A1039.

[127] Lucas, C., Mill, M., Lucas, W., Sadoff, J., Hoffmann, S., Ketner, M., Masters, J., Wilcox, B., Ensley, A., and Yoganathan, A., 1999, "Modeling the Fontan circulation: a computer simulation of the effects of respiration," Proceedings of the First Joint BMES/EMBS Conference. 1999 IEEE Engineering in Medicine and Biology 21st Annual Conference and the 1999 Annual Fall Meeting of the Biomedical Engineering Society (Cat. No.99CH37015), IEEE, p. 344.

[128] Gewillig, M. H., Lundström, U. R., Bull, C., Wyse, R. K. H., and Deanfield, J. E., 1990, "Exercise responses in patients with congenital heart disease after fontan repair: Patterns and determinants of performance," J. Am. Coll. Cardiol., **15**(6), pp. 1424–1432.

[129] Dulfer, K., Duppen, N., Kuipers, I. M., Schokking, M., van Domburg, R. T., Verhulst, F. C., Helbing, W. a, and Utens, E. M. W. J., 2014, "Aerobic exercise influences quality of life of children and youngsters with congenital heart disease: a randomized controlled trial.," J. Adolesc. Health, **55**(1), pp. 65–72.

[130] Van De Bruaene, A., La Gerche, A., Claessen, G., De Meester, P., Devroe, S., Gillijns, H., Bogaert, J., Claus, P., Heidbuchel, H., Gewillig, M. H., and Budts, W.,

2014, “Sildenafil improves exercise hemodynamics in Fontan patients.,” Circ. Cardiovasc. Imaging, **7**(2), pp. 265–73.

[131] Apostolopoulou, S. C., Papagiannis, J., and Rammos, S., 2005, “Bosentan induces clinical, exercise and hemodynamic improvement in a pre-transplant patient with plastic bronchitis after Fontan operation.,” J. Hear. Lung Transplant., **24**(8), pp. 1174–6.

[132] Yang, W., Feinstein, J. A., and Marsden, A. L., 2010, “Constrained optimization of an idealized Y-shaped baffle for the Fontan surgery at rest and exercise,” Comput. Methods Appl. Mech. Eng., **199**(33–36), pp. 2135–2149.

[133] Kung, E., Pennati, G., Migliavacca, F., Hsia, T.-Y., Figliola, R. S., Marsden, A. L., and Giardini, A., 2014, “A Simulation Protocol For Exercise Physiology In Fontan Patients Using A Closed-Loop Lumped-Parameter Model.,” J. Biomech. Eng., **136**(August), pp. 1–13.

[134] Bossers, S. S. M., Cibis, M., Gijsen, F. J., Schokking, M., Strengers, J. L. M., Verhaart, R. F., Moelker, A., Wentzel, J. J., and Helbing, W. a, 2014, “Computational fluid dynamics in Fontan patients to evaluate power loss during simulated exercise.,” Heart, **100**(9), pp. 696–701.

[135] Wei, Z., Whitehead, K. K., Khiabani, R. H., Tree, M., Tang, E., Paridon, S. M., Fogel, M. A., and Yoganathan, A. P., 2016, “Respiratory Effects on Fontan Circulation During Rest and Exercise Using Real-Time Cardiac Magnetic Resonance Imaging,” Ann. Thorac. Surg., **101**(5), pp. 1818–1825.

[136] Lin, H.-Y. Y., Bender, J. A., Ding, Y., Chung, Y.-C. C., Hinton, A. M., Pennell, M. L., Whitehead, K. K., Raman, S. V., and Simonetti, O. P., 2012, “Shared velocity encoding: A method to improve the temporal resolution of phase-contrast velocity measurements,” Magn. Reson. Med., **68**(3), pp. 703–710.

[137] Yushkevich, P. A., Piven, J., Hazlett, H. C., Smith, R. G., Ho, S., Gee, J. C., and Gerig, G., 2006, “User-guided 3D active contour segmentation of anatomical structures: significantly improved efficiency and reliability.,” Neuroimage, **31**(3), pp. 1116–28.

[138] Heiberg, E., Sjoegren, J., Ugandar, M., Carlsson, M., Engblom, H., and Arheden, H., 2010, “Design and validation of Segment -- freely available software for cardiovascular image analysis,” BMC Med. Imaging, **10**(1).

[139] Naeije, R., and Chesler, N., 2012, “Pulmonary circulation at exercise.,” Compr. Physiol., **2**(1), pp. 711–41.

[140] Papaharilaou, Y., Doorly, D. J., and Sherwin, S. J., 2001, “Assessing the accuracy of two-dimensional phase-contrast MRI measurements of complex unsteady flows,” J. Magn. Reson. Imaging, **14**(6), pp. 714–723.

[141] Figliola, R. S., and Beasley, D. E., 2011, Theory and Design for Mechanical Measurements, John Wiley & Sons.

[142] Raffel, M., Willert, C., Wereley, S., and Kompenhans, J., 2007, Particle Image Velocimetry: A Practical Guide, Springer-Verlag, Berlin.

[143] Tang, T. L. E., 2015, “Effect of Geometry, Respiration and Vessel Deformability on Fontan Hemodynamics: a Numerical Investigation,” Georgia Institute of Technology.

[144] De Zélicourt, D. A., Haggerty, C. M., Sundareswaran, K. S., Whited, B. S., Rossignac, J. R., Kanter, K. R., Gaynor, J. W., Spray, T. L., Sotiropoulos, F., Fogel,

M. A., and Yoganathan, A. P., 2011, “Individualized computer-based surgical planning to address pulmonary arteriovenous malformations in patients with a single ventricle with an interrupted inferior vena cava and azygous continuation,” J. Thorac. Cardiovasc. Surg., **141**(5), pp. 1170–1177.

[145] Duppen, N., Kapusta, L., de Rijke, Y. B. B., Snoeren, M., Kuipers, I. M. M., Koopman, L. P. L. P., Blank, A. C. C., Blom, N. A. A., Dulfer, K., Utens, E. M. W. J. M. W. J., Hopman, M. T. E. T. E., and Helbing, W. A. W. A., 2014, “The effect of exercise training on cardiac remodelling in children and young adults with corrected tetralogy of Fallot or Fontan circulation: A randomized controlled trial,” Int. J. Cardiol., **179**, pp. 97–104.

[146] Henaine, R., Vergnat, M., Bacha, E. A., Baudet, B., Lambert, V., Belli, E., and Serraf, A., 2013, “Effects of lack of pulsatility on pulmonary endothelial function in the Fontan circulation,” J. Thorac. Cardiovasc. Surg., **146**(3), pp. 522–529.

[147] Khiabani, R. H., Restrepo, M., Tang, E., de Zélicourt, D. A., Sotiropoulos, F., Fogel, M. A., and Yoganathan, A. P., 2012, “Effect of flow pulsatility on modeling the hemodynamics in the total cavopulmonary connection.,” J. Biomech., **45**(14), pp. 2376–81.

[148] Wei, Z. (Alan), Trusty, P. M., Tree, M., Haggerty, C. M., Tang, E., Fogel, M., and Yoganathan, A. P., 2016, “Can time-averaged flow boundary conditions be used to meet the clinical timeline for Fontan surgical planning?,” J. Biomech.

[149] Womersley, J. R., 1955, “Method for the Calculation of Velocity, Rate of Flow and Viscous Drag in Arteries when the Pressure Gradient is Known,” J. Physiol., **127**(3), pp. 553–563.

[150] Dur, O., DeGroff, C. G., Keller, B. B., and Pekkan, K., 2010, “Optimization of inflow waveform phase-difference for minimized total cavopulmonary power loss,” J. Biomech. Eng., **132**(3), p. 31012.

[151] Soerensen, D. D., Pekkan, K., Sundareswaran, K. S., and Yoganathan, A. P., 2004, “New power loss optimized Fontan connection evaluated by calculation of power loss using high resolution PC-MRI and CFD.,” Conf. Proc. IEEE Eng. Med. Biol. Soc., **2**, pp. 1144–7.

[152] Cibis, M., Jarvis, K., Markl, M., Rose, M., Rigsby, C., Barker, A. J., and Wentzel, J. J., 2015, “The effect of resolution on viscous dissipation measured with 4D flow MRI in patients with Fontan circulation: Evaluation using computational fluid dynamics,” J. Biomech., **48**(12), pp. 2984–2989.

[153] Munson, B. R., Young, D. F., and Okiishi, T. H., 2006, Fundamentals of Fluid Mechanics, John Wiley & Sons.

[154] Ha, H., Kim, G. B., Kweon, J., Lee, S. J., Kim, Y.-H., Lee, D. H., Yang, D. H., and Kim, N., 2016, “Hemodynamic Measurement Using Four-Dimensional Phase-Contrast MRI: Quantification of Hemodynamic Parameters and Clinical Applications,” Korean J. Radiol., **17**(4), p. 445.

[155] Stankovic, Z., Allen, B. D., Garcia, J., Jarvis, K. B., and Markl, M., 2014, “4D flow imaging with MRI.,” Cardiovasc. Diagn. Ther., **4**(2), pp. 173–192.

[156] Gewillig, M., and Brown, S. C., 2016, “The Fontan circulation after 45 years: update in physiology,” Heart, **102**, pp. 1081–1086.

[157] Tree, M., Trusty, P., Munz, B., Samuel, M., Slesnick, T., Maher, K. O., Yoganathan, A. P., and Deshpande, S. R., 2016, “In Vitro Examination of the

HeartWare Circulite VAD in the Fontan Circulation," J. Hear. Lung Transplant., **35**(4), p. S46.

VITA

MICHAEL V. TREE

TREE was born in West Lafayette, Indiana. He attended public schools in Columbus, IN and Orem, UT. He received a B.S. in Mechanical Engineering from Brigham Young University, Provo, Utah in 2011 before coming to Georgia Tech to pursue a doctorate in Mechanical Engineering. When he is not working on his research, Mr. Tree enjoys spending time with his wife and daughters and playing basketball.